DYNAMICS AND CONTROL OF AMMONIA-WATER ABSORPTION HEAT PUMPS

A Dissertation
Presented to
The Academic Faculty

by

Anurag Goyal

In Partial Fulfillment
of the Requirements for the Degree
Doctor of Philosophy in Mechanical Engineering

Georgia Institute of Technology
December 2018

DYNAMICS AND CONTROL OF AMMONIA-WATER ABSORPTION HEAT PUMPS

Approved by:

Dr. Srinivas Garimella, Advisor
G.W. Woodruff School of Mechanical Engineering
Georgia Institute of Technology

Dr. Thomas F. Fuller
School of Chemical and Biomolecular Engineering
Georgia Institute of Technology

Dr. Sheldon M. Jeter
G.W. Woodruff School of Mechanical Engineering
Georgia Institute of Technology

Dr. James E. Braun
School of Mechanical Engineering
Purdue University

Dr. Satish Kumar
G.W. Woodruff School of Mechanical Engineering
Georgia Institute of Technology

Date Approved: October 15, 2018

To my family

ACKNOWLEDGEMENTS

I am thankful to my advisor, Dr. Srinivas Garimella. He has generously supported me through this research and graduate school while constantly urging me to do my best and push the boundaries. It has been a pleasure knowing him and working with him as a mentor, advisor, and a colleague. I would also like to thank the members of my PhD committee: Dr. Sheldon Jeter, Dr. Satish Kumar, Dr. Thomas Fuller, and Dr. James Braun. Their guidance at critical junctures and a fresh viewpoint to address some of the technical challenges have helped me improve this dissertation.

This work would also not be possible without the incredible colleagues at the Sustainable Thermal Systems Lab. They have been one of the most passionate researchers that I have interacted with and have always been helpful to discuss problems, troubleshoot experiments and participate in all sorts of discussions and conversations. While I have received help from many students (past and present), I would like to particularly thank Dr. Alexander Rattner and Dr. Christopher Keinath for introducing me to the research in absorption systems and shaping my early phase in both computational and experimental research. I would also like to thank Dr. Dhruv Hoysall, Dr. Marcel Staedter, Mikko Ponkala, Dan Kromer, Girish Kini and Alex Roeder for engaging conversations on myriad research topics and helping me troubleshoot my programs and experiments.

I could not have accomplished this work without the support of my family and friends. My parents have been a constant source of support and always provided motivation to stay focused on my goal. Their unconditional love and unwavering faith in my abilities always lifted me during challenging times. My sister, Shilpi, has been a wonderful role

model throughout my career and has always been helpful in guiding my effort whenever I would start to feel lost. My brother-in-law, Nitin, has been a constant example of perseverance and excellence in research, and I hope that I continue to learn from him. Most importantly, I would like to thank my wife, Apurva. She has been incredibly calm and loving, an endless source of support and inspiration, and a sink for lot of my winded conversations. I cannot imagine accomplishing this without her being on my side as my partner and my best friend. I have a lot to learn from her, and I am greatly indebted to her for her patience, kindness and strength.

TABLE OF CONTENTS

LIST OF TABLES

LIST OF FIGURES

LIST OF SYMBOLS AND ABBREVIATIONS

Variables

A	Area (m^2)
ANN	Artificial Neural Networks
a	Integration bounds
BR	Bayesian Regularization
b	Neuron bias
C	Heat Capacity ($J\ K^{-1}$)
CF	Coupling Fluid
COP	Coefficient of Performance (-)
Cp	Specific heat capacity ($kJ\ kg^{-1}\ K^{-1}$)
C_v	Valve coefficient ($kg^{1/2}m^{1/2}$)
CV	Control Volume
D_h	Hydraulic Diameter (m)
DAE	Differential-algebraic Equation
EoS	Equation of State
e	Specific internal energy ($J\ kg^{-1}$)/error value for controller
FD	Finite Difference
FF	Feedforward
FV	Finite Volume
f	Functional representation of system of equations
f_b	Body force vector ($m\ s^{-2}$)
G	Thermodynamic property relation/ Integrand function

g	Output transformation function
HVAC	Heating, Ventilation and Air-conditioning
h	Specific enthalpy (kJ kg^{-1})
K	Sample points/Switching Parameter/Controller Gain
k	Thermal conductivity (W m^{-1} K^{-1})
L	Zone length (m)
MB	Moving-boundary
MIMO	Multiple-input Multiple-output
MPC	Model Predictive Control
MSE	Mean Squared Error
M/m	Mass (kg)
$\dot{m}$	Mass flow rate (kg s^{-1})
N/n	Number of variables, equations or nodes
NTU	Number of Transferred Units (-)
ODE	Ordinary Differential Equations
P	Pressure (kPa) / Proportional
PDE	Partial Differential Equation
Pe (= $RePr$)	Peclet Number
PI	Proportional-Integral
PID	Proportional-Integral-Derivative
Per	Channel perimeter (m)
Pr	Prandtl Number (-)
$\dot{Q}$	Volumetric heat transfer rate (J m^{-3} s^{-1})
$q``$	Heat flux vector (J m^{-2} s^{-1})

q	Vapor mass quality (kg kg^{-1})
R	Correlation Coefficient
RPC	Refrigerant pre-cooler
Re	Reynolds Number
SHX	Solution Heat Exchanger
SIMO	Single-input Multiple-output
SISO	Single-input Single-output
s	Axial velocity (m s^{-1})
T	Temperature (K or °C)
t	Time (s)
U	Heat transfer coefficient (W m^{-2} K^{-1})
UA	Heat transfer conductance (W K^{-1})
UDS	Upwind Differencing Scheme
u	Specific internal energy (kJ kg^{-1})
V	Volume (m^3)
VAS	Vapor Absorption System
VCS	Vapor Compression System
VLE	Vapor-liquid Equilibrium
v	Specific volume (m^3 kg^{-1})
w	Weight factor for neurons/ Axial velocity (m s^{-1})
x	ANN input/Ammonia mass fraction mixture or liquid (kg kg^{-1})
Y	State vector
y	Process Variable/ANN predicted variable/Ammonia mass fraction vapor (kg kg^{-1})
z	Axial coordinate (m)

Subscripts/Superscripts

1	Lower limit of integration
2	Upper limit of integration
2p	Two-phase zone
2p-sc	Zone transition interface
abs	Absorber
acc	Accumulator
actual	Training data
air	Air for final heat rejection
amb	ambient
approach	Approach Temperature
avg	Average
ch	Channel
cf	Coupling fluid
conc	Concentrated solution
cond	Condenser
cs	Cross Section/ Concentrated solution
des	Desorption, Desorber
dil/ds	Dilute Solution
evap	Evaporator
f	Working fluid/Refrigerant
final	Final time instant
fit	Curve fit
glide	Temperature glide
guess	Guess value

high	High-pressure side
i,j	Index/Node/CV boundary/Integral
in	Inlet
L, l, liq	Liquid
LM	Logarithmic Mean
low	Low-pressure side
max	Maximum
min	Minimum
out	Outlet
overall	Averaged over the entire component
p	Proportional
rec	Rectifier
ref	Refrigerant
SP	Set-point
s	Switch
sat	Saturated phase
sc	Subcooled phase/zone
seg	Segment
sh	Superheated phase/sheet
train	ANN training
V, v, vap	Vapor
vol	Volumetric
w/hx	Heat exchanger wall
*	Thermal equilibrium

Greek Symbols

α	Overrelaxation parameter
Δ	Change
δ	Perturbation from equilibrium
ε	Heat exchanger effectiveness (-)/Vapor Tray Efficiency (-)
φ	Angle subtended by half channel arc
γ	Mean void fraction (-)
ρ	Density (kg m^{-3})
σ	Stress tensor (kg $m^{-1}s^{-2}$)
τ	Shear stress tensor (kg $m^{-1}s^{-2}$)
ξ	Normalized zone length (m m^{-1})

SUMMARY

An investigation of dynamic modeling and control of small-scale absorption heat pumps is presented. Previous studies on small-capacity absorption systems demonstrated that these systems often operate under varying conditions of cooling demand and ambient temperatures. Therefore, it is important to develop control methodologies to maintain the desired performance metrics. The first step in this study involved a comprehensive review of the literature to identify the existing transient modeling and control methodologies for heat pump systems. The review included both vapor compression and absorption systems. Most of the reported studies focused on vapor compression technology as it is very widespread. Advanced control and simulation tools for vapor compression systems were identified. The research on absorption system controls was identified to be sparse and lacking the level of detail and technological development in comparison to the vapor compression systems. The literature review identified thrust areas for research on the control of absorption systems and avenues for cross-over applicability of techniques used for vapor compression systems. A detailed roadmap for advancing the state-of-the-art of controls for absorption systems was developed.

Previous studies that involved dynamic modeling of ammonia-water systems utilized iterative procedures to calculate the thermodynamic properties of the fluid mixture at various operating points of the system. Transient simulations that are used to study long duration of system response can involve millions of such property calculations. Iterative property libraries contribute significantly to the computational overhead in such simulations in addition to the non-linear system of conservation equations. Therefore, a rapid property computation method using artificial neural network (ANN) was developed. Large sets of thermodynamic property data were utilized to develop explicit functions for calculating thermodynamic properties. The new method provided up to 60% reduction in the computational time compared to the iterative methods.

Transient modeling methods for different components of an ammonia-water absorption system were developed to evaluate the time constants of different processes. It was identified in the literature review that several modeling approaches exist for vapor compression systems with a relatively fewer number of studies on absorption systems. In this study, the dynamic modeling approach was revisited to address two key aspects. First, to reduce the complexity of these models while maintaining accuracy to capture the effects essential for a control system, and second, to improve the computational efficiency. The first aspect is addressed through the development of detailed, discretized models of different components. These segmented models provide high resolution of property variation along the fluid flow path inside the component. The models included effects of both mass and energy storage inside the fluid volume and the heat exchanger wall material. To simplify the segmented models, it was assumed that the microscale geometries utilized in the small-scale systems led to negligible changes in the stored mass inside the fluid channel. The results from this simplified model demonstrated good agreement with the detailed model and validated the assumption.

Reduced-order modeling methods were developed to assist in the design of control algorithms and improve the computational efficiency. A moving-boundary method that lumped the fluid properties in each flow region of the two-phase flow was developed. This significantly reduced the computational expense (~60 times) while maintaining accuracy in the predicted properties at the outlet of the heat exchanger. The model compared well with the detailed segmented model. A similar reduced-order model was developed for the desorber component that utilized concepts from diabatic distillation columns. The desorber model agreed well with experimental data and provided accurate prediction of vapor generation rates and composition of outlet streams.

The second aspect of the transient modeling research involved identification of efficient solvers for the resulting system of differential algebraic equations (DAE). These equations can be stiff or non-stiff depending on the component that is modeled. Commonly used explicit solvers are

inefficient in solving such systems of equations. The present study identified and evaluated advanced implicit solvers that provide stable, fast and accurate solutions for such models.

Previous research identified the desorber heat source temperature and flow rate as important process variables for the control of the system. In this study, both the steady-state models and transient models were used to identify additional control degrees of freedom such as the expansion valve positions and the solution circulation rate. A system dynamic model was used to develop feedback control algorithms. The algorithms modulated the refrigerant expansion valve position to optimize the heat transfer performance of the evaporator. A second control loop modulated the desorption temperature to continuously vary the capacity of the system at part-load operation and at varying ambient temperatures. The control algorithms demonstrated improved performance of the system with good reference tracking. The COP of the system was predicted to improve by ~8% due to a 5°C decrease in the ambient temperature in comparison to a system operating without active controls. This study demonstrated the potential for energy savings and performance improvement using feedback controls.

Finally, a breadboard facility (2.6 kW design cooling capacity at a COP of ~0.6) was fabricated to evaluate the performance of different control algorithms and validate the models. The breadboard absorption chiller utilized an electrically heated mineral oil loop as the heat source for the desorber allowing simulation of different types of heat sources. The condenser and absorber were hydronically coupled and allowed flexibility in investigating the effects of varying ambient temperatures. Finally, an electrically heated water loop served as the heat source for the evaporator and enabled simulation of different cooling demands. The system included electronic expansion valves and variable speed pumps for the flow of ammonia-water mixture and the desorber heat source. These actuators allowed the utilization of all control degrees of freedom. A programmable controller was used to implement the control algorithms and continuous data acquisition.

Detailed experiments were conducted to quantify the effects of perturbations in different input variables such as the concentrated solution flow rate, heat source conditions and ambient temperatures. The experiments demonstrated the relative magnitude of the effect of these input variables on the performance of the system and allowed for synthesis of parameters for different control loops. Using this information, a multivariable feedback algorithm is developed and implemented. The capacity control loop utilizes the feedback of the supplied coolant temperature and manipulates the solution circulation rate, and the desorber heat source conditions to achieve the desired temperature of the supplied coolant. Two separate performance control loops are also implemented to monitor and regulate the performance of the desorber and evaporator. These control loops provide continuous turndown of the system capacity to as low as 50% of the design capacity while maintaining the COP at near-design values. The response to step changes in demand and ambient conditions is fast, stable and repeatable. The control algorithms developed in this study utilize few temperature measurements in the system, and therefore, are inexpensive to implement.

CHAPTER 1. INTRODUCTION

Energy consumption for heating, ventilation and air conditioning (HVAC) and thermal comfort in buildings amounts to ~10% of total electricity consumption in the world, and ~20% of electricity use in buildings. With increasing demands for air-conditioning systems, in part due to rising per-capita-income, and therefore improving standard of living in hotter regions of the world, coupled with rapid manufacturing of HVAC systems, the electrical energy required for HVAC is projected to more than triple by 2050 (IEA, 2018). US residential electricity usage is ~30% of the total electricity generation in the country (EIA, 2016). Of this electricity usage, ~36% is used for HVAC and water heating applications (EIA, 2014). A significant amount of energy (~60%) is rejected as heat or wasted in conversion losses. This rejected heat presents a significant avenue for waste heat recovery applications. Absorption heat pumps provide an alternative to the convectional electrically driven vapor compression systems (VCS). Vapor absorption systems (VAS) can utilize a variety of heat sources such as waste heat streams, solar-thermal energy, and geothermal energy, in addition to burning fossil fuels to provide cooling and heating. These systems can significantly reduce the dependence on electricity, and consequently on fossil fuels. Moreover, the working fluids for these systems can be selected to have zero global warming potential, making them environmentally benign compared to the conventional VCS using synthetic refrigerants (Srikhirin *et al.*, 2001). Despite these advantages, large scale commercialization of VAS has not occurred, and their use has been limited to large industrial applications or district heating and cooling plants.

VAS have been studied for over a century. Various cycle configurations (single-, double-, and triple- effect and generator-absorber heat exchange (GAX)) for these systems have been investigated. More complex cycles provide enhancement in system efficiency or coefficient of performance (COP) but are difficult to implement and operate in practice. The simplest configuration for these systems is a single-effect cycle (Herold *et al.*, 2016). It consists of a high-temperature heat source to supply the heat of desorption, a medium-temperature sink for rejection of heat of absorption and condensation, and a low-temperature source for the heat of evaporation for the refrigerant. The working fluid in the system is a binary mixture of absorbent and refrigerant. The single-effect cycle is a two-pressure system. The liquid mixture is pumped to the high-temperature and pressure desorber where the more volatile refrigerant is separated by application of heat. Refrigerant vapor is condensed in the condenser and the heat of condensation is released. Liquid refrigerant at high-pressure is throttled through an expansion device and provides cooling in the evaporator. The dilute solution from the desorber expands to the low-pressure side of the system and absorbs the refrigerant vapor in the absorber where the heat of absorption is released. The cycle is completed as the solution mixture is regenerated. The single-effect cycle efficiency is improved by adding recuperative heat exchangers on the solution and the refrigerant stream for internal heat recovery. Figure 1.1 shows schematics of VCS and VAS.

Advances in microscale heat and mass exchangers were exploited for VAS by Determan and Garimella (2012), Keinath (2015) and Garimella *et al.* (2016)for the development of a microscale cooling system, a residential-scale heat pump water heater, and a residential chiller, respectively. Residential- and small-scale mobile HVAC systems

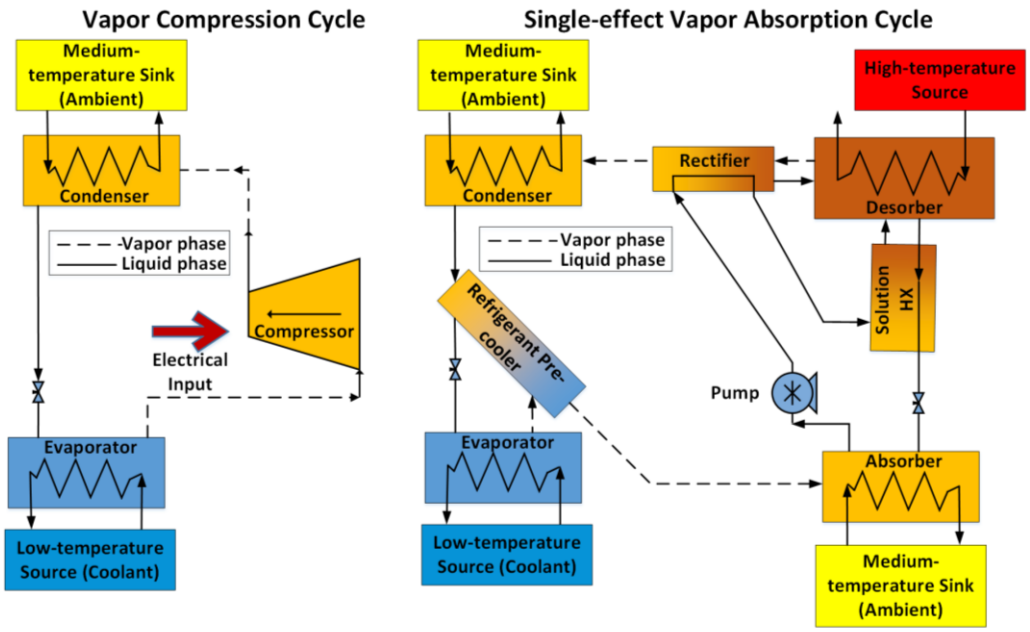

Figure 1.1: Schematics of vapor compression and single-effect absorption cycle

often operate under varying operating conditions of cooling/heating load and ambient temperature. Especially in waste-heat-driven systems, the waste heat rate and temperature can vary over wide ranges. These applications need a well-designed control system to optimize system performance over the range of operating conditions.

1.1 Transient Analysis and Control of Absorption Systems

The characterization of the transient behavior of heat pumps is important to understand the time response of the system due to variations in the manipulated variables and the associated control actions. Moreover, transient models can be implemented in real-time controllers to predict the system response a priori and provide appropriate control decisions. For the development and analysis of control algorithms, a transient model needs to capture the key system variables yet be computationally inexpensive for implementing control algorithms of varying complexity. The underlying requirement for any control

system is the ease of implementation in the real system. For most applications, a low-order controller is preferred for implementation using a digital computer (Anderson, 1993). This can be achieved either by using a reduced order system (plant) model or simplifying a higher order controller obtained from a detailed system model. Both approaches necessitate reliable prediction of transient system performance and time evolution of controlled variables in response to control actions.

There are several approaches for modeling transient behavior of thermo-fluid systems. The available methods span from simplified lumped parameter type models to very detailed discretized models. Comprehensive reviews of system modeling approaches can be found in the papers by Bendapudi and Braun (2002), Rasmussen (2012), and Afram and Janabi-Sharifi (2014a). The main challenge in transient simulation of heat pump systems is the modeling of different heat and mass exchange components in the system. The heat exchangers used in these systems typically operate with multiple fluid phases. Moreover, the components in a VAS, such as the desorber and rectifier, can contain multiple inlets and/or outlets. The resulting system of equations from conservation principles is coupled and non-linear, and is a combination of differential and algebraic equations. Advanced numerical solvers are typically used for these systems of equations. Finally, the zeotropic mixtures used as the working-fluid in VAS introduce the additional complexity of computing complex thermodynamic properties at each state-point and time step. These challenges must be addressed to develop an accurate and computationally efficient transient model to predict the response of VAS.

Current modeling techniques for VAS are limited to simplified lumped parameter models or data-based models. The accuracy of these models and their ability to be applied

for a general class of absorption systems is very limited. There is a need for developing accurate and computationally efficient transient models for absorption heat pumps. Computational efficiency can be increased by developing reduced-order models that can characterize the key parameters of the system, such as thermal capacitances and fluid flow regimes, to guide the control algorithms. Information obtained from these models is crucial in identifying the design of a system-wide control scheme to optimize the performance.

Research on the control of VAS is limited and seemingly unorganized in the literature. The control system forms a critical component if the technology has to progress as a viable alternative to the existing heat pump technologies for residential and mobile applications. Some of the earlier studies on the control of absorption heat pumps investigated on/off operation, open-loop controls, and thermodynamic optimization of the models to achieve better performance. On/off control based on variations in the duty cycle applies, with certain limitations, to VCS because the compressor dynamics are much faster than those of heat exchangers. However, for thermally driven systems, turning the heat source on/off leads to the loss of the pressure differential in the system between these switching cycles. It takes significantly amount of time to restore the system performance due to the thermal inertia of various components, and therefore this approach leads to energy losses.

The control systems for absorption systems are still very simplified and rely on basic on/off type control and single-input single-output (SISO) feedback loops. Some researchers have investigated thermodynamic optimization-based system identification, but the resulting control methodologies are not generalizable. Due to the strongly coupled dynamics between different components of VAS, it is evident that absorption heat pump

controls require more sophisticated logic. Advanced control algorithms can potentially improve system performance over a wider range of operating conditions and extend the envelope of system operation. The energy savings through active control, especially during part-load and off-design operation, can add to the value proposition of these systems. Finally, a well-designed control system can accelerate the commercialization of absorption heat pumps leading to efficient utilization of otherwise neglected sources of thermal energy and waste-heat streams.

1.2 Research Scope and Objectives

The objective of this study is to develop modeling tools for predicting the transient performance of VAS and devise control algorithms for small-capacity absorption heat pump systems. The desired characteristics of the transient system model and the control system are:

- Rapid computations and accurate prediction of component and overall system performance.
- Generalized transient modeling that accounts for relevant capacitance terms that characterize the mass and energy transport delay in different components.
- Reduced-order models to assist in the design and analysis of control algorithms.
- Control algorithms designed using the information obtained from transient model simulations
- Stable and fast control of desired system parameters leading to extension of the operating envelope of the system

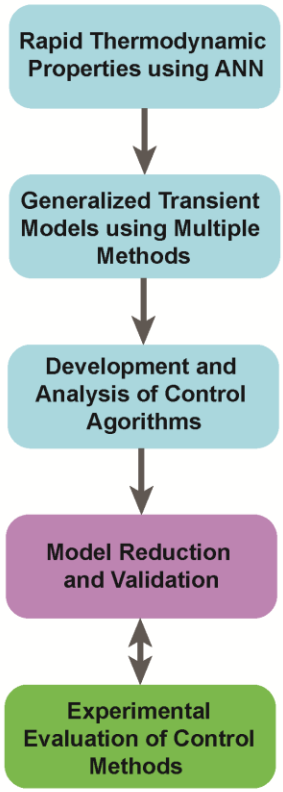

Figure 1.2: Research objectives and approach

Figure 1.2 shows a schematic of the approach used in this study.

- Previously developed cycle and component heat transfer models are used to identify the physical and heat transfer parameters of different components of a small-scale ammonia-water VAS.
- Computation of thermodynamic properties is identified as a significant bottleneck in the overall computational expense. Available property libraries for ammonia-water mixtures utilize iterative solvers that can require significant computational time during transient simulations. Rapid thermodynamic property routines are developed using artificial neural networks (ANN) that provide a significant computational speed-up.

- A comprehensive evaluation of various generalized modeling approaches is performed to identify computational bottlenecks. Single inlet/outlet heat exchangers such as the condenser, evaporator and absorber are modeled using detailed discretized methods to obtain performance results and property variations at high resolution. Simultaneously, a reduced-order moving-boundary approach is developed for these components and its performance is compared with the predictions of detailed models.
- A detailed model for the desorber component is developed to account for the specific flow configuration of liquid-vapor counterflow. The resulting model is solved using advanced numerical solvers designed specifically for the stiff system of differential-algebraic equations (DAEs).
- A transient system model is utilized to evaluate feedback control algorithms and their performance is assessed using simulations of real operating scenarios. The simulations also assist in the identification of controller gains that are ultimately used in the experimental evaluation.
- A test facility is fabricated to implement the proposed control algorithms on a complete ammonia-water absorption chiller. The breadboard system is optimized at the baseline to achieve the desired performance. The control hardware and actuators are programmed using a flexible user interface that allows evaluation of multiple control algorithms in a repeatable manner. The control algorithms are evaluated to study the system response to the two most common operating scenarios: part-load operation and varying ambient conditions.

- Finally, analyses of model reduction techniques and comparison of the transient performance of individual component and subsystem models are presented.

1.3 Organization of Thesis

The rest of the thesis is organized as follows:

- Chapter 2 presents a detailed survey of the literature to identify the current practices and deficiencies in the areas of dynamic modeling and control of VAS.
- Chapter 3 presents the development of an artificial neural network based thermodynamic property library for ammonia-water mixtures. The proposed method drastically reduces the computational time for the calculation of thermodynamic properties.
- Chapter 4 describes the methods and results from component level transient models for different components of an ammonia-water VAS. The governing equations, modeling assumptions and characteristic features of various components are presented along with simulation test cases. Multiple modeling approaches such as the spatially discretized finite volume method and the lumped parameter moving-boundary method are discussed, and their performance is compared.
- Chapter 5 presents the control algorithms developed using the system transient model and their performance is demonstrated using realistic operating scenarios simulated using the model.
- Chapter 6 describes the details of a breadboard absorption cooling system and the implementation of various control algorithms in the experiments. Advanced

feedback control algorithms are implemented, and their performance is characterized through test cases involving load variation and changes in ambient conditions.

- Chapter 7 describes the details of the model reduction process. Experimental data are also used to validate the performance of the transient models developed for the different components of the system.
- Chapter 8 summarizes the important conclusions from this research. Lastly, recommendations for future research are discussed.

CHAPTER 2. REVIEW OF DYNAMICS AND CONTROL OF HEAT PUMPS

This chapter presents a review of the literature on transient modeling and control of heat pump systems. Various methods for modeling heat pump components and overall systems with their applications in VCS and VAS are discussed. A detailed review of current practices in the control of VCS and VAS is presented. The review identifies cross-over applicability of control techniques from VCS to VAS. Lastly, the scope and objectives of the present study are identified.

2.1 Dynamic Modeling of Heat Pumps

Transient simulation of heat exchangers and complete heat pump systems has been an active area of research for the past 50 years. It is important to understand the time response of the system performance as the operating conditions and control inputs change. It is also a very powerful tool for the design and analysis of controllers for these systems that can lead to improved efficiencies. These models can be incorporated in real-time controllers to predict the system performance in response to predicted changes in operating conditions and input parameters. However, the hardware implementation requires the transient model to be computationally inexpensive, while maintaining reasonable accuracy to predict key phenomena.

Comprehensive reviews of system modeling approaches can be found in Bendapudi and Braun (2002), Rasmussen (2012), and Afram and Janabi-Sharifi (2014a). The main

This chapter adapted from: Goyal, A., Staedter, M. A., Garimella, S., A review of control methodologies for vapor compression and absorption heat pumps, International Journal of Refrigeration (2018), DOI: https://doi.org/10.1016/j.ijrefrig.2018.08.026

challenge in the transient simulation of heat pump systems is the modeling of different heat and mass exchange components in the system. The heat exchangers used in these systems typically operate with multiple fluid phases. The non-linear system of conservation equations is solved using different approaches. Modeling of heat exchangers follows similar techniques across different types of (electrically or thermally driven) HVAC systems. There are several approaches for modeling these systems, ranging from simplified lumped parameter type models to very detailed discretized models. Figure 2.1 shows the different modeling paradigms for heat pump systems. This study focusses on physics-based modeling approaches, specifically discussing the moving-boundary and discretized methods. Therefore black – and grey – box modeling methods are not presented.

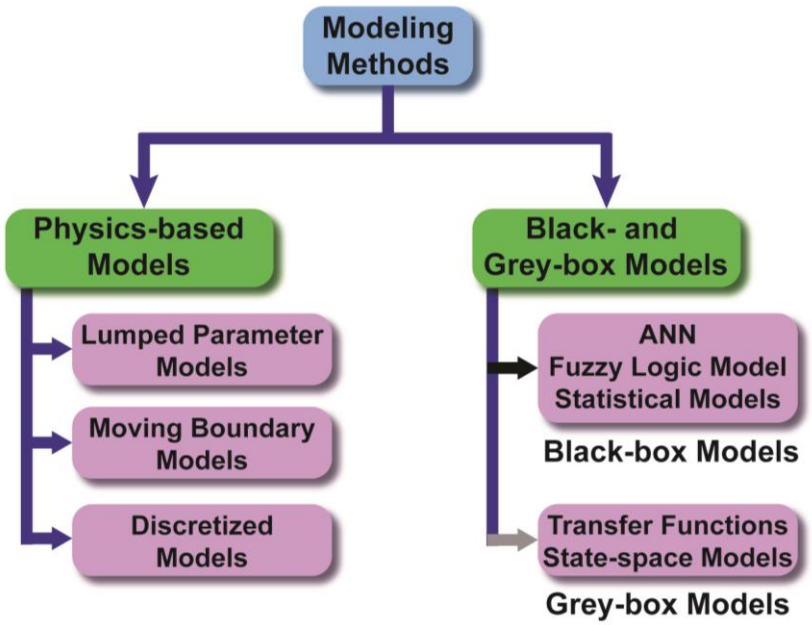

Figure 2.1: Classification of dynamic modeling approaches for heat pumps

2.1.1 Lumped Parameter Models

Lumped parameter models form a class of physics-based models where the property variations inside the heat exchanger are averaged over the entire spatial domain of the heat exchanger. This approach significantly reduces the computational expense and leads to reduced-order models suitable for model-based control design. Dhar and Soedel (1979) first presented a lumped parameter model for a vapor compression system (VCS). They neglected pressure drop in individual heat exchangers and therefore simplified the model by neglecting the momentum conservation equation. No experimental validation for the model was provided. Chi and Didion (1982) performed a lumped parameter simulation of a VCS and validated the results with experimental data. They concluded that detailed models will be required to capture the effects of compressibility and two-phase mixture properties. Sami *et al.* (1987) developed a lumped parameter model for heat pump systems using conservation equations for mass, momentum and energy. The two-phase zone model accounted for the slip between the phases as well, and good agreement was observed with experimental data. Yao *et al.* (2013) presented a lumped parameter model for a VCS and observed that the model predictions agreed with experiments within 10%. The governing differential equations of conservation principles were converted to a state-space notation by linearization and averaging of properties.

Lumped parameter modeling for absorption heat pumps has been investigated by many researchers in the past, mainly due to its lower computational cost. Among the first reported works on transient simulation of vapor absorption system (VAS) is the paper by Anand *et al.* (1982). They presented a transient model for water-lithium bromide (H_2O-LiBr) systems using a simplified transfer function and time delay for individual

components. The model was able to predict the start-up and spin-down operation of the chiller; however, detailed analysis of steady-state control was not discussed. Kaushik *et al.* (1985) presented a dynamic model of an ammonia-water VAS based on lumped parameter modeling. The model incorporated fluid mass storage in a sump as well as in the heat exchangers. Butz and Stephan (1989) presented a dynamic modeling method for absorptions systems. Mass storage inside most components was neglected. The approach involved a combination of discretized and lumped parameter models. They noted that the system of DAEs resulting from the discretized ordinary differential equations (ODE) required a special solver; however, few details of the actual solution and modeling procedure were provided. Vargas *et al.* (1998) developed a lumped parameter model for an NH_3-H_2O absorption system and designed feedback control loops guided by the transient model. Jeong (1999) presented a lumped parameter dynamic model for a H_2O-LiBr absorption system. All components were modeled as operating with saturated state fluid (pure or mixture). The model was used to evaluate system response as the operating conditions varied. Fu *et al.* (2006) presented results from a modular, object-oriented model for absorption systems. Two-phase heat and mass exchange components were modeled using a lumped approach and single-phase components were modeled as discretized systems. Kim and Park (2007) discussed a lumped-parameter model for a single-effect NH_3-H_2O absorption system and investigated typical start-up time constants. The model accounted for the thermal capacitance of only the desorber (refrigerant generating component). Kohlenbach and Ziegler (2008a, 2008b) discussed a transient modeling method for a complete H_2O-LiBr system using lumped parameter models and a thermal transport delay to account for species and mass storage in various fluid sumps. Component-

wide mass, species and energy balances were used to model the different components. Mean temperature values for external and internal sides of the system were used to model heat transfer. Experimental validation demonstrated dependence of model outputs on external source/sink temperatures, and the results differed more as the conditions varied from the baseline. Cai *et al.* (2012) presented a lumped parameter model for an ammonia-water system and accounted for pressure drop in different components. Other researchers (Bian *et al.*, 2005; Matsushima *et al.*, 2010; Monné *et al.*, 2011; Borg and Kelly, 2012; N'Tsoukpoe *et al.*, 2012; Zinet *et al.*, 2012; Evola *et al.*, 2013; Iranmanesh and Mehrabian, 2013; Marc *et al.*, 2015) also discussed lumped parameter models for H_2O-LiBr systems. Lumped parameter modeling of H_2O-LiBr systems is an attractive option because the refrigerant is pure water and therefore, the computational challenges owing to the thermodynamic properties (temperature glide during phase change and absorbent volatility) of ammonia-water are not encountered. However, most lumped parameter models that average the properties for the entire component are unable to predict experimental observations accurately as key dynamics and physics of two-phase heat exchangers are not modeled adequately. Several models use empirical correction factors to account for dynamics that are not modeled.

2.1.2 Discretized Models

On the other end of the spectrum of detail are discretized models, using finite volume (FV) or finite difference (FD) method, which divide the component into multiple control volumes. The governing equations are discretized using numerical differencing schemes and a system of simultaneous equations is solved to simulate the time response. Apart from profile assumptions for numerical differencing methods, these models are very detailed and

can be used to accurately predict and analyze property variation over smaller spatial and temporal scales. The increase in accuracy is achieved at the cost of a greater computational cost and more complex higher-order models. Several researchers investigated discretized models for VCS. Gruhle and Isermann (1985) presented an evaporator model and included momentum conservation as well. They also discussed a methodology for the control of the expansion valve. MacArthur and Grald (1989) developed a detailed discretized model of an evaporator (neglected momentum equation) and also validated the results using experiments. Wang and Touber (1991) included the momentum equation in their model of a dry-expansion evaporator and noted the importance of void fraction computations on the predictions of the overall model. Sami and Comeau (1992) developed a model for zeotropic refrigerant mixtures and included the effects of slip between different phases. Nyers and Stoyan (1994) and Jia *et al.* (1995) included the momentum conservation equation in their models and pointed toward the need for iterative DAE solvers for solving the final set of equations. Mithraratne *et al.* (2000) presented an FV model of an evaporator (neglected momentum equation) and its control using a thermostatic expansion valve. They also investigated the dynamics and the consequent hunting of the refrigerant expansion valve. Koury *et al.* (2001) and Kim *et al.* (2004) presented simulations of full systems modeled using the FV method. Garcıa-Valladares *et al.* (2004) simulated a double-pipe heat exchanger and included momentum conservation and radial discretization in the pipe wall and insulation. Partial validation with experimental data was also provided. Bendapudi *et al.* (2005) presented a discretized FV model of a VCS with experimental validation. Their model did not account for momentum conservation. Detailed model formulation and methods for numerical solution were discussed. Hermes and Melo (2008) presented a

detailed review of modeling and simulation techniques, and simulated the response of a household refrigerator. Beghi and Cecchinato (2009) developed a discretized FD model of a fin-coil evaporator using refrigerant R404a and used it to tune the controller for the electronic expansion valve.

Several researchers used detailed discretized models for VAS. However, due to the presence of additional components and binary working-fluid mixtures, these models are more complex than VCS models. Shin *et al.* (2009) presented a model of an H_2O-LiBr VAS and used it to develop control algorithms. Other researchers (Vinther *et al.*, 2015a; Ochoa *et al.*, 2016; Xu *et al.*, 2016) also used the discretized approach to simulate the response of H_2O-LiBr systems. Viswanathan *et al.* (2013) used the FV method to model and simulate an NH_3-H_2O VAS. Their model accounted for thermal capacitance of the heat exchanger structure and fluid inventory. The model required considerably long simulation times as every component was modeled in a discretized manner. For system-level transient simulations, detailed discretized models are computationally very expensive. To simplify the models, the momentum conservation equation is typically neglected as the pressure loss in the component is a small fraction of system operating pressures. These models are seldom used for controller design but focus on understanding the system and component level dynamics.

2.1.3 Moving-boundary Method

The moving-boundary (MB) method belongs to the general category of lumped parameter models. However, in this approach, the fluid properties are averaged in each individual fluid phase, and the interface between different phases is tracked. Each fluid

phase region is modeled as a separate control volume and the governing PDEs for conservation of mass and energy are integrated over the control volume boundaries. This results in a system of fewer ODEs and significantly reduces the computational expense while providing important details about phase boundaries and transient component performance (Bendapudi *et al.*, 2008). Most studies neglect the momentum conservation equation to simplify the formulation.

Several researchers studied MB models for VCS. Broersen and van der Jagt (1980) simulated the response of an evaporator using an MB model and discussed the implementation of controls using a thermostatic expansion valve. Grald and MacArthur (1992) presented a detailed model outlining the MB method for a vapor compression system. Two key assumptions in their model were: negligible dependence of latent heat of vaporization of the refrigerant with pressure, and time-invariant mean void-fraction for the two-phase region as described by Wedekind *et al.* (1978). When the inlet and outlet qualities are constant in a heat exchanger, the mean void fraction can be assumed to be time invariant. The evaporator model simulated the response of a liquid-coupled, counter-flow heat exchanger. Typical test cases involving inlet mass flow rate variation and the resulting outlet superheat variation indicated satisfactory performance. Additionally, a full-system model was also developed. He *et al.* (1997) and He *et al.* (1998) used a moving-boundary based VCS model to design multivariable feedback controllers. The models were used for their computational advantage over the discretized models. They were implemented in a state-space form to enable a compact and modular structure and allow linearization for controller design. However, they did not include capabilities to address large transients, which lead to the need for modifications in the equation structure for each

component. Willatzen *et al.* (1998) and Pettit *et al.* (1998) presented an MB model for an evaporator and presented simulation results involving larger transients. They discussed event handling constraints when a fluid regime would appear or disappear using refrigerant enthalpy as the switching parameter. A differential-algebraic equation (DAE) solver (Brenan *et al.*, 1995) was used to solve the system of equations in Maple® (Maplesoft, 1998). They discussed numerical integration methods for these ill-conditioned systems of equations. A simple controller was also implemented to demonstrate the capability of the model for use in such applications.

Several researchers improved the basic MB models. Munch Jensen and Tummescheit (2002) used a detailed void fraction model and studied its effect on the overall model. Key assumptions used in obtaining a time-varying void fraction were: the vapor generation rate is assumed to be uniform or a linear profile of quality is assumed, and the slip velocity ratio is assumed to be constant in the two-phase region (Zivi, 1964). Analysis of different dynamic modes revealed key aspects of fast and slow modes and their importance in the design of a controller. The slow modes were associated with large capacitance terms, generally arising from wall thermal capacitance values and average void fraction. They suggested simplifications to the models by assuming wall and fluid temperatures to be equal and neglecting the dynamics of the superheated region for the evaporator. The simulations were performed using Dymola® (Elmqvist *et al.*, 1996). Leducq *et al.* (2003) presented a transient model for a VCS. The average void fraction in two-phase region was calculated using an empirical correlation and assuming a linear variation of quality. The wall temperature was assumed to be constant along the length of the two-phase region. An extended MB model that incorporated the momentum conservation equation for solar

collector evaporators was developed by Yebra *et al.* (2005). It was also pointed out that MB models can mitigate chattering in two-phase simulations as compared to discretized methods because the phase transitions and property derivatives near phase transitions are not computed. Lei and Zaheeruddin (2005) presented a simplified lumped-parameter model of a water chiller by simplifying MB models and considering only the dominant fluid regimes in a heat exchanger. Their model for the condenser only included the two-phase region as it was considered to be the dominant region. For the evaporator, they considered the two-phase and superheated regions. Rasmussen and Alleyne (2006) presented an MB model for VCS. The model was developed to simulate transients in the neighborhood of the design operating point. The model could be easily linearized and advanced control algorithms were developed. Zhang and Zhang (2006) extended the model developed by Pettit *et al.* (1998) to include larger disturbances and ensured robustness through the use of a time varying void fraction. They assumed a linear variation of vapor mass quality in the two-phase region to calculate an average void fraction. Switching between different modes of evaporator operation was implemented in a continuous manner using the length of superheated region in the evaporator as the criterion. The model was implemented on the Dymola® (Elmqvist *et al.*, 1996) platform. Llopis *et al.* (2008) utilized a lumped parameter model for a condenser and tracked the volume of each zone in the condenser. However, it was unclear if the heat transfer area in the model varied for each region as well.

Eldredge *et al.* (2008) presented an extended MB model with the capability to handle variable fluid outlet phases using accumulators at the outlet of the heat exchangers. This approach did not require variable equation structure to handle large transients. McKinley

and Alleyne (2008) presented an MB model for a VCS condenser with continuous switching to simulate large transients. As discussed earlier, large transients can make the MB models numerically unstable. The switching criteria developed by them was a combination of the absolute value of switching variables (zone length and mean void fraction) and also the time derivative of these variables to ensure that the variables move above or below the threshold and continued to move in that direction. The model was developed on MATLAB® and Simulink™ platform (The Mathworks Inc., 2016). Li and Alleyne (2010) extended the model presented by McKinley and Alleyne (2008) to include start-up and shut-down transients and included a more versatile equation structure to model all likely operating scenarios of a VCS. Schurt *et al.* (2009) used an MB model to simulate the response of a double-pipe counterflow heat exchanger without including the thermal capacitance of the wall. Cecchinato and Mancini (2012) presented a switched MB model for an evaporator. To ensure mass conservation at all time steps, they presented a different choice of state variables, including the mean evaporator density instead of void fraction. As void fraction is a strong function of quality and is computed using empirical correlations, the errors introduced during transients can be large when void fraction is used as a state variable. Switching is accomplished using the density and length of the superheated zone. Qiao *et al.* (2014) discussed an MB model formulation including pressure drop in the heat exchanger. Their switching criterion combined the refrigerant outlet enthalpy and average void fraction. Bonilla *et al.* (2015) presented a detailed review of MB models and presented switched models for simulating condensers and evaporators using the enthalpy and length of the CV that is disappearing or reappearing as the switching variables. The model was developed using Modelica® (Modelica Association, 2010). Yao

et al. (2015) discussed a compact state-space representation of the VCS model using the MB method. The key objective was to demonstrate the utility of such models in the analysis of control schemes through linearization. Rodriguez and Rasmussen (2016) presented reduced-order models for heat exchangers used in VCS and compared the computational efficiency and accuracy of different approaches. In particular, their emphasis was on a non-linear reduced-order model that offers significant savings in the computational cost and maintains the high accuracy offered by full-scale, discretized models. Recently, Rodriguez and Rasmussen (2017) discussed different switching paradigms for the MB method applied to evaporator simulations. They identified the effect of threshold values on stability and accuracy of the models. It was observed that the void fraction and density-based switching criteria provided higher accuracy and stability as compared to the enthalpy-based switching criterion.

There are very few detailed studies on transient simulation of absorption heat pumps using the MB method, and only the work by Ryu (2011) on the simulation of a combined gas-turbine absorption cycle is noteworthy as it presents a discussion on modifying the conventional MB method to apply it to ammonia-water systems by incorporating new thermodynamic property data. However, most assumptions from the MB models for single-component working fluid systems were retained. Experimental validation of the MB method is still an area of active research.

Table 2.1 and Table 2.2 summarize the research on transient models for VCS and VAS, respectively. It can be observed that several control schemes have resulted from different system dynamic models, and the complexity of the algorithms varies as the modeling paradigm changes. Typically, simpler models resulting from the lumped-

parameter or moving-boundary method are preferred for the design and analysis of control algorithms due to their simplicity and computational efficiency. Simultaneously, reduced-order models can assist control engineers in system identification, linearization, and identification of dead time and time constants for different components and processes, all of which can be utilized in a computationally efficient controller.

Table 2.1: Summary of transient models for vapor compression systems

Author(s)	System	Modeling Method	Remarks	Experimental Validation
Dhar and Soedel (1979)	VC System	Lumped Parameter	Momentum equation neglected	No
Chi and Didion (1982)	VC System	Lumped Parameter	Momentum equation included	Yes
Sami *et al.* (1987)	VC System	Lumped Parameter with Drift-flux Model	Momentum equation included	Yes
Yao *et al.* (2013)	VC System	Lumped Parameter	Momentum equation neglected	Yes
Outtagarts *et al.* (1997)	VC System Evaporator	Transfer Function	Gain-scheduled PID and optimal qualitative regulation (OQR) implemented	Yes
Finn and Doyle (2000)	VC System Evaporator	Transfer Function	Feedback control strategies with tuning	Yes
Gruhle and Isermann (1985)	VC System Evaporator	Discretized FD	Momentum equation included; PI feedback controller for expansion valve	Partial Validation
MacArthur and Grald (1989)	VC System	Discretized FV	Momentum equation neglected	Yes
Bendapudi *et al.* (2005)	VC System	Discretized FD	Momentum equation neglected	Yes

Table 2.1: Summary of transient models for vapor compression systems (continued)

Author(s)	System	Modeling Method	Remarks	Experimental Validation
Beghi and Cecchinato (2009)	VC Evaporator	Discretized FV	Momentum equation included; Auto-tuning PID	Yes
Grald and MacArthur (1992)	VC System	Moving Boundary	Momentum equation neglected	Partial Validation
He *et al.* (1997)	VC System	Moving Boundary	Momentum equation neglected; Multivariable feedback control	Yes
Willatzen *et al.* (1998); Pettit *et al.* (1998)	VC System Evaporator	Moving Boundary	Momentum equation neglected; PI controller for expansion valve	Yes
Munch Jensen and Tummescheit (2002)	VC System Evaporator	Moving Boundary	Momentum equation neglected	No
Leducq *et al.* (2003)	VC System	Moving Boundary	Momentum equation neglected	Yes
Rasmussen and Alleyne (2004)	Trans-critical VC system	Moving Boundary	Momentum equation neglected	Yes
Rasmussen and Alleyne (2006)	VC System	Moving Boundary	Momentum equation neglected; Gain-scheduled MIMO control	Yes

Table 2.1: Summary of transient models for vapor compression systems (continued)

Author(s)	System	Modeling Method	Remarks	Experimental Validation
Zhang and Zhang (2006)	VC System Evaporator	Generalized Moving Boundary for large transients	Momentum equation neglected	No
Llopis *et al.* (2008)	VC System	Moving boundary	Momentum equation neglected	Yes
McKinley and Alleyne (2008)	Condenser	Switched Moving Boundary	Momentum equation neglected	No
Wei *et al.* (2008)	Organic Rankine Cycle	Moving Boundary and Discretized Models	Momentum equation neglected	Yes
Li and Alleyne (2010)	VC System	Switched Moving boundary with start-stop dynamics	Momentum equation neglected	Yes
Cecchinato and Mancini (2012)	VC system Evaporator	Switched Moving-boundary	Momentum equation neglected	Partial Validation
Bonilla *et al.* (2015)	VC System	Non-linear Switched Moving Boundary	Momentum equation neglected	Yes
Yao *et al.* (2015)	VC System	Moving Boundary with state-space formulation	Momentum equation neglected	Yes

Table 2.2: Summary of transient models for absorption systems

Author(s)	System	Modeling Method	Remarks	Experimental Validation
Anand *et al.* (1982)	H_2O-LiBr System	Time Constants for Thermal Masses	Momentum equation neglected	Yes
Kaushik *et al.* (1985)	NH_3-H_2O System	Lumped Parameter	Momentum equation neglected; accounted for charge storage	No
Butz and Stephan (1989)	Absorption System	Discretized + Lumped Parameter	Momentum equation neglected; controls using isolation valves and heat source modulation	Yes
Sami and Comeau (1992)	Systems with Zeotropic Mixtures	Discretized FD	Momentum equation neglected	Yes
Jeong *et al.* (1998)	H_2O-LiBr System	Lumped Parameter	Momentum equation neglected	Yes
Vargas *et al.* (1998)	Absorption Systems	Lumped Parameter	Momentum equation neglected; On/Off control and power law feedback control	Yes
Jeong (1999)	H_2O-LiBr System	Lumped Parameter	Momentum equation neglected; Control using heat source modulation	Partial validation
Bian *et al.* (2005)	Absorption systems	Lumped Parameter	Momentum equation neglected	Partial validation

Table 2.2: Summary of transient models for absorption systems (continued)

Author(s)	System	Modeling Method	Remarks	Experimental Validation
Fu *et al.* (2006)	Absorption Systems	Discretized + Lumped Parameter	Static pressure drop included	Yes
Kim and Park (2007)	NH_3-H_2O System	Lumped Parameter	Momentum equation included; Heat source modulation	Yes
Kohlenbach and Ziegler (2008a); Kohlenbach and Ziegler (2008b)	H_2O-LiBr System	Lumped Parameter with Thermal Transport Delay	Static pressure drop included	Yes
Shin *et al.* (2009)	H_2O-LiBr System	Discretized + Lumped Parameter	Momentum equation neglected; Heat Source temperature control; dilute solution cycling	Partial validation
Matsushima *et al.* (2010)	H_2O-LiBr System	Object-Oriented Lumped Parameter	Momentum equation neglected	Yes
Cai *et al.* (2012)	NH_3-H_2O System	Lumped Parameter	Momentum equation included	No
Monné *et al.* (2011)	H_2O-LiBr System	Object-Oriented TRNSYS (Laboratory and Klein, 1979) Model	Momentum equation included	Yes
Ryu (2011)	NH_3-H_2O System	Moving Boundary	Momentum equation neglected	No

Table 2.2: Summary of transient models for absorption systems (continued)

Author(s)	System	Modeling Method	Remarks	Experimental Validation
Borg and Kelly (2012)	H_2O-LiBr System	Lumped Parameter + Data for Calibration	Momentum equation neglected	Yes
N'Tsoukpoe *et al.* (2012)	H_2O-LiBr System	Lumped Parameter	Momentum equation neglected	No
Zinet *et al.* (2012)	H_2O-LiBr System	Lumped Parameter	Momentum equation neglected; Temperature control for part-load	No
Evola *et al.* (2013)	H_2O-LiBr System	Lumped Parameter	Momentum equation neglected	Yes
Iranmanesh and Mehrabian (2013)	H_2O-LiBr System	Lumped Parameter	Momentum equation neglected	No
Viswanathan *et al.* (2013)	NH_3-H_2O System	Discretized FV	Momentum equation neglected	No
Marc *et al.* (2015)	H_2O-LiBr System	Lumped Parameter	Momentum equation neglected	Yes
Vinther *et al.* (2015a)	H_2O-LiBr System	Discretized FV	Momentum equation neglected; Evaporator coolant flow control	Yes
Ochoa *et al.* (2016)	H_2O-LiBr System	Discretized FD	Momentum equation neglected	Yes

Table 2.2: Summary of transient models for absorption systems (continued)

Author(s)	System	Modeling Method	Remarks	Experimental Validation
Xu *et al.* (2016)	H_2O-LiBr System	Discretized + Lumped Parameter	Momentum equation neglected; PID control on chilled water delivery temperature	Yes

2.2 Control of VCS

The main objective for a controller is performance regulation and optimization of the system. Heat pump performance can be characterized as adequately meeting required cooling and heating capacity at a specified temperature. The control system must quickly and reliably accommodate external disturbances such as ambient conditions and demand variation. Figure 2.2 shows the broad classification of control methodologies for heat pump systems. The following sections will elaborate on these methods in the context of VCS and VAS.

Control systems for VCS have been extensively investigated. The studies range from understanding the dynamics of the system to implementing control algorithms for efficient operation. This section presents an analysis of degrees of freedom and a review of key research on control system development for VCS. Detailed reviews of typical HVAC

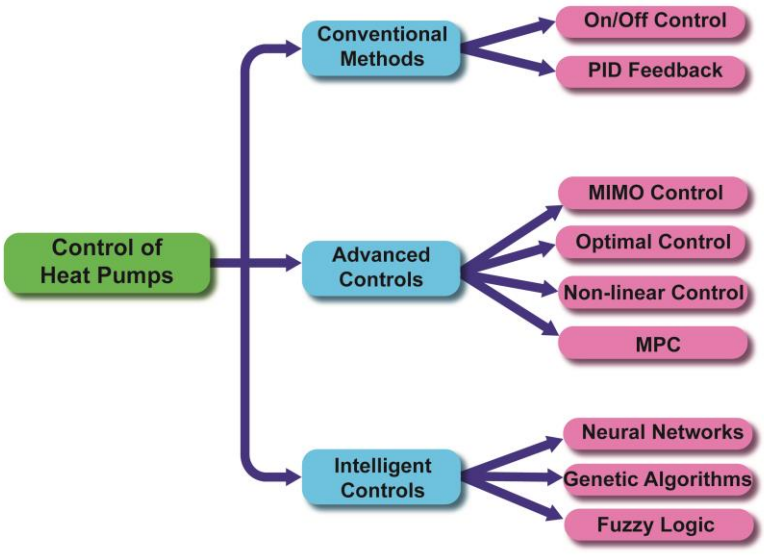

Figure 2.2: Classification of control methodologies for heat pump systems

controls are available in Naidu and Rieger (2011a), Naidu and Rieger (2011b), and Afram and Janabi-Sharifi (2014b).

2.2.1 Degrees of Freedom for VCS

Degrees of freedom are the variables in a process that can vary independently to impact the outputs. Many researchers have analyzed degrees of freedom for process control (Ponton, 1994; Luyben, 1996) and VCS (Jensen and Skogestad, 2007; Jain and Alleyne, 2011). Figure 2.3 shows the pressure enthalpy diagram of a typical VCS. Assuming ideal processes (isentropic compression, isobaric condensation and evaporation, and isenthalpic expansion across the valve), this plot shows that standard VCS systems operate with some degree of subcooling at the outlet of the condenser and superheating at the outlet of the evaporator. A small degree of superheating at the outlet of the evaporator is desired to minimize mechanical damage to the compressor from the liquid phase. At steady-state operating conditions with a pure component as the working fluid, all the state points in the system can be defined by using the three enthalpy values, at the outlet of evaporator, condenser, and compressor, and one pressure or temperature value. To compute heat transfer rates, the mass flow rate of the refrigerant is required as well. Therefore, the system has a total of five degrees of freedom (three enthalpy values, one pressure or temperature, and one mass flow rate) which can close the system of conservation equations. Ideally, all these could be manipulated to achieve the desired performance of the system. However, most of the practical control approaches manipulate the refrigerant mass flow rate and evaporator pressure or temperature to regulate the system performance. Other variables such as outlet enthalpies of the condenser and evaporator are dependent on heat transfer rate and external conditions and are typically allowed to vary as disturbances. Refrigerant

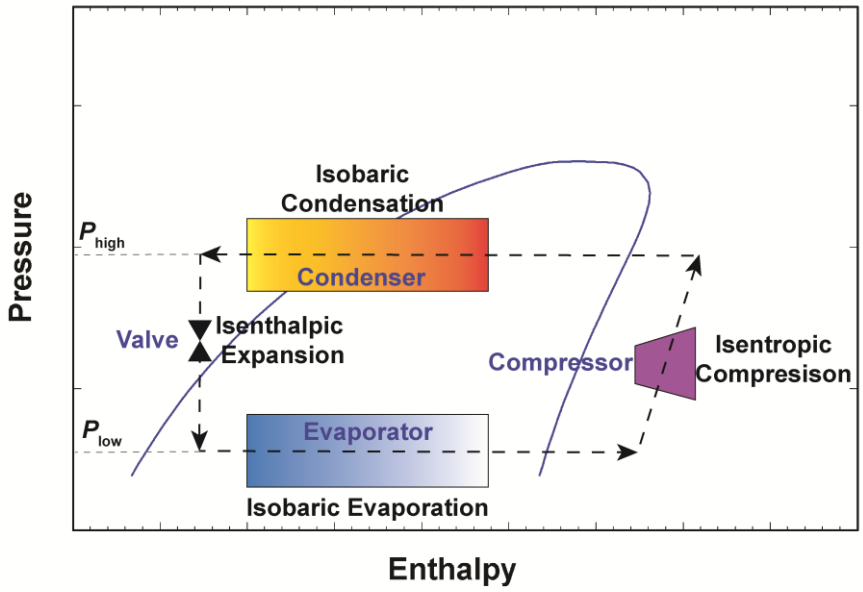

Figure 2.3: Pressure-enthalpy diagram of VCS indicating statepoints of the cycle

flow rate and evaporator conditions can be adjusted using a variable speed compressor and a variable opening expansion valve, respectively. This allows for two degrees of freedom, and for a given operating condition of refrigerant mass flow rate (or compressor speed), there will be a unique valve position satisfying the desired evaporator conditions. Most control methodologies discussed in this paper focus on manipulating one or both control degrees of freedom, with the advanced controllers focusing on integrating the manipulation of these variables with optimization of an objective function such as minimization of exergy destruction, maximization of COP, or meeting the cooling/heating demand in response to changing operating conditions. The discussion in the following sections elaborates upon these concepts.

2.2.2 Conventional Control

Early control methods for refrigeration systems involved on/off control, and refrigerant bypass (Buehler, 1968; Kirkman, 1968; Zubair and Babel, 1989). As the names suggest, these involved turning the system on/off and achieving a time-averaged desired rate of cooling, and bypassing some refrigerant from the active refrigeration loop, respectively. These approaches are easy to implement. However, on/off control leads to significant energy loss in the start-up phase as the thermal capacitance of these systems can be large. Moreover, this bang-bang type control inherently leads to instabilities and hysteresis in the regulated temperature, causing a further increase in energy consumption. Refrigerant bypass, on the other hand, reduces the system efficiency at the cost of enabling part-load operation (Yaqub and Zubair, 2001).

Den Braven *et al.* (1993) discussed the potential energy savings that can be achieved with advanced controls, particularly emphasizing the role of variable speed drives for compressors for capacity control, and microcontrollers in sensing and utilizing the operating conditions to optimize the performance of refrigeration and HVAC systems. These technologies were already being used in many residential and industrial applications (ARI, 1993). However, the true potential of combining these technologies with advanced control algorithms remained untapped until the late 1990s.

2.2.2.1 Simple Feedback Control Methods

Advances in variable-speed drives, electronic valves, and micro-processor capabilities led to the development of advanced control concepts based on linearized plant models. Linear control theory concepts are computationally inexpensive, and with

sophisticated algorithms, they can be utilized to control most non-linear systems. Variable speed controls had already been established as more efficient and stable operating mechanisms at part-load conditions (ARI, 1993). Early model-based control methods utilized variable speed compressors and variable opening valves to implement feedback controls (Broersen and van der Jagt, 1980; Gruhle and Isermann, 1985; Vargas and Parise, 1995; Qureshi and Tassou, 1996; Outtagarts *et al.*, 1997; Finn and Doyle, 2000).

Simultaneous use of variable speed compressors and expansion valves was discussed by Marcinichen *et al.* (2008) using a dual- Single Input – Single Output (SISO) strategy to regulate the compressor speed and refrigerant valve position to control the cooling capacity and evaporator superheating, respectively. Two separate proportional-integral (PI) feedback loops were devised in the proposed method. The overall controller performed satisfactorily but was constrained to a region close to the point of operation selected for the design. While simple proportional-integral-derivative (PID) feedback loops are inexpensive and easy to install, their tuning for a wide range of operating conditions, and ensuring their stability can be cumbersome. These issues lead to gain-scheduling and multivariable controls schemes.

2.2.3 Advanced Control Schemes

The control schemes presented in the preceding section are unable to provide control over a large range of operating conditions due to complex and coupled dynamics of refrigeration systems. Therefore, control schemes for such systems must consider the true dynamics and relationships between different variables of the system.

2.2.3.1 Multivariable Control Schemes

He *et al.* (1997) presented a lumped-parameter modeling paradigm based on the moving-boundary method for VCS and studied the effects of control inputs such as compressor speed, condenser fan speed, and expansion valve opening on the thermodynamic parameters of the system. They demonstrated that there is strong cross-coupling between different input-output combinations and individual single input – single output (SISO) control techniques are inadequate in regulating the system. This necessitates development of multivariable feedback control algorithms for refrigeration systems. He *et al.* (1997) found that the existing approaches for modeling refrigeration systems were either too simplistic and ignored key system parameters such as subcooling in the condenser and superheating in the evaporator, or the dynamic models were computationally very intensive as in the case of discretized models. Both of these approaches were not suitable for the design and analysis of control algorithms. Therefore, the authors presented a moving-boundary type of lumped parameter approach to model the dynamics of the system. A linearization approach was presented for controller design near the design operating point. A dynamic model for a refrigeration system consists of many states that have an insignificant contribution to overall dynamic response. For the purpose of designing a model-based controller, the lowest possible order of the model is desired as the complexity of the control law scales with the order of the model (or the number of tracked states). He *et al.* (1997) discussed model reduction in detail and provided a theoretical argument for cross-coupling between independent SISO feedback loops.

Following this work, He *et al.* (1998) presented multi-variable feedback control strategies for VCS. A multiple input – multiple output (MIMO) control system based on a

Linear-Quadratic Gaussian (LQG) method was designed and implemented to regulate compressor speed and refrigerant expansion valve opening. To address the system non-linearity, especially due to the changes in operating conditions, a gain scheduling routine was implemented to adapt the controller and maintain robust control. In comparison to SISO controllers that utilize single signal feedback to generate a single output command, MIMO control systems utilize the feedback of multiple signals to generate multiple output commands. They presented results of the controller performance based on regulation performance in the presence of unknown disturbances affecting the system dynamics, tracking performance for set-point variation, and robustness to modeling errors. Both modeling and experimental implementation were discussed. Experiments demonstrated superior performance of the MIMO control scheme over the SISO method. The MIMO controller achieved steady state almost twice as fast compared to the SISO scheme after step changes were introduced in the evaporator superheating and the cooling load. The proposed controller also remained stable under fast and large control actions. Gain scheduled MIMO control also demonstrated significant efficiency improvements when multiple inputs were varied in the system.

Many researchers presented variations of MIMO feedback control for refrigeration VCS. Shah *et al.* (2004) presented a simulation analysis of multivariable adaptive control strategy for an automotive air-conditioning system. Larsen (2006) presented an optimization-based controller for a supermarket refrigeration system to account for couplings between different variables. The controller also accounted for fast and slow dynamics of the system by using a cascaded feedback loop. Rasmussen and Alleyne (2006) implemented gain-scheduled MIMO feedback control for a refrigeration and air-

conditioning system. They presented detailed analysis of system identification and gain-scheduling using multiple SISO and MIMO control schemes. The MIMO controller utilized a H_∞ design to ensure stability of the closed-loop system.

Among other works on MIMO control, Schurt *et al.* (2009) presented a control architecture using the Linear-Quadratic-Gaussian (LQG) with an optimal state estimator, and showed that the controller was able to operate satisfactorily far from the operating point (±30%) and rejected disturbances in the cooling load. Experimental validation was also presented for reference tracking and disturbance rejection. Elliott and Rasmussen (2010) identified non-linear behavior between the opening of the expansion valve and evaporator superheat. However, to avoid the use of complex non-linear or gain-scheduled controllers, they presented a cascaded control scheme using evaporator pressure and temperature as measured values. The system demonstrated better performance as compared to gain-scheduled controllers.

2.2.3.2 Non-linear Control Methods

Non-linear control theory has gained interest for many reasons. It can provide significant enhancement over linear control methods as it can expand the range of operation of the controller, and analyze hard non-linearities such as actuator saturation, which arise in a number of engineering systems. Non-linear control methods can also be simpler and more intuitive to design than their linear counterparts as they depend on the physics of the system. Common techniques used in obtaining the control law are Lyapunov stability theory, adaptive control and feedback linearization (Slotine and Li, 1991). This section reviews some of the key non-linear control strategies for VCS.

Seem (1998) presented a pattern recognition adaptive controller to tune the gains of a closed-loop feedback system, such as a PID controller, for systems exhibiting dynamics similar to HVAC systems. The proposed strategy simplified the implementation of optimal control while utilizing significantly less computational resources.

Optimal control for refrigeration systems has been discussed by many researchers; however, in many instances, it has been limited to thermodynamic design optimization of the system, and dynamic optimization is not considered. Leducq *et al.* (2006) used a non-linear optimal control scheme to control a VCS. The optimal control scheme is used in conjunction with a model predictive control (MPC) framework that uses a model for the system (Leducq *et al.*, 2003) to predict the future response. Optimal control relies on the minimization of a cost function at each time step. The optimization routine is constrained by actuator limits and system bounds. The optimization routine has to take into account the desired refrigeration capacity as well and cannot always target the minimization of consumed energy. They reported an 8 – 20% increase in system COP as compared to classical controllers. However, the evaporator superheat was regulated using a separate PID feedback loop and the cross-couplings between evaporator superheat and rest of the system were ignored.

2.2.3.3 Model Predictive Control

Model Predictive Control (MPC) is an attractive choice for the control of heat pump systems because it can perform as an anticipatory controller rather than a corrective controller. MPC offers significant advantages by combining disturbance rejection, handling of constraints and slow dynamics in the control architecture (Garcia *et al.*, 1989).

The disadvantage is that MPC requires higher computational cost and needs an accurate model of the system. Jain and Alleyne (2015) presented an MPC controller for a refrigeration system with minimization of exergy destruction as the objective function. They modified the standard MPC framework to implement constraints on the inputs, outputs, and actuator signals such that the controller performance is always physically permitted. The results demonstrated fast and stable transient and steady-state performance of the controller both on the basis of minimization of first law energy consumption and second law exergy destruction. Overall destruction of exergy was reduced by ~15% leading to significant gains in system efficiency. MPC based methods for energy systems are under development, and these algorithms still require experimental validation. A detailed review of MPC applications in HVAC systems is provided by Afram and Janabi-Sharifi (2014b).

2.2.4 Advanced Intelligent Controls

As discussed above, significant progress has been made in the area of advanced intelligent control systems using data-based models for applications in refrigeration and heat pump systems. ANN, genetic algorithms, and fuzzy logic controllers are a few notable techniques in this area.

A number of researchers have presented optimization and supervisory control of large HVAC plants using advanced controls and optimization algorithms. Mohanraj *et al.* (2012) provided an extensive review of the application of ANN for the control of heat pump systems. Genetic algorithms are often used to solve the optimization problem along with parameter estimation using ANN. Online control implementation using these techniques does not require a very accurate system model, but utilizes parameter estimation

to continuously tune the system model (Ma and Wang, 2011). ANN-based control of refrigeration systems equipped with a variable opening expansion valve is discussed in Nanayakkara *et al.* (2002), and using a variable opening expansion valve and a variable speed compressor is shown by Ekren *et al.* (2010).

A fuzzy logic controller operates in the form of conditional statements. It can also be utilized for auto-tuning PID controller gains in a scheme where PID control operates on the faster dynamics and the fuzzy logic supervisor is used to optimize the response of the global system. Fuzzy logic controller design requires a detailed understanding of the system and its operation to define the conditional statements (Singh *et al.*, 2006). Applications of fuzzy logic controllers for heat pump systems are presented by Aprea *et al.* (2004), Li *et al.* (2004), Wu *et al.* (2005), and Tian *et al.* (2008).

Due to the limited accuracy of data-based models, these advanced intelligent control schemes suffer from lack of generalization, and the application of these methods has thus far been limited.

Table 2.3 summarizes the key control methodologies and their impact on the performance of VCS.

Table 2.3: Summary of control systems for VCS

Control Methodology	Author(s)	Control Loops	Remarks	Experimental Validation
Conventional Control	Yaqub and Zubair (2001)	Compressor Unloading and Refrigerant Bypass for part-load operation	Compressor capacity variation provides better control with increase in COP; Refrigerant bypass decreases COP at part-load	Partial
SISO Feedback Control	Gruhle and Isermann (1985)	Proportional-Integral (PI) expansion valve	Improved evaporator performance (~5% heat transfer rate increase) compared to standard thermostatic expansion valve (TEV) to control superheat	Yes
	Vargas and Parise (1995)	Variable speed compressor based on a power law	Comparison with on/off control demonstrated ~12% increase in COP with power law controller providing stable operation	Yes
	Finn and Doyle (2000)	Feedback control of evaporator superheat through the expansion valve	Comparison of different types of valve control methods (Proportional, PI) demonstrated potential for customization and optimization	Yes

Table 2.3: Summary of control systems for VCS (continued)

Control Methodology	Author(s)	Control Loops	Remarks	Experimental Validation
SISO Feedback Control	Marcinichen *et al.* (2008)	Dual SISO control of expansion valve and compressor	Dual SISO control (control of superheat through expansion valve and the control of delivered coolant temperature through compressor speed) provided optimization of COP	Yes
	Outtagarts *et al.* (1997)	SISO feedback control of evaporator	Two types of feedback control (proportional-derivative and optimal qualitative regulation) demonstrated satisfactory control of superheat	Yes
Multivariable Feedback Control	He *et al.* (1998)	MIMO control of capacity and superheat	LQG based MIMO controller provided ~15% increase in COP during transient processes and at steady state as compared to individual SISO loops	Yes
	Shah *et al.* (2004)	MIMO adaptive control	Linear Quadratic Regulator (LQR) based MIMO control of evaporator superheat and pressure demonstrated excellent disturbance rejection and reference tracking	No
	Rasmussen and Alleyne (2006)	MIMO control of capacity and superheat	Gain-scheduled MIMO controller led to significant savings in energy at part-load operation	Yes

Table 2.3: Summary of control systems for VCS (continued)

Control Methodology	Author(s)	Control Loops	Remarks	Experimental Validation
Multivariable Feedback Control	Schurt *et al.* (2009)	LQG based MIMO control with optimal state estimator	Simultaneous control of compressor speed and expansion valve opening to regulate the delivered coolant temperature and evaporator superheating provided fast and stable reference tracking and disturbance rejection performance	Yes
	Elliott and Rasmussen (2010)	Cascaded control of superheat	A cascaded feedback loop to regulate evaporator superheating was employed. The faster inner loop was used to control pressure and the slower outer loop was used to control the degree of superheating	Yes
Advanced Controls	Leducq *et al.* (2006)	Optimization-based non-linear predictive control	Superheat control using SISO PID loop; Overall optimal control using MPC with control of pressures and cooling capacity using compressor speed and heat sink flow rates; Overall COP gains of 8 – 20% observed depending on number of actuators	Yes
	Jain and Alleyne (2011)	Thermodynamic optimization based on	Based on utilizing all degrees of freedom of VCS, the steady-state optimization based on minimization of exergy destruction delivered	Yes

Table 2.3: Summary of control systems for VCS (continued)

Control Methodology	Author(s)	Control Loops	Remarks	Experimental Validation
Advanced Controls		minimization of exergy destruction	~52% in system COP by regulating compressor speed and expansion valve	
	Jain and Alleyne (2015)	Optimal control using MPC using minimization of exergy destruction	First and second law-based optimization algorithms in an MPC framework led to ~15% decrease in exergy destruction	No
Advanced Intelligent Controls	Ma and Wang (2011)	Optimal control using genetic algorithms	Linear models with recursive least squares based self-tuning estimators and optimization using genetic algorithms showed up to 2.55% increase in efficiency	Yes
	Ekren *et al.* (2010)	Control using ANN	Compressor speed and expansion valve position adjusted through a feedforward ANN based identification and control, and demonstrated 8% lower energy consumption than PID feedback control	Yes
	Aprea *et al.* (2004)	Fuzzy logic control	Exegetic based optimization in a fuzzy logic controller to manipulate compressor speed leading to 13%	Yes

Table 2.3: Summary of control systems for VCS (continued)

Control Methodology	Author(s)	Control Loops	Remarks	Experimental Validation
Advanced Intelligent Controls			decrease in energy consumption as compared to on/off control	
	Li *et al.* (2004)	Fuzzy logic control	Fuzzy logic based self-tuning PID control of expansion valve	Yes

Figure 2.4 shows a schematic of controls research for VCS. As discussed previously, the two control degrees of freedom typically utilized are the expansion valve position and the speed of the compressor. These can be utilized in a variety of control algorithms of different complexities to yield improvements in system performance of varying magnitude. The general control system design process is outlined as follows:

- Identify the variables to be controlled and their desired set-points.
- Identify relevant measurements for various process and disturbance variables and actuators for different degrees of freedom in the system.
- If an advanced control methodology such as state observer feedback, gain scheduled feedback, model-based MIMO feedback, optimal control or model predictive control, is to be utilized, then a transient system model will be required to interface with the controller.

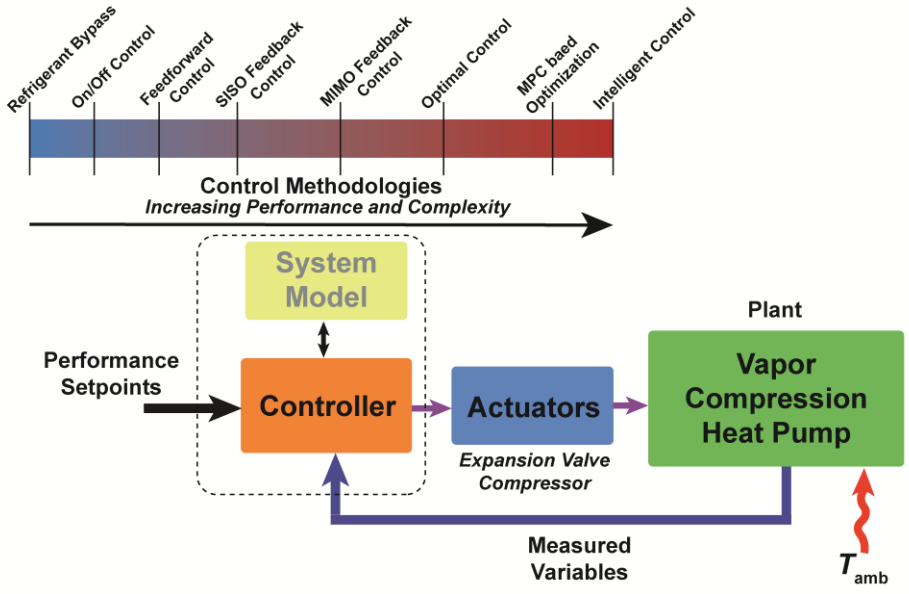

Figure 2.4: General control system design practice for VCS

- The transient model suitable for the application and the control hardware can be developed using a number of methodologies discussed in Section 2.1.
- For optimal control, define an objective function for optimization as a combination of one or more of the following: total exergy destruction rate, first law efficiency, and system capacity.
- Controller parameters must be tuned and constraints on actuator limits and controlled variables must be imposed to safeguard individual components and the overall system.

2.3 Control of Absorption Systems

Absorption systems have been in use for many decades, but research on the control of these systems is limited and seemingly unorganized in the literature. The control system forms a critical component if the technology has to progress as a viable alternative to the existing heat pump technologies for residential and mobile applications. This section discusses the state-of-the-art in control systems design and implementation for absorption heat pumps and outlines the recommendations for future research.

2.3.1 Degrees of Freedom for VAS

As discussed previously, the absorption cycle is more complex compared to the vapor compression system due to the presence of a binary mixture of refrigerant and absorbent as the working fluid, and the additional heat and mass exchangers that enable the utilization of a heat source. Figure 2.5 shows a simplified $T - P$ diagram of a single-effect absorption system. The cycle is shown in a simplified manner by not accounting for the recuperative heat exchangers typically utilized in these systems. The condenser and the

desorber operate at the high-pressure side, while the absorber and the evaporator operate at the low-pressure side of the system. The degrees of freedom can be analyzed in a manner similar to that for the VCS. The desorber can be approximated as a distillation column for the binary mixture of the refrigerant and absorbent. Seborg *et al.* (2010) demonstrated that, for a distillation column, the controlled variables are the pressure and concentration of outlet streams, and the manipulated variables are the product flow rates and the heat transfer rate. In an absorption system, the operating pressure of the desorber (high-pressure side) is determined by the condenser performance in conjunction with the ambient conditions. Product flow rates (refrigerant $\dot{m}_{ref}$, and dilute solution $\dot{m}_{dil}$) are determined by the expansion valves on these fluid lines. In an overall absorption system, the condenser and the evaporator are analogous to those in the VCS. Therefore, the control of the refrigerant flow rate is achieved through the refrigerant expansion valve, which also sets the low-pressure side of the system. If the concentrated solution flow rate ($\dot{m}_{conc}$) is manipulated using a variable-speed pump, then the dilute solution flow rate, and consequently, the position of the dilute solution expansion valve, is constrained by mass conservation applied to the desorber as shown in Eq. 2.1.

$$\dot{m}_{conc} = \dot{m}_{ref} + \dot{m}_{dil} \tag{2.1}$$

Finally, product concentrations are very important in the operation of an absorption system because even small quantities of a volatile absorbent in the refrigerant stream can lead to severe performance degradation. The heat transfer rate to the desorber from the external source provides another degree of freedom that can be manipulated to achieve the desired concentration of the refrigerant (x_{ref}) and dilute solution (x_{dil}) streams. The

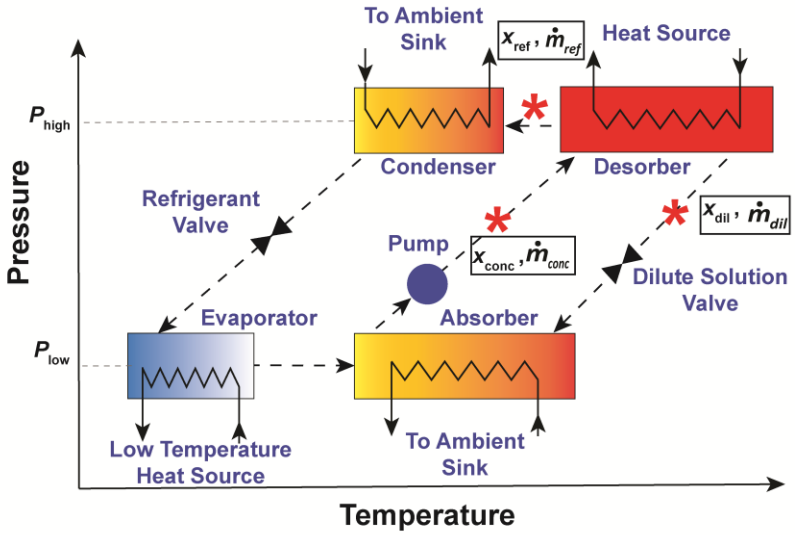

Figure 2.5: Temperature – Pressure diagram of a single-effect VAS

concentration of the dilute solution leaving the desorber can be accurately estimated as a function of the temperature at the bottom of the desorber and operating pressure, assuming the phase to be saturated liquid as shown in Eq. 2.2.

$$x_{dil} = G(P_{high}, T_{des}, q = 0) \tag{2.2}$$

The absorber serves to regenerate the concentrated solution from the refrigerant and dilute solution streams and provide the desired inlet concentration (x_{conc}) to the desorber.

Therefore, the control degrees of freedom for an absorption system are the position of the refrigerant expansion valve, the concentrated solution pump speed, and the desorber heat transfer rate. The controlled variables are the evaporator temperature glide, high-pressure of the system, and the system capacity. Control of evaporator temperature glide ($T_{evap,out} - T_{evap,in}$) is important to optimize the performance of the evaporator in an ammonia-water absorption heat pump. The refrigerant stream typically contains trace

amounts of water (< 0.5%), and therefore, as the refrigerant mixture changes phase in the evaporator, its temperature increases. Consequently, it becomes crucial to regulate this temperature glide to achieve an optimal evaporator heat transfer rate. Control of the high-pressure side is important for the performance of the condenser and desorber. Variations in pressure can cause changes in the outlet phase of the refrigerant from the condenser with possibilities of a two-phase mixture at the outlet. Such variations can also cause changes in the liquid level inside the desorber (for a pool boiling or distillation column type configuration) and cause variations in the outlet concentrations. Finally, the system capacity scales with the refrigerant flow rate, and therefore, the concentrated solution flow rate and heat input rate in the desorber should provide a direct and reliable control for the system capacity.

2.3.2 Basic Control Methods

Some of the earlier studies on the control of absorption heat pumps investigated on/off operation, open-loop controls, and thermodynamic optimization of the models to achieve better performance. Anand *et al.* (1982) discussed the transient performance of a water-lithium bromide absorption system driven by solar thermal energy. They simulated the transient performance of the chiller using TRNSYS (Klein *et al.*, 2017) and discussed key time constants and trends in the evolution of system and component performance. They indicated the need for controls to improve the overall transient performance; however, no implementation was presented. Didion and Radermacher (1984) conducted experiments to characterize part-load performance of an ammonia-water absorption heat pump and studied the effects of ambient temperature and charge migration between components during on-off cycles. The system used in the study was a 10.5 kW absorption chiller used in a 35°C

environment. The COP and cooling duty decreased as the ambient temperature increased. Moreover, at both extreme ends of the ambient temperature, the COP demonstrated a decrease. At very low ambient temperature, the air-side heat transfer in the evaporator is the limiting factor, while at the higher ambient temperature, the heat rejection capacity from the condenser and absorber is limited, leading to overall reduced performance. They also presented an on/off control strategy for the chiller. The effects of charge migration and loss of pressure degraded the on/off cycle performance, and isolation valves were suggested to hold the fluid and pressures and improve part-load performance. Experimental analysis showed significant improvement in part-load performance with isolation valves. This was the first experimental demonstration of the control of an absorption system. However, automated or algorithm-based controls were not yet implemented.

Alvares and Trepp (1987) evaluated a number of thermodynamic cycles for ammonia-water absorption systems and presented results on an ammonia-water absorption system driven by solar energy. They studied the use of on/off controllers for heat input to the system to maximize system COP. The controller was based on a duty-cycle adjustment based on the temperature difference between the solar collector and the absorption system. On/off control based on variations in the duty cycle applies, with certain limitations, to VCS because the compressor dynamics are much faster than those of heat exchangers. However, for thermally driven systems, turning the heat source on/off leads to the loss of the pressure differential in the system between these switching cycles. It takes significantly more time to resume the system performance due to the thermal inertia of various components, and leads to energy losses. Bong *et al.* (1987) used an open-loop control with thermal storage to implement capacity control on a 7 kW cooling duty water-lithium

bromide chiller. Controls were implemented for hot water supply in the desorber and chilled water supply in the fan coils. The performance of the system was stable but did not demonstrate significant energy savings. Butz and Stephan (1989) developed a dynamic model of an ammonia-water system using distributed and lumped capacitance models for components, which incorporated an expansion valve model to maintain appropriate fluid charge in the high- and low-pressure system components. They suggested that an improved control strategy will include isolation at each throttle valve or using electronic expansion valves to restrict fluid migration and pressure equalization during the off state of the system. They also suggested that continuous turn-down of the desorber heating rate combined with a reduction of the concentrated solution flow could yield improved performance during part-load operation. Level control using storage tanks at appropriate locations in the system to ensure a sufficient amount of working fluid at varying operating conditions were also recommended. However, experimental validation of these methods was not provided. Kim and Park (2007) also suggested a step-wise turn-up and turn-down sequence for the exhaust gas providing heat input to the desorber during the start-up phase. This was performed to shorten the overall system time constant. Li and Sumathy (2001) experimentally investigated a solar cooling system with a partitioned hot water storage. The partitioned hot water storage reduced the overall volume of hot water storage and also reduced the start-up time, especially during low sunlight hours such as morning. They reported a 15% increase in system COP.

The studies discussed above reported work do not consider detailed internal thermodynamics and heat transfer phenomena in the absorption system, and mostly explored open-loop controls. However, to achieve automated control with thermodynamic

optimization, it is necessary to account for these internal phenomena in the controller design.

2.3.3 Thermodynamic Optimization for Controller Design

Some studies present results of optimizing generation temperature in the desorber and consequent effects on the system performance. Most of these approaches involve evaluating the cycle models at different conditions and expressing the optimal generation temperature as a function of global system inputs. Sun (1997) used a simplified computer model to predict an optimal desorption temperature to maximize system COP. The data were generated by varying absorber, condenser, evaporator and generator temperatures for constant cooling capacity. The proposed control methodology involves storing data sets for optimal performance in an automatic controller to maintain high system COP during off-design operation. Fernández-Seara *et al.* (1998) presented thermodynamic modeling of a waste heat driven ammonia-water absorption system that drives a chiller for trawler fishing vessels, and performed parametric sweeps on operating conditions and geometric design of system components. The optimized operating conditions were used in developing a control law for exhaust gas by-pass control of the desorber. Jeong (1999) used a numerical model to study the effects of desorption temperature on cooling capacity of a water-lithium bromide absorption system and proposed capacity control by varying the desorption temperature and coupling-fluid flow rate into the desorber. Using a similar approach, Fernández-Seara and Vázquez (2001) proposed an optimal desorption temperature to maximize the COP. The control strategy predicted an optimal desorption temperature using the condenser and absorber coolant temperatures, and set the desorption temperature to the calculated value under varying ambient conditions. The optimal desorption temperature

was predicted as a linear function of the coolant temperature. The results showed that the control of optimal generation (desorption) temperature (OGT) leads to a higher system COP. They presented a dual-loop control strategy to optimize the desorption temperature and also maintain the refrigerated space at a constant temperature. The control algorithm maintained the chilled water temperature using on/off control of refrigerant flow rate. Thermostat feedback was connected to the solution pump, and isolation valves on refrigerant and dilute solution streams enabled separation of the two-pressure levels. The desorption temperature was modulated using a closed loop PID control with the reference optimal temperature calculated from the model equation and the actual desorption temperature.

Prevention of salt crystallization is a major operational requirement for water-lithium bromide systems. Accurate thermodynamic calculation of working fluid properties can assist in predicting the limits of crystallization. Thermodynamic criteria for crystallization control in water-lithium bromide systems were discussed by Liao and Radermacher (2007)) and Wang *et al.* (2011).

Explicit thermodynamic optimization-based control designs accomplish direct optimization of the variables of interest. However, these methods can suffer from lack of generalization, and may require redesigning the controller for systems of different capacity due to variation in the heat exchangers and driving heat sources.

2.3.4 Feedback Control Methods

Feedback controllers are the most ubiquitous due to the ease of implementation of a wide range of algorithms and availability of instrumentation required for them. After

identification of system parameters to be used as control inputs, feedback controllers aim to optimize pertinent process variables such as system COP and delivered coolant temperature. There is still a very important link to thermodynamic optimization as discussed in the previous section in terms of the identification of control parameters. However, the link can sometimes be implicit in the controller design and the search for optimality can be accomplished without explicit computations using a steady-state model.

Vargas *et al.* (1998) developed a dynamic model for VAS and compared the performance of closed-loop control to on/off controllers. The closed-loop feedback control was implemented using a power-law equation to drive the fuel flow in the desorber based on the difference between the delivered coolant temperature and its set-point. The on/off controller is implemented using a thermostat, and in the activated state, the fuel pump provides maximum fuel flow rate into the desorber. Experiments showed superior performance of closed-loop control over on/off control with respect to oscillations in the temperature of the delivered coolant, fuel consumption, and disturbances in evaporator coolant inlet temperature. Sibik (1999) developed a multi-variable and multi-objective control algorithm for H_2O/LiBr absorption chillers. The proposed controller accounted for capacity regulation and crystallization control in a MIMO control scheme. The algorithm considered the effects of parameters such as heat source temperature, solution mass flow rate, and condenser coupling fluid flow rate and temperature. Safety procedures and override commands were included for operation at extreme conditions. Experimental validation demonstrated the performance of the proposed controller. Chen *et al.* (2002) proposed computer-based monitoring and closed loop control strategies for an ammonia-water absorption heat pump. They identified refrigerant flow rate, coupling fluid

temperatures and flow rates in the absorber and condenser, and dilute solution flow rate as the key variables affecting system performance. The control loops aimed at regulating refrigerant and dilute solution flow rates using solenoid valves, and hydronic coupling fluid flow rate. For instance, the refrigerant flow rate was regulated based on the temperature differential across the evaporator or refrigerant pre-cooler. The proposed controller automated the start-up, monitoring, and on-line control of the heat pump.

Kohlenbach (2006) presented dynamic models for a 10 kW cooling capacity water-lithium bromide absorption chiller using a transfer function-based approach and a transient model with delay times and thermal mass and storage in the heat exchangers. Various control strategies specifically focusing on solar cooling systems were discussed. Existing methods for controlling hot water and cooling water temperatures and mass flow rates, and chilled water temperature were discussed. The control strategies included hot water mass flow rate control though on/off operation of pumps, solar collector temperature based proportional feedback control of hot water mass flow rate, and solar irradiation based hot water flow control. Chilled water temperature control was accomplished by varying hot water or cooling water parameters. A transfer function based transient model of the chiller was presented using simulations and experimental data. The simplified transfer function predicted the chilled water supply temperature as a function of control input of hot water valve. Transfer function-based model development, however lacks generality as it is accurate only for the range of input parameter variation considered in developing the model. Physics-based transient modeling involves solving a system of non-linear equations for mass, species and energy balance for different components, and includes a time delay for fluid transport between components of the chiller, and mass and thermal

storage in different components. The model is then used to derive a transfer function for system response. This approach reduces the non-linearities arising from a detailed model and simplifies the controller design for the chiller system. However, the approach presented in the work addresses only the external input variables and no control scheme is mentioned for internal variables of the absorption system such as solution pump speed and the position of expansion valves.

Shin *et al.* (2009) used a dynamic model for developing control algorithms for a double-effect water-lithium bromide absorption chiller. Two feedback loops were proposed to maintain the chilled water supply temperature and level control by varying the solution pump speed. The first feedback loop implemented a proportional controller with chilled water supply temperature as the process variable and air flow rate in the gas burner as the control variable. To account for the slow response time due to component thermal capacities, a dilution cycle was implemented to cut-off fuel flow rate if the chilled water temperature dropped below a threshold. Level control in the desorber was accomplished by varying the solution pump speed based on feedback from level switches indicating minimum and maximum levels in the desorber. The proposed control schemes were tested using simulations and prevented solution crystallization at part-load operation. The results emphasized the use of a secondary control structure in addition to feedback loops, such as the dilution cycle, to accommodate the thermal delay during abrupt changes. Feedback control on the solution level in the desorber of a double-effect water-lithium bromide water cycle was proposed by Seo *et al.* (2012). Zinet *et al.* (2012) also discussed feedback control of chilled water supply temperature regulated by varying the hot water mass flow rate in a water-lithium bromide absorption chiller. No experimental validation or quantitative

estimates of energy savings were presented. Rêgo *et al.* (2014) demonstrated the performance of a PI feedback loop to regulate the desorption temperature in an automotive exhaust-driven ammonia-water system. The control loop actuated exhaust gas valves to maintain the desorption temperature at a set-point and allowed the system to provide nearly constant cooling capacity at varying engine speeds.

Goyal *et al.* (2015) presented a model-based feedback control of a small-capacity ammonia-water absorption chiller driven using natural gas. The controller was based on proportional control of the refrigerant valve opening to regulate the temperature glide in the evaporator, and another proportional-integral (PI) controller for regulating the desorption temperature based on the coolant temperature supplied by the evaporator. The feedback control loop involved dead-time for the controller to account for thermal inertia in the system. The results indicated ~8 – 10% COP enhancement under varying operating conditions of ambient temperature and part-load operation. However, experimental validation of these methods was not provided. Garimella *et al.* (2016) discussed the use of a single feedback control loop for regulating temperature glide in the evaporator of a similar chiller system. The experimental system demonstrated stable performance of the controller.

Xu *et al.* (2016) implemented a PID feedback controller on a water-lithium bromide chiller simulation using two approaches. The first approach utilized the chilled water supply temperature as the controlled variable and desorber heat source flow rate as the manipulated variable. The second approach utilized the desorption temperature as the controlled variable. A correlation was developed between the desorption temperature and the chilled water supply temperature to ultimately use the control of the desorption temperature to regulate the capacity of the system. The system demonstrated more stable

and fast performance with desorber solution temperature as the control variable. However, this method requires a system specific correlation between the desorption temperature and the system capacity.

Most feedback control strategies in the literature use single or multiple SISO loops. As described above, this approach does not address the coupled dynamics of system variables and tends to be less effective in system-wide control schemes.

2.3.5 Advanced Control Methods

As mentioned in Section 2.2, advanced data-based system models and control methods originating from more sophisticated algorithms have gained interest over the last two decades. Among these techniques, optimal control, artificial neural network, and genetic algorithm-based approaches are noteworthy.

Neural network models bypass the complicated internal system physics and operate based on the examples provided by the user to train the algorithm. These algorithms also 'learn' from future cases. Neural networks require significantly less memory to store the information. Palau *et al.* (1999) used neural networks and expert systems to model, control and diagnose faults in an adsorption system. They presented a feedforward method to train the model with target input and output states and control the valves in the system at different stages of the cycle. The discussion did not include any experimental procedure to implement neural networks and only partial validation of the model was provided.

Koeppel *et al.* (1995) used a global optimization algorithm along with a detailed system model to determine an optimal control strategy for a double-effect water-lithium

bromide chiller. Chow *et al.* (2002) also used genetic algorithms (GA) coupled with neural networks to design an optimal control scheme for a complete system, including a water-lithium bromide absorption chiller and the conditioned space. The ANN model is used to perform simulation of the system for different inputs while the GA is used to map the input space to find the parameters to optimize the cost function at each time step. The cost function accounts for the total cost of fuel usage and electricity usage to operate different pumps. The manipulated variables in their approach were the chilled and cooling water mass flow rates and temperatures. The optimal control scheme demonstrated improved performance as compared to the baseline design, but the optimization was based on steady-state operation of the chiller for different operating conditions rather than optimizing the transient performance. Also, any control internal to the chiller system was not discussed. Vinther *et al.* (2015a) presented a non-linear dynamic model for a water-lithium bromide absorption heat pump and validated it with experimental data. The non-linear model was linearized about the nominal operating point to provide a simplified framework for controller design. Vinther *et al.* (2015b) discussed optimization of the COP for the same system in the presence of multiple inputs. Following the development of the model, Vinther *et al.* (2015b) presented a detailed discussion using Relative Gain Array (RGA) analysis to identify optimal input-output combinations for controller design. RGA is a useful tool to identify input-output pairings in a MIMO control strategy. The identified control inputs included desorber hot water mass flow rate, expansion valve openings, and solution pump flow rate. The transfer function for each input is determined by perturbing the individual input and obtaining the associated transfer function. Various input-output parings were identified, and feedback control was investigated. The system demonstrated improved

performance. However, this approach also suffered from lack of generality as the controller design was performed at a typical operating point of the heat pump.

Among other methods, the characteristic equation method (Hellmann and Ziegler, 1999) was used by Kühn *et al.* (2008). They proposed a new feedback control strategy to regulate the chilled water supply temperature as a function of the hot water and cooling water temperatures for a given cooling load. The controller incorporated a characteristic equation that relates the cooling capacity to the temperatures of the external fluid coupling loops. The optimization function regulates all three temperatures based on the control setting of either minimization of energy consumption or meeting the desired system capacity. This strategy allowed for maximization of the use of the available solar radiation and provided significant energy savings as the cooling tower fan can be optimally utilized.

While these advanced approaches do not require detailed phenomenological understanding and are computationally inexpensive, their reliability is limited by the number of test cases used to collect the data and train the algorithm. As these methods are similar to curve-fitting techniques, their predictions become increasingly inaccurate as the input parameters deviate from the training data set.

Table 2.4 summarizes the research available on the control of VAS.

Table 2.4: Summary of control systems for VAS

Control Methodology	Author(s)	Control Loops	Remarks	Experimental Validation
Conventional Control	Didion and Radermacher (1984)	On/Off control; Isolation valves	On/Off control led to ~ 25% decrease in system COP at part-load. Use of isolation valves improved the performance and the degradation in the COP was ~11%.	Yes
	Sun (1997)	Feedforward control of desorption temperature	Model simulations were used to generate maps for optimal desorption temperature as a function of different operating conditions.	No
	Li and Sumathy (2001)	Storage of hot water for desorber	Partitioning the hot water storage led to ~15% increase in system COP due to faster system dynamics	Yes
	Kim and Park (2007)	Feedforward control of heat source	Control of heat source during startup reduced the overall time constant of the system	Yes
SISO Feedback Control	Vargas *et al.* (1998)	Power law-based feedback control of desorber heat input	Stable control of evaporator temperatures and system capacity were achieved with ~50% reduction in fuel consumption to drive the system as compared to on/off control.	Yes

Table 2.4: Summary of control systems for VAS (continued)

Control Methodology	Author(s)	Control Loops	Remarks	Experimental Validation
SISO Feedback Control	Jeong (1999)	Feedback control of system capacity using desorber heat transfer rate	Desorber coupling fluid temperature and flow rate was varied to control system capacity for a H_2O- LiBr system	No
	Sibik (1999)	Feedback control of capacity and prevention of crystallization	Two feedback loops were implemented on a H_2O-LiBr chiller to control capacity through changes in solution flow rate to the desorber.	Yes
	Fernández-Seara and Vázquez (2001)	Feedback control of desorption temperature and on/off control of flow rates	An optimal desorber temperature as a function of absorber/condenser heat sink temperature is implemented and a PID feedback controller is used to regulate the heat flux. On/Off controller for refrigerant flow regulation maintains the desired capacity.	No
	Shin *et al.* (2009)	Feedback control of delivered coolant temperature and prevent crystallization	A dilution circuit improves the system performance at part-load in preventing crystallization. Quantitative estimation of performance variation was not presented.	Partial validation
	Rêgo *et al.* (2014)	Feedback control of desorber heat transfer rate to	Using desorption temperature feedback (PI loop) to control the exhaust gas flow	Yes

Table 2.4: Summary of control systems for VAS (continued)

Control Methodology	Author(s)	Control Loops	Remarks	Experimental Validation
SISO Feedback Control		maintain system capacity	rate in an automobile heat recovery-based cooling system.	
	Goyal *et al.* (2015)	Feedback control of temperature glide and cooling capacity	Two SISO feedback loops using proportional control for: controlling evaporator temperature glide using the expansion valve position; controlling cooling capacity using natural gas firing rate. 8 – 10% increase in system COP was predicted.	No
	Xu *et al.* (2016)	Feedback control of system capacity using desorber heat input rate	Two different SISO PID feedback loops were analyzed to identify faster and stable control architecture. Better control of system capacity was observed using desorption temperature as the controlled variable with a model-based correlation between desorption temperature and system capacity.	Yes
Advanced Controls	Palau *et al.* (1999)	ANN based control of adsorption systems	Implemented ANN models for control of different valves in the system and fault diagnosis.	Partial validation

Table 2.4: Summary of control systems for VAS (continued)

Control Methodology	Author(s)	Control Loops	Remarks	Experimental Validation
Advanced Controls	Chow *et al.* (2002)	ANN and GA based optimal control	Optimization of operating cost using chilled and cooling water flow rates and temperatures provided ~19% savings in the fuel consumption to operate the H_2O-LiBr system.	Yes
	Kühn *et al.* (2008)	Feedback control using system characteristic equation	Variable speed control of all coupling loops led to improvement in system performance.	Yes

2.4 Conclusions from Literature Review

The current research on control methodologies for absorption systems can be generally summarized as:

- employing on/off type intermittent controls, which are relatively straightforward to implement, but typically lead to significant performance degradation during start-up and shut-down periods,
- relying on simplistic models for the identification of critical operational parameters, which can be valid for certain ranges of operational conditions, but may not apply under off-design conditions,
- lacking detailed system identification and MIMO control to account for coupled dynamics of different system variables,
- not focusing on internal system control parameters such as control of expansion valves and solution pump speed to optimize heat and mass transfer performance, and
- lacking experimental studies and validation for control of small-scale systems.

These observations necessitate design and development of advanced controls for thermally activated absorption heat pumps, especially for residential and mobile applications. As discussed earlier, the research on control systems for VCS has spanned a multitude of control algorithms leading to component and system level characterization and optimization. This breadth of research is still unavailable for VAS. Figure 2.6 shows a summary and path for future research in the area of VAS controls. As VCS and VAS are

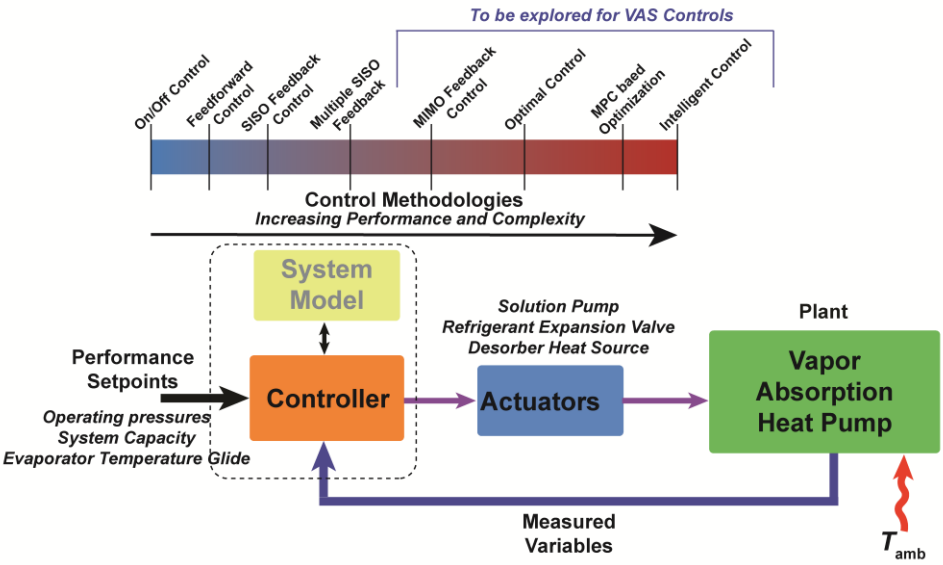

Figure 2.6: Control system research and design practice for VAS

both utilized in refrigeration and HVAC applications, the controlled variables for both VCS and VAS are similar. The controlled variables, from the viewpoint of overall system performance, are the delivered cooling/heating capacity and the temperature of the conditioned space. For an advanced control strategy that can optimize system efficiency and also maintain controlled variables at their set points, the operational efficiency or system COP can be computed online and incorporated into an optimization routine. The external disturbance variable, in the form of the ambient temperature that determines the heat transfer to or from the surrounding environment, is also identical for these systems. Therefore, the advanced control methodologies for VCS can be extended to VAS with some modifications arising due to specific dynamics and processes involved in VAS. An accurate system model should take into account those dynamics, and with the identification of input-output pairings, the advanced control algorithms for VCS can be applied to VAS as well.

2.5 Scope and Objectives of Present Study

The following research directions are identified for VAS controls.

- While there are numerous modeling and control methodologies, an appropriate combination of performance and complexity must be achieved.
- The design of control algorithms should be guided by accurate numerical models that can efficiently predict transient system performance.
- The thermodynamic and process degrees of freedom, identified in Section 2.3.1, should be paired with relevant process variables.
- Finally, the proposed control algorithms should be experimentally evaluated.

Current modeling techniques for VAS are limited to simplified lumped parameter models or data-based models. The accuracy of these models and their ability to be applied to a general class of absorption systems is very limited. There is a need for developing accurate and computationally efficient transient models for these systems. Computational efficiency can be increased by developing faster thermodynamic property calculation routines and reduced-order models that can characterize the key parameters of the system, such as thermal capacitances and fluid flow regimes, to guide the control algorithms.

The first part of this study demonstrates various modeling approaches for different components of VAS. The models account for thermal capacitances related to the heat exchanger material and the fluid mass, and range from very detailed segmented models to reduced-order MB and lumped-parameter models. Gains in computational efficiency are obtained through the development of fast thermodynamic property calculation routines using artificial neural networks. Additional gains in computations are obtained through the

use of advanced numerical solvers for the system of DAEs. Information obtained from these simulations is crucial in identifying the design of a system-wide control scheme to optimize performance.

The second part of this study investigates control of VAS. It is evident from the available literature that absorption heat pump controls require more sophisticated logic for the complex dynamics of these systems. A system transient model is utilized to design feedback control algorithms. These algorithms utilize the inherent system dynamics to guide control decisions, and are generalizable to a wider class of VAS. This study demonstrates, though numerical simulations, the improvement in the performance of the system at off-design operating conditions using feedback control loops on the evaporator temperature glide and the conditions of the heat source driving the capacity of the system.

Finally, an experimental test facility is constructed for a small-capacity ammonia-water absorption chiller. The experimental setup is equipped with computer-controlled actuators and instrumentation for various process variables, and allows for flexible deployment of many control algorithms via a computer-based controller. Detailed experiments simulating various scenarios of system operation demonstrate the applicability of the proposed control algorithms and the enhancement in system performance at off-design operation.

CHAPTER 3. COMPUTING THERMODYNAMIC PROPERTIES OF AMMONIA-WATER MIXTURES USING ARTIFICIAL NEURAL NETWORKS

3.1 Introduction

Ammonia-water is one choice for a working fluid pair in absorption systems. It offers various advantages, in addition to its zero ozone depletion and global warming potential, such as low saturation temperature of ammonia at above-atmospheric pressures, which enables use in refrigeration systems, and high heat of vaporization and vapor-phase density, leading to compact geometries of the heat and mass exchangers used in these systems. Optimal design of these systems is necessary for meeting cooling/heating load requirements at different operating conditions. This requires steady and transient simulations of the system and prediction of various state points in the cycle. Detailed transient models typically require millions of property computations for simulation of realistic operating time scales. The accuracy and computational cost of these cycle calculations depend on the calculation of thermodynamic properties of the working fluid, which in this case is a zeotropic mixture of ammonia and water.

Calculation of thermodynamic properties of mixtures can be a difficult computational problem using the typical equation of state (EoS) methods. For zeotropic mixtures, the thermodynamic states are highly non-linear functions of the independent properties used to compute them, and the resulting equations require an iterative solver for calculation of each state point. Detailed reviews and implementation of EoS formulation

for ammonia-water mixtures are provided by Ziegler and Trepp (1984), Tillner-Roth and Friend (1998), and Rattner and Garimella (2016). Pátek and Klomfar (1995) presented simple regression-based equations for ammonia-water properties in vapor-liquid equilibrium. However, they used limited data for the development of the model and the application of those equations is limited to specific steady-state cycle calculations. The most widely used software implementations of ammonia-water property routines are found in National Institute of Standards and Technology (NIST) REFPROP application (Lemmon *et al.*, 2013) and Engineering Equation Solver (EES) property libraries (Klein, 2016).

Neural network-based methods are used in solving highly non-linear problems where the complex physics of the system introduces a prohibitive computational expense. The massively parallel network formed by linking the inputs to the outputs utilizes adaptive weight functions for each input and correlates them to the output. The algorithm can also continuously train itself with additional data sets to improve the accuracy of the predictions as compared to most static models resulting from statistical analyses. Artificial neural networks (ANN) have been used in imitating learning and processing similar to the human brain, and have found extensive application in solving complicated problems in image processing, pattern recognition, and fitting multivariable input-output relationships (Lippmann, 1987).

Many researchers have investigated the use of ANN to predict thermodynamic properties of relatively new refrigerants and mixtures used in sorption heat pumps using very limited experimental data with promising accuracy and significantly lower computational expense. Petersen *et al.* (1994) presented perhaps the first implementation of ANN in estimation of VLE data of binary mixtures. Sharma *et al.* (1999) used ANN

with a backpropagation learning algorithm to predict vapor-liquid equilibrium (VLE) data for ammonia-water and methane-ethane mixtures with high accuracy. Thirteen hidden layer nodes achieved best results for both mixtures. Sözen *et al.* (2004) and Sözen *et al.* (2005) presented ANN based thermodynamic property calculation for methanol – lithium bromide and methanol – lithium chloride refrigerant/absorbent pairs. Limited data for mixture temperature, pressure and concentration were used to predict the specific volume. Multiple training algorithms were compared to select the most accurate network architecture. Scaled conjugate gradient (SCG) and Levenberg – Marquardt (LM) algorithms produced the least errors and correlated the data accurately. Good agreement was found between model predictions and experimental data. Şencan and Kalogirou (2005) determined the VLE data for water – lithium chloride and water – lithium bromide + lithium nitrate + lithium iodide + lithium chloride mixtures using temperature and concentration as the inputs and vapor pressure as the output of the model. They determined that feedforward LM algorithm based ANN resulted in good agreement with experimental data with high correlation coefficient (*R*) values. Şencan (2007) used data mining methods to determine the specific volume of methanol – LiBr and methanol – LiCl mixtures using pressure, temperature and concentration values. A back-propagation ANN using 7 hidden neurons with LM training was compared against other statistical and data mining techniques and was found to perform better.

Urata *et al.* (2002) investigated ANN for estimating VLE properties of 18 binary mixtures of hydroflouroether refrigerants with reasonable accuracy. Thermodynamic property computation of binary refrigerant mixtures was also investigated by Karimi and Yousefi (2007). An ANN model was developed to predict VLE data for four different

binary mixtures of refrigerants over a wide range of pressures and temperatures. The proposed neural net is a feedforward network with backpropagation learning through the LM algorithm. The results were compared with Redlich-Kwong-Soave (Soave, 1972) EoS predictions, and it was found that the ANN based models were more accurate. Nguyen *et al.* (2007) used ANN to calculate VLE data for ternary mixtures of solvents saturated with salts. The network contained two hidden layers for optimal performance. Şencan *et al.* (2011) used ANN to calculate thermophysical properties (thermal conductivity, density, viscosity, thermal diffusivity and specific heat) of mixed refrigerants.

This study extends the application of ANN models for computing thermodynamic properties of ammonia-water mixtures by incorporating the estimation of properties of both single- and two-phase regions using a unified network. It should be noted that the superheated vapor phase is not typically encountered in ammonia-water absorption systems, especially in the low-pressure components. For example, in an evaporator, instead of superheat, due to the significant difference in water and ammonia saturation temperatures, as evaporation proceeds, the mixture temperature primarily approaches the saturation temperature of water, resulting in a steep temperature gradient. The network predictions for superheated vapor phase in this work are based on the calculation of the specific heat capacity of single-phase vapor. Some of these predictions demonstrate relatively larger error due to limited training data available for the superheated vapor phase. The computational efficiency of the proposed property routines is compared with the conventional EoS-based formulation. In the subsequent chapters of this thesis, the proposed property libraries are utilized in developing a component model to study the dynamic response of a small-capacity ammonia-water VAS.

3.2 Neural Network Modeling

3.2.1 ANN Model and Parameters

ANN are formulated using a set of training, validation and test data points. In this study, the input parameters to the net are three independent thermodynamic variables, while the output is a desirable calculated state variable. MATLAB® Neural Network Toolbox (MathWorks, 2016) is used to train the network and develop the model. Figure 3.1 shows the schematic of a neural network. The inputs are provided to the system (a representative vector of temperature (T), pressure (P) and mixture mass quality (q) triplet) in the first layer (input layer) of the net. To train the algorithm, the input and target (known values of enthalpy (h), internal energy (u), specific volume (v), and ammonia mass fraction (x)) samples are normalized in the range [-1, 1] using *mapminmax* function in MATLAB®.

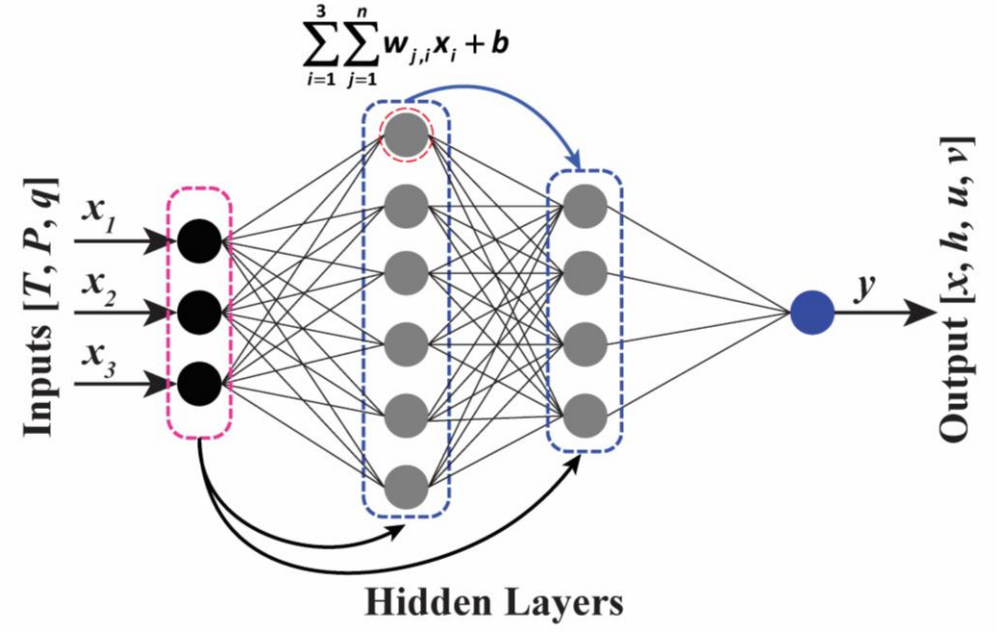

Figure 3.1: Schematic of a multilayer cascaded feedforward neural network for *TPq* property triplet

This is performed internally by the Neural Network Toolbox after receiving the raw input data.

The normalized inputs are manipulated using adaptive weight functions ($w_{j,i}$) in the hidden layers. All the weighted values are summed along with a bias (b_i) for each hidden layer neuron. The hidden layers establish the correlation between the inputs and the outputs by iteratively optimizing the values of the weights and biases. Finally, a transfer function is used for each layer to generate an output. The transfer function can be of different types depending on the relationship between inputs and outputs and can be selected appropriately for individual layers of the network. The performance of the neural net is measured in terms of mean squared error (*MSE*) (Eq. 3.1) and correlation coefficient (*R*) values of the fit between predicted values and known training values. A low *MSE* and high *R* (close to unity) are desirable.

$$MSE = \frac{\sum_{i=1}^{K_{train}} (y_i - y_{actual})^2}{K_{train}} \tag{3.1}$$

In this work, a cascaded feedforward network with two to four hidden layers is used for calculating the outputs. The optimum number of hidden layers for each network is identified iteratively. In a cascaded network, the outputs of the previous layers are supplied as additional inputs to the following layer. Typically, this leads to improved performance of the network and increased capability to correlate complex relationships. The number of neurons in the hidden layers varies for each property triplet. The training is performed using the Bayesian Regularization (BR) backpropagation algorithm. This algorithm uses a modified *MSE* function by including a mean squared sum of the network weights to

improve the generalization capabilities and prevents overfitting. This algorithm does not require a validation dataset separate from the training data and uses all the data provided to it for training, making it more suitable for instances with small or sparse datasets. The training data for ammonia-water properties is sampled from EES property libraries (Klein, 2016). Built-in data sampling algorithms in MATLAB® (*haltonset* and *sobolset*) are used to generate a near-random dataset of 29,667 property points for training the ANN. These properties are sampled within the vapor-liquid equilibrium region of the mixture. Table 3.1 summarizes the ranges of different parameters for each property routine. A total of 10,075 training points are used for training the $Txq \rightarrow P$ property routine. Separate property routine networks are developed for the specific heat capacity of subcooled liquid and superheated vapor phases. The subcooled liquid phase is assumed to be incompressible and its specific heat capacity, $Cp_{liq}(T, x)$, is used to calculate the enthalpy and internal energy at the operating pressure. A total of 674 training points are used to develop the network for subcooled liquid phase specific heat capacity. Similarly, 488 training points are used in the development of the network for computing the specific heat capacity of the superheated

Table 3.1: Thermodynamic property ranges

Property	Range
Temperature (T)	250 – 536 K
Pressure (P)	100 – 5000 kPa
Vapor Mass Quality (q)	0 – 1 kg kg^{-1}
Ammonia Mass Fraction (x)	2.57 ×10^{-05} – 0.999994 kg kg^{-1}
Enthalpy (h)	-305.99 – 2815.7 kJ kg^{-1}
Internal Energy (u)	-306.12 – 2610.8 kJ kg^{-1}
Specific Volume (v)	0.00104 – 1.6878 m^3 kg^{-1}

phase, $Cp_{vap}(T, x)$, which is used to compute the enthalpy and internal energy of the vapor phase at the operating pressure.

Neural network modeling is initialized by defining the structure of the cascaded net with the number of neurons in each hidden layer. Training parameters such as optimization algorithm, maximum iterations during training, criterion to stop, division of data between training and validation sets, input transfer function, and performance parameter are specified. These parameter values are listed in Table 3.2. As mentioned previously, the training algorithm used in this research is Bayesian regularization due to its enhanced capability to correlate complex relationships. The maximum iteration parameter stops the training once that iteration value is achieved. Typically, the maximum iteration parameter is set higher than the iterations required to converge to the solution. The training is performed by varying the number of neurons in the hidden layer until satisfactory performance and prediction abilities are achieved. The network performance can be tested by applying it to a set of test data different from the training data and the outputs can be compared with the state points computed from the EoS relations. The networks are trained repeatedly to ensure robustness and avoid overfitting or effects of the random initialization at each training session. After the training converges, the network is exported as a function script for standalone use with MATLAB® models and codes.

Table 3.2: ANN training parameters

Parameter	Value
Maximum Iterations	10000
Stop Criterion	MSE < 10^{-8}
Training Algorithm	BR
Performance Parameter	*MSE*
Input Transfer Function	Sigmoid

3.3 Thermodynamic Property Routines

As ammonia-water is a binary mixture, it required three independent thermodynamic properties to completely define the state and determine the remaining properties. To enable fast computations and utilization in numerical models, many combinations of property triplets (three independent property values) and the associated output variables are generated. Each of these combinations is then trained using the procedure described in the previous section.

Table 3.3 summarizes the training parameters of each property triplet developed in this study. The network structure and training MSE for each property routine are provided. ANN training performance is estimated in terms of convergence rate of the training algorithm as a function of the *MSE* and iteration of the optimization algorithm. Final performance of the network is also estimated using the error between target output values and output values predicted by the network. Finally, to assess the performance of the trained networks in this work, an additional test dataset was utilized to compare the predictions of the network. Performance results for the property routine $TPq \rightarrow x$ are presented. Figure 3.2 shows the variation of *MSE* with iteration count for the training of this network. As the training proceeds, *MSE* for training data and test data decreases and achieves a steady value. The optimization algorithm terminates the training after no further decrease in *MSE* can be achieved (in this case after 10000 iterations). The network parameters are obtained for the minimum *MSE* value. A separate database of random state-points was utilized to compare the network prediction with EoS calculations. Figure 3.3 shows the difference between the predicted values and the predictions using EoS routines for 174 datpoints. It can be observed that most datapoints exhibit insignificant errors and

Table 3.3: ANN based thermodynamic property routines for ammonia-water mixtures

Property Routine	Network	*MSE*	Single-phase Computation
Pxq	$T \rightarrow 3-9-6-6-3-1$	6.42×10^{-4}	×
	$h \rightarrow 3-9-6-6-3-1$	0.0073	
	$u \rightarrow 3-9-6-6-3-1$	0.0159	
	$v \rightarrow 3-9-6-6-3-1$	4.64×10^{-8}	
TPq	$x \rightarrow 3-12-9-6-3-1$	2.4×10^{-10}	×
	$h \rightarrow 3-12-9-6-3-1$	2.12×10^{-4}	
	$u \rightarrow 3-12-9-6-3-1$	2.22×10^{-4}	
	$v \rightarrow 3-12-9-6-3-1$	6.33×10^{-11}	
Txq	$P \rightarrow 2-15-9-9-3-1$	0.0094	×
Pxh	$T \rightarrow 3-12-9-6-3-1$	9.21×10^{-5}	✓
	$q \rightarrow 3-12-9-6-3-1$	9.49×10^{-10}	
	$u \rightarrow 3-12-9-6-3-1$	8.62×10^{-5}	
	$v \rightarrow 3-12-9-6-3-1$	1.01×10^{-9}	
TPx	$[q, h, u, v] \rightarrow$ Iteratively solved using $TPQ \rightarrow X$	–	✓
$Cp_{liq}(T, x)$	2 – 9 – 6 – 1	5.45×10^{-5}	✓
$Cp_{vap}(T, x)$	2 – 12 – 7 – 1	0.0014	✓

the entire dataset lies exhibits a prediciton error of $[-1, 2] \times 10^{-4}$. **For a larger set of 9541 random state-points, the prediction error is less than 0.5% for all data points.** Figure 3.4 shows a histogram of pridiction erorr at the completion of training of the network. The plot shows the prediction erorr between the supplied training output values and the predictions using the network. The converged network demonstartaed a small error for a large fraction of data points (more than 18,000 data points out of 29,667 training points have an error of $\sim 3 \times 10^{-6}$). Finally, the correlation coefficient (R) for the network is computed to be ~0.99994 which indicates a good correlation fit.

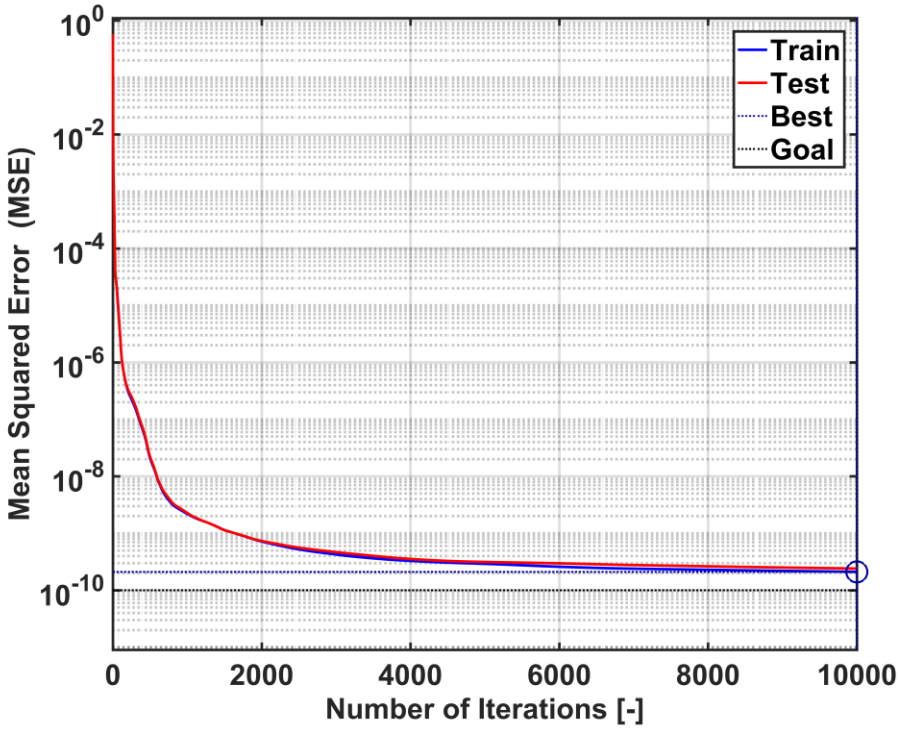

Figure 3.2: Variation of MSE during training for $TPq \rightarrow x$

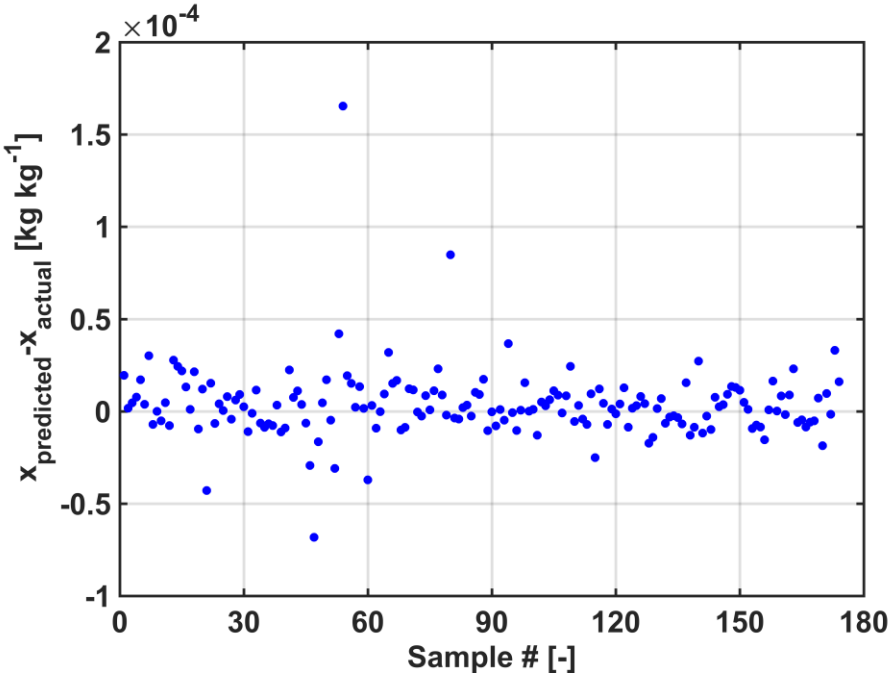

Figure 3.3: Comparison of predicted values and EoS computations for $TPq \rightarrow x$

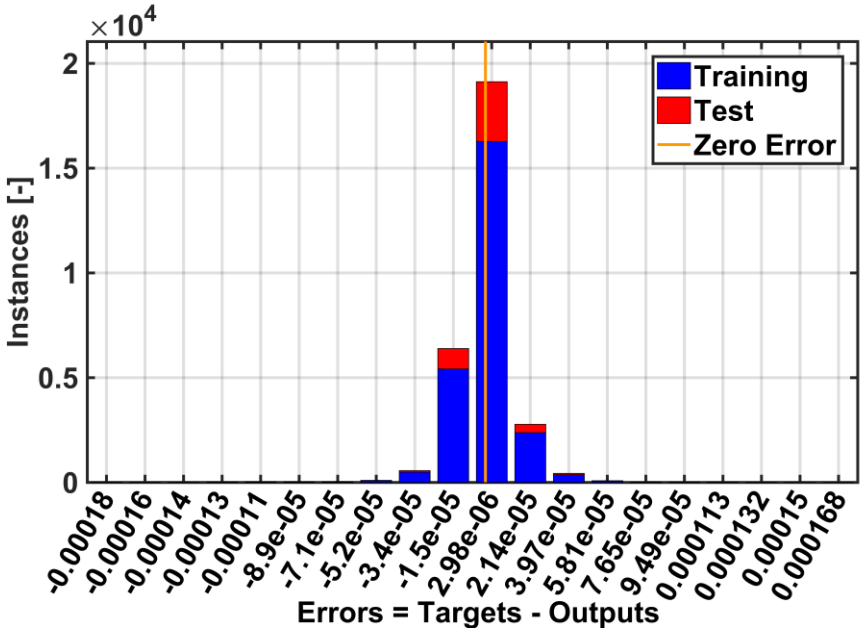

Figure 3.4: Comparison of network predicted values and target training data for *TPq* → *x*

The property triplets containing vapor mass quality or mixture specific volume (*TPq*, *Pxq*, *Txq*) as an input parameter can only be used to compute saturated phase and two-phase region properties. In this work, a good network fit for *TPx* routine was not obtained despite many trials with size of network, training algorithm and other network parameters. To overcome this limitation, an iterative solution for *TPx* → *q* is developed that utilizes the abovementioned *TPq* and *Pxq* routines. Figure 3.5 shows the algorithm for the solver. The iterative solver utilizes the *Pxq* routine to identify the phase region of the queried state-points. It iteratively solves for the queried ammonia mass fraction using the *TPq* routine and converges to the corresponding vapor mass quality. The iterations are performed using successive over-relaxation method (parameter α = 2) to increase the convergence rate of the iterative algorithm. The properties of subcooled and superheated phases, encountered when using *TPx* and *Pxh* property routines, are calculated using

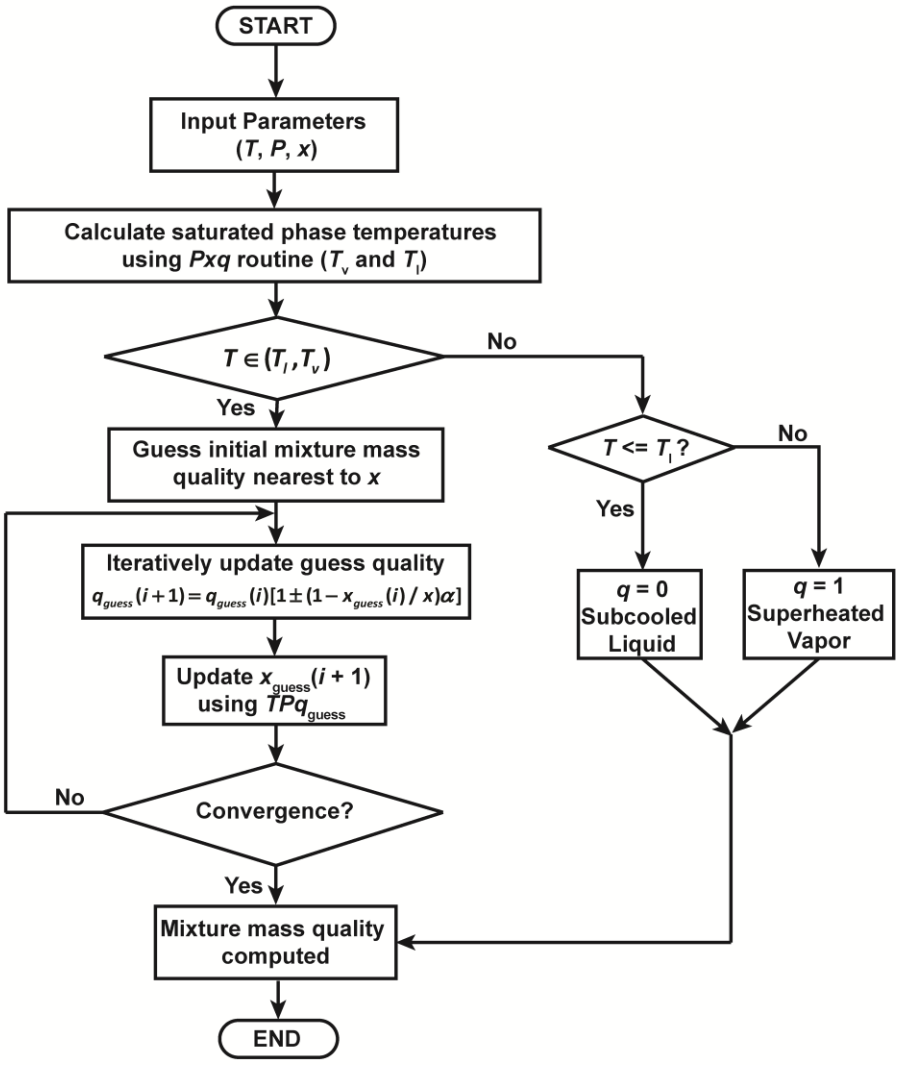

Figure 3.5: Flowchart of iterative solver for *TPX* → *q* property routine

single-phase property computations that utilize the specific heats of liquid and vapor phase to calculate enthalpy values. The subcooled liquid phase is assumed incompressible. Therefore, the effects of variations in pressure on density are neglected. These are shown in Eq. 3.2 – 3.10.

$$h_{liq,sc} = h_{liq,sat} - Cp_{liq}(T_{liq,sat} - T) \tag{3.2}$$

$$h_{liq,sat} = TPq \rightarrow h(T, P, 0) \tag{3.3}$$

$$T_{liq,sat} = Pxq \rightarrow T(P, x, 0) \tag{3.4}$$

$$Cp_{liq} = Cp_{liq}(T, x) \tag{3.5}$$

$$h_{vap,sh} = h_{vap,sat} + Cp_{vap}(T - T_{vap,sat}) \tag{3.6}$$

$$h_{vap,sat} = TPq \rightarrow h(T, P, 1) \tag{3.7}$$

$$T_{vap,sat} = Pxq \rightarrow T(P, x, 1) \tag{3.8}$$

$$Cp_{vap} = Cp_{vap}(T, x) \tag{3.9}$$

$$v_{liq,sc} \approx v_{liq,sat} = TPq \rightarrow v(T, P, 0) \tag{3.10}$$

3.4 Performance of Thermodynamic Property Routines

This section presents the computational performance of the proposed property routines and their comparison with available EoS programs. A comparison of computational efficiency is performed by computing 9541 random property calls using the proposed methodology and the existing EoS property library.

The proposed property routines are direct ANN functions implemented in MATLAB® to facilitate faster property computations as compared to iterative property routines passed through external library functions. Computational time is recorded for the computation of 9541 *TPq* triplets using EES® property routines, MATLAB® implementation of the property routines developed by Rattner and Garimella (2016), and the ANN based routines developed in this work. Figure 3.6 shows the comparison of

computational time using the above-mentioned three methods. It can be observed that using ANN for property calculation leads to ~60% decrease in the computational time (3.38 s as compared to 8.4 s with conventional EoS routines in MATLAB®). Calculations using EES property routines take ~45 s to complete. Increase in computational efficiency is attributed to direct functional relationship between the input variables and the outputs. EoS based methods (both EES library routines and MATLAB® implementations) require linking external library files for each calculation and an iterative solver, which amounts to significant computational expense. All these computations were performed on an Intel® Core-i7 machine with a clock frequency of 3.4 GHz and 24 GB of RAM. The *TPx* routine developed in this work utilized an iterative solver as discussed in the previous section. The iterative solver requires additional computational expense and leads to negligible improvement over the existing methods.

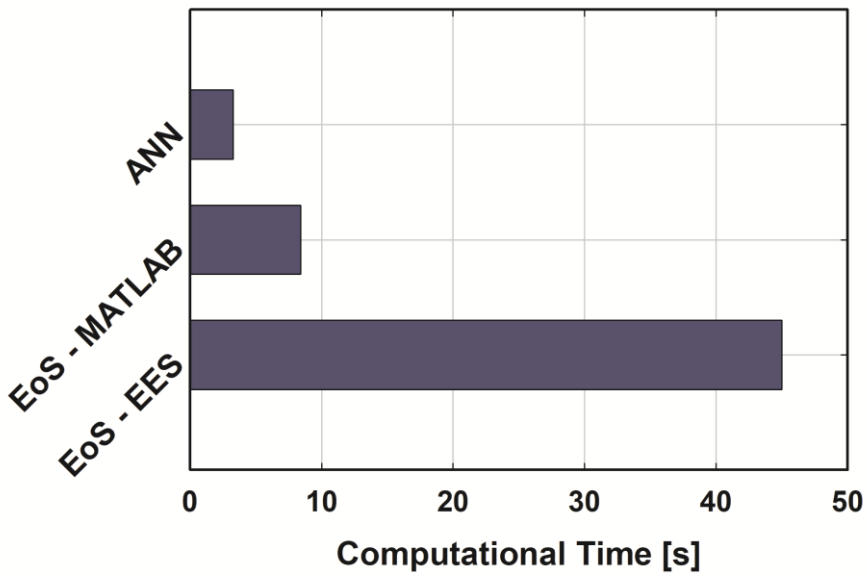

Figure 3.6: Comparison of computational time using three different property routines

3.5 Summary

ANN based property routines for computing the thermodynamic properties of ammonia-water mixtures are developed. ANN based property calculations offer significantly enhanced computational speeds that can be a major advantage for large cycle simulations such as transient analysis, which can involve millions of property calculations. Cascaded neural networks with multiple hidden layers are used to develop explicit property routines that can utilize many combinations of property triplets as inputs and provide the desired thermodynamic states as outputs. The performance of these neural networks is assessed by comparing the predictions with stablished EoS property calculations. The error in the predictions is observed to be less than 0.5%. The computational efficiency of these routines is compared with two EoS implementations in EES® and MATLAB® respectively. It is observed that ANN based property routines offer ~60% speedup in computing thermodynamic properties of ammonia-water mixtures. In the following chapters of this thesis, the implementation of a complete system transient model utilizing these ANN-based property calculation routines will be discussed.

CHAPTER 4. DYNAMIC MODELING OF HEAT EXCHANGERS

4.1 Introduction

This chapter presents the details of transient modeling of different components in an absorption system. The heat exchangers can be classified as single-inlet single-outlet type (absorber, condenser, evaporator, and recuperative heat exchangers,) and single-inlet dual-outlet type (desorber and rectifier). This study focuses on physics-based models, specifically the moving-boundary method, and the discretized finite volume method. Details of geometrical and heat transfer parameters of different components are provided. The geometry of the components is utilized in determining the fluid volumes and heat transfer areas. All the models presented in this chapter account for the thermal capacitance of both the internally stored working fluid and the coupling fluid stored in the heat exchangers, and the heat exchanger material. The discussion also elucidates the numerical features of the system of equations and the solvers implemented in the simulations.

4.2 Mathematical Modeling

The governing equations for mass, momentum and energy conservation for a Newtonian fluid are:

This chapter adapted from: Goyal, A., Garimella, S., Generalized transient simulation of two-phase heat exchangers using zeotropic fluid mixtures, International Journal of Refrigeration (2018), https://doi.org/10.1016/j.ijrefrig.2018.07.031

The sections pertinent to the desorber are adapted from a collaborative effort with Mr. Alexander A. Roeder. Detailed model formulation and analyses are available in the MS thesis entitled: “Transient Simulation of Ammonia-Water Mixture Desorption for Absorption Heat Pumps & Optimal Control of an Electric Vehicle Cabin Air Conditioning System” by Mr. Alexander A. Roeder (2018), Georgia Institute of Technology.

$$\frac{\partial \rho}{\partial t} + \nabla \cdot (\rho s) = 0 \tag{4.1}$$

$$\frac{\partial \rho s}{\partial t} + \nabla \cdot (\rho s s) = \rho f_b + \nabla \cdot \sigma \tag{4.2}$$

$$\frac{\partial \rho \left[e + \frac{s \cdot s}{2} \right]}{\partial t} + \nabla \cdot \rho s \left(h + \frac{s \cdot s}{2} \right) = -\nabla \cdot q`` + \rho f_b \cdot s + \nabla \cdot (\tau \cdot s) + \dot{Q} \tag{4.3}$$

These equations represent the unsteady conservation equations in their generalized form, and are utilized in different modeling paradigms as applicable to the different components of the system.

4.2.1 Thermodynamic Properties

Thermodynamic property computations are required at each time step of the simulation to evaluate the state points for the working fluid. As mentioned previously, the working fluid for the absorption systems under consideration here is a binary mixture of ammonia and water. However, the methodology outlined here is applicable to other fluid mixtures as well. For a binary mixture, three independent thermodynamic variables must be specified to completely define the thermodynamic state. For instance, if temperature (*T*), pressure (*P*), and concentration (*x*) are specified, then the complete thermodynamic state [specific enthalpy (*h*), vapor mass quality (*q*), specific volume (*v*), internal energy (*u*)] can be computed. Ammonia-water property routines developed by Rattner and Garimella (2016) are used in this work. Property triplets can be queried using the routines and the corresponding dependent state variables can be computed. The permissible triplets are *TPx*, *Pxh*, *TPq*, *Txv*, *xvu*, and *Pxq*.

Ammonia-water mixture is a non-ideal, zeotropic mixture, and therefore the temperature of the fluid mixture does not remain constant during phase change processes, in contrast to pure substances. Also, some highly non-linear property trends are observed especially at the operating concentration and pressures for ammonia-water VAS. Figure 4.1 shows a plot of the variation in the temperature of the mixture for known pressure and concentration values and varying vapor mass quality. It can be observed the mixture temperature changes very significantly at the higher quality values with a sharp non-linear relationship. This implies that a two-phase heat exchanger such as an evaporator or condenser will encounter these profiles of temperature, and consequently for enthalpy. The values of pressure and concentration are based on operating points for an actual system. Figure 4.2 shows a *TPx* surface for the mixture with a specified ammonia concentration of 0.997 kg kg^{-1} and enthalpy on the *z*-axis. The plot shows highly non-linear behavior of mixture enthalpy near saturation conditions. These highly non-linear property trends have implications on the choice of the solver (implicit or explicit), maximum time step size, and calculation of property derivatives such that these sharp gradients are addressed in an appropriate manner and the solver remains stable. Also, these sharp changes in properties render the system of governing equations to be *stiff*, which implies that the solved variables can demonstrate strong oscillations in the neighborhood of a solution. Typically, this feature renders the commonly used ODE solvers to be computationally very inefficient. Further details are presented in the following sections.

4.2.2 Single-inlet Single-outlet Heat Exchanger Models

This section presents the model development for components such as the absorber, condenser, evaporator and the recuperative heat exchangers used in an absorption system.

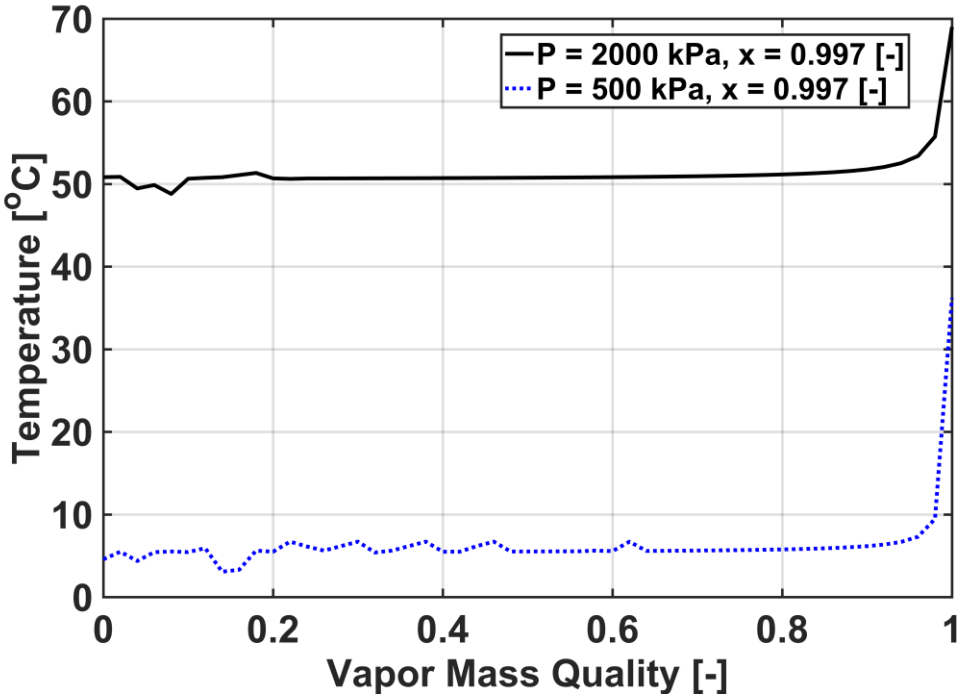

Figure 4.1: Ammonia-water mixture temperature as a function of quality

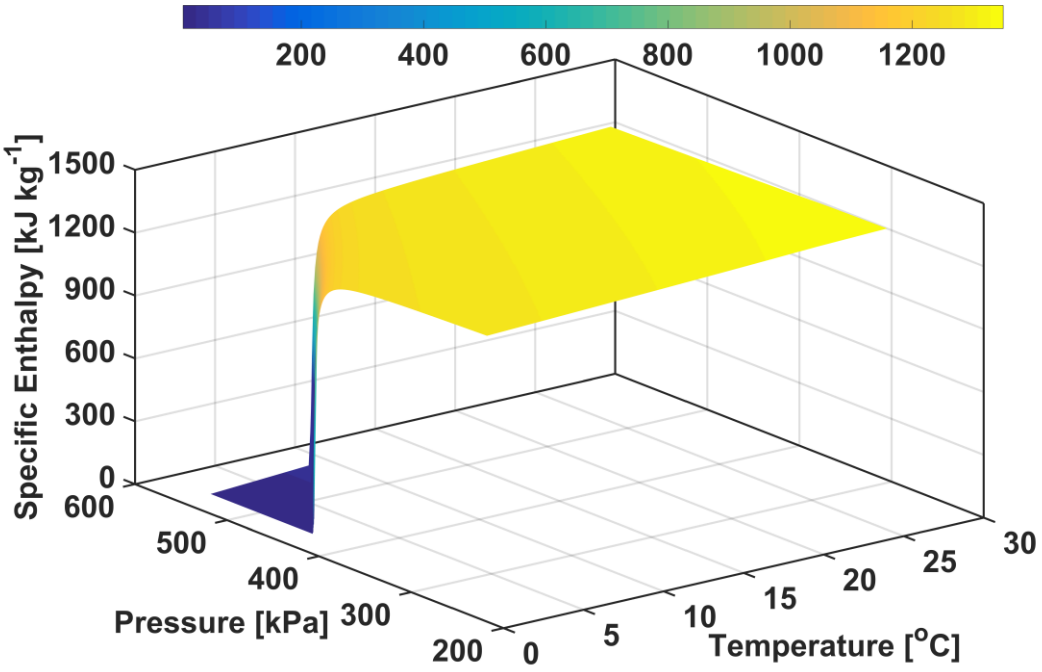

Figure 4.2: Ammonia-water mixture enthalpy variation at ammonia concentration of 0.997

Both the FV discretized and MB models presented in this study include several simplifying assumptions based on experimental observations and engineering knowledge. Other assumptions pertinent to the individual techniques are discussed in the following sections. Key assumptions in the counter-flow heat exchanger models are:

- 1-D compressible flow of ammonia-water working fluid
- Uniform but time-varying pressure imposed on the ammonia-water side as the pressure wave is assumed to propagate significantly faster than the thermal and mass storage effects
- Viscous dissipation effects and body forces neglected
- Axial conduction effects neglected as the Peclet ($Pe = RePr$) number is typically large
- Pressure drop in the heat exchanger neglected, leading to omission of the conservation of momentum equation from the final set of equations
- Liquid and vapor phases in thermal equilibrium and homogenous flow assumed
- Constant cross-sectional area of flow and wall
- Uniform heat transfer coefficient assumed in the control volume for both fluids
- Axial conduction in the wall material neglected
- 1-D incompressible coupling fluid; neglected pressure drop, viscous dissipation, and axial conduction effects; counterflow orientation

These assumptions lead to simplifications in the governing equations and remove second-order derivatives and non-linear coupling between pressure and velocity. Following the procedure outlined by MacArthur and Grald (1989), the simplified governing equations for refrigerant mass and energy conservation are:

$$\frac{\partial \rho_f}{\partial t} + \frac{\partial \rho_f s_f}{\partial z} = 0 \tag{4.4}$$

$$\frac{\partial [\rho_f h_f - P_f]}{\partial t} + \frac{\partial (\rho_f s_f h_f)}{\partial z} - \frac{U_f Per_f (T_f - T_w)}{A_{cs}} = 0 \tag{4.5}$$

These form a set of parabolic differential equations with refrigerant enthalpy and velocity as the field variables and require specification of initial conditions and time-dependent boundary conditions. The boundary conditions at the inlet and outlet are determined by the components upstream and downstream, respectively, in the complete heat pump system. As the working fluid is a binary mixture of refrigerant and sorbent for absorption heat pumps, in this study NH_3-H_2O, the species conservation equation is also included to account for species storage and transport as the inlet mass flow rate and concentration vary. The species transport equation is:

$$\frac{\partial \rho_f x_f}{\partial t} + \frac{\partial (\rho_f s_f x_f)}{\partial z} = 0 \tag{4.6}$$

As the refrigerant mass flow rate is a measured variable, the equations presented above are converted to their mass flow forms by multiplying with cross-sectional area of the flow, and represent a system of equations for calculating refrigerant mass flow rate, concentration, and enthalpy over time.

$$\frac{\partial A_{cs}\rho_f}{\partial t}+\frac{\partial \dot{m}_f}{\partial z}=0 \tag{4.7}$$

$$\frac{\partial A_{cs}\rho_f x_f}{\partial t}+\frac{\partial \dot{m}_f x_f}{\partial z}=0 \tag{4.8}$$

$$\frac{\partial A_{cs}[\rho_f h_f - P_f]}{\partial t}+\frac{\partial \dot{m}_f h_f}{\partial z}+U_f Per_f (T_f - T_w)=0 \tag{4.9}$$

The energy conservation equations for the wall material and incompressible coupling fluid are:

$$\rho_w Cp_w A_{cs,w}\frac{\partial T_w}{\partial t}-U_f Per_f (T_f - T_w)+U_{cf} Per_{cf} (T_w - T_{cf})=0 \tag{4.10}$$

$$\rho_{cf} Cp_{cf} A_{cs,cf}\frac{\partial T_{cf}}{\partial t}+\frac{\partial (\dot{m}_{cf} Cp_{cf} T_{cf})}{\partial z}-U_{cf} Per_{cf} (T_w - T_{cf})=0 \tag{4.11}$$

Eq. 4.7-4.11 form the governing unsteady partial differential equations (PDEs) for the counterflow heat exchanger. The first term of these equations represents the storage/capacitance terms and accounts for mass and energy storage in the fluid or wall volume. The computed variables are the refrigerant outlet mass flow rate, outlet concentration, enthalpy, wall temperature, and coupling fluid outlet temperature. The time varying boundary conditions for the system are refrigerant inlet mass flow rate, concentration, temperature, and coupling fluid inlet mass flow rate and temperature. The geometric parameters and physical component dimensions are fixed constants for the component under consideration. Heat transfer coefficients are determined by utilizing the system cycle model as discussed by Garimella *et al.* (2016). The overall condenser heat transfer rate at design conditions is used as an input. First, the heat transfer coefficient on the coupling fluid side of the condenser is estimated using the geometrical parameters and

inlet mass flow rate of the coupling fluid. A single-phase, laminar heat transfer correlation for circular ducts (Kakac *et al.*, 1987) is utilized to compute the heat transfer coefficient. As a segmented model relies on the local temperature difference between the participating media, an arithmetic mean temperature difference between the heat exchanger wall and the coupling fluid is used to determine the average wall temperature. The average wall temperature is then used on the refrigerant side of the condenser to estimate the heat transfer coefficient, with the total heat transfer rate of the component known from the cycle model.

4.2.2.1 Finite Volume Formulation

Figure 4.3 shows a discretized representation of a counter-flow condenser with refrigerant and coupling fluid exchanging heat through a wall element. FV formulation involves discretizing the heat exchanger in several control volumes of constant area and volume. Eqn. 4.7-4.11 are integrated over the control volume and discretized using an

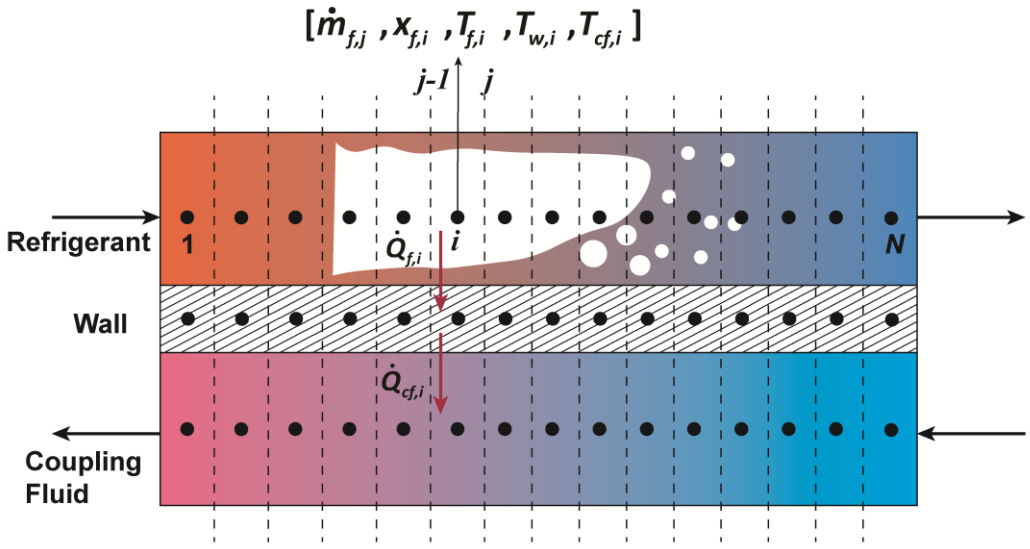

Figure 4.3: Schematic of 1-D finite volume discretization of a condenser

upwinding differencing scheme (UDS) (Patankar, 1980) for flux terms to formulate the system of ODEs for all nodes that are solved simultaneously. The discretized equations for mass, species, and energy conservation for refrigerant, wall and coupling fluid are:

$$\frac{d\rho_{f,i}}{dt} = \frac{1}{V_{f,seg}}\left[\dot{m}_{f,j-1} - \dot{m}_{f,j}\right] \tag{4.12}$$

$$\frac{d\left(\rho_{f,i}x_{f,i}\right)}{dt} = \frac{1}{V_{f,seg}}\left[\dot{m}_{f,j-1}x_{f,j-1} - \dot{m}_{f,j}x_{f,j}\right] \tag{4.13}$$

$$\frac{d\left(\rho_{f,i}h_{f,i}\right)}{dt} - \frac{dP_f}{dt} = \frac{1}{V_{f,seg}}\left[\dot{m}_{f,j-1}h_{f,j-1} - \dot{m}_{f,j}h_{f,j} - (UA)_f\left(T_{f,i} - T_{w,i}\right)\right] \tag{4.14}$$

$$(m_w Cp_w)_i \frac{dT_{w,i}}{dt} = (UA)_f\left(T_{f,i} - T_{w,i}\right) - (UA)_{cf}\left(T_{w,i} - T_{cf,i}\right) \tag{4.15}$$

$$(m_{cf} Cp_{cf})_i \frac{dT_{cf,i}}{dt} = \dot{m}_{cf} Cp_{cf}\left(T_{cf,j} - T_{cf,j-1}\right) + (UA)_{cf}\left(T_{w,i} - T_{cf,i}\right) \tag{4.16}$$

$$h_{f,j} = h_{f,i} \tag{4.17}$$

$$x_{f,j} = x_{f,i} \tag{4.18}$$

$$T_{cf,j} = T_{cf,i+1} \tag{4.19}$$

Eq. 4.12 – 4.16 along with Eq. 4.17 – 4.19 (UDS scheme) are formulated for all *N* nodes and result in a system of 5*N* equations with 5*N* unknowns: nodal fluid concentration and enthalpy, wall and coupling fluid temperatures, and interfacial refrigerant flow rates. As Eq. 4.12 is an algebraic equation with outlet mass flow rate as the dependent variable, the complete system of equations becomes a DAE system. To simplify the system and mitigate any numerical issues with typical solvers, Eq. 4.12 is used to recursively substitute the

value of $\dot{m}_{f,j}$ in Eq. 4.13 and 4.14. The refrigerant species and energy conservation equations are simplified as:

$$V_{f,seg}\rho_{f,i}\frac{dx_{f,i}}{dt} = \dot{m}_{f,j-1}(x_{f,i-1} - x_{f,i}) \tag{4.20}$$

$$V_{f,seg}\rho_{f,i}\frac{dh_{f,i}}{dt} = \dot{m}_{f,j-1}(h_{f,i-1} - h_{f,i}) - (UA)_f(T_{f,i} - T_{w,i}) + V_{f,seg}\frac{dP_f}{dt} \tag{4.21}$$

The final system of equations (Eq. 4.12, 4.15 – 4.21) leads to 5*N* unknowns with an equal number of equations. Eq. 4.12 is separately used at each time step to determine the outlet mass flow rate leaving the i^{th} CV. The profiles for time-dependent boundary condition of inlet mass flow rates, inlet temperatures of both fluids, and inlet concentration of the refrigerant are provided to the model. Appropriate initial conditions for start-up from room temperature or computed from a previous steady state operation are specified to completely define the system of equations. In a full system model, the boundary conditions are supplied from upstream components or accumulator models that are typically employed to set the pressure and concentration.

4.2.2.2 Moving-boundary Method

As discussed previously, MB methods belong to the class of lumped parameter models in which the fluid properties are averaged over different regions of multi-phase flow and the pertinent states are computed using spatially averaged forms of unsteady conservation equations. This provides a significant computational advantage as compared to the discretized schemes using FV and finite difference (FD) methods where the discretized PDEs are solved for each node. In MB methods, the PDEs for conservation of mass and energy are converted into a system of ordinary differential equations (ODE) by

integrating them over the length of each region. Simplified conservation equations are integrated over each fluid region using Leibnitz's rule (Eq. 4.22).

$$\frac{d}{dt}\int_{a_1(t)}^{a_2(t)} G(t,z)dz = \int_{a_1(t)}^{a_2(t)} \frac{\partial G(t,z)}{\partial t} dz + G(t,a_2(t))\frac{da_2(t)}{dt} - G(t,a_1(t))\frac{da_1(t)}{dt} \qquad (4.22)$$

Figure 4.4 shows a schematic of the MB method applied to a typical condenser used in absorption systems with two fluid zones present: two-phase and subcooled regions. Additional scenarios with fewer or additional fluid regions can also be formulated.

For a switched moving boundary method that accounts for time-varying outlet fluid phase from the heat exchanger, Eq. 4.7 – 4.11 are integrated using Eq. 4.22 and the time derivatives of the state variables are computed. In the two-zone model, the state vector consists of the position of the two-phase to subcooled liquid transition, the outlet enthalpy of the working fluid, the outlet mass flow rate from the two-phase and subcooled zones, the average wall temperature for each zone, and the average temperature of the coupling fluid for each zone.

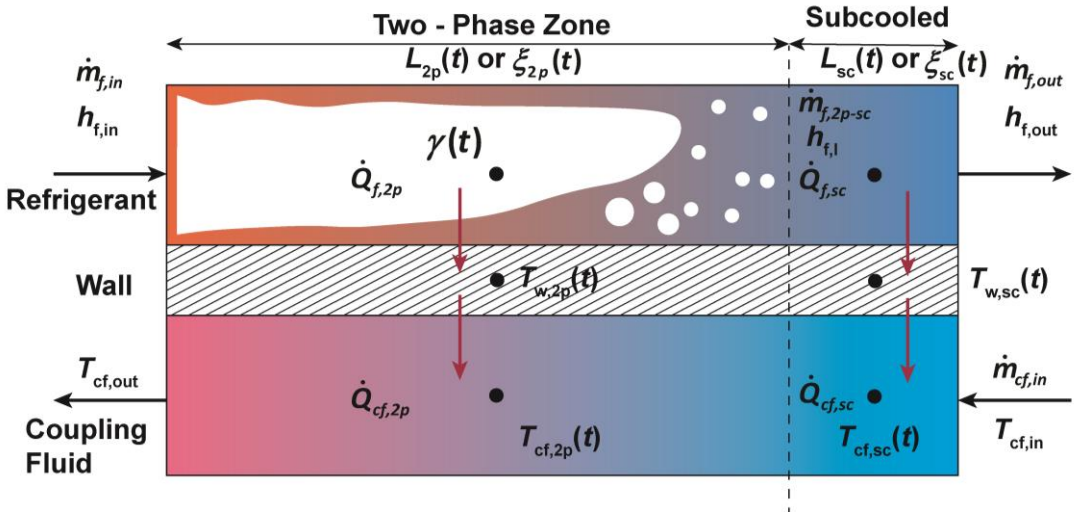

Figure 4.4: Schematic of moving-boundary model of a condenser

$$Y(t) = [\dot{m}_{f,2p-sc}, \dot{m}_{f,out}, \xi_{2p}, h_{f,out}, T_{w,2p}, T_{w,sc}, T_{cf,2p}, T_{cf,sc}] \tag{4.23}$$

Averaging of fluid-properties in the MB method is important to ensure accurate computations. Referring to Figure 4.4, the inlet conditions of the refrigerant are known, and the average enthalpy in the two-phase zone is calculated as the arithmetic mean of inlet and outlet enthalpy. Once the average enthalpy is known, using the pressure and concentration, the average refrigerant temperature and density can be calculated. This average temperature is used to calculate the heat transfer rate to the wall. It should be noted that an average temperature can also be calculated as the arithmetic mean of the inlet and outlet temperature from any zone. However, from Figure 4.1, this can lead to a large error in two-phase region calculations as the mean temperature corresponds to a very high quality of the two-phase zone. Instead, if the averaging of enthalpy is used, it predicts the mean quality to be approximately at 0.5, which is closer to a linear profile as assumed in the arithmetic mean. Similar enthalpy averaging is performed for the subcooled region and the outlet mass flow rate and subcooled region enthalpy are calculated as the heat transfer area and heat exchanger volume for two-phase region are known. The following equations are used to develop the MB model.

Two-Phase Zone

$$\frac{dT_{cf,2p}}{dt} = \frac{\begin{array}{c}\dot{m}_{cf} Cp_{cf} (T_{cf,2p}(\xi_{2p}) - T_{cf,out}) + U_{cf} A_{cf} \xi_{2p} (T_{w,2p} - T_{cf,2p}) \\ -\left[(mCp)_{cf} (T_{cf,2p} - T_{cf}(\xi_{2p})\right] \frac{d\xi_{2p}}{dt}\end{array}}{(mCp)_{cf} \xi_{2p}} \tag{4.24}$$

$$\dot{m}_{f,2p-sc} = \dot{m}_{f,in} - V_f \xi_{2p} \frac{d\rho_{f,2p}}{dt} - K_s \left[V_f (\rho_{f,2p} - \rho_{f,2p,out}) \frac{d\xi_{2p}}{dt} \right] \tag{4.25}$$

$$\frac{d\xi_{2p}}{dt} = \frac{\dot{m}_{f,in}h_{f,in} - \dot{m}_{f,2p-sc}h_{f,2p,out} - U_f A_f \xi_{2p}(T_{f,2p} - T_{w,2p}) + V_f\left[\xi_{2p}\frac{dP_f}{dt} - \xi_{2p}\rho_{f,2p}\frac{dh_{f,2p}}{dt} - \xi_{2p}h_{f,2p}\frac{d\rho_{f,2p}}{dt}\right]}{V_f(\rho_{f,2p}h_{f,2p} - \rho_{f,2p,out}h_{f,2p,out})} \quad (4.26)$$

$$\frac{dT_{w,2p}}{dt} = \frac{U_f A_f \xi_{2p}(T_{f,2p} - T_{w,2p}) - U_{cf} A_{cf} \xi_{2p}(T_{w,2p} - T_{cf,2p}) - K_s\left[(mCp)_w(T_{w,2p} - T_w(\xi_{2p})\right]\frac{d\xi_{2p}}{dt}}{(mCp)_w \xi_{2p}} \quad (4.27)$$

$$\begin{aligned} h_{f,2p} &= \frac{h_{f,in} + h_{f,2p,out}}{2} \\ T_{f,2p} &= F(P_f, x_f, h_{f,2p}) \\ \rho_{f,2p} &= F(P_f, x_f, h_{f,2p}) \end{aligned} \quad (4.28)$$

Subcooled Zone

$$\frac{dT_{cf,sc}}{dt} = \frac{\dot{m}_{cf}Cp_{cf}\left[T_{cf,in} - T_{cf}(\xi_{2p})\right] + U_{cf}A_{cf}\xi_{sc}(T_{w,sc} - T_{cf,sc}) - (mCp)_{cf}\left[T_{cf,sc} - T_{cf}(\xi_{2p})\right]\frac{d\xi_{2p}}{dt}}{(mCp)_{cf}\xi_{sc}} \quad (4.29)$$

$$\frac{dT_{w,sc}}{dt} = K_s \frac{U_f A_f \xi_{sc}(T_{f,sc} - T_{w,sc}) - U_{cf} A_{cf} \xi_{sc}(T_{w,sc} - T_{cf,sc}) + (mCp)_w\left[T_{w,sc} - T_w(\xi_{2p})\right]\frac{d\xi_{2p}}{dt}}{(mCp)_w \xi_{sc}} \quad (4.30)$$

$$\dot{m}_{f,out} = \dot{m}_{f,2p-sc} + K_s\left[(\rho_{f,sc} - \rho_{f,2p,out})V_f\frac{d\xi_{2p}}{dt} - V_f\xi_{sc}\frac{d\rho_{f,sc}}{dt}\right] \quad (4.31)$$

$$\frac{dh_{f,sc,out}}{dt} = K_s \left\{ \begin{array}{l} 2\left[\begin{array}{l} \dot{m}_{f,2p-sc} h_{f,2p,out} - \dot{m}_{f,out} h_{f,out} - U_f A_{fsc} \xi_{sc} (T_{f,sc} - T_{w,sc}) + \\ V_f \left[\begin{array}{l} \xi_{sc} \dfrac{dP_f}{dt} - \xi_{sc} h_{f,sc} \dfrac{d\rho_{f,sc}}{dt} + \\ (\rho_{f,sc} h_{f,sc} - \rho_{f,2p,out} h_{f,2p,out}) \dfrac{d\xi_{2p}}{dt} \end{array} \right] \end{array} \right] \\ \hline \rho_{f,sc} V_f \xi_{sc} \\ - \dfrac{dh_{f,2p,out}}{dt} \end{array} \right\} + (1 - K_s) \frac{dh_{f,2p,out}}{dt} \tag{4.32}$$

$$\frac{dh_{f,2p}}{dt} = \frac{\begin{array}{l} \dot{m}_{f,in} h_{f,in} - \dot{m}_{f,2p-sc} h_{f,2p,out} - U_f A_f \xi_{2p} (T_{f,2p} - T_{w,2p}) + \\ V_f \left[\xi_{2p} \dfrac{dP_f}{dt} - \dfrac{d\xi_{2p}}{dt} (\rho_{f,2p} h_{f,2p} - \rho_{f,2p,out} h_{f,2p,out}) - \xi_{2p} h_{f,2p} \dfrac{d\rho_{f,2p}}{dt} \right] \end{array}}{V_f \xi_{2p} \rho_{f,2p}} \tag{4.33}$$

$$\frac{dh_{f,2p,out}}{dt} = (1 - K_s) \left[2 \frac{dh_{f,2p}}{dt} - \frac{dh_{f,in}}{dt} \right] + K_s \frac{dh_{f,l}}{dt} \tag{4.34}$$

$$\begin{aligned} h_{f,sc} &= \frac{h_{f,2p,out} + h_{f,out}}{2} \\ T_{f,sc} &= F(P_f, x_f, h_{f,sc}) \\ \rho_{f,sc} &= F(P_f, x_f, h_{f,sc}) \end{aligned} \tag{4.35}$$

All the time-derivative terms of the state-vector $Y(t)$ and mass flow rate terms are computed at each time step and numerically integrated to proceed in time. This approach significantly reduces the computational cost as a maximum of two control volumes per component are solved as compared to the significantly larger number of control volumes in a discretized model. This compact formulation of transient response is also more suitable for the analysis and design of control algorithms.

It is possible that large amplitude variations in the input conditions of the heat exchanger can cause a fluid region to disappear or reappear. In the absence of a mechanism to treat this situation, the state vector for such an operation will vary in size and most numerical solvers will detect that as a singularity in the system of equations and fail. To avoid these failures, a switching approach is used in the above set of equations where a switching parameter (K_s) modifies the structure of Eq. 4.24-4.27 and Eq. 4.29-4.33. For instance, if there is a transient phenomenon such that the subcooled region disappears, the switching parameter will modify the subcooled zone equations such that the state variable derivatives will go to a very small value tending to zero, but the overall state vector size will remain constant and avoid discontinuities in the solver. Similarly, when the subcooled zone reappears, the corresponding state derivatives will become active and initialize with physically consistent boundary conditions. The variation of the Boolean variable K_s is shown in Eq. 4.36 (if the two-phase zone length and outlet enthalpy remain below a threshold then K_s is unity, and it becomes zero if these conditions are not true). This type of switching algorithm based on zone length and enthalpy is shown to be stable and accurate (Rodriguez and Rasmussen, 2017).

$$\begin{aligned} &\text{IF } (\xi_{2p} < 0.9995 \text{ AND } h_{f,out} < 0.9999 h_{f,l}) \\ &\text{THEN} \\ &\quad K_s = 1 \\ &\text{ELSE} \\ &\quad K_s = 0 \end{aligned} \tag{4.36}$$

Property Conservation in MB Model

It is crucial to ensure conservation of mass and energy on an integral basis for the entire component. As opposed to the finite volume method, which is inherently

conservative, the MB formulation requires a mathematical framework to conserve properties as the zones move. In this work, a simplified upwinding formulation is used to transport the temperature of the zone downstream of the direction of the movement of the interface. This is shown in Eq. 4.37.

$$\begin{aligned} &\frac{d\xi_{2p}}{dt} > 0 \rightarrow T_w(\xi_{2p}) = T_{w,sc}, T_{cf}(\xi_{2p}) = T_{cf,sc} \\ &\frac{d\xi_{2p}}{dt} <= 0 \rightarrow T_w(\xi_{2p}) = T_{w,2p}, T_{cf}(\xi_{2p}) = T_{cf,2p} \end{aligned} \tag{4.37}$$

These two methods will be implemented in the simulation of the transient response of a condenser coupled to an ambient heat exchanger. The parameters of the heat exchangers, operating conditions, boundary conditions and key transient response scenarios will be discussed in the following sections.

4.2.3 Desorber Model

The desorber is the main refrigerant generating component in a vapor absorption system. Several studies have demonstrated miniaturization of absorption systems for small-capacity residential systems. Particular emphasis is on desorber designs to ensure the most efficient refrigerant generation and stable operation of the overall system (Determan and Garimella, 2011; Delahanty *et al.*, 2015; Garimella *et al.*, 2016). These designs also ensure small fluid inventories that minimize the thermal capacitance. One of these designs, a branched-tray desorber presented by Delahanty *et al.* (2015), demonstrates features analogous to distillation columns used in chemical separation processes such as pool-boiling in trays and stage-wise purification of the generated vapor. It should be noted that distillation columns differ markedly from the desorber column as they are typically not

heat assisted along the length of the column. However, the conservation equations and tray inefficiency formulation are found to be analogous to those employed for the desorber. Comprehensive reviews of transient models for distillation columns are available in the literature (Gani *et al.*, 1986; Luyben, 1989; Skogestad, 1997; Bequette, 1998). Figure 4.5 shows a schematic of a compact branched-tray desorber used in this study (Garimella *et al.*, 2016). In this configuration, the concentrated solution (rich in ammonia) is received from the solution heat exchanger and flows downward through the desorber. At each tray, the liquid solution exchanges heat through the desorber wall and the coupling fluid flows in a counter-flow configuration. Vapor is predominantly generated by pool boiling at each

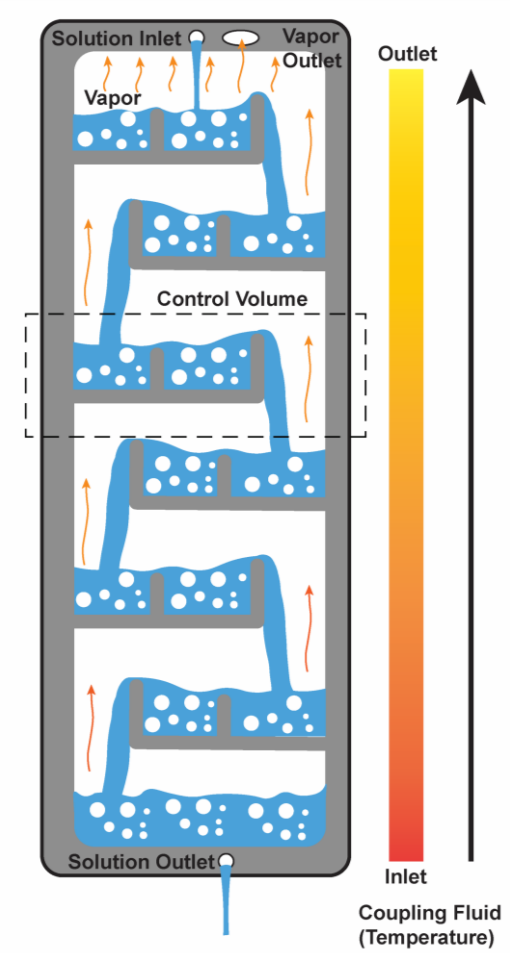

Figure 4.5: Schematic of the branched tray desorber

tray, rising counter-current to the liquid solution flow due to buoyancy, and exits at the top of the desorber. The dilute solution (poor in ammonia concentration) exits at the bottom of the desorber, returning to the solution heat exchanger. Finally, the dilute solution and refrigerant vapor mix in the absorber, regenerating the concentrated solution.

In addition to the assumptions listed in Section 4.2.2, the key assumptions applied to the desorber component of a small-scale ammonia-water absorption system to further simplify the system of equations are as follows:

- The liquid and vapor phases throughout the component are at saturated thermodynamic states as the desorber is continuously heated along the length and vapor and liquid phases exist at each location.
- Heat transfer between the component wall and vapor is neglected as the convective heat transfer coefficient for vapor flow is significantly smaller than the boiling heat transfer coefficient.
- Phase equilibrium is approximated using thermal equilibrium between the liquid and vapor phases. It is assumed here that the interaction between the two phases is primarily driven by thermal inequilibrium, with chemical interactions having a small effect.
- Vapor holdup is neglected in all control volumes. Although the volume occupied by the vapor is large, the liquid density is much higher than that of the vapor, and therefore, the mass of each control volume can be assumed to be liquid-only.

- The liquid on all trays is assumed perfectly mixed and incompressible. Therefore, the liquid solution exiting the trays is assumed to be at the tray temperature and concentration.
- All trays are assumed inefficient, requiring the inclusion of a tray efficiency equation. A vapor-phase tray efficiency expression is used with the efficiency values (Eq. 4.38) for each tray selected based upon experimentally observed steady-state vapor outlet temperatures and concentrations (Delahanty *et al.*, 2015).

$$\varepsilon_{v_i} = \frac{y_j - y_{j-1}}{y_j^* - y_{j-1}} \tag{4.38}$$

The term y_j^* is the concentration of vapor exiting the tray if it was in thermal equilibrium with the liquid on the tray.

These assumptions do not change the governing differential equations 4.7 – 4.11 when applied to the desorber. However, the discretized governing equations for the desorber are modified, as presented in the following section.

4.2.3.1 Discretized Equations

Figure 4.6 shows the discretized counter-flow desorber. The control volumes (CV) are chosen such that one boiling tray is centered in each segment. Equations 4.7 – 4.11 are integrated over each CV and discretized using an upwinding differencing scheme (UDS) (Patankar, 1980) for liquid flux terms to formulate a system of ordinary differential equations (ODEs) for all nodes. Vapor flux terms are not discretized using UDS because

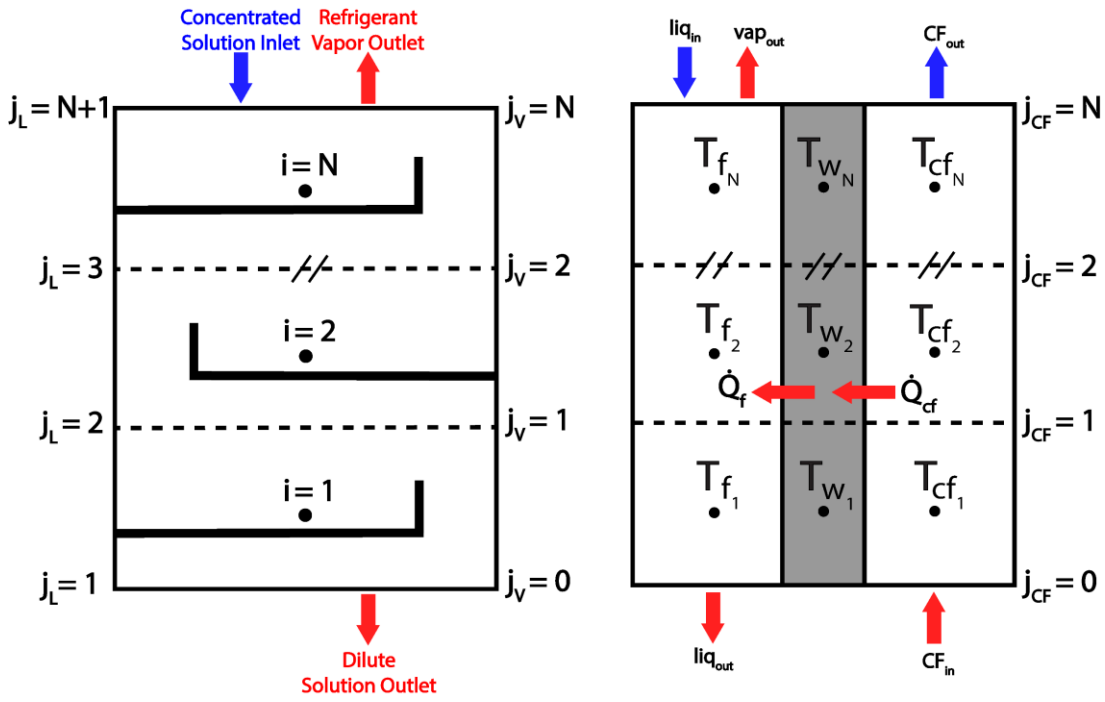

Figure 4.6: Discretized desorber component; Left: solution-side discretization; Right: solution, wall, and coupling fluid region discretization

the vapor exiting each CV is not at the tray temperature due to tray inefficiencies. These ODEs are solved simultaneously to obtain the transient response of the desorber.

Figure 4.7 shows an individual tray with solution-side CV. Liquid solution and vapor enter the CV from the trays above and below, respectively. The outlet vapor state is defined using vapor concentration (from tray efficiency definition in Eq. 4.38), the component pressure (known boundary condition), and the saturated vapor quality (q = 1).

The discretized equations for mass, species, and energy conservation for the solution, wall, and coupling fluid are:

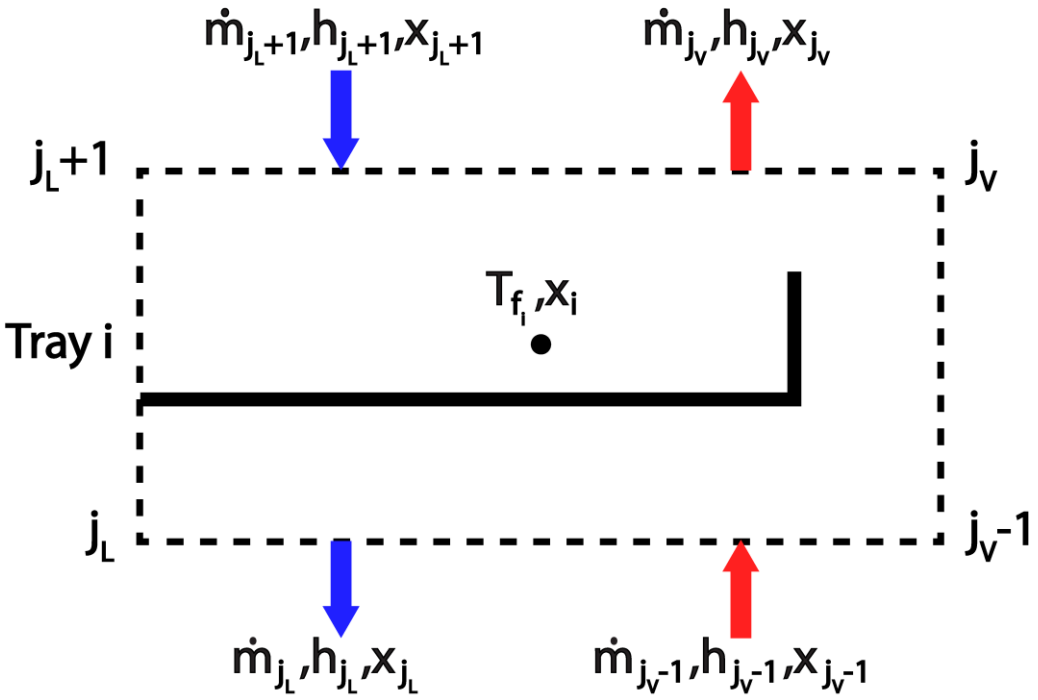

Figure 4.7: Solution-side tray control volume

$$\left(\frac{\partial \rho_{f,i}}{\partial P_f}\right)\frac{dP_f}{dt}+\left(\frac{\partial \rho_{f,i}}{\partial x_i}\right)\frac{dx_i}{dt}+\left(\frac{\partial \rho_{f,i}}{\partial h_{f,i}}\right)\frac{dh_{f,i}}{dt_i}= \frac{1}{V_{f,seg}}\left[\dot{m}_{L,j+1}-\dot{m}_{L,j}+\dot{m}_{V,j-1}-\dot{m}_{V,j}\right] \tag{4.39}$$

$$\left(x_i\frac{\partial \rho_{f,i}}{\partial P_f}\right)\frac{dP_f}{dt}+\left(\rho_{f,i}+x_i\frac{\partial \rho_{f,i}}{\partial x_i}\right)\frac{dx_{f,i}}{dt}+\left(x_i\frac{\partial \rho_{f,i}}{\partial h_{f,i}}\right)\frac{dh_{f,i}}{dt}= \frac{1}{V_{f,seg}}\left[\dot{m}_{L,j+1}x_{j+1}-\dot{m}_{L,j}x_j+\dot{m}_{V,j-1}y_{j-1}-\dot{m}_{V,j}y_j\right] \tag{4.40}$$

$$\left(\frac{\partial \rho_{f,i}}{\partial P_f}-\frac{1}{V_{f,seg}}\right)\frac{dP_f}{dt}+\left(\frac{\partial \rho_{f,i}}{\partial x_i}\right)\frac{dx_i}{dt}+\left(\frac{\partial \rho_{f,i}}{\partial h_{f,i}}h_{f,i}+\rho_{f,i}\right)\frac{dh_{f,i}}{dt}= \frac{1}{V_{f,seg}}\left[\dot{m}_{L,j+1}h_{L,j+1}-\dot{m}_{L,j}h_{L,j}+\dot{m}_{V,j-1}h_{V,j-1}-\dot{m}_{V,j}h_{V,j}+(UA)_f\left(T_{w,i}-T_{f,i}\right)\right] \tag{4.41}$$

$$(m_w Cp_w)_i\frac{dT_{w,i}}{dt}=(UA)_{cf}\left(T_{cf,i}-T_{w,i}\right)-(UA)_f\left(T_{w,i}-T_{f,i}\right) \tag{4.42}$$

$$(m_{cf} Cp_{cf})_i \frac{dT_{cf,i}}{dt} = \dot{m}_{cf} Cp_{cf} \left(T_{cf,j-1} - T_{cf,j}\right) - (UA)_{cf} \left(T_{cf,i} - T_{w,i}\right) \tag{4.43}$$

$$y_j = y_{j-1} + \varepsilon_{v_i} \left(y_j^* - y_{j-1}\right) \tag{4.44}$$

$$y_j^* = F\left(T_{f,i}, P_f, q = 1\right) \tag{4.45}$$

$$x_{f,i} = F\left(T_{f,i}, P_f, q = 0\right) \tag{4.46}$$

$$h_{L,j} = h_{f,i} \tag{4.47}$$

$$x_j = x_{f,i} \tag{4.48}$$

$$T_{cf,j} = T_{cf,i} \tag{4.49}$$

Equations 4.39 – 4.46 along with Equations 4.47 – 4.49 (UDS) are formulated for all *N* trays, which results in a system of 8*N* equations with 8*N* unknowns: nodal liquid enthalpy and concentration, ideal outlet vapor concentration, actual outlet vapor concentration, nodal wall and coupling fluid temperature, and outlet liquid and vapor mass flow rates. Equations 4.38 – 4.46 form a system of differential-algebraic equations (DAEs).

4.3 Heat Exchanger Parameters

4.3.1 Condenser

Typical microchannel plate heat exchangers utilize a repeating pattern of working fluid and coupling fluid sheet pairs, and multiple such pairs are bonded to achieve design performance. The heat exchanger simulation framework presented here models one pair of refrigerant and coupling fluid sheets by uniformly distributing the inlet mass flow rate and fluid phase between all the sheet pairs. The outlet mass flow rate and heat transfer rate is

obtained by multiplying these parameters by the number of shims. Table 4.1 summarizes the physical parameters and heat transfer coefficients for the heat exchanger.

Figure 4.8 shows the setup of the modeled system including the condenser and the ambient heat exchanger. Inlet conditions of the refrigerant are determined from the saturated vapor phase leaving the rectifier at a specified temperature and at the same pressure as the condenser. The ambient heat exchanger determines the temperature of the coupling fluid entering the condenser after it rejects the heat of condensation to the air stream. In a typical system, this heat exchanger has a crossflow configuration. For simplification, this heat exchanger is modeled in a static and lumped manner using the effectiveness – NTU relation (Incropera *et al.*, 2007). The governing equations for the ambient heat exchanger are:

$$NTU_{amb} = \frac{UA_{amb}}{C_{\min}} \tag{4.50}$$

$$\varepsilon_{amb} = 1 - \exp\left[\left(\frac{C_{\max}}{C_{\min}}\right) NTU_{amb}^{0.22} \left\{\exp\left(-\frac{C_{\max}}{C_{\min}} NTU_{amb}^{0.78}\right) - 1\right\}\right] \tag{4.51}$$

$$\dot{Q}_{amb} = \varepsilon_{amb} C_{\min} (T_{cf,in} - T_{air,in}) \tag{4.52}$$

Table 4.1: Physical and heat transfer parameters of the condenser

Parameter	Refrigerant	Coupling Fluid	Wall
Heat transfer area per sheet (m^2)	0.0229	0.0174	
Mass of sheet pair (kg)			0.159
Number of channels per shim	75	75	
Number of sheets	25		
Channel hydraulic diameter (m)	440×10^{-06}		
Fluid volume per sheet (m^3)	2.67×10^{-06}	2.02×10^{-06}	
Heat transfer coefficient (W m^{-2} K^{-1})	950	4500	
Total inlet mass flow rate (kg s^{-1})	0.0031	0.112	
Specific heat capacity (J kg^{-1} K^{-1})		3993	500
Density (kg m^{-3})		1003	7860

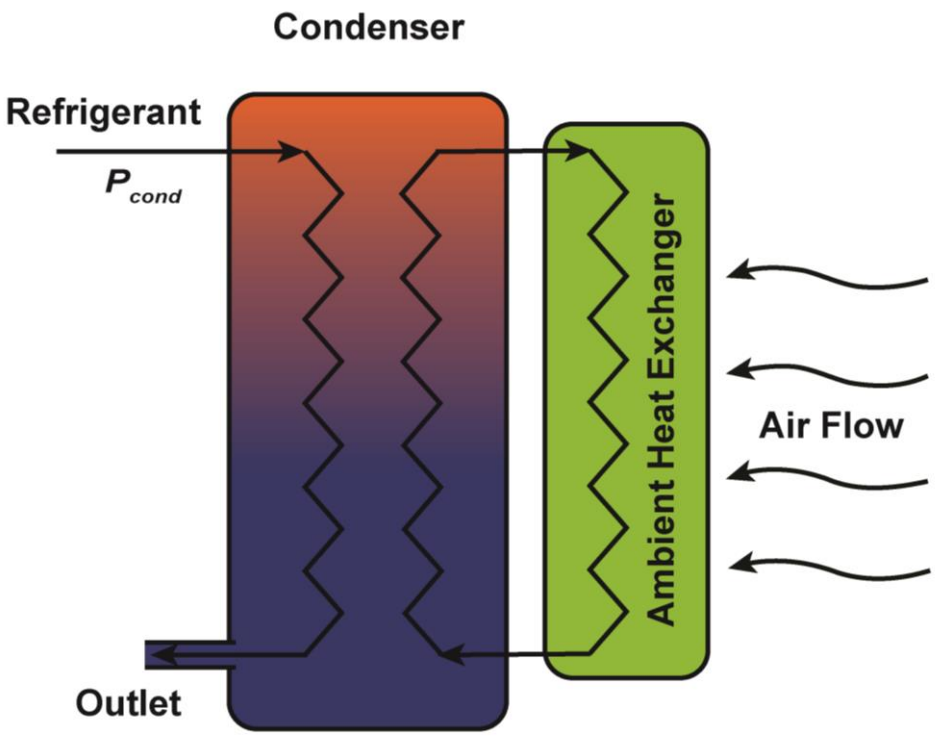

Figure 4.8: Schematic of the simulated condenser and air-coupled heat exchanger

Thermal capacitance of the coupling fluid loop is accounted for by using a well-mixed tank model with a total coupling fluid volume of 0.002 m^3. An effectiveness of 0.745 is used for the air heat exchanger.

4.3.2 Desorber

The geometric and heat transfer parameters used in this study are representative of the desorber-rectifier components developed by Keinath *et al.* (2015) and Delahanty *et al.* (2015). The compact ammonia-water desorber-rectifier developed by Keinath *et al.* (2015) is shown in Figure 4.9. The solution plate of the component (left) consists of three sections: the desorber, analyzer, and rectifier. Each solution plate has two coupling fluid sheets (right) attached to it. The focus of this section is on the desorber section of the complete desorber-rectifier component. Any dynamic effects of the analyzer are neglected, and the

rectifier is not simulated. However, the methods presented in this study can be adapted to include these sections.

Table 4.2 provides a summary of the key parameters of a single solution plate and coupling fluid sheet set of the desorber. The number of trays is based upon the geometry shown in Figure 4.9. The two tray channels are assumed to be lumped into one solution channel with enlarged trays. The solution fluid region volume is approximated by the overall desorber region volume minus the volume of the tray material. The solution heat transfer conductance is representative of the results of Delahanty *et al.* (2015), which take into account heat loss to the surroundings. Due to relatively large uncertainty in experimental values, the present study assumes a uniform average value for the solution heat transfer conductance. The wall mass is approximated as the mass of the desorber section of one solution tray and two coupling fluid shims, calculated using engineering

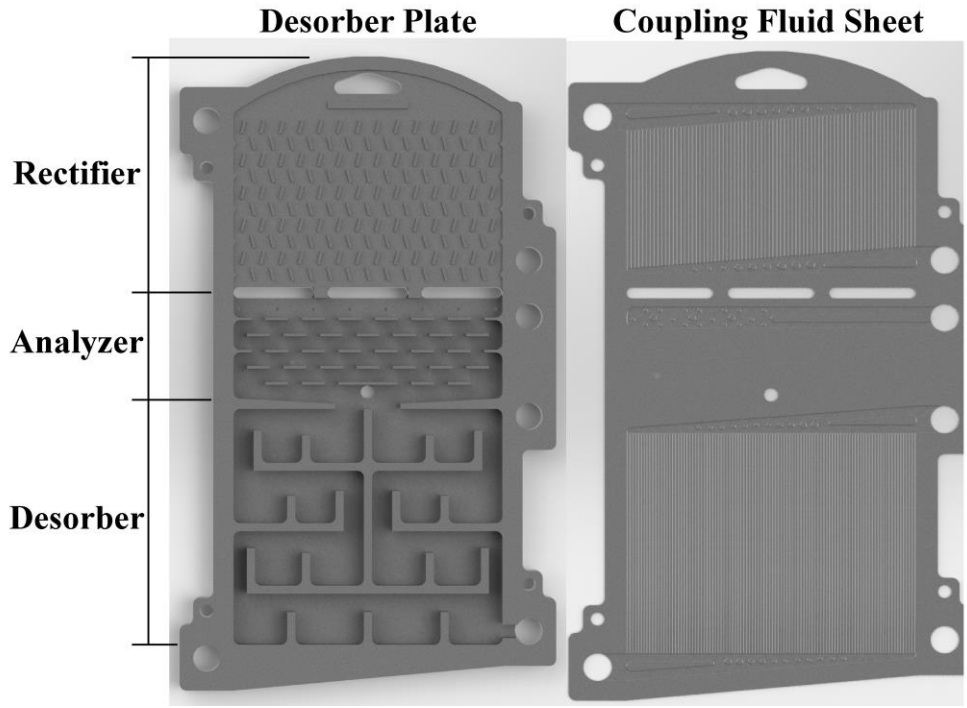

Figure 4.9: : Complete desorber solution plate (left) and coupling fluid sheet (right) pair (Keinath *et al.*, 2015)

Table 4.2: Properties of desorber per solution plate and coupling fluid sheet pair

	Description	Units	Nomenclature	Value
Component	Number of plate/sheet sets	-	N_{set}	8
NH_3-H_2O solution	Number of trays	-	N_{tray}	4
	Fluid region volume	m^3	V_f	7×10^{-5}
	Heat transfer conductance	W K^{-1}	$(UA)_f$	67.5
Wall	Mass of wall	kg	m_w	6.37
	Specific heat	J kg^{-1} K^{-1}	Cp_w	480
CF	Density	kg m^{-1}	ρ_{cf}	789
	Fluid region volume	m^3	V_{cf}	3.18×10^{-6}
	Mass of fluid	kg	m_{cf}	2.51×10^{-3}
	Specific heat	J kg^{-1} K^{-1}	Cp_{cf}	2690
	Overall conductance	W K^{-1}	$(UA)_{cf}$	26.625

drawings of the sections made of AISI 304 steel. The specific heat capacity of the wall material is also representative of AISI 304 steel. The coupling fluid for the desorber is heated Paratherm NF™, a mineral-oil heat transfer fluid. Thermophysical properties were calculated at an average coupling fluid temperature of 165°C. The coupling fluid region volume is calculated using the number of coupling fluid channels per sheet (102), channel length (0.101 m), and channel hydraulic diameter (442×10^{-6} m). The coupling fluid heat transfer conductance is also representative of the desorber investigated by Delahanty *et al.* (2015).

4.4 Solver Implementation

Figure 4.10 shows a schematic of the ODE solver. The systems of equations resulting from the modeling of unsteady conservation laws is non-linear and coupled. The derivative of the state vector is a function of computed states, external inputs and heat exchanger parameters, and related by function *f*(t). An initial condition, *Y*(0), satisfying the conservation equations is provided to initialize the solution. Both FV and MB formulations lead to a system of non-linear, coupled DAEs for each node as the mass flow rate expressions are algebraic equations coupled with differential equations for other state variables. Moreover, the stiffness in these equations requires that the solver be specifically designed for these types of equations. The assembled form for each mode can be solved by an explicit or implicit integration method. Typically, explicit methods lead to smaller time steps in order to satisfy the stability criterion defined by Courant *et al.* (1928). Small time steps also induce chatter in the computed variables especially near the solution. The chatter is prominent in these systems because of highly non-linear property variations. While it can become a stability concern for the solver, it is mainly an efficiency issue because the

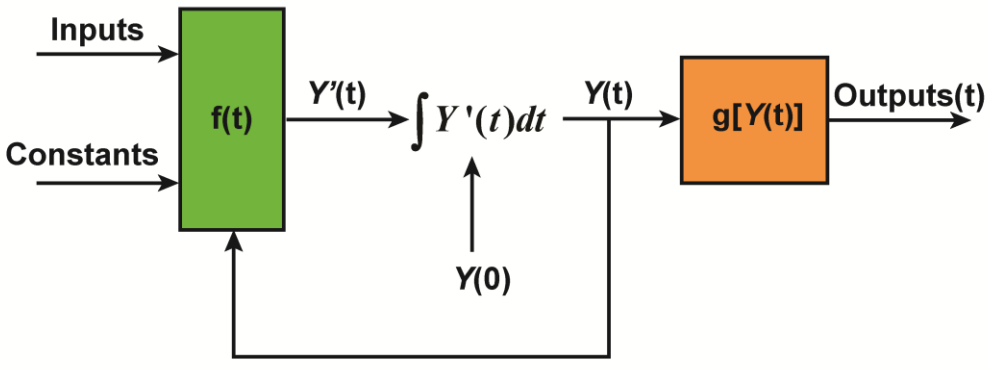

Figure 4.10: Schematic of ODE solver

solver takes extremely small time steps. To overcome these issues, an implicit solver is preferred. A packaged ODE solver, *ode15s* (The Mathworks Inc., 2016), is used in this study. This is an implicit solver for stiff equations. *ode15s* is a numerical differencing based implicit solver that allows variable order of differentiation and variable time stepping to solve a wide range of differential equations. Specifically, this solver is designed to solve stiff DAE sets, making it a promising choice for the system presented here. Common numerical solvers (especially explicit solvers) become highly inefficient or fail to achieve the tolerance of the integration. Stiff numerical solvers perform additional computations at each time step regarding the Jacobian (calculated and supplied by the user or computed numerically) and its sparsity pattern. While this adds to the computational cost per time step, the additional computations enable the solver to take larger time steps and the overall efficiency of the solver increases significantly. The packaged solver has additional features that assist in performing fast and stable computations, such as specifying the initial slope, relative tolerance and maximum time step. Shampine and Reichelt (1997) provide a comprehensive overview of packaged ODE solvers in MATLAB®.

Figure 4.11 shows a flow chart of the solver for the transient models as implemented in the simulations. The solver is initialized by defining the geometric and heat transfer parameters of the heat exchanger. Following this, the initial conditions for all the computed states (working fluid interfacial mass flow rate, nodal concentration and enthalpy, wall temperature, and coupling fluid temperature) are specified for all nodes leading to $5N$ initial states. Time varying boundary conditions are specified as anticipated from upstream components and are simulated as smooth cubic spline variations from their initial values to final values. The conservation equations are then assembled in the DAE form as described

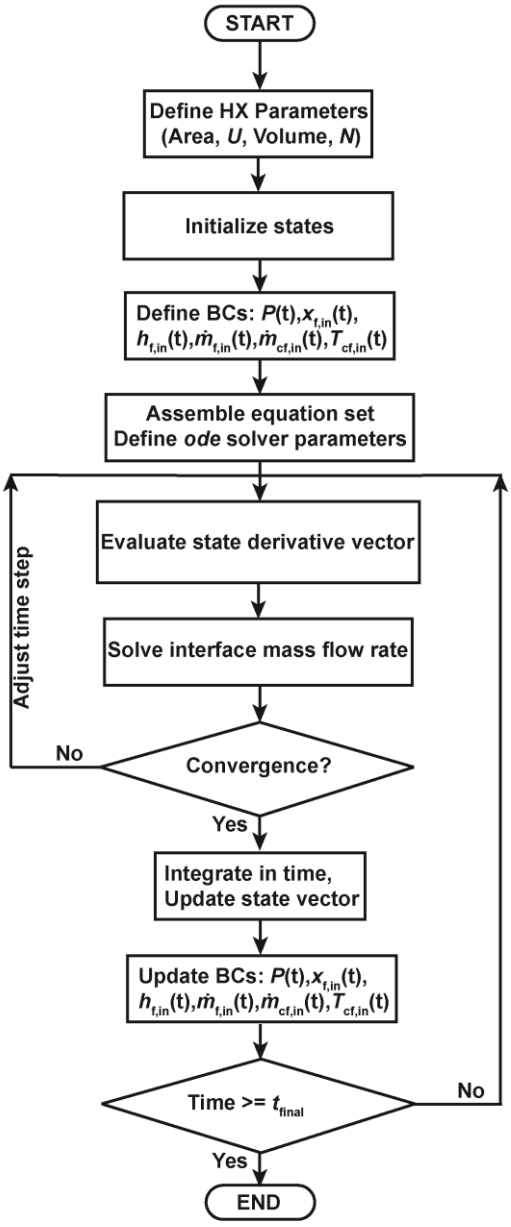

Figure 4.11: Flowchart of the DAE solver

above and the state derivative is computed at each time step. The calculated states are then used to check for convergence. If the convergence criterion is achieved, the simulation proceeds in time, otherwise the time step is adjusted, and the computations are repeated until convergence is achieved.

A similar approach is used for solving the MB model. The model initializes with an initial condition of the heat exchanger operation at steady state design conditions. The difference in the MB method solver is that the equation system is modified according to the governing state derivative equations and the switching parameter is evaluated at each time step.

4.5 Simulation Results

4.5.1 Condenser

A standalone condenser model is simulated using both, FV and MB methods. Table 4.3 and Table 4.4 present the initial states and time varying boundary conditions for the FV and MB model, respectively. Baseline operating conditions of the heat exchanger are utilized to define the initial conditions of individual zone length of the two-phase and single-phase regions. The baseline operating conditions of the coupling fluid are also known, and knowing the refrigerant inlet and outlet phase, and heat transfer rates in each zone, energy balances are utilized to calculate average wall temperatures, zone lengths, and refrigerant side overall conductance values. With the prescribed initial conditions, the

Table 4.3: Initial and boundary conditions for FV condenser model

Parameter	Refrigerant	Coupling Fluid	Wall
Initial Pressure (kPa)	300	101.3	
Final Pressure (kPa)	2087	101.3	
Initial Temperature (°C)	25	25	25
Final Inlet Temperature (°C)	68.39	40.44	
Inlet Refrigerant Mass Quality (kg kg^{-1})	1		
Initial Refrigerant Concentration (kg kg^{-1})	0.9973		
Final Refrigerant Concentration (kg kg^{-1})	0.9975		
Initial Mass Flow Rate (kg s^{-1})	1.24×10^{-6}	0.0045	
Final Mass Flow Rate (kg s^{-1})	1.24×10^{-4}	0.0045	

Table 4.4: Initial conditions for MB condenser model

Parameter	Two-phase Zone			Subcooled Zone		
	Ref.	CF	Wall	Ref.	CF	Wall
Temperature (°C)	52.34	44.37	46.16	50.89	40.49	42.80
Pressure (kPa)	2087	101.3		2087	101.3	
Inlet Temperature (°C)	68.39	40.54		52.19	40.44	
Inlet Refrigerant Mass Quality (kg kg^{-1})	1			0		
Refrigerant Concentration (kg kg^{-1})	0.9975			0.9975		
Mass Flow Rate (kg s^{-1})	1.24×10^{-4}	0.0045		1.24×10^{-4}	0.0045	
Zone Length (m m^{-1})	0.9908			0.0092		
Heat Transfer Coefficient (W m^{-2} K^{-1})	974.1	4500		974.1	4500	

system of equations is used to compute the zone lengths as a state variable and a function of time. The heat transfer coefficient for the incompressible coupling fluid is determined using a single-phase heat transfer coefficient (Kakac *et al.*, 1987) applicable for microchannel geometries utilized in this study. With the knowledge of the heat transfer rate in each fluid region at baseline operating conditions, the average coupling fluid and refrigerant temperatures, energy balances on individual fluid regions allow computation of the refrigerant-side heat transfer coefficient and the average wall temperatures.

4.5.1.1 Effect of Simulation Parameters

Grid independence studies were conducted on the FV model to identify the grid resolution that would provide accurate results. Figure 4.12 shows the results of this study. The model was simulated for a fixed case of system startup from room temperature and was simulated with the supplied boundary conditions to achieve a steady-state. The

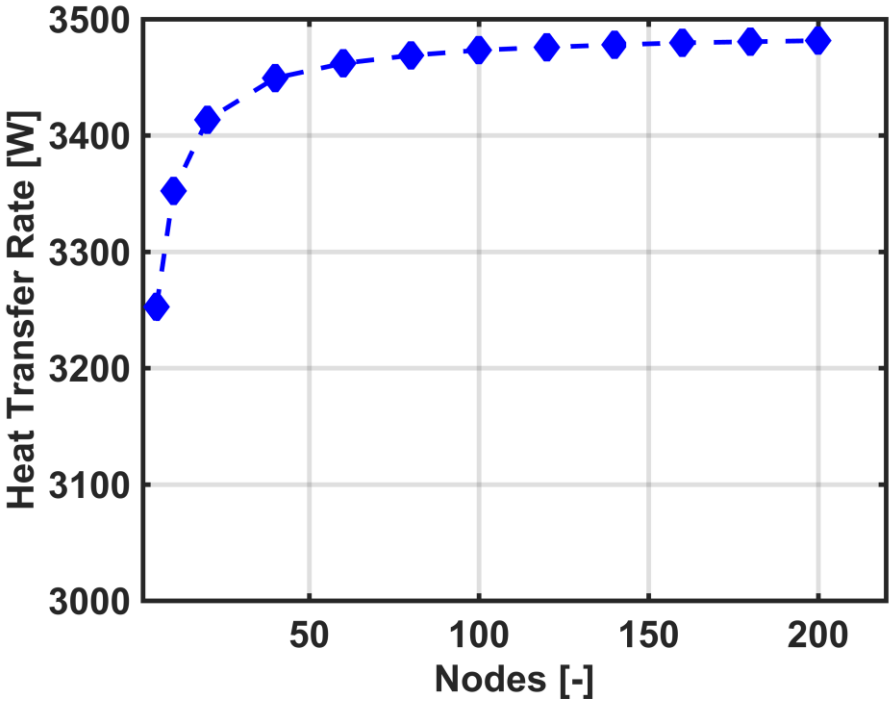

Figure 4.12: Grid independence study: Total heat transfer rate with number of nodes

component heat transfer rate was computed at different grid resolutions ranging from 5 nodes to 200 nodes. It was identified that grid independent results with high resolution inside the subcooled region of the flow were obtained using a mesh of 100 nodes or higher. At the design condition of the condenser, the subcooled region is predicted to be ~2% of the total length of the heat exchanger with an outlet subcooling of ~2°C. A computational mesh of 100 nodes accurately predicted the last two control volumes to be at subcooled condition (2% of the computational domain) with an outlet subcooling of 2.5°C. Therefore, for the subsequent analyses presented in this paper, a computational mesh of 100 nodes is utilized. During these test cases, the total time to complete the simulation was also recorded. All the simulations presented in this work were performed on an Intel Core i7 CPU (3.4 GHz) with 24 GB of RAM. Figure 4.13 shows the computational time as a function of grid resolution. It is observed that the computational time scales approximately

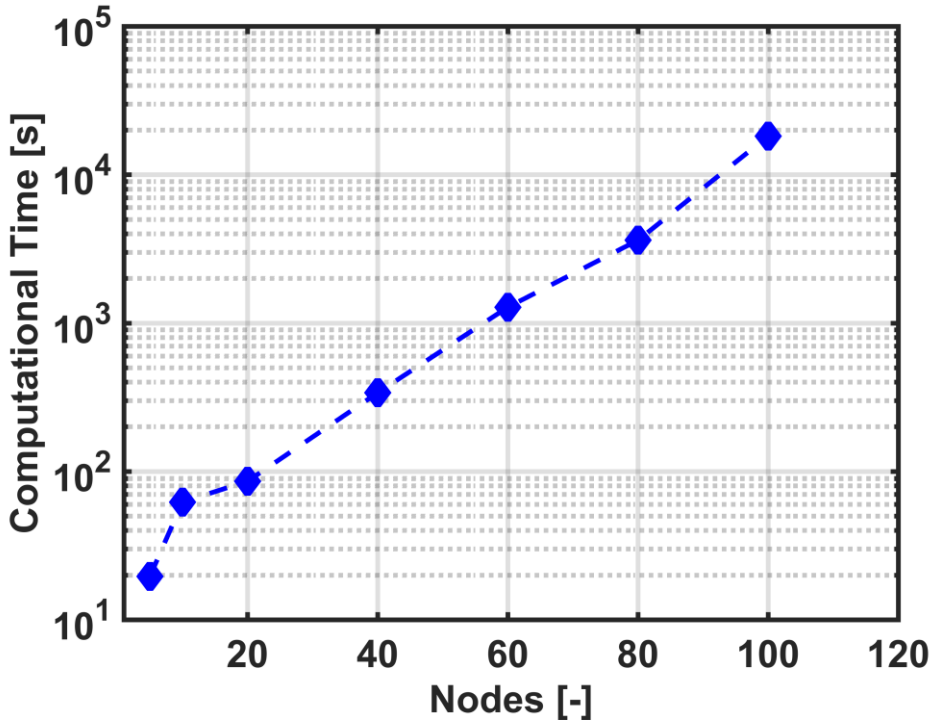

Figure 4.13: FV model performance: Computational time with number of nodes

as a cube [$O(n^3)$] of the grid resolution. The *ode15s* solver is a numerical differentiation-based solver that assembles the Jacobian of the system of equations at each time step. The final solution step is similar to direct matrix inversion, which scales as a cube of the matrix size, which renders the solver computationally very expensive for large number of control volumes. However, the numerical robustness to solve DAEs is a major advantage.

Figure 4.14 shows the segmental variation in temperatures and heat transfer rates during steady-state operation of the condenser. The left axis shows the variation of temperatures of the refrigerant, wall and coupling fluid nodes. Due to the zeotropic nature of the ammonia-water mixture, the first few nodes from the inlet experience a large change in refrigerant temperature as the vapor begins to condense. The inlet of the condenser on the refrigerant side (node #1) is also the hottest segment. As the condensation of the refrigerant vapor proceeds, the refrigerant temperature achieves an approximately constant

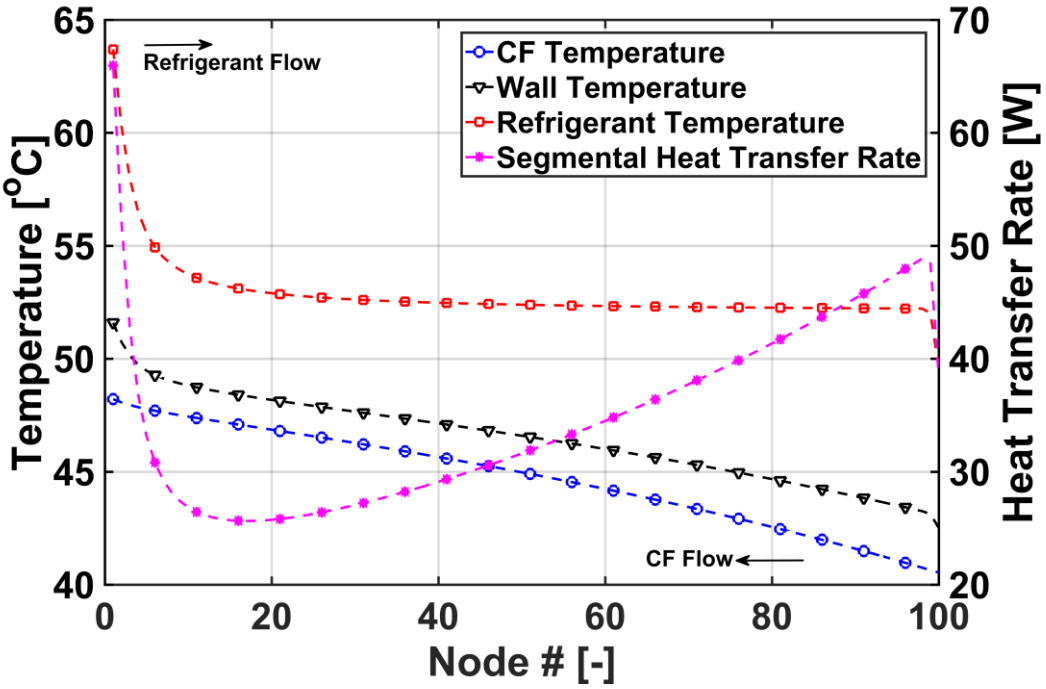

Figure 4.14: FV model performance: Segmental temperatures and heat transfer rates at steady-state

value in the bulk of the phase-change region. In this phase, the wall and the coupling fluid temperatures exhibit a more gradual decrease. Finally, as the refrigerant is fully condensed and begins to be subcooled near the outlet of the heat exchanger, the refrigerant temperature decreases sharply to its final value. In this model, as the heat transfer coefficient is assumed to be uniform, the trends in the segmental heat transfer rate (shown on the right axis) follow the trends in the temperature difference between the wall and the two fluids. Due to the large temperature difference at the inlet of the refrigerant, the heat transfer rate is maximum in the beginning and then decreases sharply. During the bulk of the condensation process, the heat transfer rate gradually increases along the length of the heat exchanger as the refrigerant temperature remains approximately constant. Finally, the heat transfer rate decreases sharply in the subcooled region due to smaller temperature difference. A variable heat transfer coefficient calculation that takes into account the flow regime along the flow

direction would lead to improved accuracy in predicting the segmental temperatures and heat transfer rates.

4.5.1.2 Comparison between FV and MB Methods

Both FV and MB methods require consistent initial conditions. It should be noted that the MB model presented here does not include startup simulations and therefore is initialized with design steady-state operating conditions satisfying the governing equations. Both models were used to simulate the response of the condenser to changes in inlet refrigerant mass flow rate and ambient temperature. Changes in mass flow rate can occur due to variations in the conditions of the heat source that is coupled to the desorber and provides the heat input for refrigerant generation. Refrigerant mass flow rate was increased by 25% over 30 seconds of simulation time using a smooth profile. All other parameters were kept constant. This change causes the subcooled zone to move out of the condenser and a new steady-state is achieved with the condenser operating with a partial two-phase outlet. After the component achieves the new steady state, the refrigerant flow rate is decreased in a similar manner to the original value. This causes the system to return to the original steady state and the subcooled region reappears. This test case allows for the evaluation of the zone switching algorithm due to its direct impact on refrigerant mass flow rate.

Figure 4.15 shows the response of the outlet mass flow rate of the refrigerant to the change in the inlet mass flow rate. As the inlet mass flow rate increases from the design operating condition, the subcooled section in the condenser shrinks and the condenser becomes undersized to achieve complete condensation of 25% additional mass flow rate.

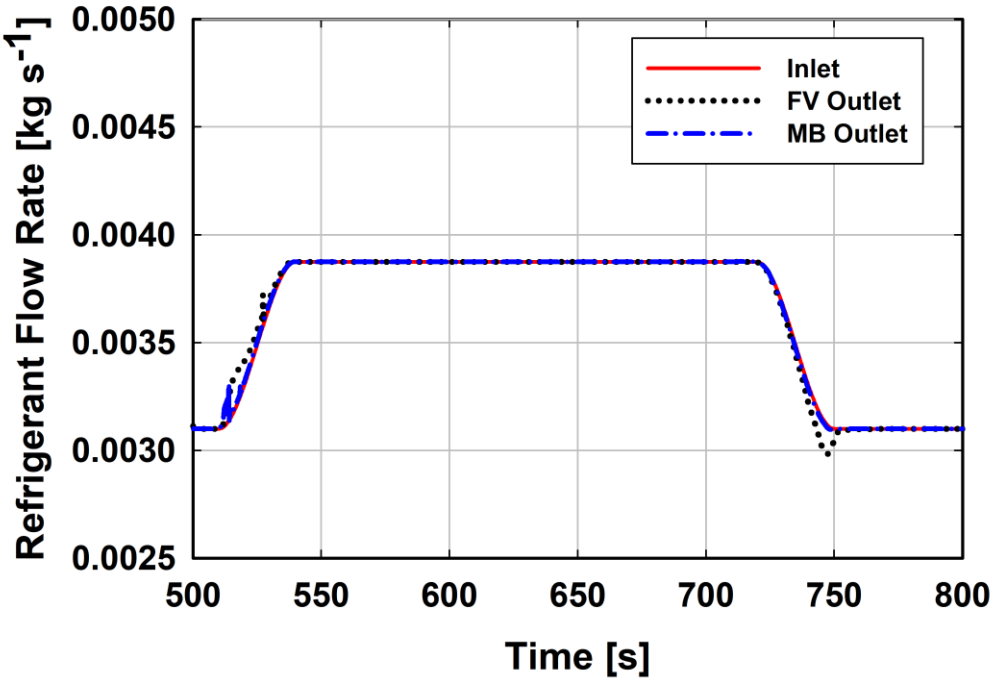

Figure 4.15: Mass flow rate response to changes in the inlet mass flow rate

It can be observed that the outlet mass flow rate increases at a steeper rate than the inlet mass flow rate. This can be attributed to the fact that the subcooled region is pushed out of the condenser and consequently the stored liquid mass in the component at the initial steady state is rejected from the component. Therefore, the average density inside the heat exchanger decreases and the outlet mass flow rate remains ahead of the inlet flow rate. As the inlet mass flow rate is restored to the original value, the subcooled region reappears. This accumulation of the subcooled liquid inside the component leads to the behavior shown in the plot and the outlet mass flow rate trails the inlet mass flow rate. Both MB and FV models predict the trends and absolute values with high accuracy and show good agreement.

Figure 4.16 shows the variation of outlet refrigerant mass quality in response to changes in inlet mass flow rate. It can be observed that the 25% increase in the inlet mass

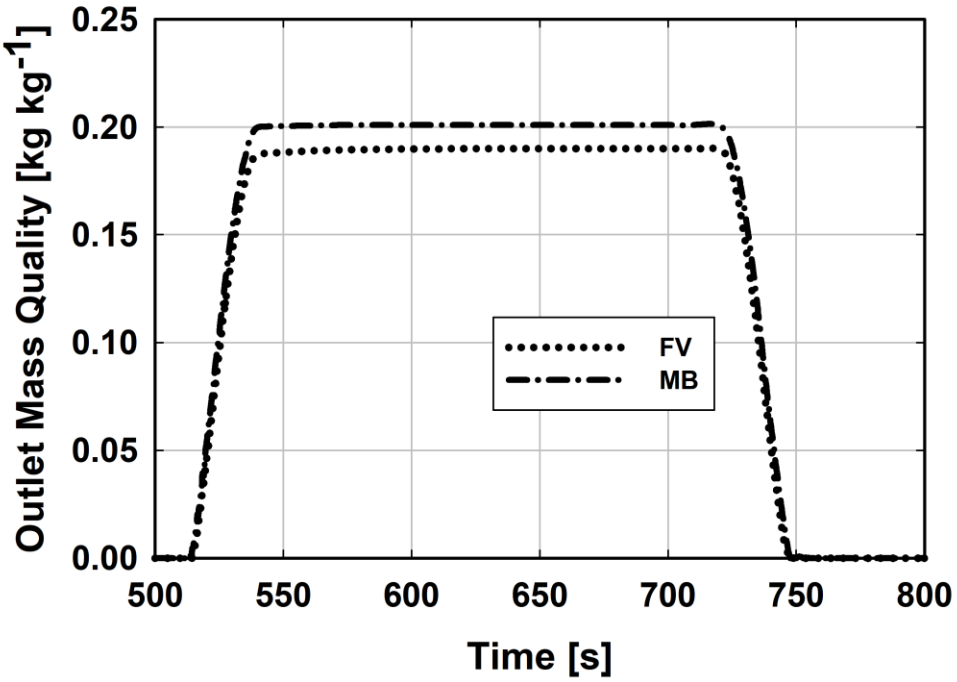

Figure 4.16: Effect on refrigerant outlet mass quality due to changes in the inlet mass flow rate

flow rate causes the outlet phase of the condenser to become a partial two-phase mixture. Both models predict the variation accurately with the MB model predicting a slightly higher quality at the outlet as compared to the FV model. The discrepancy is due to the averaging process that takes place in the MB model and assumed linear profile of enthalpy in all the regions. This test case also helps in evaluating the switching algorithm that is used at each time step to evaluate the state vector derivative.

Figure 4.17 shows the variation of fluid temperatures in response to changes in the inlet mass flow rate. As the mass flow rate is increased, the refrigerant temperature at the condenser outlet increases corresponding to the partial two-phase mixture at the exit. Because of the constant area of the ambient heat exchanger, the coupling fluid temperatures also increase. As the inlet mass flow rate is restored to the design condition, the

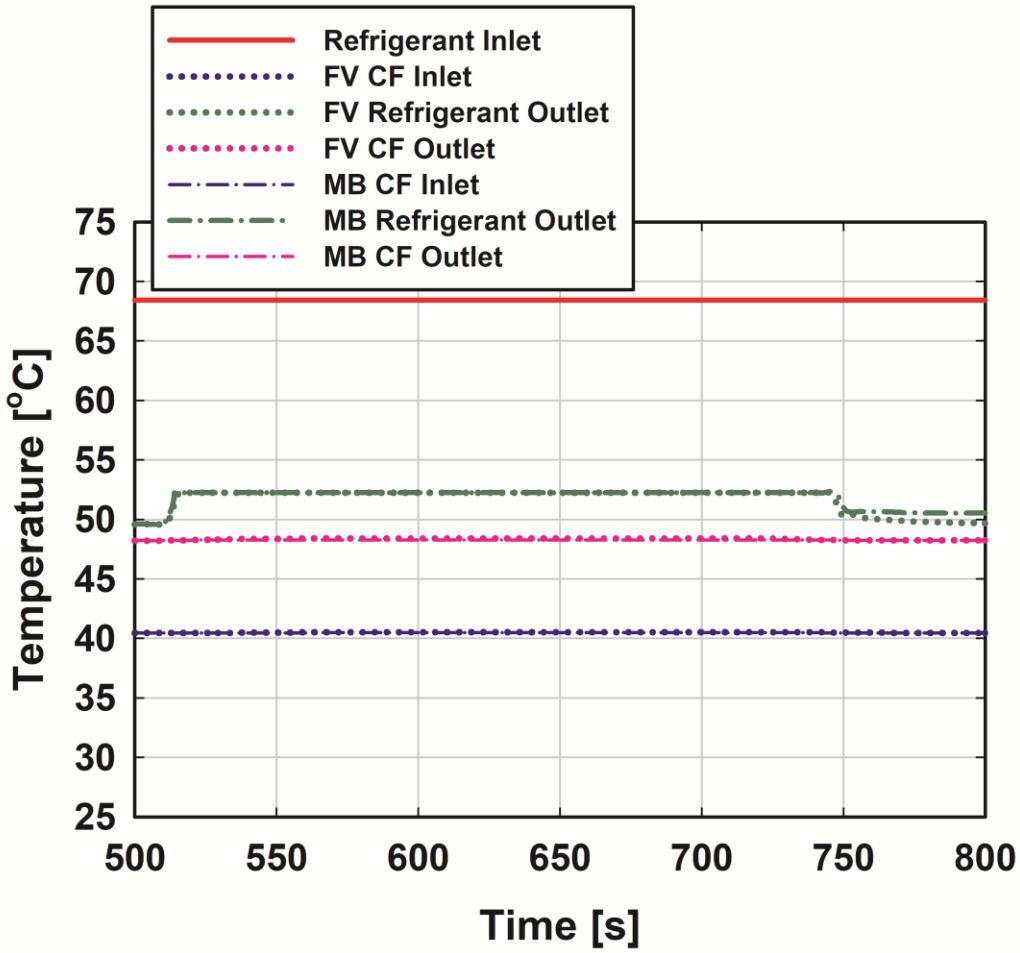

Figure 4.17: Temperature response to changes in the inlet mass flow rate

temperatures return to the original value as well. Both models predict the variation accurately and demonstrate similar time constants for this transient phenomenon.

Lastly, Figure 4.18 shows the heat transfer response of both methods. As the inlet mass flow rate increases, the condenser heat transfer rate increases because of a larger average temperature difference that drives the heat transfer rate. Similarly, when the mass flow rate is decreased to the original value, the two heat transfer rates return to their original value as well. There is a discrepancy of ~20-25 W (~0.75% of the component heat transfer rate) at the new steady state between the two models. This is also reflected in Figure 4.16 as the MB model predicts a higher outlet mass quality. The trends between the two models

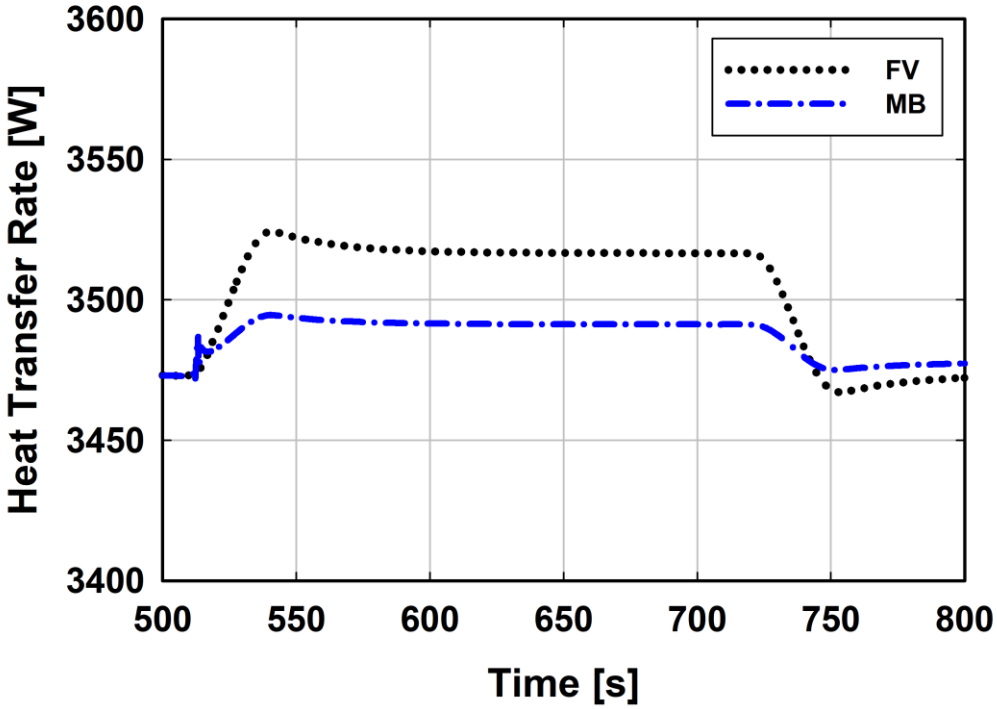

Figure 4.18: Heat transfer response to changes in the inlet mass flow rate

and the time constants are similar, and the discrepancy is a small fraction of the total heat transfer rate.

Comparison of computational time for these test cases indicates that the **MB model took only 12.5 s to simulate 500 s of simulation**, whereas for the same simulation, the FV model took 782.1 s. **Therefore, the MB method provides a computational advantage of ~60 times**. In control system design, this computational advantage is significant at a small penalty in the accuracy of predicting heat transfer rates.

In another set of simulations, the ambient temperature is increased by 5°C from the design condition of 35°C over a period of 300 s while keeping all the other parameters constant. Figure 4.19 and Figure 4.20 show the response of fluid temperatures and heat transfer rate for this test case, respectively. It can be observed that as the ambient

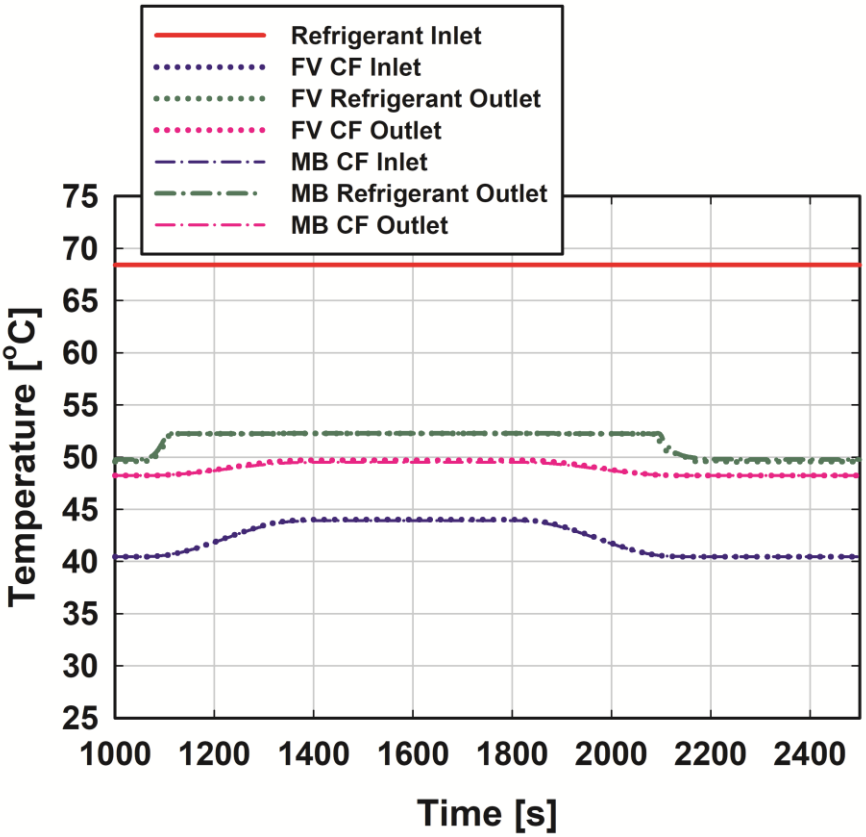

Figure 4.19: Temperature response to changes in ambient temperature

temperature increases, the coupling fluid inlet temperature increases and for constant refrigerant inlet temperature, the refrigerant outlet temperature increases as well. This causes the performance of the condenser to decrease as the heat transfer rate decreases due to lower driving temperature difference between the refrigerant and the coupling fluid.

Both methods predict similar trends and time constants and the MB method predictions closely replicate the results from the FV model. The minor discrepancy in heat transfer rate (~50 W) is observed due to the averaging process in the MB model as mentioned previously. Finally, Figure 4.21 presents the outlet refrigerant mass quality predicted by both models. It can be observed that the predictions of both the models agree and an increase in ambient temperature leads to performance limitations in the condenser and the outlet phase is a two-phase mixture. When the ambient temperature is restored to

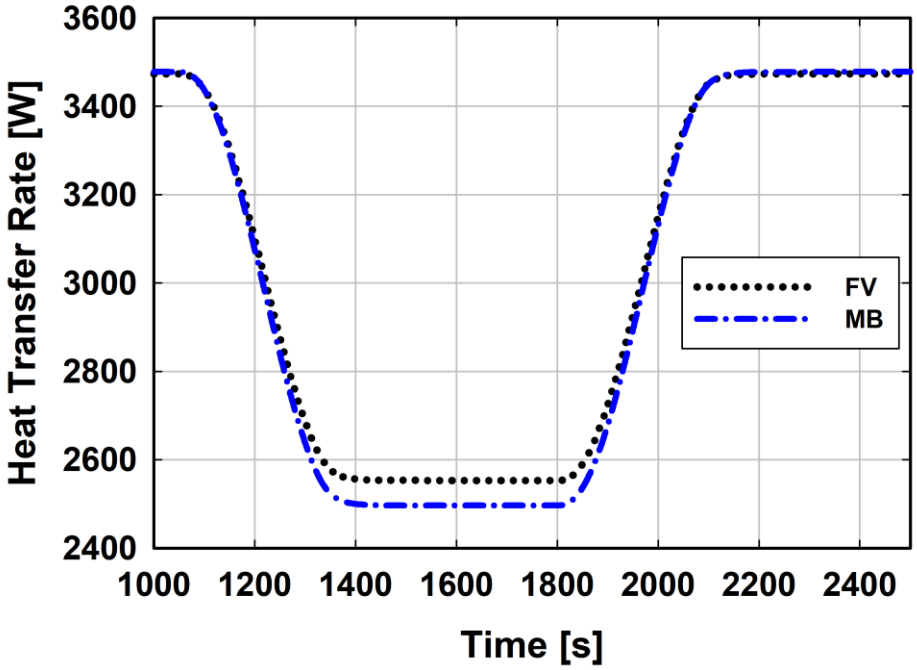

Figure 4.20: Response of heat transfer rate to changes in ambient temperature

the original value, the initial steady state is achieved again. Computational time for these simulations was also recorded. FV method simulations were completed in ~312 s, while the MB method simulations were performed in 5.8 s, showing a computational savings

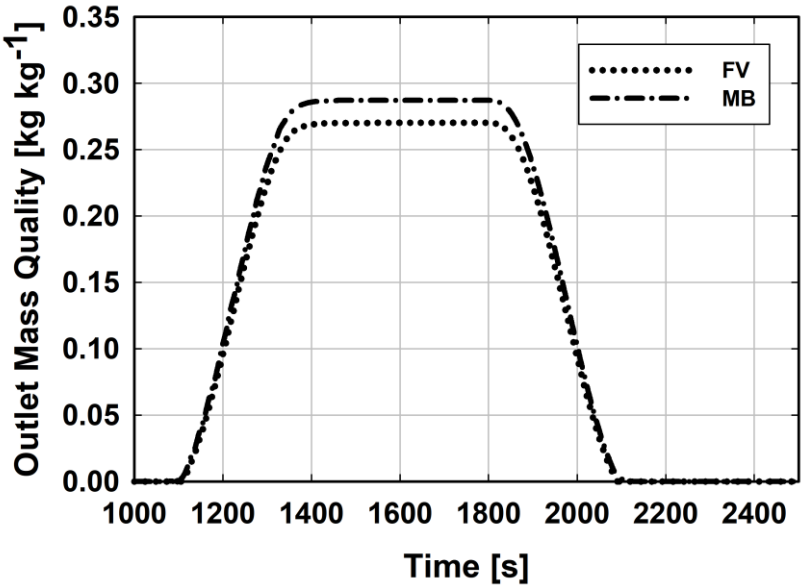

Figure 4.21: Refrigerant outlet mass quality in response to changes in ambient temperature

of ~54 times. These simulations demonstrate the switching algorithm in the MB model and the performance of FV and MB models.

4.5.2 Desorber

A standalone desorber model is developed and simulations are performed to gain insight into the performance of the component as a function of time. The results of the transient model of an ammonia-water desorber using the finite volume method described above are discussed in the following sections. First, the steady-state performance of the dynamic model is compared with experimental and simulation data available in the literature. Second, the transient response of the desorber to changes in one of the input variables is analyzed. As mentioned before, detailed analysis and simulations involving variations in many input variables are presented by Mr. Alexander A. Roeder in his MS thesis.

The tray efficiencies are set assuming a spatially linear variation in the efficiency starting from the bottom tray ($i = 1$) and moving up the desorber. The top tray ($i = N$) efficiency is chosen to be 0.6 through trial and error to achieve outlet vapor concentration and temperature at design conditions comparable to those demonstrated by Delahanty *et al.* (2015) and (Keinath *et al.*, 2015).

4.5.2.1 Steady-state Performance

The results of the dynamic model developed in this study were compared with those from an experimental study of the desorber geometry discussed in Section 4.3.2 (Delahanty, 2015). Table 4.5 shows the comparison between inputs for the present model

Table 4.5: Comparison of dynamic model and Delahanty (2015) component inputs

Parameter	Dynamic Model	Delahanty (2015)	Percentage Deviation
Solution inlet temperature (°C)	82.8	82.8	-
Pressure (kPa)	1626	1626	-
Solution inlet vapor quality (-)	0	*Subcooled*	-
Solution inlet concentration (kg kg^{-1})	0.5235	0.479	9.29
Solution mass flow rate (kg s^{-1})	0.0009	0.0009	-
Coupling fluid inlet temperature (°C)	180	179.5	0.279
Coupling fluid mass flow rate (kg s^{-1})	0.00765	0.00765	-

and the experimental procedure presented by Delahanty (2015). The solution inlet temperature, pressure, solution inlet mass flow rate, and coupling fluid mass flow rate are identical for both studies. The variation in inlet concentration between the numerical study of the present work and the experimental study is due to the solution entering the experimental test section being subcooled, whereas the present model assumes a saturated liquid inlet. It was, however, determined that for temperature and heat transfer rate comparison purposes, matching the solution inlet temperature was more important.

A comparison of the spatial variation of fluid temperatures within one set of passages of the desorber is presented in Figure 4.22. In the plot, the top of the desorber, where the concentrated solution enters the component and refrigerant vapor exits, is denoted with normalized location ‘1’. The coupling fluid enters the desorber and the dilute solution exits at location ‘0’. For the present study, liquid temperatures are computed at the center of the control volumes while vapor temperatures are calculated at the control volume boundaries

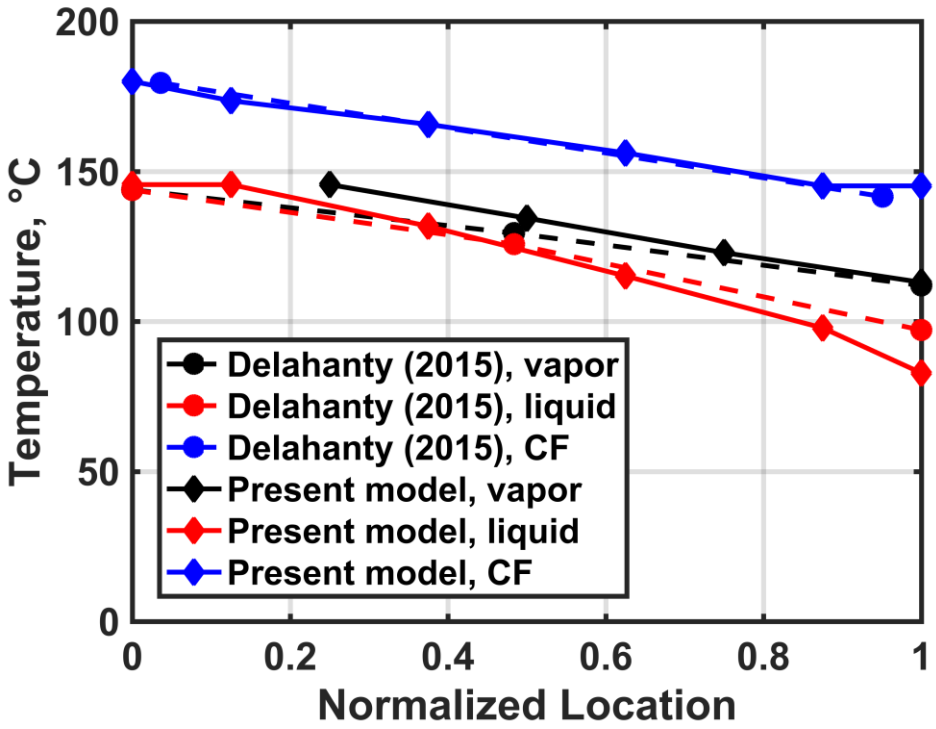

Figure 4.22: Comparison of the spatial variation of refrigerant vapor, dilute solution, and coupling fluid temperatures in the desorber at steady-state

due to thermal inequilibrium with the liquid on each tray. The transient model compares well with the experimental results. Outlet temperatures for all three fluid streams (dilute solution, refrigerant vapor and coupling fluid) are in close agreement. The discrepancies in the trends of the refrigerant vapor and liquid temperatures are due to the assumptions made in temperatures from the upwinding differencing scheme and the saturated inlet quality assumption of the present model.

The effect of solution inlet flow rate on heat transfer rate is compared in Figure 4.23 for the present model, the EES cycle model of Garimella *et al.* (2016), and the experimental results of Delahanty (2015). The experimental heat transfer data used in Figure 4.23, taken from Figure 4.6 of Delahanty (2015), are for the coupling fluid heat duty. For the model developed in the present study, the heat loss rate to the ambient is assumed to be zero. As

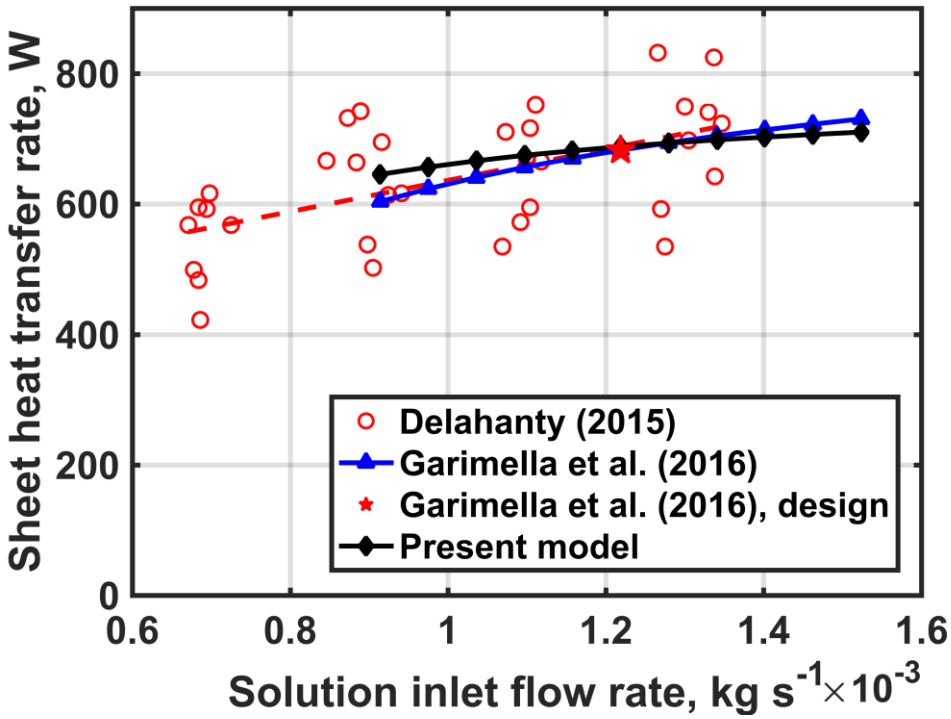

Figure 4.23: Comparison of sheet heat transfer as a function of solution inlet mass flow rate

shown in the figure, the predictions of the two numerical models compare well with experimental data at design, as well as at off-design operating conditions. The desorber heat duty increases with solution inlet flow rate. Both models maintain constant heat transfer conductance values. Therefore, the key parameter governing the heat transfer rate is the driving temperature difference. The coupling fluid inlet conditions remain unchanged, but the solution inlet temperature changes due to variations in pressure and concentration. Therefore, the additional mass flow rate leads to the corresponding variation in the heat transfer rate. The difference in the slope of the heat duty profiles is attributed to the difference in the inlet quality for the two models and assumption of constant temperature inequilibrium between exiting vapor and entering solution in the EES cycle model. The saturated liquid inlet assumption causes the present model to predict a higher

heat transfer rate at solution flow rates below design due to a larger temperature difference between the solution and coupling fluid sides. Above the design solution flow rate, the EES system model predicts higher heat transfer rate as compared to the present study, because the constraint on the vapor-liquid inequilibrium temperature causes the exiting vapor enthalpy to be significantly lower than that predicted by the present model. *Overall, the solution mass flow rate is observed to have a significant effect on the performance of the desorber. This knowledge may be used later by utilizing the solution mass flow rate as a key process variable.*

4.5.2.2 Transient Performance

The response of the desorber to a change in the solution flow rate is investigated here. These transient studies provide insights about desorber performance at off-design conditions that can be used in the design of a control system to adjust input parameters to maintain system cooling demand. Each simulation starts with the desorber at its steady-state design conditions presented in Table 4.6 and ambient temperature of 35°C.

The open-loop nature of the present model requires manual ramping of the solution inlet properties in addition to the coupling fluid properties. Future integration into a system model would remove the solution side manual ramping requirement, as the desorber outlet conditions would feed back through other system components to set the inlet conditions of the concentrated solution. The open-loop results presented here still provide valuable insight into the dynamic response of the desorber and can be used to develop control strategies for the component and the overall system. The desorber is held at the initial conditions for 15 seconds at the beginning of all cases to mitigate any numerical

Table 4.6: Initial design conditions for transient perturbation simulations

Constant Parameters	Value
Solution inlet flow rate (kg s^{-1})	0.00975
Coupling fluid flow rate (kg s^{-1})	0.084
Solution inlet vapor quality (-)	0
Solution inlet temperature (°C)	102.5
Pressure (kPa)	2087
Solution inlet concentration (kg kg^{-1})	0.4789
Coupling fluid inlet temperature (°C)	180

instabilities during start-up simulation. The coupling fluid and solution side property ramps are initiated simultaneously following this "*dead*" period. For the analysis, solution-side, wall, and coupling fluid heat transfer rates are considered, including transverse heat flux, streamwise convective heat transfer, and energy storage terms. Axial conduction is neglected. Eq. 4.53– 4.56 define the overall energy balance and individual rate terms. The mass stored in the desorber is calculated using Eq. 4.57.

$$\dot{E}_{store} = \dot{Q}_{flux} + \dot{Q}_{conv} \tag{4.53}$$

$$\dot{E}_{store} = \frac{1}{\Delta t}\sum_{i=1}^{N}\left[m_i(t)\cdot u_i(t) - m_i(t-\Delta t)\cdot u_i(t-\Delta t)\right] \tag{4.54}$$

$$\dot{Q}_{flux}(t) = \sum\left[\dot{m}_{in}(t)\cdot h_{in}(t)\right] - \sum\left[\dot{m}_{out}(t)\cdot h_{out}(t)\right] \tag{4.55}$$

$$\dot{Q}_{conv}(t) = UA\cdot\left[\sum_{i=1}^{N}\Delta T_i\right] \tag{4.56}$$

$$M_{store}(t) = \sum_{i=1}^{N_{tray}}\rho_{f,i}(t)\times V_{f,seg} \tag{4.57}$$

Response to change in solution mass flow rate

One of the key control methods for an absorption system is the tuning of the solution mass flow rate through the adjustment of a variable speed solution pump. The input conditions and simulation times for the solution inlet mass flow rate cases are presented in Table 4.7.

Two cases are considered in this category: 1) the solution inlet mass flow rate is ramped down to 0.00731 kg s^{-1} from the design condition of 9.75×10^{-3} kg s^{-1} over 15 seconds, and 2) the solution inlet mass flow rate is ramped up to 12.19×10^{-3} kg s^{-1} from

Table 4.7: Initial and final conditions, and simulation times for desorber solution inlet mass flow rate perturbation cases

Constant Parameters		**Value**
Coupling fluid inlet temperature (°C)		180
Coupling fluid flow rate (kg s^{-1})		0.084
Solution inlet vapor quality (-)		0
Ambient temperature (°C)		35
Ramped Parameters	**Initial**	**Final**
Solution inlet flow rate ($\times 10^{-3}$ kg s^{-1})	9.75	7.31, 12.19
Solution inlet temperature (°C)	102.5	96.86, 106.26
Pressure (kPa)	2087	2001, 2123
Solution inlet concentration (kg kg^{-1})	0.4789	0.4982, 0.4639
Simulation Time Name		**Time**
Total simulation time (s)		400
Solution side dead time (s)		15
Solution inlet mass flow rate ramp time (s)		15
Pressure ramp time (s)		60
Solution inlet temperature ramp time (s)		60
Solution inlet concentration ramp time (s)		60

the design condition of 9.75×10^{-3} kg s^{-1} over 15 seconds. During both transients, the coupling fluid inlet temperature and mass flow rate remain at their design conditions, and solution inlet conditions and operating pressure vary because of overall system response. The simulations are conducted for 400 seconds total, after which steady state is deemed to have been achieved as the energy and mass residuals decrease below 1% of the steady-state conditions.

Figure 4.24 (A) and (B) show the variation of inlet and outlet mass flow rates in response to an increase and decrease of 25% in the solution inlet mass flow rate, respectively. As discussed in the previous section, the model maintains constant heat transfer conductance values. Therefore, the key parameter governing heat transfer rate is the driving temperature difference. The coupling fluid inlet conditions remain unchanged, but the solution inlet temperature changes due to variations in pressure and concentration. The additional mass flow rate coupled with species and energy conservation equations leads to a corresponding variation in the heat transfer rate. In general, an increase in the inlet mass flow rate results in increases in the refrigerant vapor and dilute solution mass flow rates. The stored fluid mass in the component remains relatively constant as the

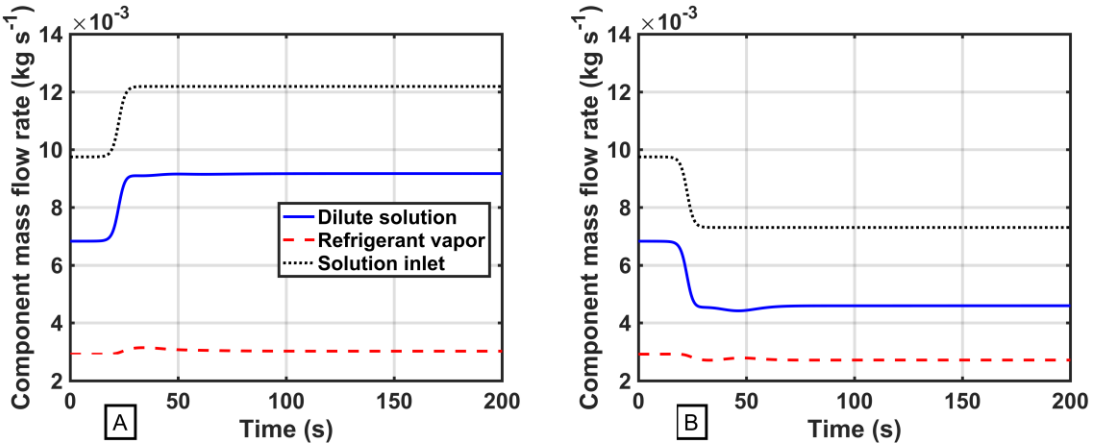

Figure 4.24: Response of desorber flow rates to an increase (A) and decrease (B) of solution inlet mass flow rate

density of ammonia-water at the inlet remains approximately constant with simultaneous changes in inlet temperature, pressure and concentration.

As shown in the Figure 4.24 (A), an increase in the solution inlet flow by 25% results in an increase in the refrigerant vapor flow rate from 2.917×10^{-3} kg s^{-1} to 3.021×10^{-3} kg s^{-1}, and an increase in the dilute solution flow rate from 6.833×10^{-3} kg s^{-1} to 9.171×10^{-3} kg s^{-1}. During the transient period, the dilute solution mass flow rate increases quickly and smoothly. This effect is driven by the inlet solution flow and is affected very little by variations in other properties. The refrigerant vapor flow rate, however, is affected by other thermodynamic property changes, such as temperature, pressure and concentration during transients. In the 15-second period of inlet flow rate ramping, the vapor flow rate peaks at a flow rate of 3.142×10^{-3} kg s^{-1}, and then settles at its final steady-state value of 3.021×10^{-3} kg s^{-1} in the following 70 seconds (t = 100 s). This overshoot is due to the rapid influx of additional mass into the system while the component thermodynamic properties (pressure, temperature, concentration) lag. After the variation in the inlet flow rate of the concentrated solution, the pressure and solution inlet temperature continue to increase, which reduce vapor generation due to decreased heat transfer as compared to the peak of the transients. Figure 4.24 (B) presents the similar response of outlet mass flow rates due to a decrease in the solution inlet mass flow rate. The mass flow rate of dilute solution decreases from 6.833×10^{-3} kg s^{-1} to a new steady-state value of 4.596×10^{-3} kg s^{-1}, while the refrigerant vapor decreases from 2.917×10^{-3} kg s^{-1} to 2.712×10^{-3} kg s^{-1}.

Figure 4.25 (A) and (B) show the variation in desorber heat transfer rates due to an increase and decrease in the solution inlet flow rate, respectively. In general, the desorber

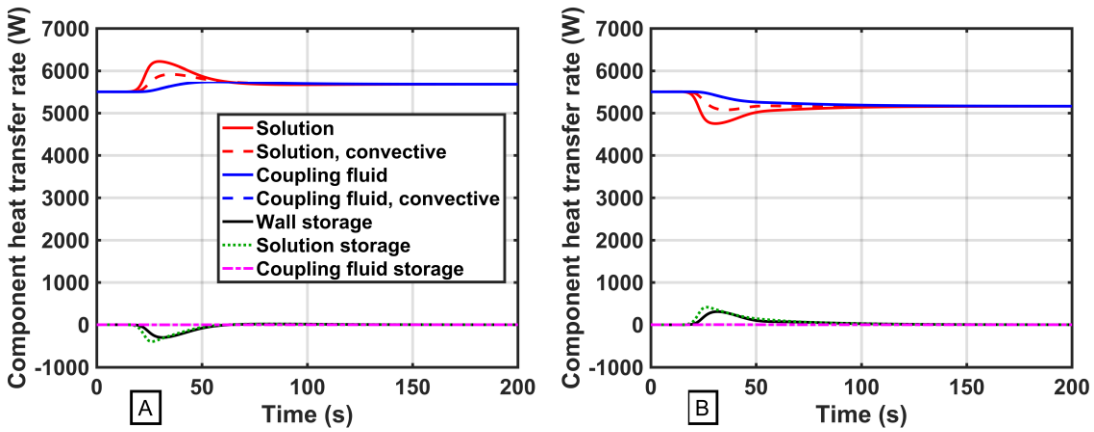

Figure 4.25: Response of desorber heat transfer rates to an increase (A) and decrease (B) of solution inlet mass flow rate

heat transfer rates increase with an increase in the solution inlet mass flow rate and decrease with a decrease in the solution inlet mass flow rate.

As shown in Figure 4.25 (A), the desorber heat transfer rate response to an increase in solution inlet flow rate results in an increase in the desorber heat transfer rate from 5.50 kW to 5.68 kW. The peaks in the solution flux and convective heat transfer rates are an initial response to the increase in the mass flow rate in the system, while the thermodynamic properties experience a time delay imposed by the ramping conditions that are representative of typical values observed in experiments. As the temperatures in the component decrease, the heat transfer rate from the coupling fluid increases due to a larger temperature differential. The system then settles at its new steady-state, and component energy storage rates decrease to zero as the pressure, inlet temperature, and inlet concentration reach their final values. A similar trend in heat transfer rate is shown in Figure 4.25 (B) due to a 25% decrease in the solution flow rate. The steady-state heat transfer rate of the system decreases from 5.50 kW to 5.16 kW. This results in higher heat transfer rate from the coupling fluid than the solution. In response, the solution and wall storage rates increase and the solution temperature increases.

Figure 4.26 (A) and (B) present the variation in the desorber inlet and outlet temperatures in response to an increase (A) and decrease (B) in the solution inlet mass flow rate. Due to an increase in the solution mass flow rate, the dilute solution steady-state temperature decreases from 145.2°C to 140.4°C due to the increased mass flow rate in the system and the increased dilute solution concentration. Similarly, the refrigerant vapor steady-state temperature decreases from 120.2°C to 119.7°C due to the increase in the refrigerant concentration and increased mass flow rate. During the transient period of mass flow rate and solution inlet property ramping (t = 15 s to t = 75 s), the dilute solution temperature decreases smoothly to its new steady-state position. On the other hand, the refrigerant vapor temperature first decreases to 118.4°C before settling at its new steady-state value of 119.7°C. This underdamped response is a result of the rapid mass flow rate variation. The increased heat transfer rate also causes the reduction of the coupling fluid outlet temperature from 155.6°C to 154.8°C. As shown in Figure 4.26 (B), the refrigerant vapor temperature increases from 120.2°C to 121.9°C, while the dilute solution temperature increases from 145.2°C to 152.4°C due to a decrease in the solution mass flow rate.

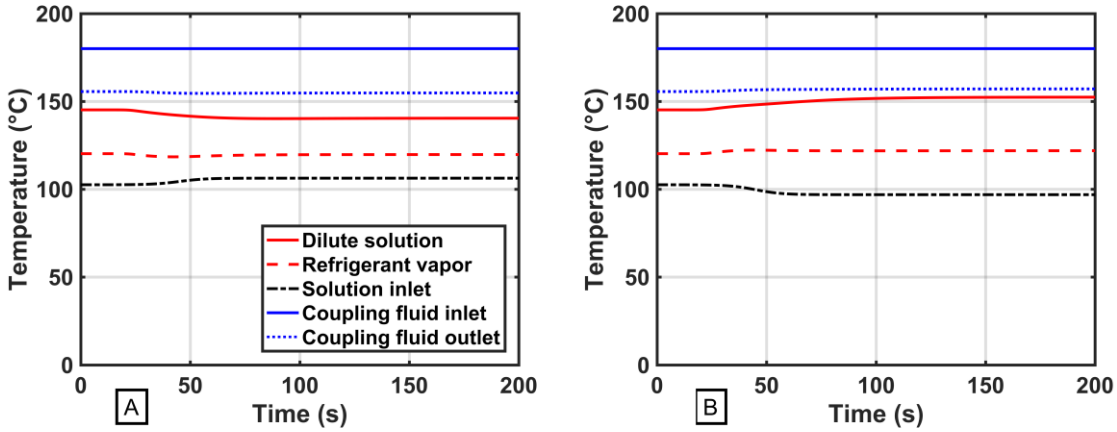

Figure 4.26: Response of desorber temperatures to an increase (A) and decrease (B) of solution inlet mass flow rate

The results presented above and by Mr. Alexander R Roeder indicate that control algorithms can be developed to adjust tunable parameters such as solution flow rate and coupling fluid inlet temperature to maintain desired performance for a range of operating conditions. For example, as the ambient temperature increases, the solution flow rate and coupling fluid inlet temperature can be increased in a manner that mitigates variations in the refrigerant mass flow rate and concentration, thereby maintaining a near-constant capacity delivered by the system. At lower than design ambient conditions, the solution flow rate and coupling fluid inlet temperature can be reduced to match the desired capacity of the system and ultimately increasing the efficiency of the system. A similar combination of control approaches can be implemented for optimizing the system performance at part-loads.

4.6 Summary

This chapter presents a detailed formulation for simulating the transient response of heat exchangers utilized in an ammonia-water absorption system. For single-inlet single-outlet components such as the condenser, evaporator and the absorber, emphasis is placed on the non-linear, DAE solver implementation, and comparison of FV and MB methods for solving the unsteady conservation equations is presented. The representative results are for a condenser; however, the formulation remains identical for simulating an evaporator or an absorber. The only modification is in initial conditions and the formulation of heat transfer terms. The analysis of modeling and solution methods highlight the advantages of both FV and MB methods. While the FV method is simpler to formulate and the equation structure is fixed, the computational expense is very high for accurate simulations involving large number of nodes. The MB method provides significant computational

savings (more than 50 times reduction in computational time) and comparable accuracy. These features are presented through simulation test cases involving changes in refrigerant inlet mass flow rate and ambient temperature. Therefore, it is a recommended modeling paradigm for applications involving multiple evaluations of transient models and control design.

A detailed, physics-based dynamic model was developed to study the transient behavior of a small-scale ammonia-water desorber. A finite volume method was used to model the branched-tray desorber, with CVs placed around each desorber tray. The results of the steady-state models validated the modeling assumptions and demonstrated good agreement with the literature for the steady-state temperature profiles and heat transfer rate. Finally, simulation of perturbations in the solution flow rate is performed in which the desorber experienced a change from its design operating conditions by either increasing or decreasing the solution inlet mass flow rate. The results of these simulations show the flexibility, accuracy, and efficiency of the detailed dynamic desorber model developed in this study. This model can be incorporated into a larger system model and assist in the evaluation of detailed and accurate system dynamics, as well as the development of robust control algorithms to improve the performance of small-scale ammonia-water absorption systems.

CHAPTER 5. CONTROL SYSTEM DESIGN

As outlined in the previous chapters, the system transient model is useful in designing control algorithms and evaluating their performance. This chapter presents the details of the design of feedback control algorithms and model implementation for a small-capacity ammonia-water absorption chiller. Design and implementation of control algorithms is discussed. The dynamic model is employed to study the response of the system under varying ambient temperatures and cooling load demands. Two strategies are investigated for feedback control of the system. The first control loop maintains the evaporator temperature glide set-point ($T_{f,evap,out} - T_{f,evap,in}$), while the second control loop regulates desorption temperature to provide the desired cooling duty and maintain the delivered coolant temperature at a set-point.

5.1 Transient Model Description

A previously developed dynamic model (Viswanathan *et al.*, 2013) of a single-effect ammonia-water absorption chiller with a design cooling capacity of 3.5 kW was used to develop and evaluate the performance of feedback control algorithms. The desorber receives thermal input from a heat transfer fluid, which is in turn heated by a gas-fired heat exchanger. The condenser and absorber coupling fluid streams are cooled by air-coupled heat exchangers. The cooling capacity is calculated in the model by using the inlet and outlet temperature and flow rate of the coolant flowing through the evaporator. The coolant

This chapter adapted from: Goyal, A., Rattner, A. S., Garimella, S., Model-based Feedback Control of an Ammonia-water Absorption Chiller, Science and Technology for the Built Environment (2015), 21 (3), pp. 357-364. DOI: 10.1080/10789669.2014.982412.

circulates through a conditioned space heat exchanger that applies a load. The coolant then flows through a storage tank where external perturbation in cooling load can be introduced to simulate varying load demand. In this investigation, the coolant was selected to be a 25% mixture of propylene glycol and water with a specific heat of 3.97 kJ kg^{-1} K^{-1} and a mass flow rate of 0.16 kg s^{-1}. A schematic of the system configuration with thermal capacities of all the heat exchangers is presented in Figure 5.1. Refrigerant flow rate from the high-pressure tank to the evaporator is evaluated dynamically using a simulated valve, the flow-restriction through which can be adjusted as part of the transient model. The

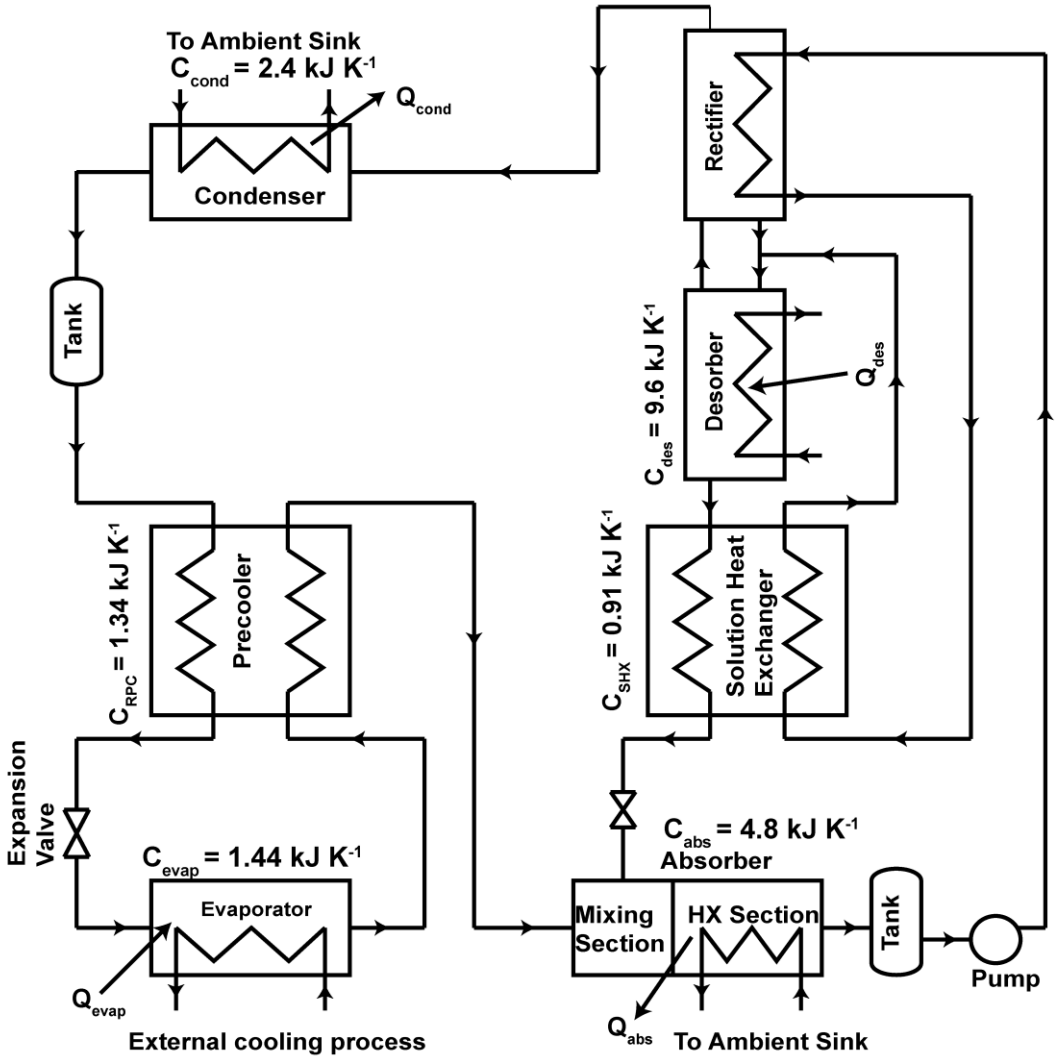

Figure 5.1: Schematic of the modeled absorption system

transient model is implemented in MATLAB and Simulink® (The Mathworks Inc., 2016), which allows for intuitive representation of the system components as model blocks, and fluid and heat flows as input/output connections.

5.2 Control Algorithms

Viswanathan *et al.* (2013) found that the evaporator temperature glide and system performance are strong functions of the refrigerant expansion valve restriction. A dynamically controlled expansion valve for refrigerant flow provides excellent control of the evaporator temperature glide. Also, they reported that the evaporator cooling rate can be effectively controlled by varying the desorption temperature. The gas-fired desorber temperature can be adjusted by varying the air and fuel flow rates into the combustion module. The control algorithm proposed in this study utilizes two proportional feedback loops. For evaporator temperature glide control, the expansion valve restriction is the control variable, while temperature glide is the process variable. Delivered coolant temperature control utilizes coupling-fluid inlet temperature in the desorber as control variable, and delivered coolant temperature as process variable. The control algorithm receives the process variable, $y(t)$, as the input and compares it to the set-point. The error signal, $e(t)$, is calculated as the difference between the two values and given in Eq. 5.1.

$$e(t) = y_{SP}(t) - y(t) \tag{5.1}$$

The error value is multiplied by a suitable multiplier or gain, $K_p(t)$, which generates a change in the manipulated variable, $x(t)$ (Eq. 5.2).

$$\Delta x(t) = K_p(t) \times e(t) \tag{5.2}$$

The multiplier value may change with time and can be increased or decreased if the magnitude of the error signal is large or small, respectively. In a proportional control scheme, the time required to reach steady state depends on the magnitude of the proportional gain. Generally, a higher value of gain leads to a reduced time to reach steady state.

5.2.1 Evaporator Temperature Glide Control

Evaporator temperature glide is defined as the difference between the refrigerant temperature at the evaporator inlet and outlet, and it is non-zero because the refrigerant is a zeotropic mixture of ammonia and water. Because the more volatile ammonia species evaporates preferentially, the water fraction in the liquid phase increases along the evaporator length, raising the mixture temperature near the outlet. Ideally, the refrigerant mixture should exit the evaporator in a two-phase state because the temperature glide grows rapidly as the flow quality approaches unity, and single-phase vapor or dryout region heat transfer resistances are usually greater than those in phase-change processes. Therefore, control of temperature glide becomes crucial for maximizing evaporator performance.

It is important to characterize the response of the system to a small step change in valve position before specifying controller parameters such as the magnitude of proportional gain and controller cycling frequency. In a previous study by Viswanathan *et al.* (2013), it was observed that the low-pressure components, such as the evaporator and the absorber have slow dynamics. The high-side pressure reaches a value within 2% of steady state in ~500 s, while the low-side pressure reaches steady state in ~800 s after start-up. Thus, the response of evaporator temperature glide to a change in valve opening is

slow; therefore, a small magnitude gain ($K_{glide} = -2 \times 10^{-11}$) and low controller frequency (0.05 Hz) are employed. The evaporator temperature glide controller is activated for 10% of the operating cycle. Thus, the controller is active for 2 s in every 20 s cycle. The small-magnitude controller-gain value prevents *valve hunting*. This is a phenomenon wherein the expansion valve opens or closes excessively and keeps fluctuating in an attempt to reach the set-point. Proportional-integral-derivative (PID) and Proportional-derivative (PD) control schemes were also considered, but not implemented as they can lead to valve hunting due to accumulation of error by integral action, and sharp changes associated with derivative action. A schematic of the implemented evaporator glide control model is presented in Figure 5.2. The proportional gain, K_{glide}, is set to a negative value due to the inverse relationship between temperature glide and valve restriction. As the valve restriction is reduced, the temperature glide decreases due to an increase in refrigerant mass flow rate. To prevent valve hunting, temperature glide control is only activated once there are no sharp changes in temperature glide and the system reaches near- design pressures.

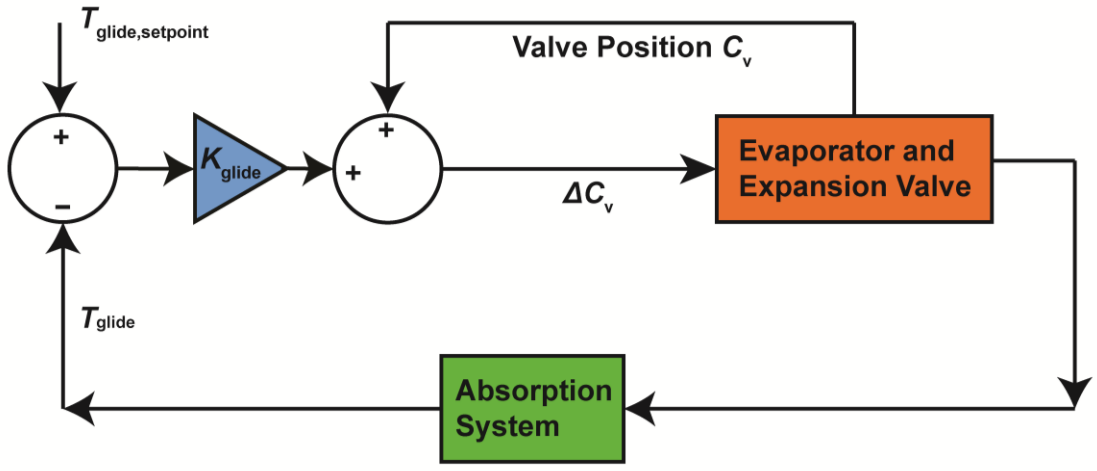

Figure 5.2: Schematic of evaporator temperature glide control

5.2.2 Delivered Coolant Temperature Control

In a practical application, the system operates under varying load demand and operating conditions. As the condenser and absorber reject heat to the surroundings, ambient temperature variations can also significantly affect system performance. The cooling demand may also fluctuate due to operating changes in the auxiliary systems coupled to the delivered coolant from the evaporator. For instance, in many applications, the desired delivered coolant temperature (set-point) may be fixed while cooling demand and ambient conditions vary continuously. Therefore, dynamic controls are required to appropriately respond to such situations. The modeled vapor-absorption system is driven by heat input into the desorber, which can be modulated to control the delivered cooling. In the proposed control methodology for delivered coolant temperature, a proportional feedback loop is employed, which takes the actual delivered coolant temperature and compares it to the set-point. The resulting error signal is multiplied by a gain (K_{des}), and the obtained signal specifies a change in the fuel flow rate through the gas valve in the combustion module. The resulting change in heating rate to the desorber coupling fluid loop leads to a new steady-state desorption temperature. In a practical system, the combustion module has an upper limit on heating rate, so the desorber coupling-fluid temperature can only be set within some range. For the system modeled in this study, the upper limit of coupling fluid temperature is set to 195°C. Compared to the low-pressure side components, the dynamics of high-pressure side components are faster; therefore, a higher-frequency controller update schedule can be employed without causing instabilities. The controller frequency is set to 0.1 Hz, and it is activated for 20% of the operating cycle. Therefore, the controller remains active for 2 s in each cycle lasting 10 s. A schematic of

the proposed control methodology is presented in Figure 5.3. The proportional gain (K_{des} = −0.05) is set to a negative value because of the inverse relationship between desorption temperature and coolant outlet temperature. As desorption temperature increases, the refrigerant generation rate increases, leading to an increased evaporator cooling capacity.

Both control loops are activated once the system reaches near-design pressures after start-up from ambient conditions – at t = 1000 s in this investigation. While the cooling duties of different heat exchangers reach 80% of design performance in ~300 s of simulation time, the temperatures of certain fluid streams take more time to reach steady state because of thermal masses of different storage vessels for working fluid and coupling fluids.

5.3 Results and Discussion

The control algorithms are implemented in the dynamic model developed in MATLAB & Simulink® platform. Reference tracking-based analyses, which determine the capability of control algorithms to track the set-points of process variables, were conducted

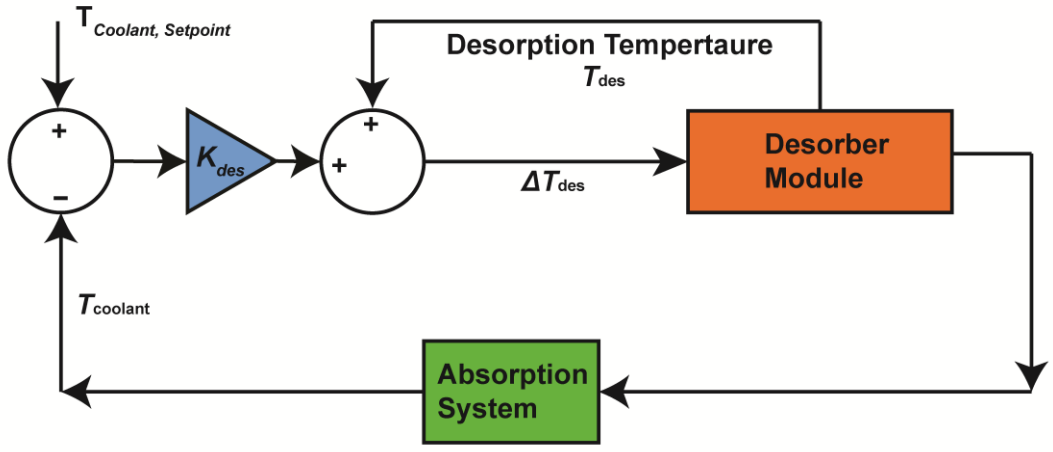

Figure 5.3: Schematic of delivered coolant temperature control

to evaluate the performance of the algorithms and study system responses. The employed test scenarios are summarized as follows:

1. A step change is applied to the evaporator temperature glide set-point to study the effectiveness of the dynamically controlled expansion valve in tracking the set-point signal
2. A gradual change is applied to the external heating rate to the coolant loop to evaluate the performance of both control schemes in maintaining the coolant and evaporator glide temperature set-points
3. A gradual change in ambient conditions is applied with fixed delivered coolant temperature set-point to evaluate the performance of both control schemes in concert

In all these cases, the model was initiated from ambient conditions, and was allowed to run without active control procedures for ~1000 s of simulation time. The flow rates of different coupling fluids and air-coupled heat exchangers for condenser, absorber and evaporator were ramped from zero to design values in the first 120 s. At the end of this start-up period, on-design operating conditions were achieved, with a desorber coupling fluid inlet temperature of 180°C and an ambient temperature of 35°C. The solution flow rate was fixed at 9.75×10^{-3} kg s^{-1}.

5.3.1 Evaporator Temperature Glide Control

After 1000 s of simulation time, the evaporator temperature glide reached a steady state value of ~5.5°C, which is higher than the set-point of 3°C. At this instant, the glide temperature control was activated, and it modulated the valve restriction by varying the valve coefficient in the model. The valve was modeled as a variable restriction, isenthalpic

device, and the refrigerant mass flow rate was calculated using Eq. 5.3, where c_v is the valve coefficient and P_{high} and P_{low} are high- and low-side pressures, respectively.

$$\dot{m}_{ref} = c_v \times \sqrt{P_{high} - P_{low}} \tag{5.3}$$

Valve adjustment continued until the temperature glide reached the set-point after ~250 s of controller activation. The performance of the controller in tracking the set-point for evaporator temperature glide is presented in Figure 5.4. After reaching new steady-state conditions, a step change of 1.5°C was introduced in the evaporator temperature-glide set-point signal at t = 2000 s, and it was brought back to the original value of 3°C at t = 2500 s. It can be concluded that using a dynamic expansion valve with a proportional feedback control drives the system satisfactorily towards the desired operating conditions. The controller achieved a quick response and returned the system to new steady state in ~250 s after the step change was introduced. The relatively slow dynamics of the evaporator

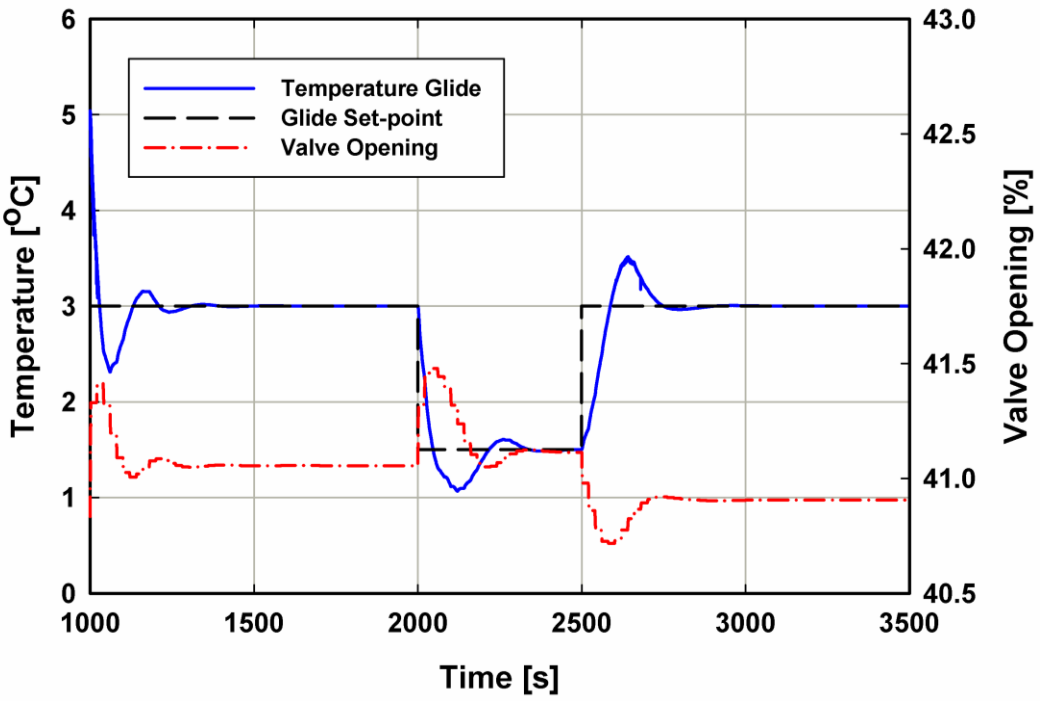

Figure 5.4: System response to step changes in evaporator glide set-point

temperature-glide response to the refrigerant-valve opening can also be observed in this test case. There is a finite time lag between refrigerant valve adjustment and evaporator temperature glide as observed between t = 2000 and t = 2250 s of simulation. The valve coefficient started to decrease after reaching a maximum, but the temperature glide continues to decrease for a ~60 s before it starts to increase. This also led to a slight overshoot while tracking the reference signal.

The variations of refrigerant flow rate and low-side pressure during the test case are presented in Figure 5.5. As the valve restriction was reduced, the low-side pressure increased, and the evaporator temperature glide decreased. While the pressure difference across the refrigerant valve decreased during this process, the net effect led to an increase in refrigerant mass flow rate. The low-side pressure increased due to the increased flow rate of refrigerant vapor at the absorber inlet.

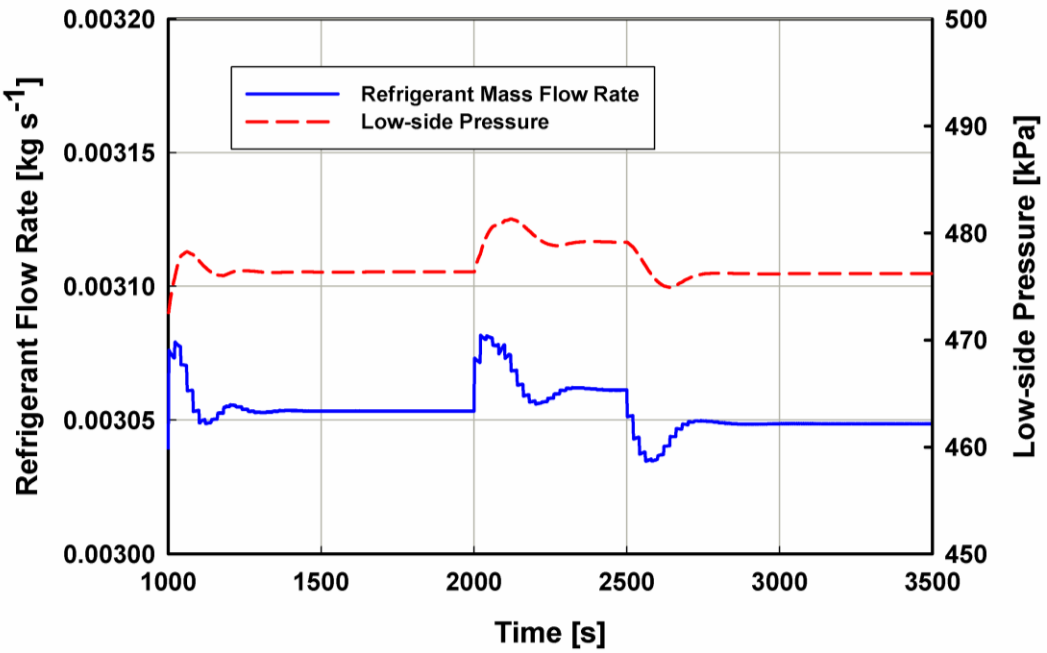

Figure 5.5: Refrigerant flow rate and low-side pressure variation with time

5.3.2 Delivered Coolant Temperature Control

In this test case, the delivered coolant temperature is automatically regulated by varying the desorber coupling-fluid temperature under off-design operating conditions. Similar to the previous case, the evaporator temperature-glide control loop was employed to automatically modulate the refrigerant expansion valve restriction. After the system achieved steady-state, on-design operation in 2000 s of simulation time, the heating load in the external process coupled to the coolant loop was artificially reduced by introducing a perturbation to simulate a change in cooling demand. The load was slowly reduced by 500 W over 1500s of simulation time, decreasing the evaporator cooling demand from the design value of 3.5 kW to 3.0 kW. This led to a decrease in coolant temperature at the inlet of the evaporator by ~0.7°C as compared to the design condition inlet temperature of 12.9°C. As the evaporator cooling requirement decreased, the desorber temperature control triggered a reduction in heat input to the desorber coupling-fluid loop. In turn, desorption temperature and refrigerant generation rates decreased, lowering the evaporator cooling rate and returning the delivered-coolant to the set-point temperature. Due to the reduced vapor generation rate, there was an increase in the ammonia concentration of the weak solution flowing out of the desorber. To adjust for this change in concentration, the solution pump flow rate was manually reduced by 20%. Autonomous integrated solution flow-rate control is discussed in the next chapter. During this process, the ambient temperature was maintained at the design condition of 35°C. Slight temperature oscillations of approximately ±0.25°C in the delivered coolant temperature were observed during this test case. These oscillations are numerical in nature, resulting from the explicit simulation time-stepping scheme (*ode45*), and are unlikely to significantly affect overall system behavior.

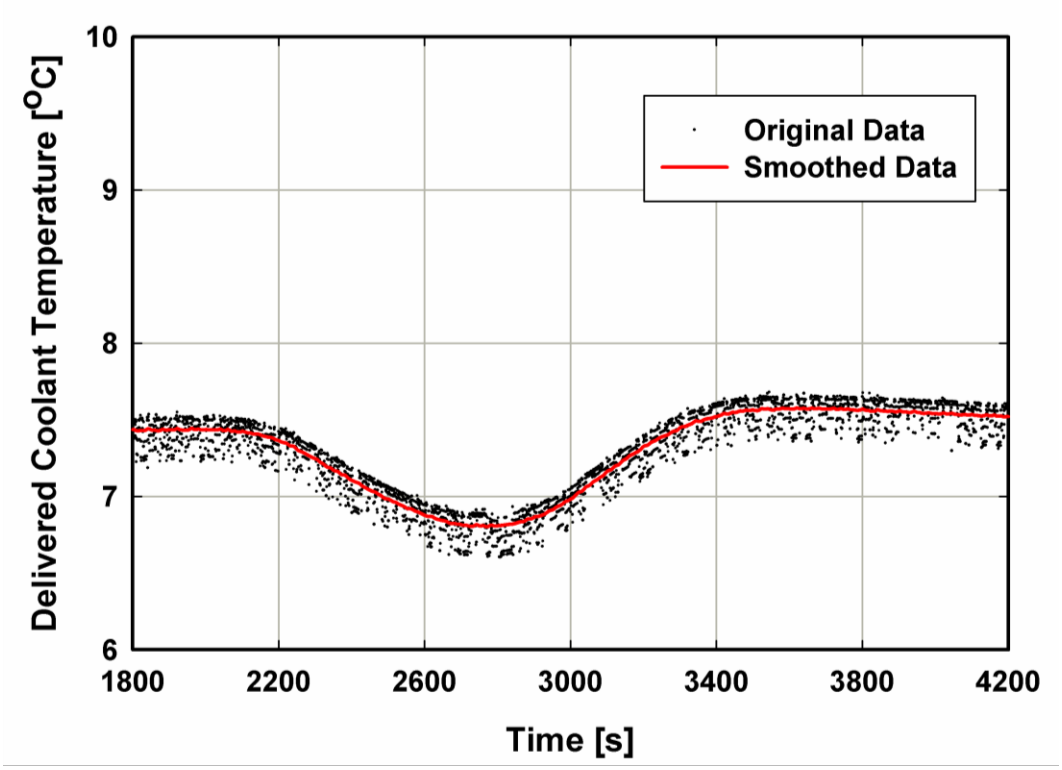

Figure 5.6: Actual delivered coolant temperature data and smoothed curve fit

The results presented in this study are smoothed using a spline fit (Figure 5.6), but the actual control system operates based on the slightly noisy raw data.

The variations in delivered coolant temperature and desorption temperature are presented in Figure 5.7. It can be observed that the controller satisfactorily maintained the delivered coolant temperature within $\pm 0.75°C$ of the set point during transient processes. In absence of control action, the coolant temperature decreases to $2°C$ below the set point. Additionally, with the proposed desorber temperature control loop activated, the overall system COP increased by 8.2% during this test case, as shown in Figure 5.8. The COP calculation, as shown in Eq. 5.4, is based on the ratio of the cooling capacity in the evaporator calculated on the coolant side, and the heat input into the desorber calculated from the change in enthalpy and flow rate of the heat transfer fluid. Pump and fan power

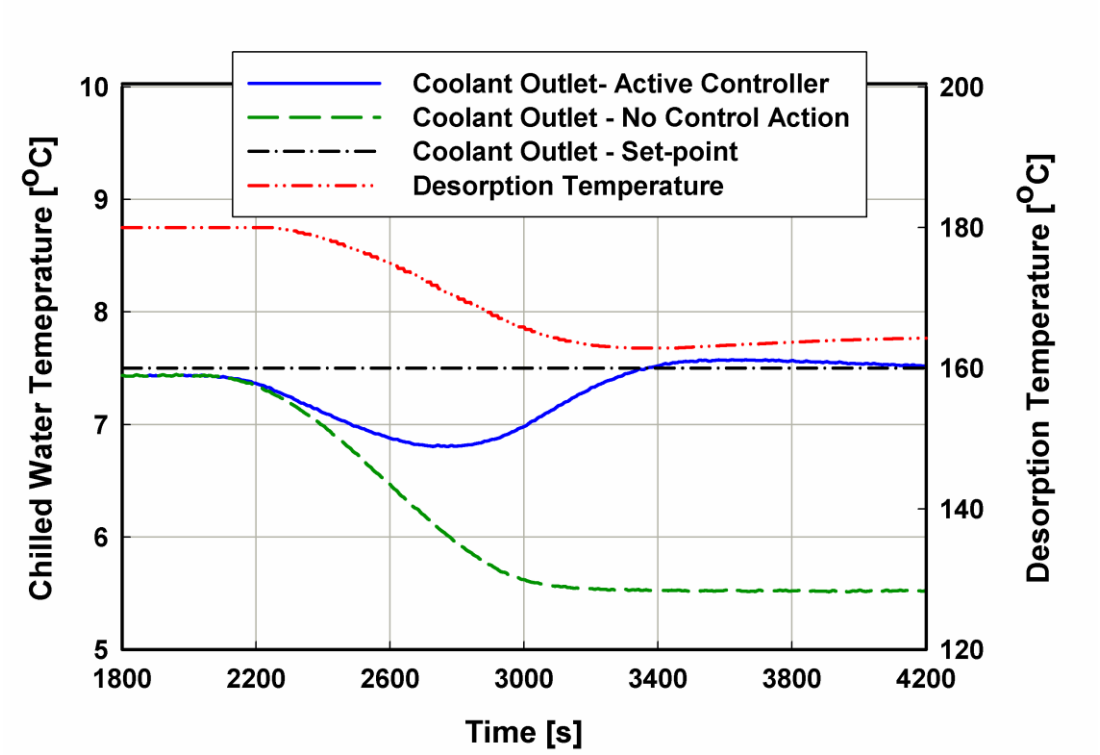

Figure 5.7: Variation of delivered coolant temperature and desorption temperature

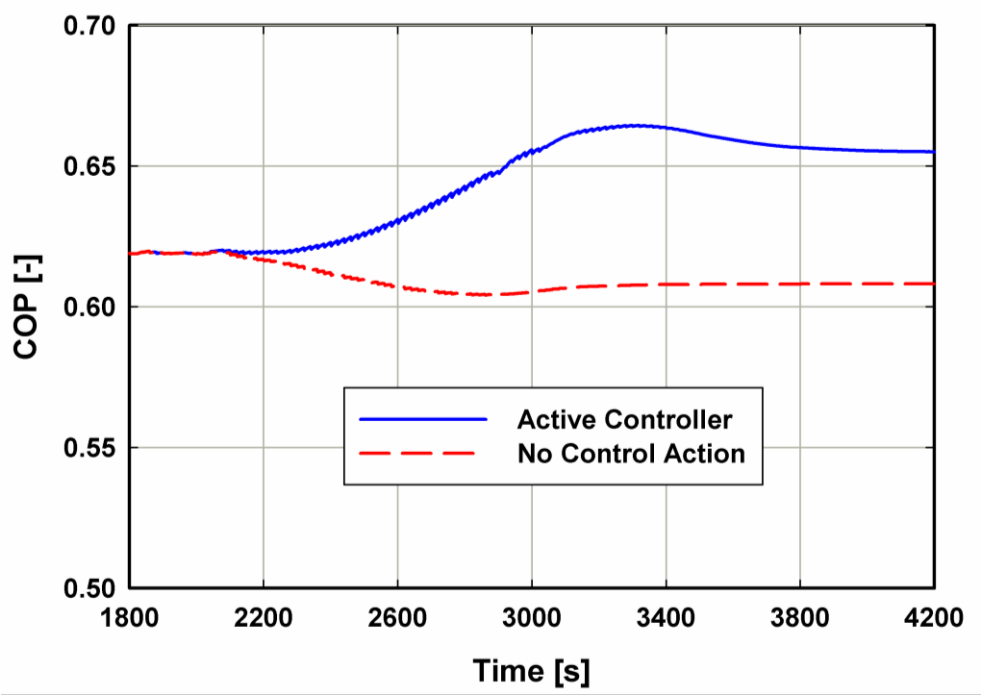

Figure 5.8: COP variation between the cases with and without active control system

consumptions were generally found to be small compared to the evaporator and desorber heat transfer rates, and were thus neglected from this metric, which is primarily intended to enable performance comparisons of the same system under different operating conditions.

$$COP = \frac{\dot{Q}_{evap}}{\dot{Q}_{des}} \tag{5.4}$$

Variations in obtained evaporator and desorber heat-transfer rates are presented in Figure 5.9. At part-load operation, the evaporator cooling rate decreased due to a perturbation in the heating load on the coolant (3.5 kW to 3 kW). However, the relative reduction in desorber heat input required to maintain the coolant delivery temperature was greater (5.6 kW to 4.5 kW). This can be attributed to fixed overall thermal resistance and

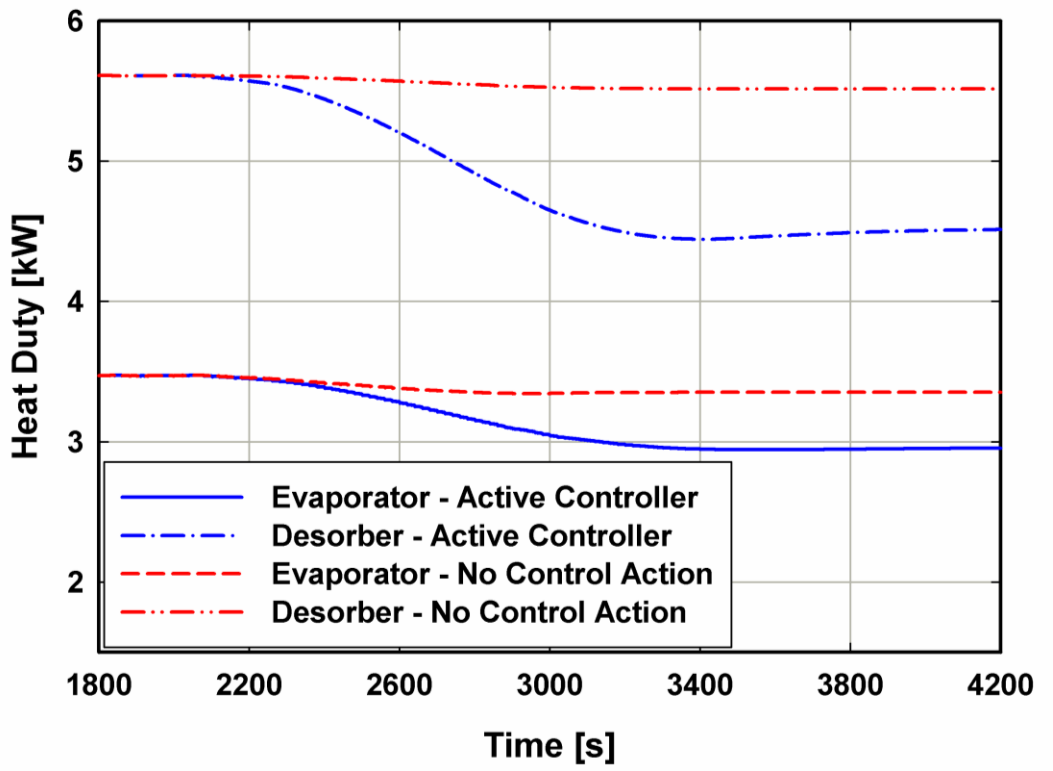

Figure 5.9: Variation in evaporator and desorber heat duties

size of different heat exchangers in the model. Using active control at part-load operation decreased the temperature of the heat transfer fluid in the desorber, and decreased the flow rate of concentrated solution, which led to an increase in the heat exchanger effectiveness. Similarly, a decrease in the flow rate of the refrigerant in the evaporator led to an increased effectiveness. Without the delivered-coolant temperature control loop, the evaporator cooling rate was found to decrease slightly because of a reduced temperature difference between the refrigerant and coolant streams, while the desorber heat load remained unaffected. Therefore, the system COP increased from 0.61 to 0.66 (8.2%) between the cases without and with active feedback control, respectively. The evaporator temperature-glide control loop satisfactorily tracked the set-point of 3°C in all simulations discussed in this section.

5.3.3 System Control in Response to Variation in Ambient Conditions

In another set of control response tests, a 5°C gradual reduction in ambient temperature was simulated. This reduction led to improved heat-transfer rejection from the condenser and absorber, and thus increased overall system cooling capacity. Improved absorber heat-transfer rejection also leads to reduced low-side system pressure, and thus lower refrigerant temperature at the evaporator inlet and greater evaporator cooling capacity. The variations in delivered coolant temperature and desorption temperature, and comparison between the cases with and without active control schemes, are presented in Figure 5.10. To maintain the delivered coolant temperature at the set-point of 7.5°C, the desorption temperature and heating rate were decreased by the control system. The controller tracked the coolant set-point temperature satisfactorily within ±0.5°C. The

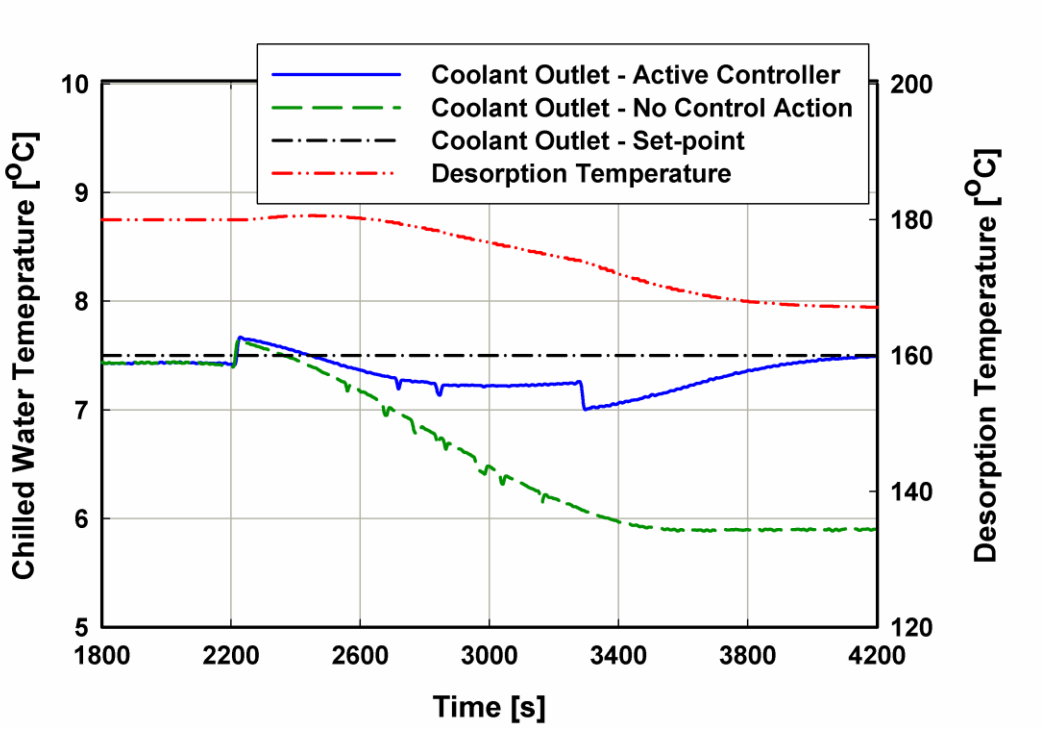

Figure 5.10: Delivered coolant and desorption temperature variation

solution pump flow rate was manually reduced by 20% to prevent a large decrease in desorption temperature. This led to a reduced refrigerant generation rate, matching the evaporator cooling rate to the external heat input rate to the coolant loop. Some oscillations were observed in the output data during transient operation, which can be attributed to issues associated with the explicit simulation time-stepping scheme. There were no oscillations after the system reached steady state at t = 3500 s.

System COP results from this test-case simulation are presented in Figure 5.11 and are compared to those without any active control strategies. In concert, the evaporator temperature-glide controller, desorber-temperature controller, and manually adjusted solution-pump flow rate lead to an increase in system COP by ~8%. Evaporator temperature glide control was activated for all the simulations discussed in this section.

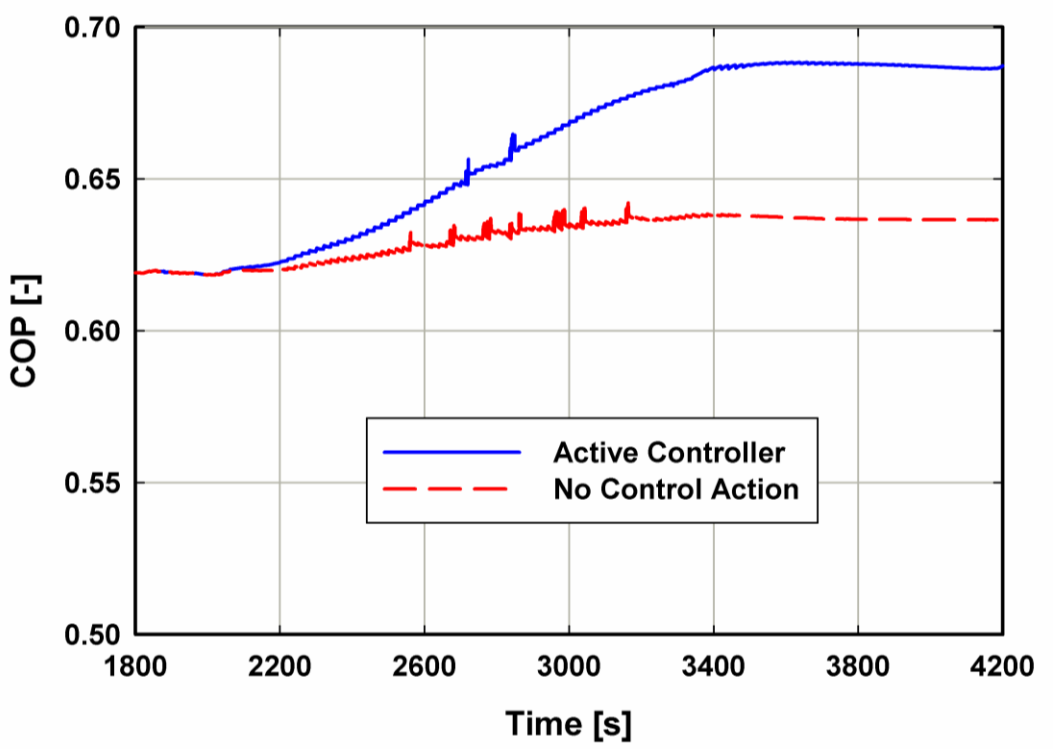

Figure 5.11: Variation in COP between the cases with and without active control system

5.4 Conclusions

In this computational study, novel control strategies were proposed for a small-scale (3.5 kW) ammonia-water absorption chiller. Using a dynamic model to simulate the system and control schemes, it was found that chiller performance can be controlled to yield an optimal evaporator temperature glide and modulate the evaporator cooling rate so that the delivered coolant temperature remains at a set-point. Two separate feedback loops with proportional control were evaluated for controlling evaporator temperature glide and delivered coolant temperature. For a step change of 1.5°C in the evaporator temperature glide set-point, the controller requires ~250 s to bring the system to the new steady state condition. Also, combined control action using both loops was shown to satisfactorily track changes in load demand and ambient temperature, and leads to ~8% increase in COP as

compared to a system operating without active control mechanisms. The proposed strategies for system control can potentially lead to effective control and energy savings under part-load operation and off-design ambient conditions.

Experimental validation and tuning of the control algorithms discussed above are presented in the next chapter. This investigation helped down-select potential techniques and determine starting-point control parameter values prior to experimental investigations.

CHAPTER 6. EXPERIMENTS ON ABSORPTION SYSTEM CONTROLS

This chapter presents the details of the experimental setup fabricated in this study and utilized to evaluate the performance of a small-capacity ammonia-water absorption chiller. Design and implementation of control algorithms is discussed. The approach utilized in the data analysis is presented. First, sample cases studies involving perturbations in different input variables are discussed with an emphasis on identifying system characteristics and the rate of change in different process variables. This information is utilized in tuning different control loops. Next, sample cases of overall system control are presented to study part-load operation and variation in external conditions of the system. The effectiveness of the control algorithms in regulating system performance and maintaining various set-points is elucidated using these experiments.

6.1 Experimental Setup

6.1.1 System Components

Figure 6.1 shows a schematic of the breadboard test facility, which enables the evaluation of the complete system, as well as individual component performance. The key features of each component are specified in Appendix I. The condenser, evaporator and recuperative heat exchangers utilize a brazed-plate microchannel design. The desorber design is based on the concept of a diabatic distillation column and utilizes a microchannel sheet for heat source coupling. The desorber design integrates heat transfer stages with purification stages and provides a compact design with very small liquid-vapor approach

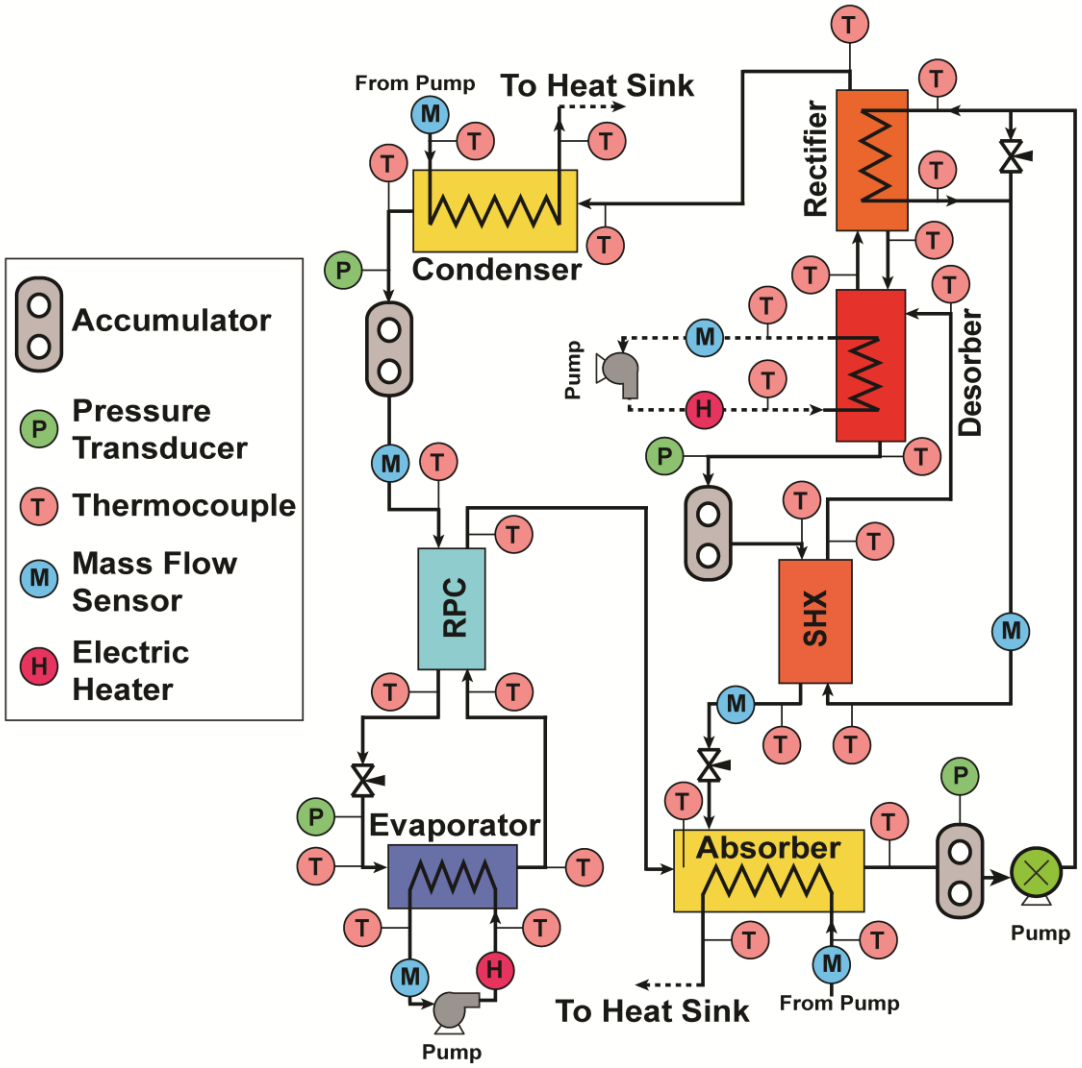

Figure 6.1: Schematic of breadboard test facility and instrumentation

temperature differences, and consequently, high-purity vapor leaving the desorber. A small, integrated analyzer section in the component further improves ammonia concentration in the vapor stream and decreases the rectification requirement. The rectifier is a custom-designed component with a wire-mesh packing on the condensing-side and a microchannel sheet on the coolant side. Finally, the absorber is a shell-and-tube heat exchanger. Figure 6.2 shows the fabricated test facility.

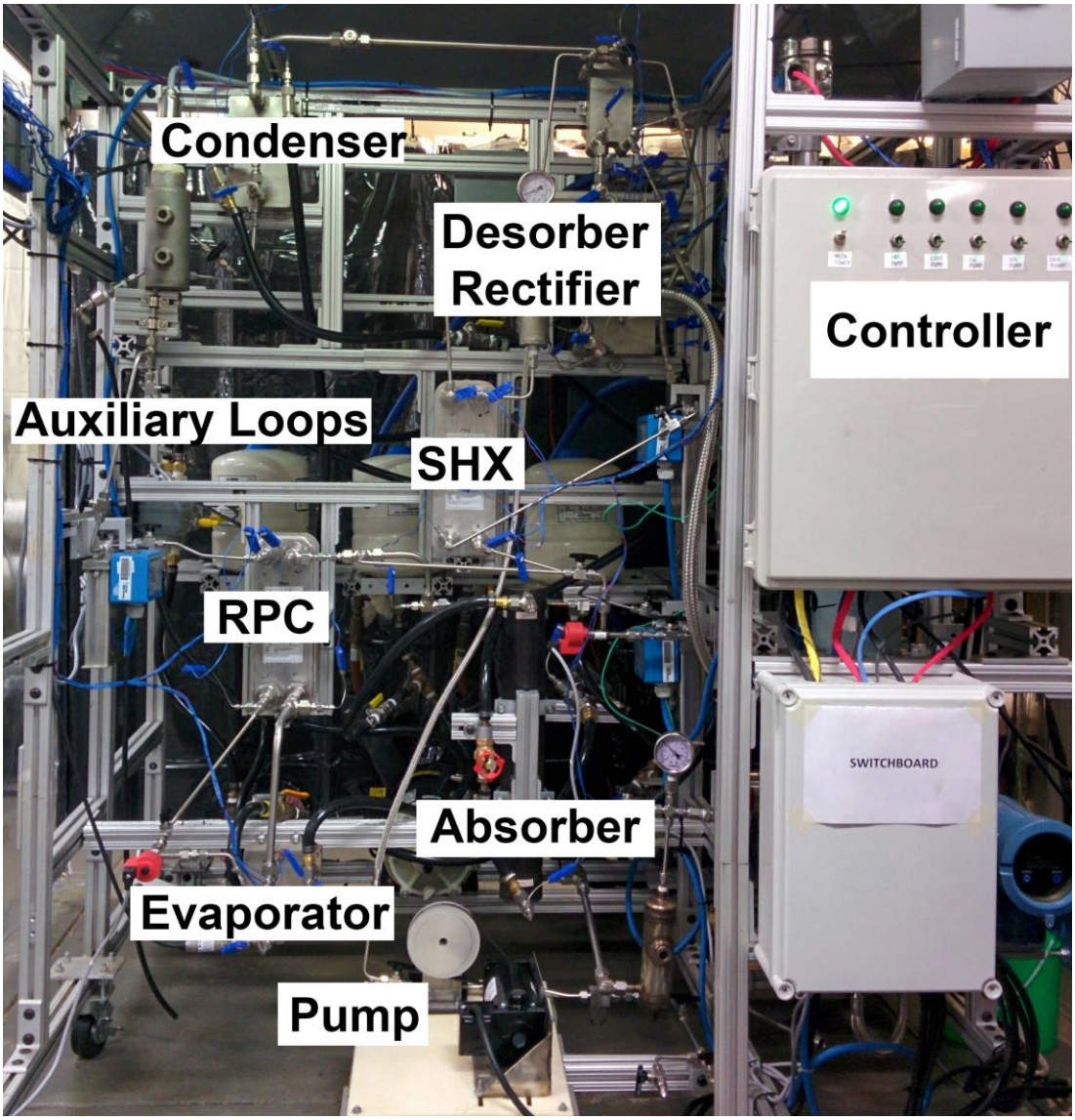

Figure 6.2: Breadboard test facility

6.1.2 Heat Source and Sink Coupling

The evaporator is coupled to a distilled water loop heated using an electrical cartridge heater. The heater is controlled using a silicon-controlled rectifier (SCR) and provides continuous variation of electrical input to the heater. A proportional-integral (PI) feedback control loop is implemented to provide the desired temperature set-point of water (coolant return) inlet to the evaporator. The feedback loop continuously adjusts the input power to the heater to maintain the desired temperature set-point.

The absorber and condenser are hydronically coupled using distilled water and the heats of absorption and condensation are ultimately rejected to the chilled water supply available in the laboratory. Both components receive identical temperature of the cooling water at the inlet as they are connected in parallel to the cooling water supply. This allows for accurate control of operating conditions for both the components. A PI feedback loop manipulates an electronic valve on the chiller flow line to provide control of cooling water inlet temperature to the absorber and condenser. This can be used to simulate different ambient conditions for the operation of the absorption chiller.

The desorber is coupled to an electrically heated mineral oil loop. The mineral oil used in this study is Paratherm NF® which demonstrates stable thermodynamic properties at high temperatures. The heat source inlet temperature in the desorber is continuously controlled using a PI feedback loop and an SCR power controller that regulates the electrical power input to the heater. A variable-speed gear pump circulates the mineral oil, and the flow rate can be adjusted by varying the speed of the motor.

6.1.3 Auxiliary Components

The concentrated solution in the system is circulated using a variable-speed diaphragm pump. The constant displacement volume of the diaphragm provides repeatable performance and the supplied volumetric flow rate can be accurately correlated to the speed of the motor. Electronic expansion valves are used on the dilute solution and refrigerant streams. These valves are operated by precise motion of a stepper motor and provide accurate control of flow rates. The dilute solution valve supplies the liquid at the inlet of

the absorber in a tube-in-tube injector that allows mixing between the refrigerant vapor and the dilute solution streams.

The reflux (condensate) stream exiting the rectifier enters the desorber along with the concentrated solution stream. This allows for extraction of ammonia from the reflux stream and improves the system performance. The coupling fluid in the rectifier is the concentrated solution stream, and the inlet port to the rectifier contains a bypass valve. The valve allows for variations in the coupling fluid flow rate supplied to the rectifier. If the rectifier is oversized, a fraction of the total solution flow rate can be bypassed. This prevents over-condensation of the generated refrigerant in the rectifier.

In addition to all the components mentioned above, the experimental system also contains fluid accumulators at the outlet of the condenser, absorber and at the bottom of the desorber. These accumulators serve as buffer fluid inventory for different fluid streams in the system and compensate for the flow rate variations during transient processes. Additionally, these accumulators ensure that the outlet phase of the fluid is saturated or subcooled liquid. This is particularly important for the solution pump as the presence of vapor in the outlet from the fluid accumulator located downstream of the absorber can lead to large variations in the supplied mass flow rate of the concentrated solution.

6.1.4 Instrumentation

As shown in Figure 6.1, temperatures at the inlet and outlet of each stream of individual heat exchangers are measured using T-type thermocouples. Pressures are measured using electronic pressure transducers at the outlet of the desorber, the outlet of the condenser, inlet to the evaporator, and outlet of the absorber. The two pressure

measurements on the low-pressure side also help in characterizing the total pressure drop on the low-pressure side components. Four high accuracy (±0.1%) Coriolis mass flow sensors are used to measure the mass flow rates of the concentrated solution, dilute solution, refrigerant solution, and evaporator coolant. It should be noted that this leads to very small uncertainties in calculated variables due to mass flow rate measurement, and the corresponding error bars are not visible on the plots. A capacitance-based level measurement probe is used on the refrigerant tank to measure the liquid level. This is used to monitor and regulate appropriate liquid storage level in the tank during transients and change in operating conditions. In addition, two magnetic flow sensors are used to measure the flow rate of the coupling fluid supplied to the absorber and condenser. The absorber and the condenser reject heat to a water stream coupled to the laboratory chiller. A solenoid valve on the chiller supply line regulates the flow rate. A gear flow meter is used to measure the volumetric flow rate of the coupling fluid supplied to the desorber. For safety of the system components from catastrophic damage at high pressures, a pressure relief valve is installed at the outlet of the condenser. Table 6.1 shows the details of all the instrumentation hardware.

All the signals from various measurement probes are digitally sampled by a National Instruments® programmable controller and data acquisition module shown in Figure 6.3. The sampling frequency is set to 10 Hz and data points are recorded at a frequency of 1 Hz. This is performed to allow for time averaging of certain variables for control applications and will be discussed in the following sections. For continuous data recording, such as when evaluating controller performance or transient response of the system, the signals are recorded continuously until steady-state performance is achieved. For other data

Table 6.1: Equipment and measurement probe specifications

Instrument	Manufacturer/Model	Range	Accuracy
Thermocouple	Omega® T-type Omega® J-type	-250 – 300°C 0 – 750°C	±0.5°C ±1.1°C
Pressure Transducer	Omega® 4-20 mA Output® Absolute	0 – 1034.2 kPa 0 – 3447.3 kPa	±0.03% Range
Mass Flow Sensor	Rheonik® Coriolis Sensor	0 – 0.01 kg s^{-1} 0 – 0.1 kg s^{-1}	±0.1%
Evaporator Coolant Mass Flow Sensor	MicroMotion® Coriolis Sensor	0 – 0.6056 kg s^{-1}	±0.1%
Cooling Water Flow Sensor	Omega® FMG83 Series	0.000013 -0.0013 m^3s^{-1}	±1%
Paratherm Flow Sensor	AW Lake JVM-30KG Gear Flow Meter	0 – 0.00044 m^3s^{-1}	±0.5%
Level Measurement Probe	Endress+Hauser® Liquicap M FMI51	0 – 0.152 m	±0.5%
Electronic Expansion Valves	Carel® E2V Series	480 motor steps	–
Data Acquisition and Control	National Instruments® c-RIO 9022	–	–
Paratherm Heater	Watlow® Firebar FON713J10S Baffled Circulation Heater	0 – 9 kW	–
Evaporator Coolant Heater	Watlow® Firerod Cartridge Heater	0 – 5 kW	–
Chiller Flow Control Valve Actuator	Honeywell® M7435F Series	–	–
Heater Power Controllers	Watlow® DIN-A-MITE SCR Controller	–	–

points for analyses of steady-state-performance, the signals are recoded at a frequency of 1 Hz for 20-min duration and then the time-averaged values of different measured variables are used in the subsequent data analysis.

6.2 Data Analysis

Experiments were first conducted to analyze the system performance at nominal ambient conditions of 34°C. Data analysis is conducted as described by Lee *et al.* (2012),

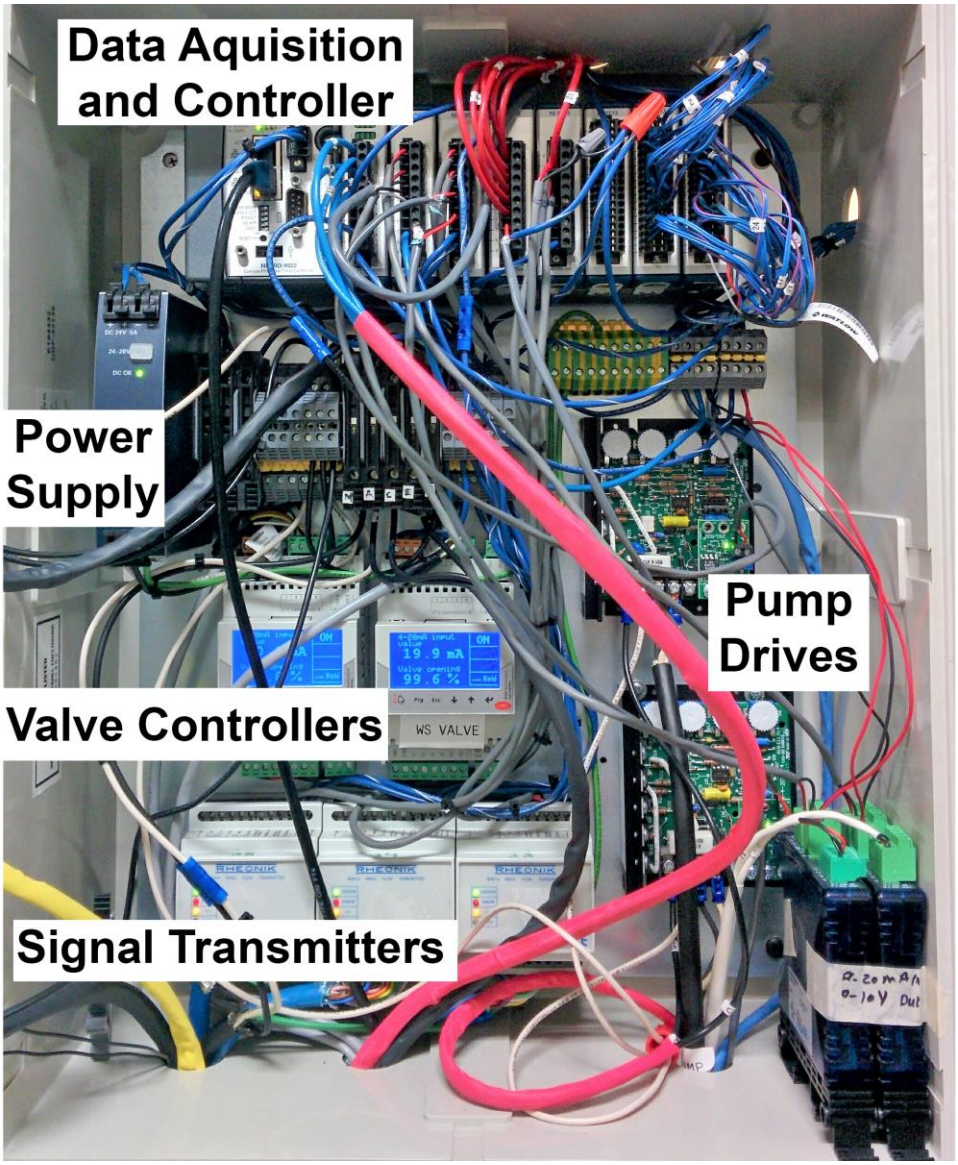

Figure 6.3: Control and data acquisition hardware

using time-averaged values of different measured variables to define inlet and outlet states of each component. Heat transfer rate in each component is then calculated and system performance analyzed. As the ammonia concentration is difficult to measure in experiments, phase quality assumptions are made regarding the outlet streams from the desorber. The desorber is a continuously heated component and a two-phase mixture is assumed to exist along its entire length. Therefore, it can be assumed that:

- the refrigerant vapor leaves the desorber/analyzer section in the saturated state, and
- the liquid leaves the bottom of desorber in the saturated state.

These phase-quality assumptions are required to determine the concentration of the vapor and dilute solution streams exiting the desorber, and hence set the third required state property along with the measured pressure and temperature. With the measured mass flow rates and computation of fluid enthalpy at the inlet and outlet of each component, the heat transfer rate for each component is calculated. Engineering Equation Solver (EES) (Klein, 2016) is used for data analysis. The equations describing the behavior of individual components are presented below.

Condenser

The heat transfer rate is calculated on both the refrigerant and coupling fluid sides using the measured mass flow rates, temperatures, condenser pressure, and the refrigerant vapor concentration exiting the rectifier, Eqs. 6.1 – 6.3.

$$\dot{Q}_{f,cond} = \dot{m}_{f,cond}(h_{f,cond,in} - h_{f,cond,out}) \tag{6.1}$$

$$h_{f,cond} = f(T_{f,cond}, P_{cond}, x_{f,cond}) \tag{6.2}$$

$$\dot{Q}_{cf,cond} = \dot{m}_{cf,cond} Cp_{cf,cond}(T_{cf,cond,out} - T_{cf,cond,out}) \tag{6.3}$$

where, $x_{f,cond}$ is refrigerant vapor concentration, P_{cond} is pressure measured at the condenser outlet, and $T_{f,cond,in}$ is temperature measured at the inlet of the condenser. The heat transfer rate is calculated using the measured mass flow rates, $\dot{m}_{f,cond}$ and $\dot{m}_{cf,cond}$, of the refrigerant and coupling fluid, respectively.

Refrigerant Pre-cooler (RPC)

The refrigerant pre-cooler serves to provide heat transfer between the high-pressure refrigerant in liquid and the colder, low-pressure vapor leaving the evaporator. This helps in reducing the enthalpy of the liquid refrigerant at the inlet of the expansion valve. Both the streams have identical ammonia-concentration and refrigerant mass flow rate supplied by the rectifier. The heat transfer rates are calculated using Eqs. 6.4 and 6.5.

$$\dot{Q}_{liq,RPC} = \dot{m}_{f,RPC}(h_{liq,RPC,in} - h_{liq,RPC,out}) \tag{6.4}$$

$$\dot{Q}_{vap,RPC} = \dot{m}_{f,RPC}(h_{vap,RPC,out} - h_{vap,RPC,in}) \tag{6.5}$$

Equating the two heat transfer rates provides the refrigerant ammonia mass fraction that is utilized in the condenser, evaporator, rectifier outlet and the absorber vapor inlet.

Evaporator

The refrigerant enters the evaporator as a low-quality (<0.1) two-phase mixture and exits typically as a high-quality (>0.9) two-phase mixture. Due to the zeotropic nature of the ammonia-water working fluid, the refrigerant temperature increases along the length of the evaporator and for optimal heat transfer performance, the evaporator glide is usually maintained at 2.5 – 3.5°C. Owing to this small temperature difference on the refrigerant side and strong dependence of refrigerant enthalpy on temperature, the heat transfer rate is calculated on the coupling fluid side of the evaporator. The heat transfer rate is determined using Eq. 6.6:

$$\dot{Q}_{cf,evap} = \dot{m}_{cf,evap} Cp_{cf,evap}(T_{cf,evap,in} - T_{cf,evap,out}) \tag{6.6}$$

Desorber

The heat transfer rate in the desorber is calculated on the coupling-fluid and the solution streams as shown in Eq. 6.7 and 6.8, respectively.

$$\dot{Q}_{cf,des} = \dot{m}_{cf,des} Cp_{cf,des} (T_{cf,des,in} - T_{cf,des,out}) \tag{6.7}$$

$$\begin{aligned} \dot{Q}_{f,des} = {} & \dot{m}_{vap,des,out} h_{vap,des,out} + \dot{m}_{liq,des,out} h_{liq,des,out} - \dot{m}_{liq,des,in} h_{liq,des,in} \\ & - \dot{m}_{refl,des,in} h_{refl,des,in} \end{aligned} \tag{6.8}$$

where, $\dot{m}_{vap,des,out}$ is the vapor phase mass flow rate leaving the desorber, and the enthalpy of vapor, $h_{vap,des,out}$, is determined using measured temperature and pressure assuming a saturated vapor (quality = 1) state. Similarly, $\dot{m}_{liq,des,out}$ is the liquid dilute solution exiting the desorber and the enthalpy $h_{liq,des,out}$ is calculated using measured temperature and pressure, assuming a saturated liquid (quality = 0) state. The inlet streams into the desorber are the concentrated solution from solution heat exchanger and reflux from the rectifier, with their states determined from the absorber and rectifier, respectively.

Rectifier

The rectifier heat transfer rates are calculated on both the coupling fluid and refrigerant streams as shown in Eq. 6.9 – 6.10.

$$\dot{Q}_{cf,rec} = \dot{m}_{cf,rec} (h_{cf,rec,out} - h_{cf,rec,in}) \tag{6.9}$$

$$\dot{Q}_{f,rec} = \dot{m}_{vap,des,out} h_{vap,des,out} - \dot{m}_{vap,rec,out} h_{vap,rec,out} - \dot{m}_{refl,rec,out} h_{refl,rec,out} \tag{6.10}$$

Mass and species balances (Eq. 6.11 – 6.12), along with equating the heat transfer rate on the refrigerant and coupling fluid side are required to completely define the system of equations.

$$\dot{m}_{vap,des,out} = \dot{m}_{vap,rec,out} + \dot{m}_{refl,rec,out} \tag{6.11}$$

$$\dot{m}_{vap,des,out} x_{vap,des,out} = \dot{m}_{vap,rec,out} x_{vap,rec,out} + \dot{m}_{refl,rec,out} x_{refl,rec,out} \tag{6.12}$$

Solution Heat Exchanger (SHX)

The heat transfer rates are calculated as shown in Eqs. 6.13 and 6.14, using the measured temperature and pressure on the dilute solution and concentrated solution streams, and known concentrations and mass flow rates from the absorber and desorber.

$$\dot{Q}_{cs,SHX} = \dot{m}_{cs,SHX} (h_{cs,SHX,out} - h_{cs,SHX,in}) \tag{6.13}$$

$$\dot{Q}_{ds,SHX} = \dot{m}_{ds,SHX} (h_{ds,SHX,in} - h_{ds,SHX,out}) \tag{6.14}$$

Absorber

The heat transfer rate is calculated on the working fluid-side using measured flow rates and temperatures of the inlet and outlet streams of the absorber. The species conservation equation is used to establish the concentration in the absorber. Eqs. 6.15 – 6.16 show this calculation. Coupling fluid heat transfer rate is calculated using the measured mass flow rate and temperatures of the cooling water stream as shown in Eq. 6.17.

$$\dot{Q}_{cs,abs} = \dot{m}_{cs,abs} (h_{cs,abs,in} - h_{cs,abs,out}) \tag{6.15}$$

$$\dot{m}_{f,RPC} x_{f,cond} + \dot{m}_{ds,SHX} x_{liq,des,out} = \dot{m}_{cs,abs} x_{cs,abs} \tag{6.16}$$

$$\dot{Q}_{cf,abs} = \dot{m}_{cf,abs} Cp_{cf,abs} (T_{cf,abs,out} - T_{cf,abs,out}) \tag{6.17}$$

At steady-state operating conditions, mass and species continuity between upstream and downstream components are established to close the system of equations. Finally, the thermal COP of the system is defined as the ratio of the heat transfer rate in the evaporator and the desorber, defined in Eq. 6.18.

$$COP_{th} = \frac{\dot{Q}_{cf,evap}}{\dot{Q}_{cf,des}} \tag{6.18}$$

6.3 System Performance

6.3.1 Baseline Operation

The fabricated system is charged with ammonia-water mixture after evacuation. The initial amount of total charge and ammonia mass fraction is estimated from the system cycle model, component models that provide estimates of average void fractions at steady-state, and a safety factor to account for fluid storage in the connecting tubes. The breadboard system is charged with 1.25 kg each of water and ammonia. During the initial phase of system performance evaluation, the charge is adjusted to achieve steady performance and stable fluid inventory inside different accumulators. In this process, some concentrated solution or liquid ammonia is discharged to achieve the required charge and concentration. Table 6.2 summarizes the steady-state baseline performance of the system. The system delivered ~2.65 kW of cooling at a COP of ~0.6. The supplied coolant

Table 6.2: Steady-state system operation at baseline (design) conditions

Component	Heat Transfer Rate (kW)	Overall Conductance (kW K^{-1})
Absorber	4.25	1.064
Condenser	2.88	0.906
Desorber	4.48	0.304
Evaporator	2.65	0.536
Rectifier	0.84	0.029
RPC	0.39	0.106
SHX	3.32	0.331

temperature from the evaporator was 9°C. The cooling water inlet temperature for the absorber and the condenser was 37°C, which translates to a 34°C ambient assuming a 3°C temperature approach if an air-coupled heat exchanger was utilized for heat rejection. Finally, the desorber received heat input from the heated mineral oil stream entering at 145°C and at a flow rate of ~0.10 kg s^{-1}. The mass flow rate of the concnetrated solution was 0.012 kg s^{-1}. The ammonia mass fraction of the refrigerant, dilute solution and the concentrated solution streams were 0.9951, 0.2723, and 0.4244 kg kg^{-1}, respectively. Appendix II shows a sample calulcation at baseline operating conditions.

6.3.2 Perturbation Studies

After establishing the baseline performance of the system, different input variables were selected for perturbation studies. These studies involved varying the input variables individually or in concert with another input variable to quantify their effect on the performance of the system. These studies also provide insight into the transient response of the system during such variations, and help characterize key time constants for final control algorithms. The input variables studied in this work are:

- Desorber heat source inlet temperature
- Desorber heat source mass flow rate

- Concentrated solution mass flow rate
- Combined effects of concentrated solution flow rate and heat source inlet temperature
- Absorber and condenser heat sink temperature

The following sections elaborate upon these experiments and discuss the key results.

6.3.2.1 Desorber Heat Source Inlet Temperature

Heat source modulation is known to be an effective parameter for modulation of system capacity, and many researchers have utilized it as key parameter for controlling system capacity (Sun, 1997; Jeong, 1999; Fernández-Seara and Vázquez, 2001; Kohlenbach, 2006; Staedter, 2018). In this work, the heat source modulation is split into its two components: heating fluid inlet temperature and mass flow rate. This helps in identifying the effects of both variables and allow for selection of control parameters for different heat sources. Sources such as natural gas combustion or combustion of other fossil fuels provide the flexibility in directly modulating both the inlet temperature and the mass flow rate. On the other hand, sources such as solar-thermal, waste-heat, and geothermal may be less flexible and often allow control over the mass flow rate only.

In this study, first the effects of heat source temperature were investigated. The temperature of the coupling fluid entering the desorber was varied between 130 – 155°C by varying the heat input to the circulation heater on the mineral oil loop. All the other parameters such as cooling water temperature, evaporator coolant temperature, dilute solution valve position, solution flow rate, and the evaporator temperature glide remained constant. Figure 6.4 shows the variation of heat transfer rates in the desorber and the

evaporator, and the system COP. As the heat source temperature increased, the desorber heat input rate increased (3.53 – 4.50 kW) due to a greater driving temperature difference. The cooling capacity, however, demonstrated a marginal increase from 2.21 – 2.38 kW. The system COP decreased from 0.63 to 0.53. The cooling capacity increased marginally because the mass flow rate of the generated refrigerant did not change significantly during these experiments (0.0021 – 0.0023 kg s^{-1}), and the refrigerant concentration decreased from 0.997 kg kg^{-1} to 0.993 kg kg^{-1}. The concentration of the refrigerant decreased because of hotter refrigerant vapor exiting the desorber at higher source temperatures, which has a higher water fraction. Increased water fraction in the refrigerant and constant glide temperature led to only a marginal increase in the cooling capacity.

Figure 6.5 shows key temperatures in the system as the heat source temperature changes. As shown, the coolant return temperature to the evaporator was kept constant at

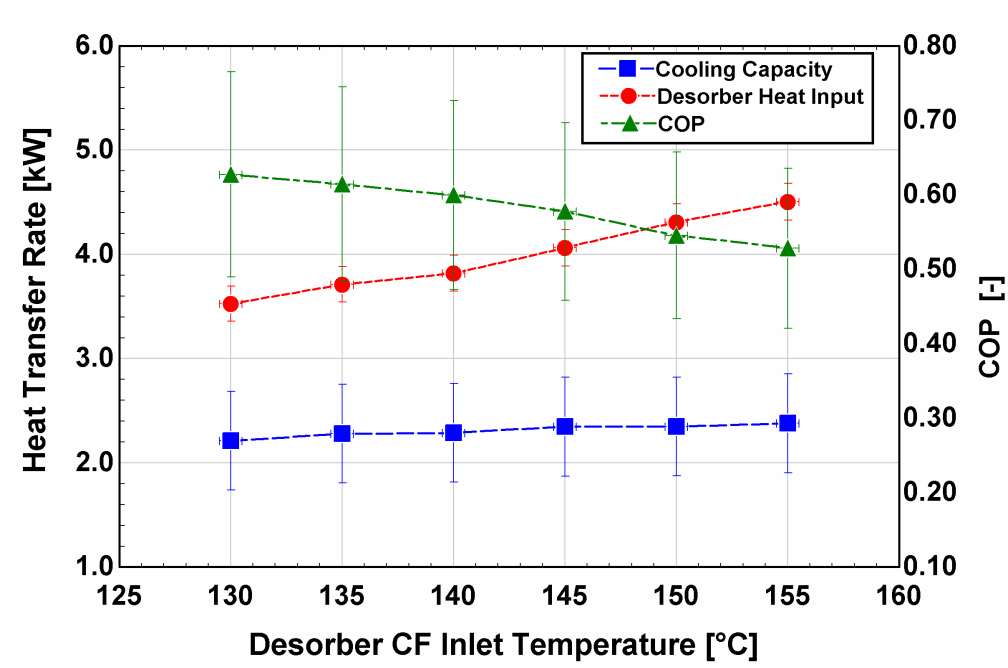

Figure 6.4: Effect of heat source temperature: heat transfer rates and COP

13°C. As the cooling capacity increased with increasing heat source temperature, the coolant supply temperature decreased from 9.70°C to 9.44°C. Evaporator temperature glide control (described in the next section) was successful in maintaining the glide temperature at its set-point of 2.5°C. As the dilute solution valve position remained unchanged, the solution heat exchanger approach temperature increased from 2.68°C to 9.34°C. The approach temperature is measured as the difference between the temperature of the dilute solution outlet and the concentrated solution inlet from the solution heat exchanger. This is indicative of some refrigerant vapor exiting the bottom of the desorber along with the dilute solution stream. The phenomenon is visually confirmed at the outlet of the desorber by using a sight glass. This leads to loss of the generated refrigerant vapor without providing any cooling. This also indicated that the approach temperature in the solution heat exchanger is a good indication of the hydrodynamic performance of the desorber.

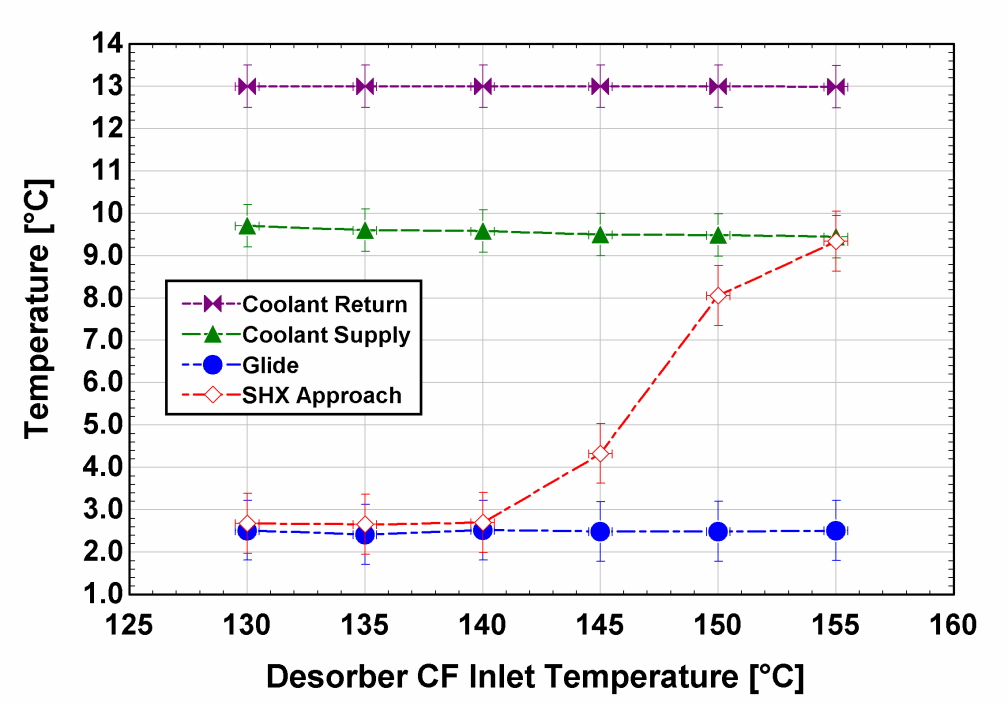

Figure 6.5: Effect of heat source temperature: important temperatures

6.3.2.2 Desorber Heat Source Mass Flow Rate

Figure 6.6 shows the variation in the cooling capacity, the desorber heat input rate, and COP of the system as the desorber coupling fluid mass flow rate is varied from 0.069 – 0.117 kg s^{-1}. The effects of mass flow rate variations are negligible. The cooling capacity varies from 2.64 – 2.68 kW, with the desorber heat transfer rate varying from 4.45 – 4.62 kW. The heat transfer rate is insensitive because of two reasons. First, the heat source coupling sheets in the desorber employ a microchannel design. For single-phase flow, the heat transfer coefficient is a weak function of the mass flow rate (Kakac *et al.*, 1987), and therefore, it remains approximately invariant (at the typically low Reynolds numbers under consideration) when the heat source flow rate is varied. Second, the logarithmic temperature difference increases during the transient period when the heat source mass flow rate is increased, but at steady-state, it returns to its design value. As the new steady-state is achieved, the solution temperature also increases, and the driving temperature

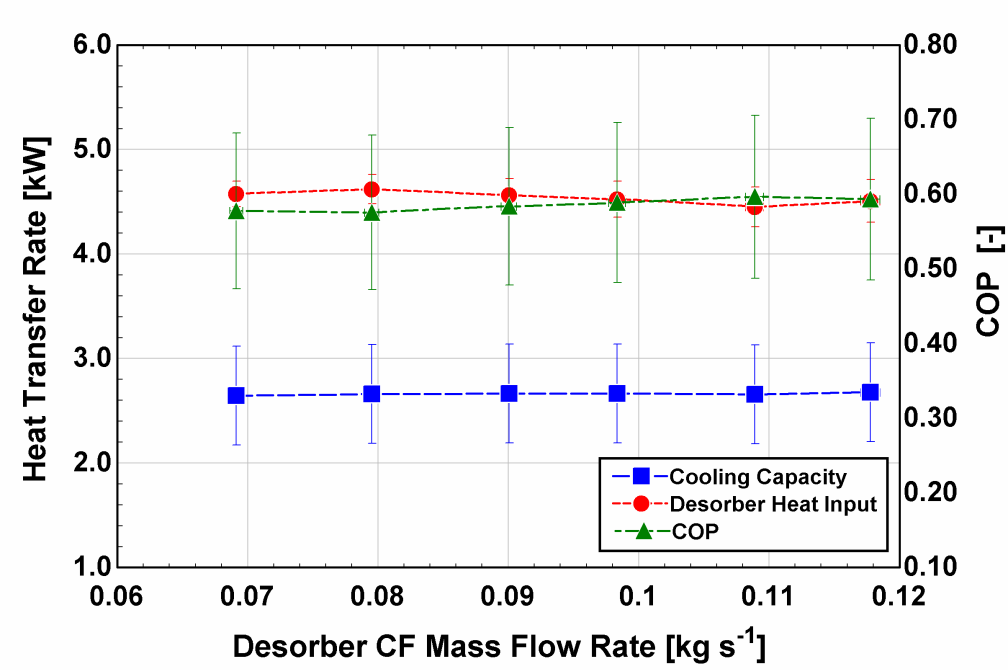

Figure 6.6: Effect of heat source mass flow rate: heat transfer rates and COP

difference returns to its original value. Therefore, the heat transfer rate remains invariant. Consequently, the system COP also remained largely unchanged and varied between 0.575 – 0.596.

While the coupling fluid mass flow rate seems to be less impactful on the overall system performance, it is useful in bringing about faster changes in the heat source inlet temperatures in systems that receive heat input from a combustion-based heat source (simulated in this study using an electric heater). This is because reducing the mass flow rate of the coupling fluid leads to decrease in the heat transfer rate from the heat source to the fluid. For systems activated using sources such as solar-thermal, geothermal and waste-heat streams, the coupling fluid mass flow rate is the only parameter to be manipulated on the heat source side, making it a very important process variable for capacity control schemes.

6.3.2.3 Concentrated Solution Mass Flow Rate

The concentrated solution flow rate was identified as a key control variable in the previous chapter and in the data-based control methodology presented by Staedter (2018). To evaluate the effects of variation of the solution flow rate on system performance, it was varied between 0.0065 – 0.0125 kg s^{-1}. Other inputs to the system, such as the coolant return temperature, desorber coupling fluid inlet temperature and mass flow rate, and the cooling water temperature remained constant at their design values.

Figure 6.7 shows the effect of the solution flow rate on the key temperatures in the system. As mentioned before, the coolant return temperature provided by the heating loop attached to the evaporator remained constant at 13°C during all the experiments. The

coolant supply temperature decreased with increasing solution flow rate because of increased refrigerant generation and lower low-side pressure that led to lower saturation temperatures. The glide control loop successfully maintained the temperature glide in the evaporator at 2.5°C. The solution heat exchanger approach temperature demonstrated an interesting trend. During the last four experiments, the dilute solution valve position remained unchanged (at 69.6% opening). In the last three experiments, the approach temperature remained close to its setpoint of 2.5°C, however for solution flow rates below that value, the approach temperature would increase drastically. This is again attributed to some vapor phase exiting through the bottom of the desorber. This was confirmed visually at the outlet of the desorber as well by inspecting the flow through a sight glass. This phenomenon of rapid vapor generation in the bottom part of the desorber can be attributed to a combination of low solution flow rate with constantly high desorber coupling fluid

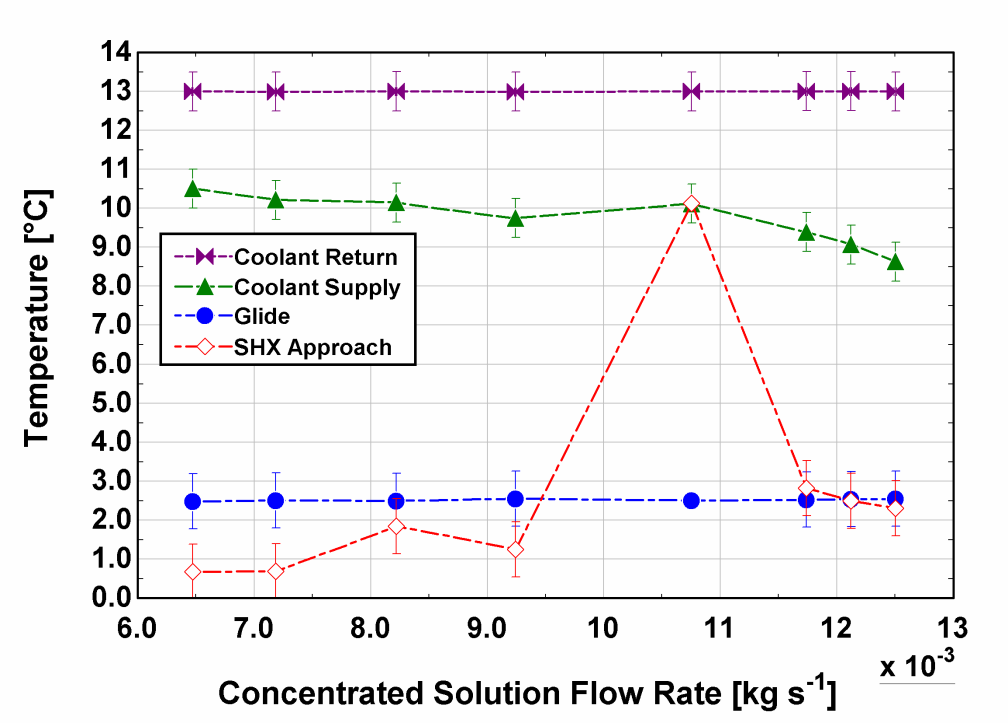

Figure 6.7: Effect of concentrated solution mass flow rate: important temperatures

temperature. Closing the dilute solution valve to increase the flow resistance mitigated this phenomenon and is seen in the first four experiments where the dilute solution valve position was manually adjusted. This indicated that the dilute solution valve can effectively control the performance of the desorber by controlling the approach temperature of the solution heat exchanger.

Figure 6.8 shows the variation of cooling capacity, desorber heat input rate, and system COP with the concentrated solution flow rate. It can be observed that the cooling capacity increased from 1.67 kW to 2.92 kW and the desorber heat input rate increased from 2.82 kW to 4.81 kW with an increased solution flow rate. This can be attributed to an increase in the heat transfer coefficient in the desorber leading to higher rate of refrigerant generation (shown in Figure 6.9). The heat transfer coefficient increases in a falling-film type boiling configuration with an increase in the liquid flow rate even though the liquid

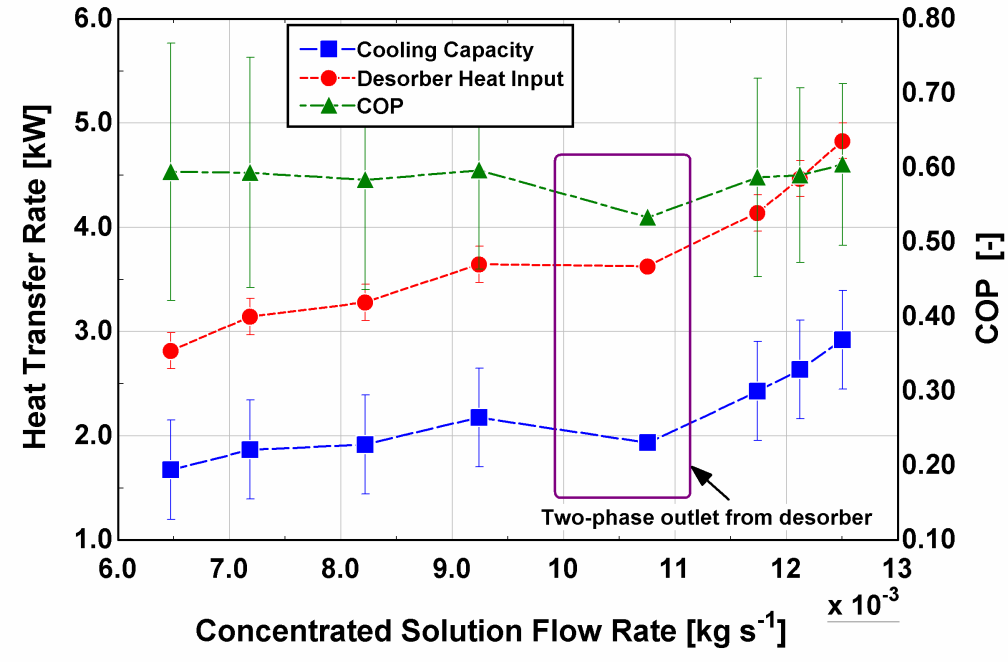

Figure 6.8: Effect of concentrated solution mass flow rate: heat transfer rates and COP

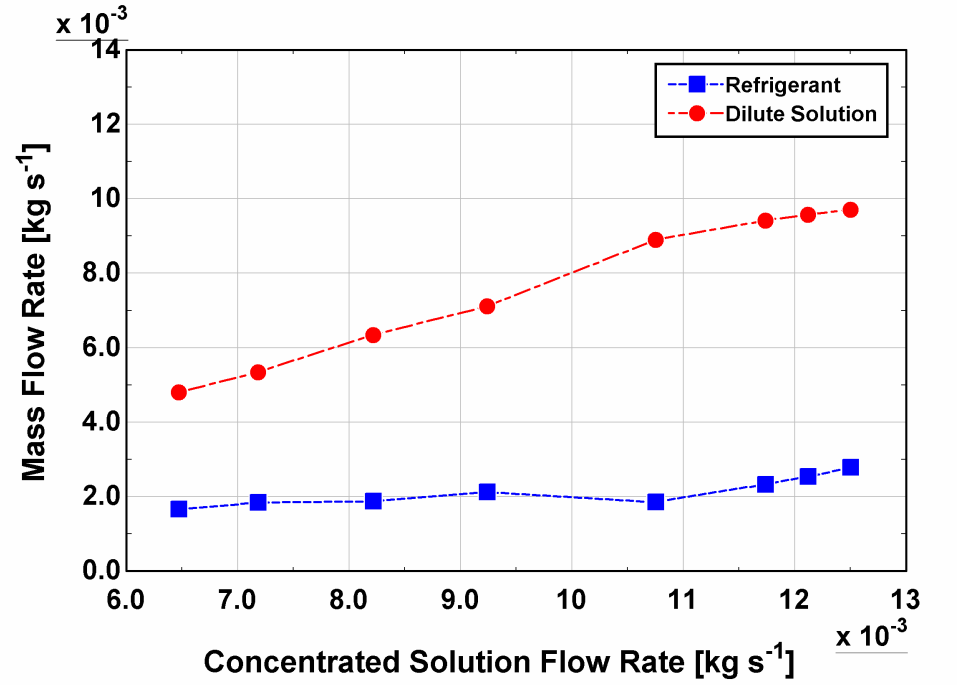

Figure 6.9: Effect of concentrated solution mass flow rate: refrigerant and dilute solution mass flow rates

film is expected to thicken and increase the heat transfer resistance. This is explained by a greater flow velocity and a consequent change in the flow regime and flow features at the liquid-vapor interface. An increase in the waviness at the interface can compensate for the increased thermal resistance due to a thicker film and promote higher heat transfer rates. Moreover, a greater liquid flow rate can allow larger wetted surface area in the desorber leading to an increase in the heat transfer rate. The increased refrigerant flow rate coupled with the decrease in the low-side pressure (536.4 kPa to 494.4 kPa) led to lower saturation temperature (6.21 – 4.41°C) in the evaporator, and consequently a higher cooling capacity. In general, the COP of the system remained constant at 0.59 – 0.60. The anomaly in this trend is highlighted in Figure 6.8 (shown in purple box). The cooling capacity and the COP decrease from the general increasing trend because of the outlet of the desorber becoming two-phase. The loss of refrigerant vapor led to a reduction in the refrigerant mass flow rate available for providing cooling in the evaporator. The desorber heat transfer rate continued

the increasing trend, leading to a decrease in system COP. This phenomenon also increased the low-side pressure to 577.7 kPa due to a higher concentration of ammonia in the dilute solution stream, and further degraded the performance of the evaporator.

6.3.2.4 Combined effects of concentrated solution flow rate and heat source inlet temperature

The experimental results from previous sections demonstrated that variations in the concentrated solution flow rate can cause significant changes in system performance. The second significant process variable is the heat source inlet temperature. These two parameters are also easily tunable in an actual system. This section presents results from experiments in which both these parameters were varied simultaneously. The desorber heat source inlet temperature was varied between 130 – 155°C. The solution flow rate was varied between 0.0114 – 0.013 kg s^{-1}. All other parameters, including the position of the dilute solution valve, were kept constant at their design values.

Figure 6.10 shows the variation in the heat transfer rates in the evaporator and the desorber, and the system COP. The solution flow rate and desorber heat source temperature were increased simultaneously and manually. It can be observed that higher source temperatures coupled with higher solution flow rate led to increase in the cooling capacity from 2.20 kW to 3.09 kW, and the desorber heat input rate increased from 3.51 kW to 5.36 kW. The increase in the desorber heat input rate was greater than the increase in the cooling capacity, leading to a slight decrease in the system COP from 0.63 to 0.58.

Figure 6.11 shows the variations in mass flow rates of the refrigerant, the dilute solution, and the concentrated solution. The cooling capacity of the system increased

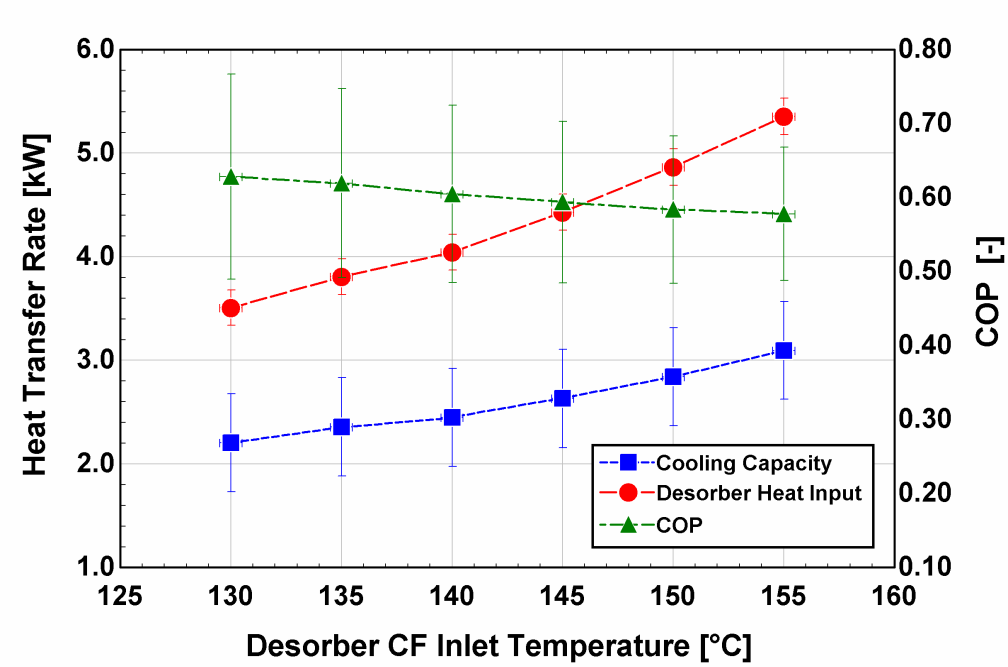

Figure 6.10: Effect of concentrated solution mass flow rate and heat source inlet temperature: heat transfer rates and COP

because of an increase in the refrigerant flow rate from 0.0021 kg s^{-1} to 0.003 kg s^{-1}. The dilute solution flow rate also increased slightly from 0.0093 kg s^{-1} to 0.0098 kg s^{-1}.

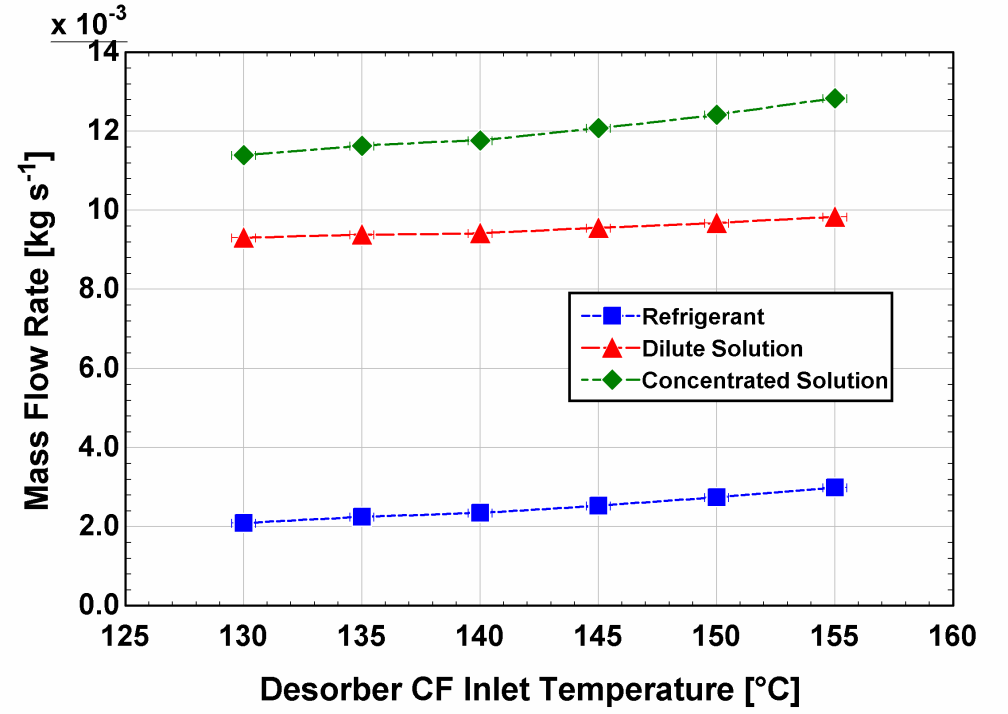

Figure 6.11: Effect of concentrated solution mass flow rate and heat source inlet temperature: mass flow rates

The key temperatures of the system are shown in Figure 6.12. The coolant return temperature was maintained at its setpoint of 13°C. It can be observed that higher source temperatures coupled with higher solution flow rate led to increase in the cooling capacity, and the coolant supply temeprature decreased from 9.71°C to 8.35°C. The glide control loop performed well to maintain the temperature glide at its setpoint of 2.5°C. Finally, due to increased solution flow rate at higher source inlet temperatures, the approach temperature in the solution heat exchanger was also maintained near the design value of 2.5°C, and varied between 2.19 – 2.58°C. The phenomenon of the vapor phase leaving through the dilute solution stream, observed in Section 6.3.2.1, was mitigated as the additional solution flow rate suppressed the rapid vapor generation at the bottom tray of the desorber.

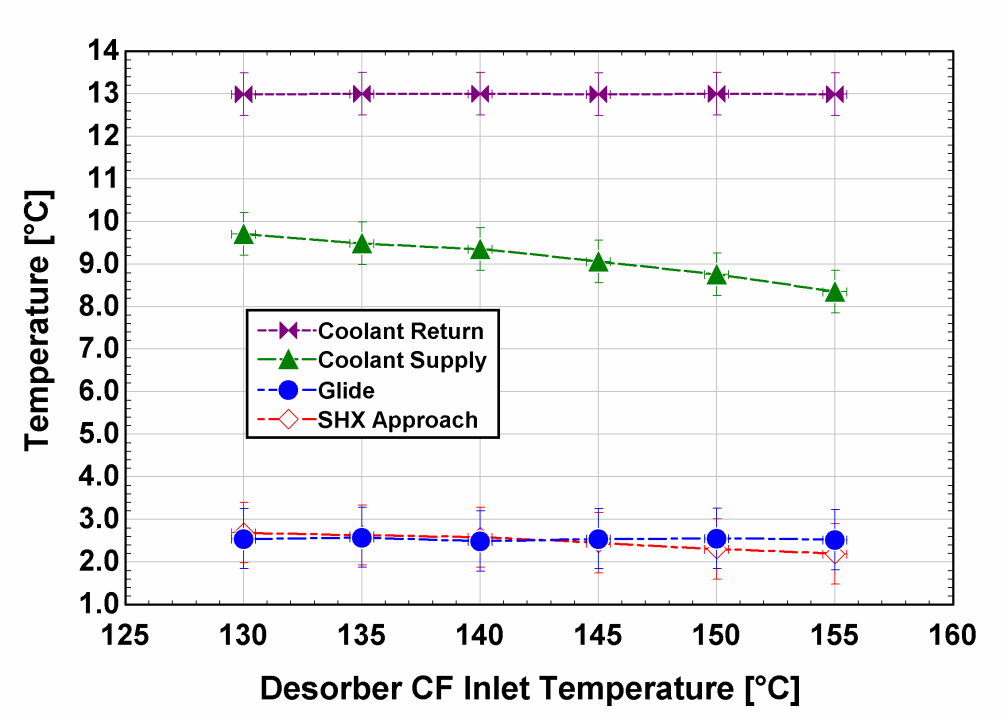

Figure 6.12: Effect of concentrated solution mass flow rate and heat source inlet temperature: important temperatures

Finally, Figure 6.13 shows the variation of ammonia mass fraction of the refrigerant, the dilute solution, and the concentrated solution streams. The right vertical axis shows the variation in the accumulated amount of the liquid refrigerant in the accumulator located downstream of the condenser. The refrigerant concentration decreased from 0.997 kg kg^{-1} to 0.994 kg kg^{-1} owing to hotter vapor at the exit of the desorber at higher source inlet temperatures. Due to hotter temperature of the dilute solution stream, its concentration also decreased from 0.321 kg kg^{-1} to 0.244 kg kg^{-1}. The steady increase in the refrigerant flow rate as the source temperature and the solution flow rate increased led to a steady increase in the amount of liquid refrigerant stored in the accumulator. As the amount of stored ammonia increased for a fixed amount of total charge, the ammonia mass fraction in the concentrated solution decreased from 0.444 kg kg^{-1} to 0.418 kg kg^{-1}. These changes in the ammonia mass fractions also led to a decrease in the low-side pressure from 505.5 kPa to

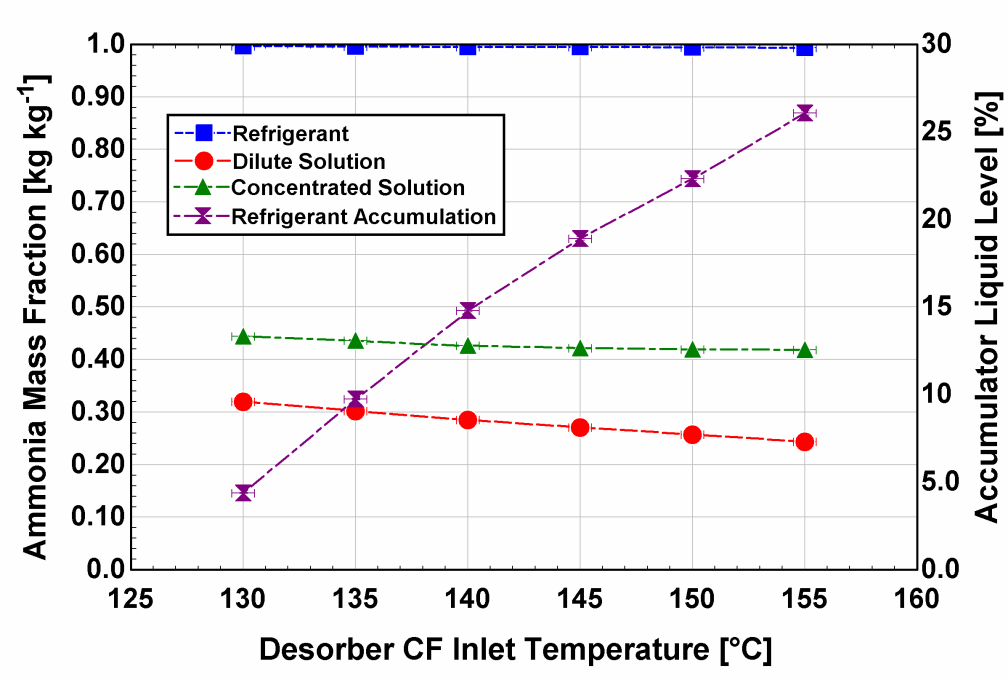

Figure 6.13: Effect of concentrated solution mass flow rate and heat source inlet temperature: ammonia mass fraction and refrigerant accumulation

488.5 kPa. This variation in the low-side pressure aided in increasing the cooling capacity of the system by decreasing the saturation temperature in the evaporator.

6.3.2.5 Effects of Cooling Water Temperature for Condenser and Absorber

Residential and mobile heat pumps frequently encounter variations in ambient temperatures during a day. As the absorber and the condenser reject heat to the ambient heat sink, their performance varies as the ambient temperature changes. An effective control system should compensate for such changes and ensure desired system performance. This section presents the results from studies involving variations in the cooling water temperature supplied to the absorber and the condenser while keeping other parameters in the system constant at their design conditions. The cooling water temperature was varied from 31°C to 43°C, representing a change in ambient temperature from 28°C and 40°C.

Figure 6.14 shows the variation of the cooling capacity, desorber heat input rate and the system COP due to the variation in cooling water temperature. As the cooling water temperature decreased, the absorber performance improved with the outlet solution at a lower temperature and greater ammonia mass fraction compared to the design value (0.45 kg kg^{-1} at 31°C to 0.40 kg kg^{-1} at 43°C). The desorber coupling fluid temperature remained constant and with a higher concentration of the inlet solution and lower solution temperature, the desorber heat transfer rate increased from 3.42 kW at 43°C to 5.53 kW at 31°C. The increased desorber heat input led to an increase in the refrigerant mass flow rate and consequently greater cooling capacity in the evaporator. The cooling capacity increased from 1.90 kW at 43°C to 3.38 kW at 31°C. The increase in the cooling capacity

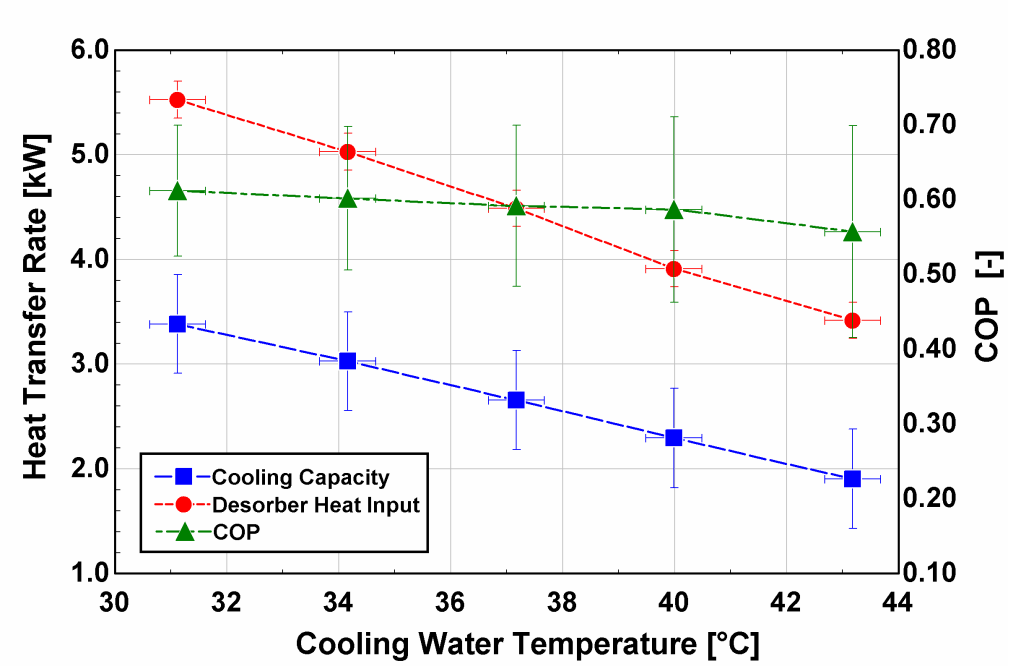

Figure 6.14: Effect of cooling water temperature: heat transfer rates and COP

was greater than the increase in the desorber heat input as the cooling water temperature decreased. This led to an increase in the system COP from 0.56 at 43°C to 0.62 at 31°C.

Figure 6.15 shows the variation in the mass flow rates of the refrigerant and dilute solution as the cooling water temperature changed. The refrigerant flow rate increased from 0.0018 kg s^{-1} at 43°C to 0.0032 kg s^{-1} at 31°C. As the concentrated solution flow was kept constant in these experiments at ~0.012 kg s^{-1}, the dilute solution flow rate decreased with a decrease in the cooling water temperature. The dilute solution flow rate varied from 0.010 kg s^{-1} at 43°C to 0.009 kg s^{-1} at 31°C.

Other important system parameters affected by the change in cooling water temperature are the two pressures. Figure 6.16 shows the variation in the high- and low-side pressures due to changes in the cooling water temperature. Both pressures increase with an increase in the cooling water temperature. The high-side pressure changed from

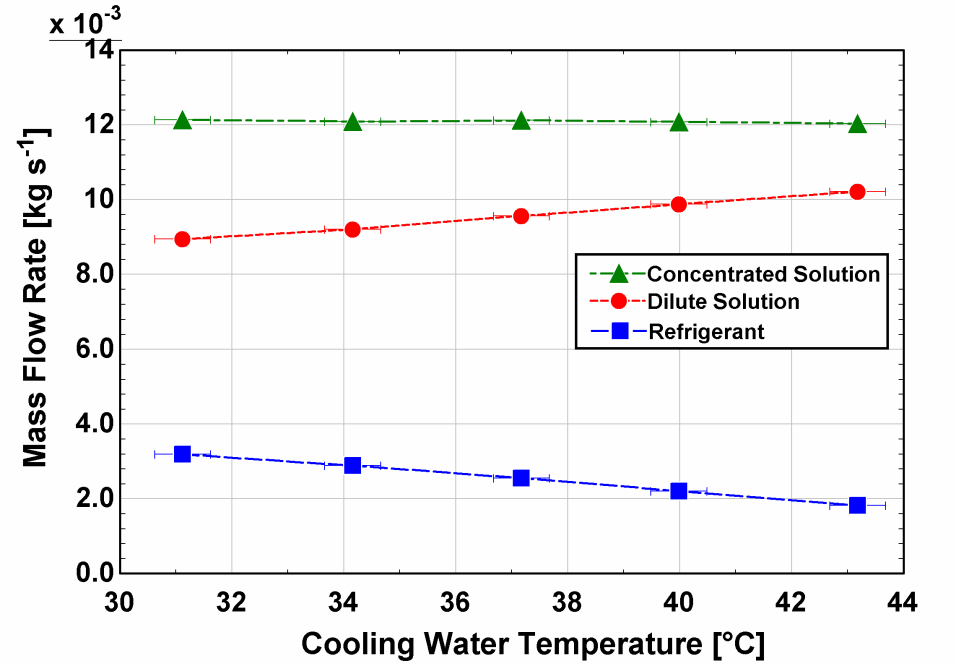

Figure 6.15: Effect of cooling water temperature: mass flow rates

1537 kPa at 31°C to 1921 kPa at 43°C. The high-side pressure is strongly influenced by the condensation temperature in the system. As the cooling water temperature increased, the condensation temperature also increased. At an approximately constant ammonia mass

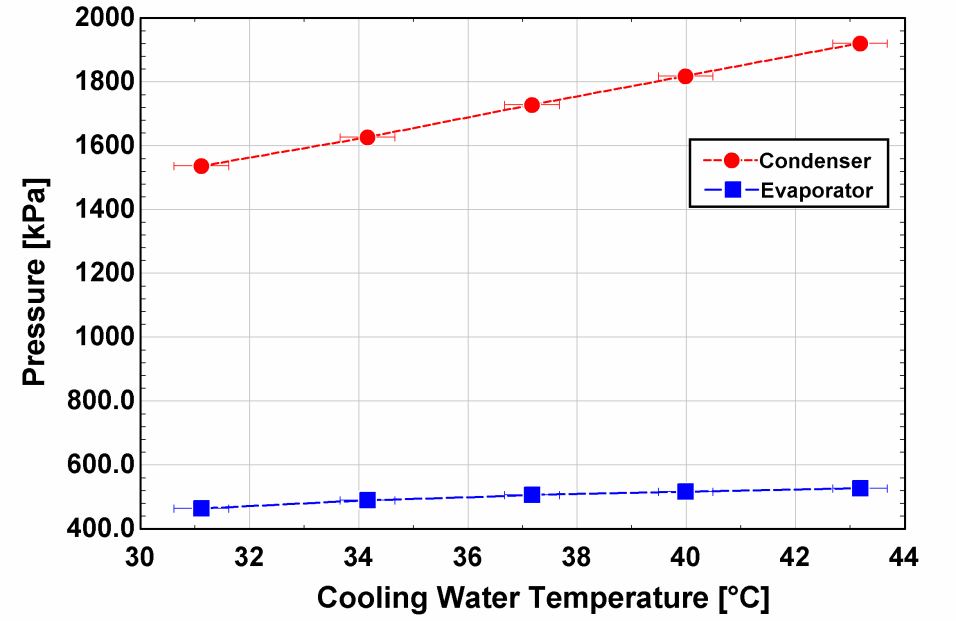

Figure 6.16: Effect of cooling water temperature: pressures

fraction of the refrigerant vapor, the increase in condensation temperature led to the significant increase in the high-side pressure. The low-side pressure changed from 464.8 kPa at 31°C to 526.6 kPa at 43°C. The increase in the low-side pressure is attributed to the change in absorber conditions of ammonia mass fraction and fluid temperature. The increase is, however, less pronounced as compared to the high-side pressure because the low-side pressure also depends on the evaporator heat source conditions which were unchanged.

Figure 6.17 shows the variation in the key temperatures of the system. Similar to other test cases, the coolant return temperature to the evaporator remained constant at 13°C. Due to the increase in the cooling capacity with a decrease in the cooling water temperature, the coolant supply temperature decreased from 10.17°C at 43°C cooling water to 7.80°C at 31°C cooling water. The glide temperature was maintained at its setpoint of 2.5°C. The approach temperature in the solution heat exchanger increased with an increase in the

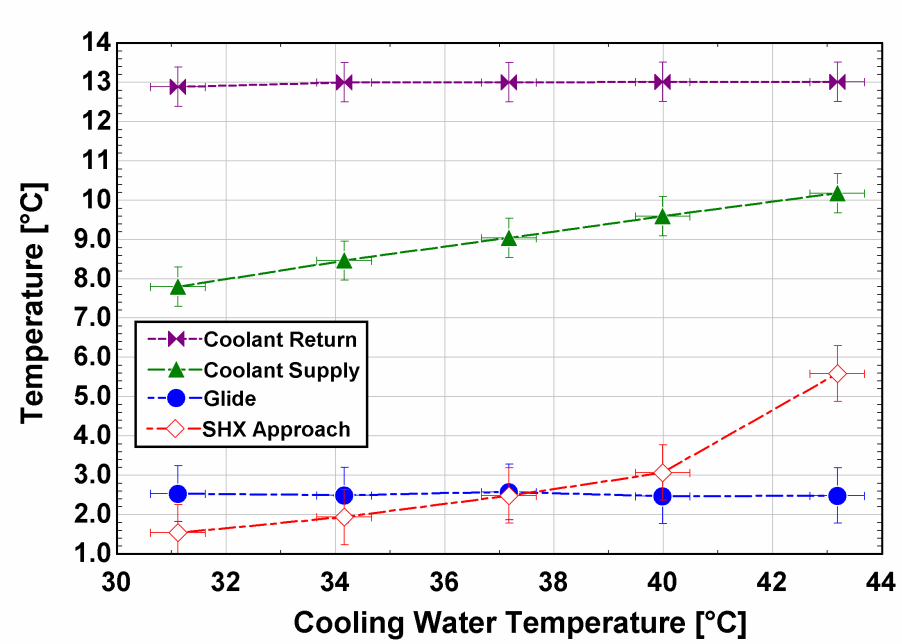

Figure 6.17: Effect of cooling water temperature: important temperatures

cooling temperature. However, visual inspection of outlet phase from the desorber did not indicate presence of two-phase mixture in the dilute solution stream. This increase in the approach temperature from 1.54°C to 5.59°C can be attributed to hotter inlet solution in the desorber at elevated cooling water temperatures. This would lead to a hotter dilute solution at the exit of the desorber, and consequently a hotter dilute solution temperature at the exit of the solution heat exchanger.

6.3.3 Transient Analysis of Perturbations

The perturbation studies were also utilized to study the transient response associated with changes in the input variables. Since the digital control systems are discrete-time, each control action can be assumed to be a step change in the manipulated variable. Therefore, the perturbation studies provide a first method to experimentally characterize different input variables and how the system responds to changes in their values. The objective is to identify the relative time constants and utilize that information in the subsequent design and tuning of control algorithms. The parameters studied in this section are: rapid change in the desorber source temperature, concentrated solution flow rate, and the cooling water temperature.

6.3.3.1 Heat Source Temperature Transience

Figure 6.18 shows the transient response of the system to a 5°C increase in the temperature at the inlet of the desorber coupling fluid. The change in the coupling fluid temperature occurred over 550 s starting at 200 s. The initial temperature was 145°C, while the final temperature was 150°C. As shown in the plot on the top, the coolant supply temperature did not vary significantly and remained at its original value before this change

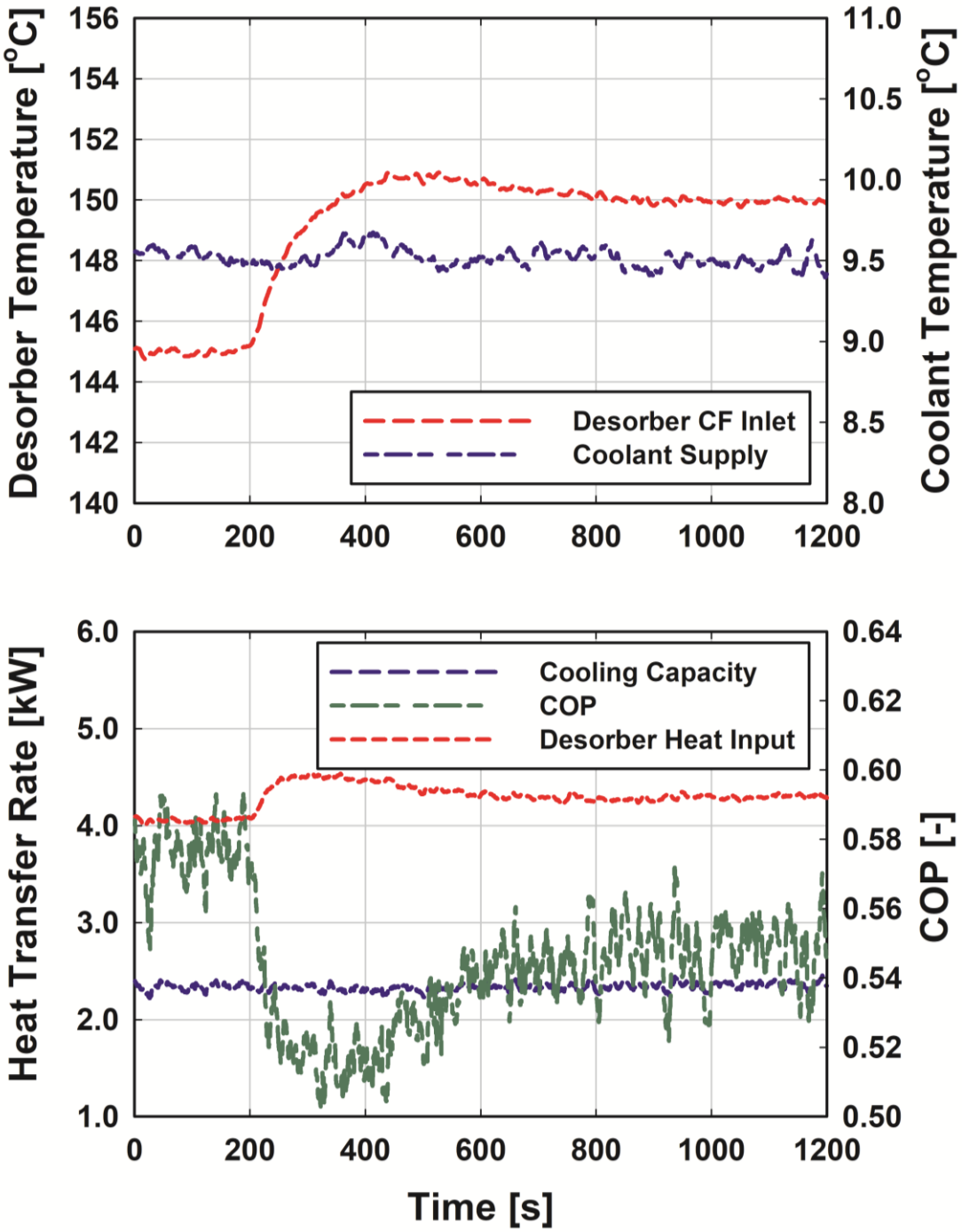

Figure 6.18: Transient response towards change in heat source temperature: temperatures (top) and system performance (bottom)

was introduced. A slight decrease of ~0.2°C was observed between the two steady states which is within the uncertainty of temperature measurements. The bottom plot shows the variation in the heat transfer rate. It can be observed that the desorber heat input rate

responded almost at the same rate as the coupling fluid temperature, and changed from 4.07 kW to 4.30 kW in approximately the same duration of 550 s. The evaporator heat transfer rate demonstrated a small increment and varied from 2.33 kW to 2.35 kW. As the change in the cooling capacity was less than the heat input rate, the COP of the system decreased from 0.58 to 0.55. The desorber heat transfer rate demonstrated a small amount of overshoot during the transient period. This is attributed to the increase in the driving temperature difference between the ammonia-water solution and the heat source temperature. The solution temperature increased at a slower rate due to the thermal inertia of the system to achieve the new steady-state. During this transient period, the desorber heat transfer rate increased rapidly to 4.5 kW before finally settling at the steady-state value of 4.3 kW. Due to this effect, the COP of the system decreased rapidly during the transient period demonstrating an undershoot to ~0.51, and finally achieved a steady-state value of 0.55. The system achieved the new steady state in ~550 s. Therefore, changes in the heat source temperatures have a) marginal impact on the cooling capacity (also shown in the previous section), and b) the response of the system is slow.

6.3.3.2 Concentrated Solution Flow Rate Transience

Figure 6.19 shows the effects of decreasing the solution mass flow rate from 0.0121 kg s^{-1} to 0.0114 kg s^{-1} over a duration of ~30 s. As the solution flow rate is decreased, the cooling capacity decreases (shown in the bottom plot) from 2.92 kW to 2.42 kW. This change occurred gradually over ~500 s. The cooling capacity decreased because of reduced refrigerant generation rate in the desorber. The desorber heat input rate decreased from 4.85 kW to 4.17 kW. Overall, the decrease in the desorber heat transfer rate was less compared to the decrease in the cooling capacity, leading to a decrease in the COP from

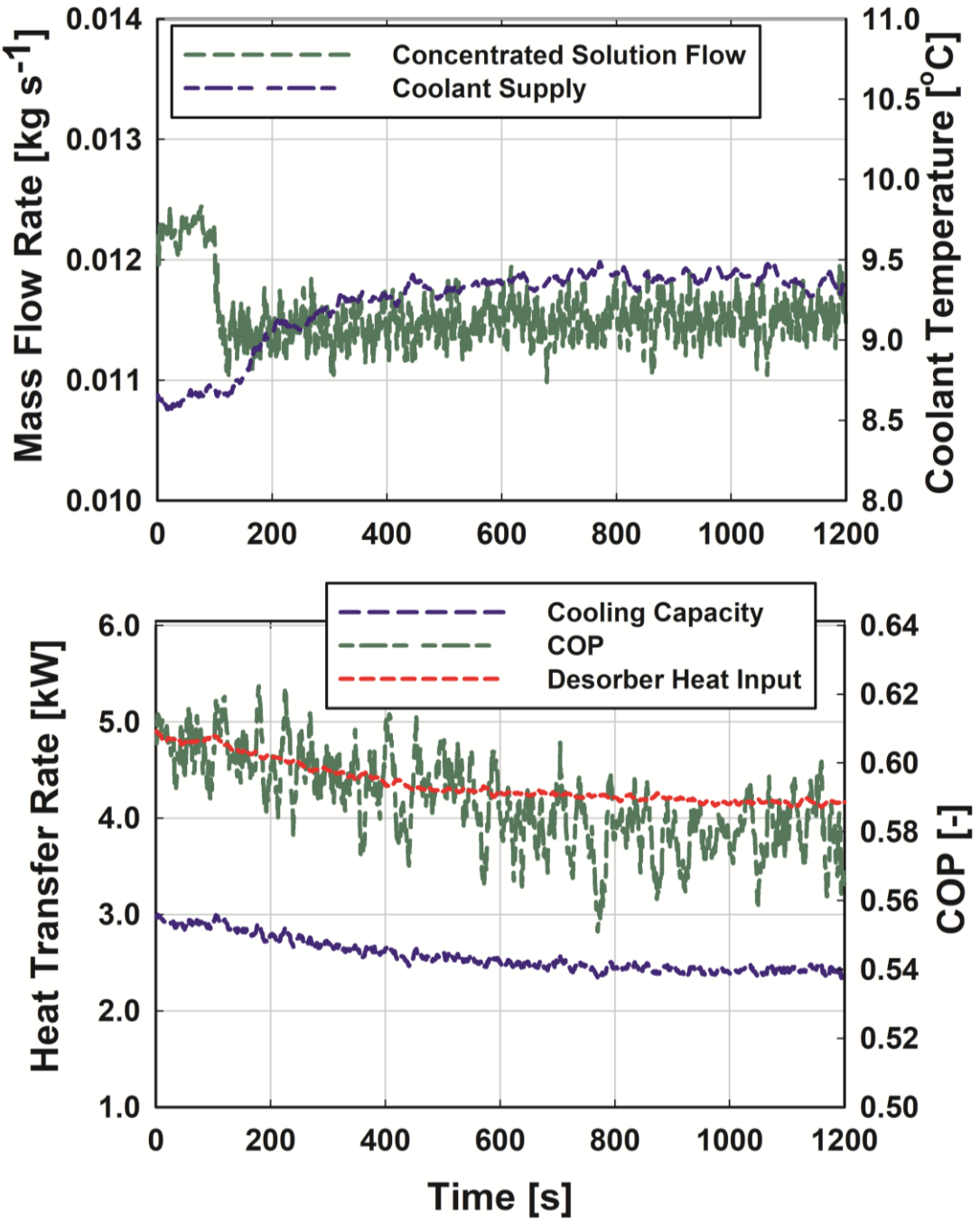

Figure 6.19: Transient response towards change in concentrated solution flow rate: coolant temperature (top) and system performance (bottom)

0.61 to 0.58. As a result of the decrease in the cooling capacity, the coolant supply temperature increased from 8.65°C to 9.35°C. This change occurred over a duration of ~500 s. Therefore, the effects of variations in the solution mass flow rate are slightly faster

than the effects of changes in the heat source temperature. In addition, as discussed in the previous sections, the effects of variation in the solution flow rate are significant on the overall system capacity. This information is useful in tuning the capacity control algorithm discussed in the following sections.

6.3.3.3 Cooling Water Temperature Transience

Figure 6.20 shows the effects of variation in the cooling water temperature on system performance. The cooling water temperature was reduced from 43°C to 34°C over a duration of ~900 s starting at t = 165 s. The bulk of this change occurred in the initial ~400 s and the cooling water temperature reduced to 35°C. The coolant supply temperature decreased from 10.15°C to 8.40°C at the final steady state. The coolant supply temperature decreased to ~8.5°C in the initial 650 s of the transience. Meanwhile, the cooling capacity increased from 1.90 kW to 3.03 kW at the final steady state at t = 1050 s. In the initial 650 s of the transient, the cooling capacity increased to 2.77 kW. The desorber heat input rate also increased during this transient, changing from 3.38 kW to 4.95 kW at the final steady state. Finally, the COP of the system increased from 0.55 to 0.60. The COP increased rapidly during the transient period as the evaporator heat transfer rate varied at a faster rate in comparison to the desorber heat input rate. Significant delay in system response was observed as the cooling water temperature varied.

The transient analysis of various perturbations indicates significant delay in the response of the system. This delay is typically a manifestation of energy accumulation in

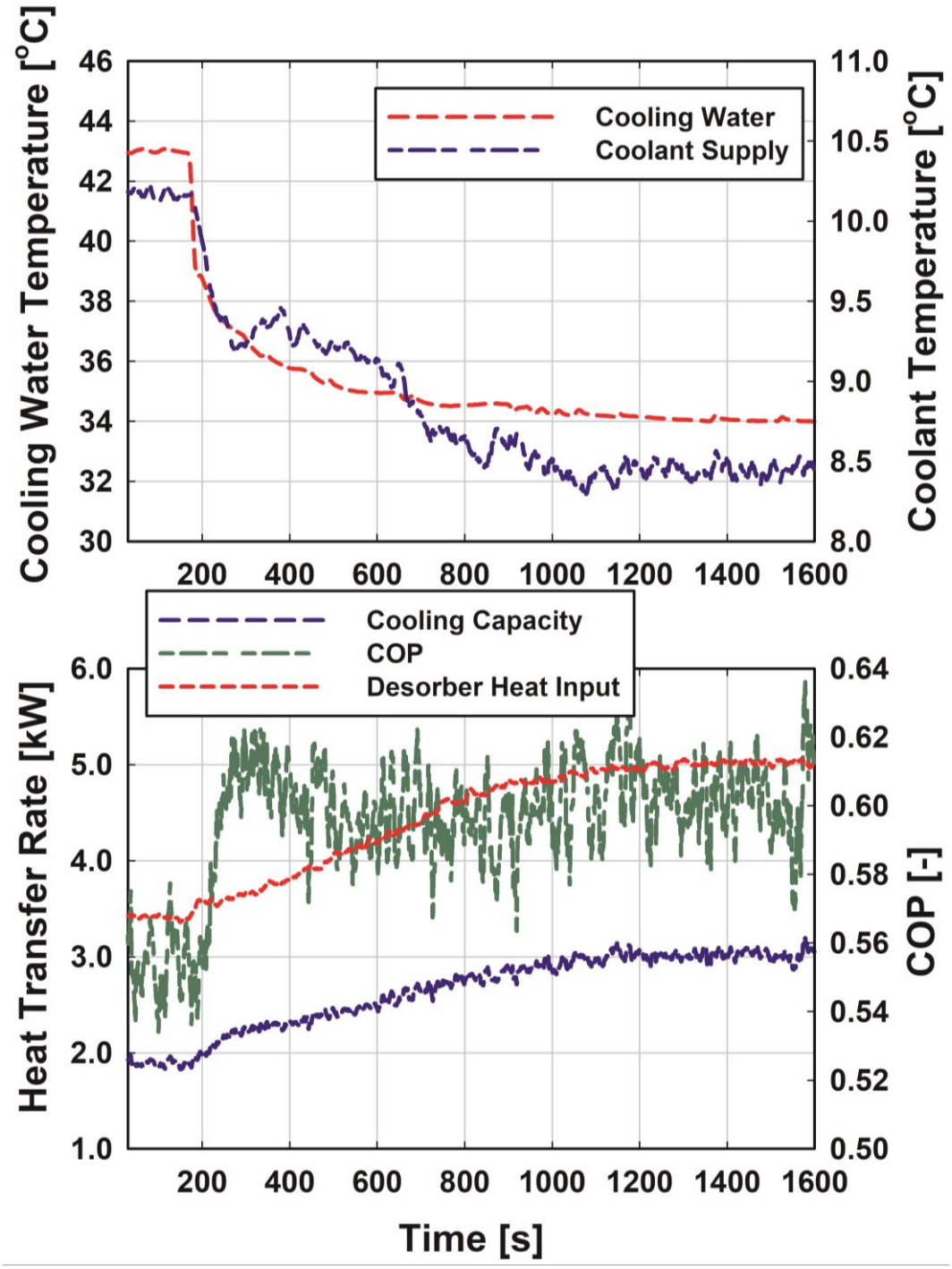

Figure 6.20: Transient response towards change in cooling water temperature: coolant temperature (top) and system performance (bottom)

different components of absorption systems. The thermal capacitance of additional heat and mass exchangers used in these systems in comparison to the vapor compression systems is a key contributor. In addition, some fraction of the delay in the response can be

attributed to the concentration adjustment that occurs in different fluid accumulators in the system. With the binary fluid mixture, the accumulation of one component of the working-fluid in a particular part of the system can take longer in comparison to accumulation of a pure component working-fluid.

6.3.4 Conclusions from Perturbation Studies

The perturbation studies indicated the relative impact of different inputs to the absorption system. It was observed that the system capacity was most significantly affected by changing the concentrated solution flow rate, followed by the change in desorber heat source conditions. The studies also highlighted the fact that a low-grade heat source could be utilized effectively by adjusting the concentrated solution flow rate. This can potentially enable the operation of ammonia-water absorption systems using a wider range of heat sources. A combination of the concentrated solution flow rate and heat source conditions could significantly change the system performance over wide range of cooling capacities.

The perturbation studies also indicated that the dilute solution valve position could be used to effectively control the outlet phase from the desorber. The refrigerant valve provided excellent control over the temperature glide in the evaporator. Therefore, the two valves could be used to optimize the performance of the desorber and the evaporator.

The transient response of the system to these perturbations indicated that the effects of temperature changes required significantly longer time to propagate through the system in comparison to the changes in the solution mass flow rate. This information, summarized in Table 6.3, will be used in the design of control algorithms and tuning of controller parameters and will be discussed in the following sections.

Table 6.3: Summary of perturbation studies for control system design

Parameter	Variation	Cooling Capacity (kW)	COP	Comments
Solution Flow Rate	0.0065 – 0.0125 kg s^{-1}	1.67 – 2.92	~0.6	Fast transient response with almost one-to-one effect on the flow rate and system outputs
Heat Source Temperature	130 – 155°C	2.21 – 2.38	0.63 – 0.53	Slow response due to thermal inertia effects
Heat Source Flow Rate	0.069 – 0.117 kg s^{-1}	2.64 – 2.68	0.58 – 0.60	Negligible change in system performance
Cooling Water Temperature	31 – 43°C	3.38 – 1.90	0.62 – 0.56	Significant impact on system performance with time delay due to thermal inertia

6.4 Control Algorithms

Feedback control algorithms are implemented on the breadboard system. These algorithms are implemented as pure feedback of the controlled variables and account for the dynamics identified in the perturbation studies. The control algorithms are divided into two categories. The first category is for performance control and monitors the key process variables that are indicative of the performance of the evaporator and the desorber. The second category is for capacity control involving a multivariable feedback approach to adjust the concentrated solution flow rate, desorber coupling fluid flow rate, and desorber coupling fluid inlet temperature in concert to regulate the system capacity. The following sections present the details of each feedback loop.

6.4.1 Performance Optimization of Evaporator and Desorber

Optimization of component performance is crucial for overall system operation. The importance of maintaining optimal evaporator temperature glide was discussed in Chapter 5. A large value of temperature glide would lead to underutilization of the available heat transfer area in the evaporator, and a low value of glide would suppress the heat transfer coefficient as the fluid will not demonstrate significant change in enthalpy along the length of the evaporator. Therefore, the refrigerant mass flow rate is utilized as a process variable in a feedback control loop to maintain the temperature glide at an optimal setpoint. Continuous variation in the refrigerant mass flow rate is achieved by adjusting the opening of the refrigerant valve that utilizes a stepper motor-controlled needle actuator to change the valve opening. Figure 6.21 shows the implementation of the glide control loop. The measured evaporator temperature glide is compared with its setpoint and the resulting difference is manipulated by a proportional-integral (PI) control law (Eq. 6.19) to actuate the refrigerant expansion valve. The term $e(t)$ represents the difference between the setpoint and the measured value of the controlled variable, and K_p and K_i are the proportional and

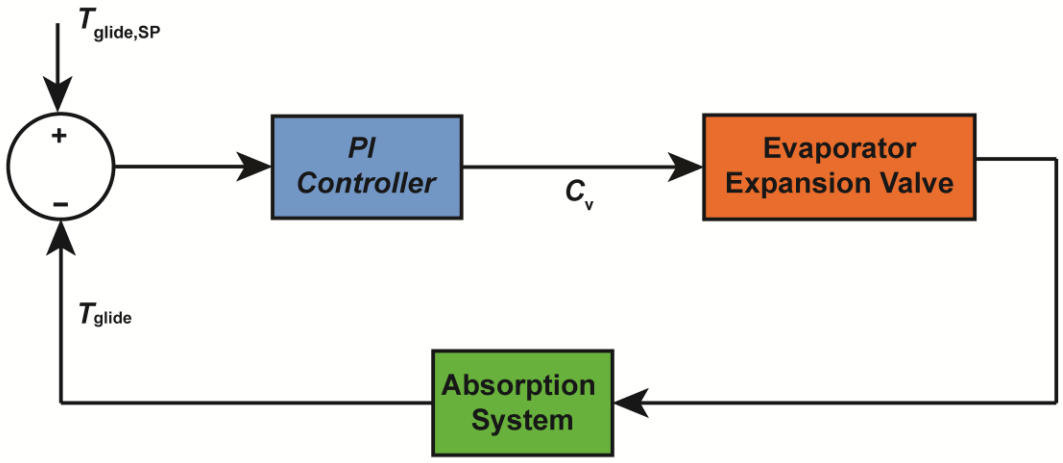

Figure 6.21: Implementation of glide control loop on the breadboard system

integral gains, respectively. The difference between the control loop presented here and the one discussed in Chapter 5 is that the experimental system utilized a PI feedback loop instead of a proportional-only feedback. This modification is required to dampen some of the effects of measurement noise and enhance the stability and accuracy of the control algorithm as the controlled variable achieves values near its setpoint.

$$\Delta C_v(t) = K_p e(t) + K_i \int_0^t e(t)dt \tag{6.19}$$

Similarly, the importance of controlling the outlet phase from the desorber was demonstrated in the perturbation studies discussed in the previous section. As shown there, at low solution flow rates or at high desorber source temperatures, the increased vapor generation rate in the bottom segment of the desorber can lead to some of the generated refrigerant vapor to exit via the dilute solution stream. This leads to decrease in the system efficiency, as a part of the generated refrigerant is directly absorbed in the dilute solution without providing any cooling. To mitigate this phenomenon at varying operating conditions and capacities of the system, the approach temperature in the solution heat exchanger, measured as the difference between the temperatures of the dilute solution stream outlet and the concentrated solution inlet, is controlled using the dilute solution flow rate as the process variable. This provides excellent control over the outlet phase of the desorber as shown in the case studies discussed in the following section. Figure 6.22 shows the implementation of the desorber phase control loop. The measured approach temperature in the solution heat exchanger is compared against its setpoint (typically ~2.5°C at baseline system operation), and the resulting difference is manipulated using a PI control law to actuate the dilute solution expansion valve.

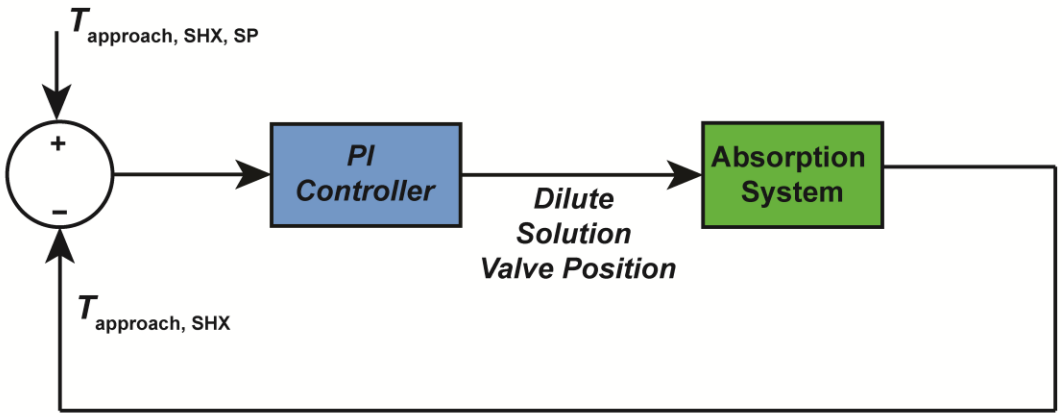

Figure 6.22: Desorber phase control loop

The parameters of both performance control loops are summarized in Table 6.4. The gains of the glide control loop are negative owing to the inverse relationship between the refrigerant valve opening and the evaporator temperature glide. On the other hand, the gains on the desorber control loop are positive as the solution heat exchanger approach temperature decreases with a decrease in dilute solution flow, and vice versa. Another feature of the control loops is the sample time. As discussed in Chapter 5, to account for the thermal capacitance of the system and transport delay, the control actions are not implemented continuously at the same sampling rate as the data acquisition. Both the performance control loops actuate the valves every 9 seconds to allow for the effects of the changes to propagate through the system. The values of controller gains and sampling times were obtained through an iterative approach during the experimentation. Lastly, limits on actuator positions are implemented to prevent the valves from opening or closing completely. Both valves were mostly operated in their linear range of operation where the

Table 6.4: Parameters of performance control loops

Control Loop	Proportional gain (K_p)	Integral gain (K_i)	Sample Time (s)	Actuator Limits
Glide Control	-2.8	-0.025 s	9	5 – 55%
Desorber Phase Control	2.5	0.03 s	9	45 – 75%

valve coefficient varied linearly with the percentage of valve position. This information was provided by the manufacturer. The lower and upper limits on valve position also prevented the valves from being completely open or close; both situations can be potentially catastrophic for system operation.

6.4.2 Capacity Control

The perturbation studies indicated that the cooling capacity of the system is a strong function of the solution flow rate and a relatively weaker function of the desorber heat source temperature and flow rate. The capacity control loop utilized these relationships in the form a multivariable feedback control loop as shown in Figure 6.23. The setpoint of the supplied coolant temperature is compared with the measured value from the system and is manipulated using three PI control laws to actuate the solution pump, desorber coupling fluid inlet temperature and the desorber coupling fluid pump. This single-input multiple-output approach (SIMO) combines the three key variables for regulation of the system capacity. The controller gains and sampling times (shown in Table 6.5) consider the relative effect of each manipulated variable on the system capacity and the transport lag

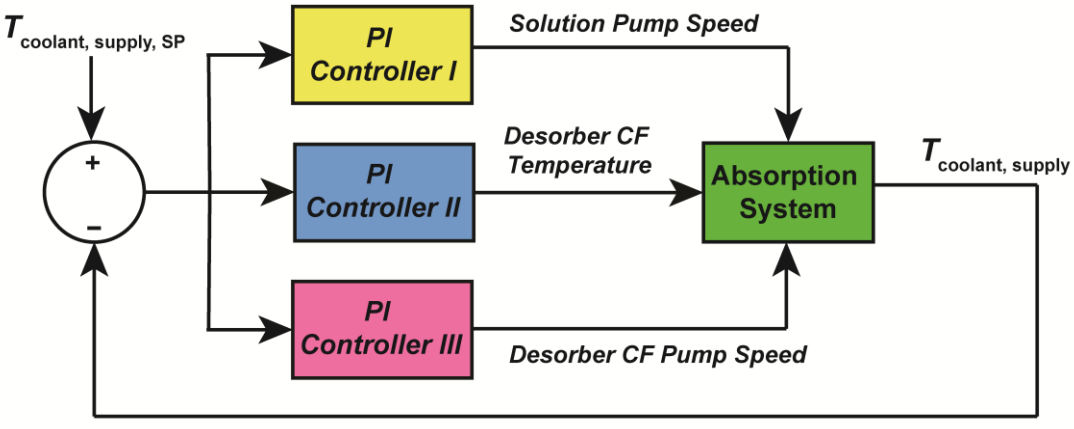

Figure 6.23: Capacity control loop

Table 6.5: Parameters of capacity control loop

Control Loop	Proportional gain (K_p)	Integral gain (K_i)	Sample Time (s)	Actuator Limits
Solution Pump Speed	-3	-0.04 s	6	25 – 45%
Desorber CF Pump Speed	-2	-0.025 s	6	6 – 18%
Desorber CF Inlet Temperature	-5	-0.1 s	12	CF Heater 0 – 80%

associated with each effect. The perturbation studies demonstrated that the effects of changes in mass flow rates propagate through the system faster than the effects of changes in temperatures. Therefore, the sampling time of the solution pump and desorber coupling fluid pump control are shorter than the sampling time for the desorber coupling fluid inlet temperature control. Finally, all the actuators demonstrate an inverse relationship with the controlled variable, which is reflected in the negative value of the controller gains. For instance, an increase in the solution flow rate or the desorber coupling fluid temperature or mass flow rate leads to an increase in the cooling capacity, and therefore, a decrease in the temperature of the supplied coolant. The minimum limits on pump speeds were based on the minimum flow rate required for system activation. Positive displacement pumps were utilized for the flow of concentrated solution and Paratherm™ oil for the desorber. The positive displacement pumps allowed accurate prediction of flow rate as a linear function of the pump speed. The maximum speed limit for the concentrated solution pump was determined based on flooding limits to prevent the liquid to flow out of the vapor outlet port of the desorber. The maximum speed limit on the Paratherm™ oil pump was set to ensure that the vapor outlet temperature from the desorber would not increase leading to a decrease in the refrigerant ammonia concentration. The limits on the electric heaters were placed to prevent their operation at 100% capacity in case any hot spots develop, leading to potential permanent damage to the heater.

6.5 Controller Performance

The performance of the control loops presented above was evaluated using the experimental setup. The control experiments performed included:

- Step-change in the setpoint of **evaporator temperature glide**
- **Part-load operation** scenario where the user demand for cooling capacity decreases to 75% and 50% of design cooling capacity with constant coolant return temperature at design conditions of 13°C. This leads to changes in the supplied coolant temperature set-point and the controller performance is evaluated in this set-point tracking experiment.
- **Part-load operation** with cooling load decreasing to 75% and 50% of the design cooling load leading to variation in the coolant return temperature. The performance of the control system is evaluated in maintaining the supplied coolant temperature at its set-point of 9°C.
- Finally, a change in the cooling water temperature supplied to the absorber and the condenser is introduced because of **change in ambient temperature**. The temperature of the cooling water is reduced to 34°C and 31°C in comparison to the design condition of 37°C. Once again, the response of the controller in maintaining the temperature of the supplied coolant at its design condition of 9°C is evaluated.

6.5.1 Glide Control

The importance of controlling the evaporator temperature glide via the refrigerant expansion valve was discussed in Chapter 5. In the experimental results presented here, the performance of the glide control loop in achieving the desired set-point is evaluated. Figure

6.24 shows the response of the system when the setpoint of the temperature glide is changed in a step fashion from 2.5°C to 1°C. In response to this command, the controller actuated the refrigerant valve to open from 39.4% to ~40% to allow more refrigerant flow and

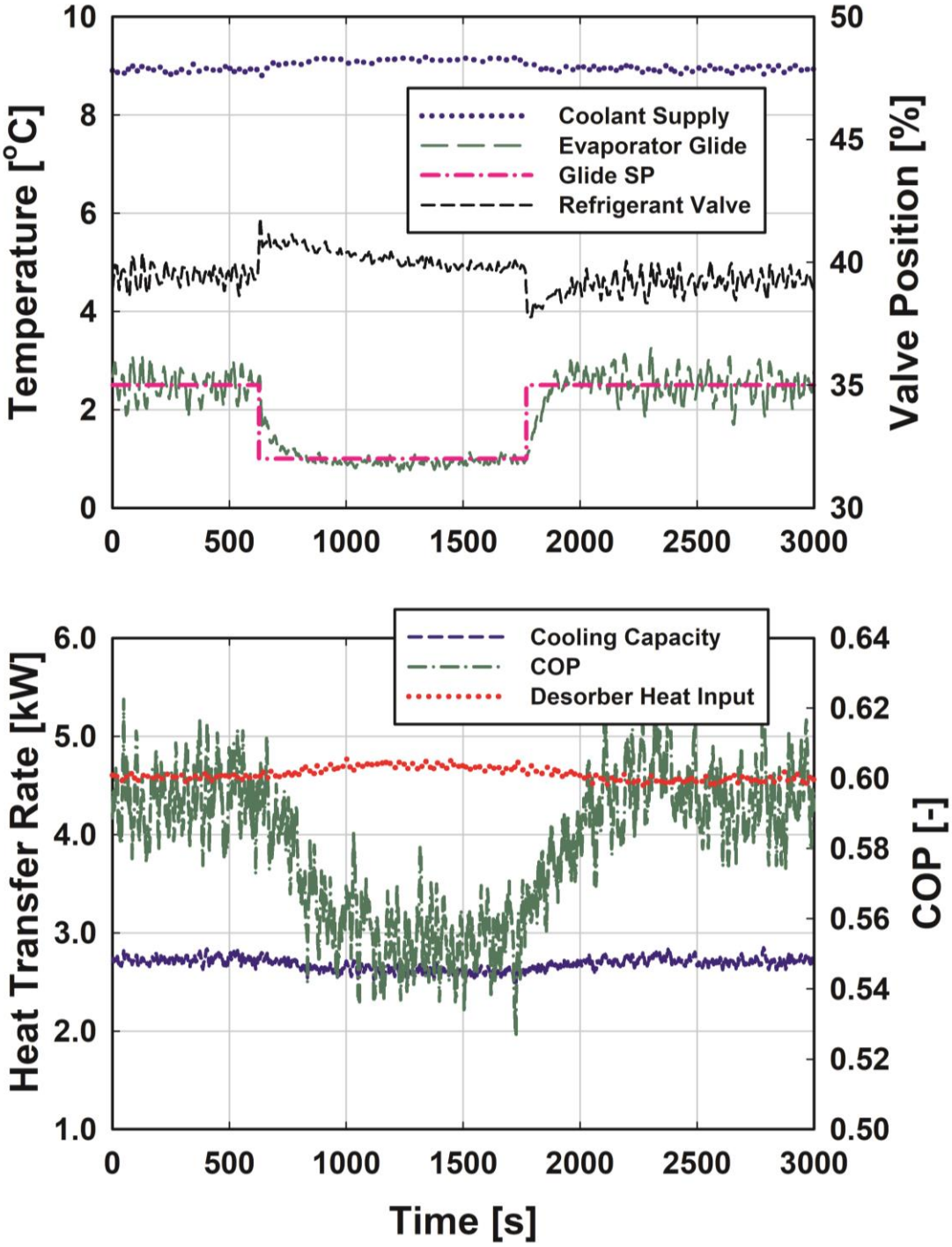

Figure 6.24: Glide control: response to change in setpoint and corresponding valve position (top) and system performance (bottom)

reduce the temperature glide. This translated to opening the valve by 3 stepper motor steps. The step-change is made at t = 627 s. The PI controller demonstrated fast and stable response towards the new steady-state conditions. The system achieved the new set-point value of the temperature glide in ~180 s. The plot on the bottom shows the variation in the heat transfer rates and the system COP. Due to reduced temperature glide, the cooling capacity decreased from 2.72 kW to 2.59 kW. The decrease in the capacity is attributed to insufficient evaporation in the evaporator at a greater mass flow rate, and higher pressure on the low-side that decreased the driving temperature difference between the refrigerant and the coupling fluid. This also led to an increase in the temperature of the supplied coolant from 8.90°C to 9.15°C. Due to an increase in the refrigerant mass flow rate, the ammonia-mass fraction of the concentrated solution increased and led to a higher heat transfer rate in the desorber. The desorber heat input rate increased from 4.57 kW to 4.70 kW. This increase in the desorber heat transfer rate and the decrease in the cooling capacity led to a decrease in the COP from 0.60 to 0.55. When the setpoint of the temperature glide was restored to its original value of 2.5°C, identical trends of response time, valve position, and system performance were observed.

Figure 6.25 shows the variations in the refrigerant flow rate and the evaporator pressure due to a step-change in the glide. Due to lower temperature glide, a greater mass flow rate of the refrigerant was required. The refrigerant flow rate increased from 0.0026 kg s^{-1} to 0.0027 kg s^{-1}. The increased refrigerant flow from the evaporator to the absorber, with all other inputs remaining unchanged, led to an increase in the low-side pressure from 516 kPa to 547 kPa. Both variables, the refrigerant mass flow rate and the evaporator

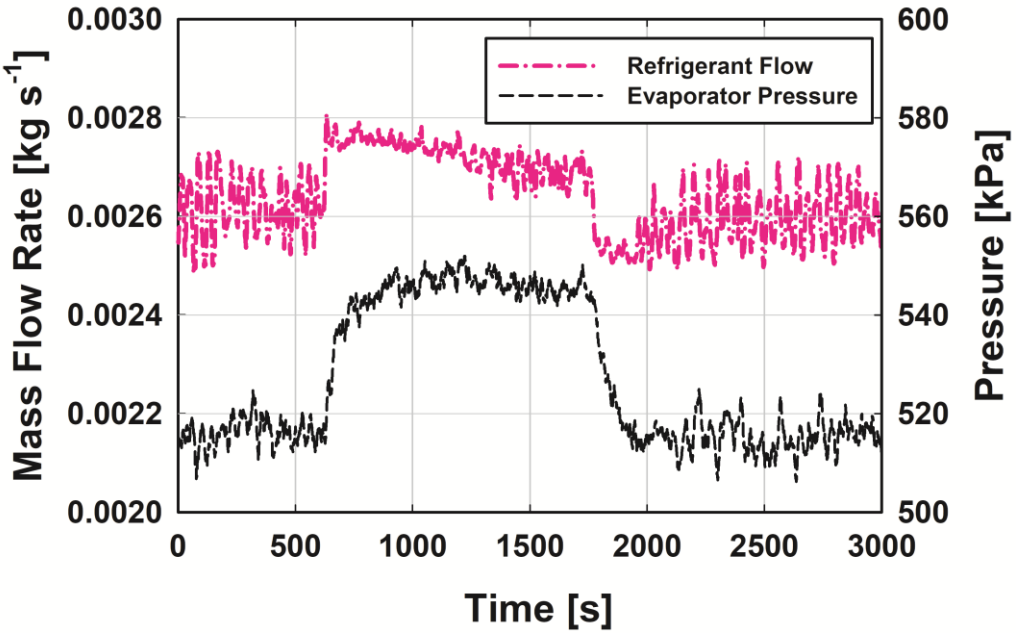

Figure 6.25: Glide control: refrigerant mass flow rate and evaporator pressure

pressure, returned to their original steady-state values after the setpoint of the temperature glide was restored to 2.5°C.

6.5.2 Part-load Operation

6.5.2.1 Reduced User Demand

The first case study on part-load operation involved a reduction in the cooling capacity demanded by the user and is manifested by a change in the supplied coolant temperature from the system. This study would represent a change in the cooling temperature and cooling demand directed by the user. The return temperature of the coolant to the evaporator from the conditioned space remained constant at 13°C. The design temperature differential between the coolant return and supply is 4°C at a mass flow rate of 0.16 kg s^{-1} (cooling capacity of ~2.7 kW). The set-point of the supplied coolant temperature was changed in a step fashion and the temperature of the supplied coolant is

measured in experiments. The inlet temperature of the cooling water to the absorber and the condenser remained constant at 37°C (representative of outdoor air temperature of 34°C) for this case.

The resulting temperature profiles of the coolant temperatures, and heat transfer rates and COP are shown in Figure 6.26 (a) and (b), respectively. The temperature profiles show the step change of 1°C in the coolant supply temperature demanded by the user. The coolant return temperature remained approximately constant at 13°C. The measured temperature of the supplied coolant shows quick response to a step change (at t =405 s) in the demand to 75% of the design capacity. As observed in Figure 6.26 (a), the system achieved new steady state (defined as within ±0.25°C of the set-point) in ~225 s (at t = 630 s). The response time for the demand change from 75% to 50% (at t = 2571 s) of the system capacity was ~450 s. The longer response time can be attributed to the reduced heat transfer rates taking place through approximately the same thermal capacitance of the system, leading to longer time to achieve the new steady state. It can be hypothesised that at further reduced capacities, the system response will be much slower. The system capacity is then restored to design capacity in two similar step changes from 50% to 75% (at t = 5319 s) and 75% to 100% (at t = 7473 s). The temperature responses are fast considering the large thermal capacitance of absorption systems, and stable. The system response was recorded for 10000 s with each new steady-state recorded for over 2000 s.

Figure 6.26 (b), shows the variation in the heat transfer rates in the desorber and the evaporator. As the key changes in the system during capacity control occur in the solution flow rate and desorber heat source conditions to actively adjust the refrigerant generation rate, the initial change in the desorber heat transfer rate was steeper than in the evaporator.

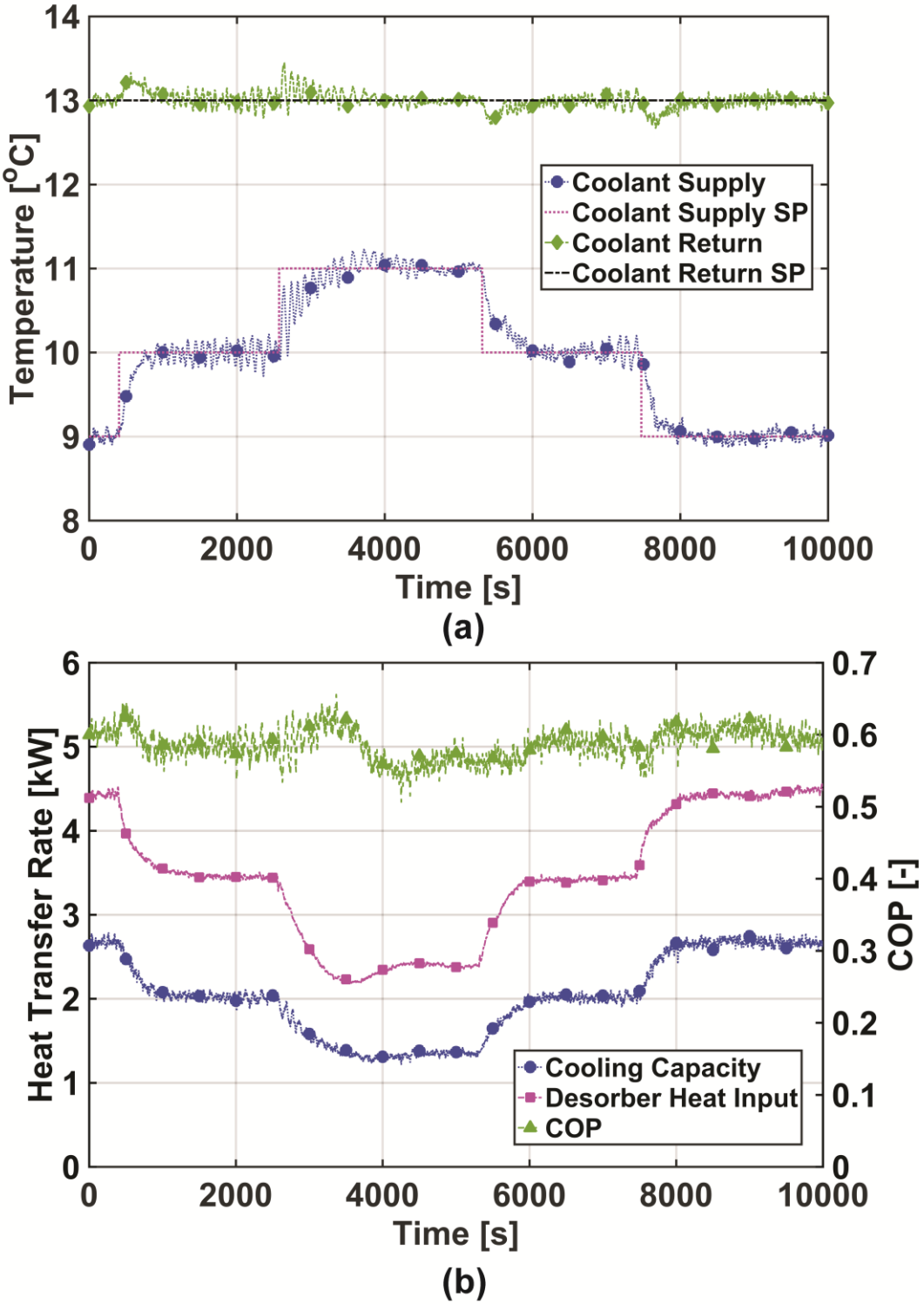

Figure 6.26: Coolant temperatures (a) and system performance (b) at part-load operation demanded by the user

However, due to a greater thermal capacitance, the approach to steady-state is much gentler for the desorber. At the design capacity, the desorber heat transfer rate was 4.42 kW and during the 25% reduction in system capacity, it decreased to 3.45 kW in ~700 s. The cooling capacity decreased from 2.7 kW to 2.0 kW in approximately the same time duration. Similarly, at 50% capacity, the desorber heat transfer rate decreased from 3.45 kW to 2.40 kW, and the cooling capacity decreased to 1.35 kW.

The variation in the COP of the system is also shown. The design COP is ~0.6. Due to the rapid rate of variation of desorber heat transfer rate in comparison to the evaporator, the COP increased during the transient period to ~0.63, but finally achieved a slightly lower value of ~0.58 at the new steady state of 75% system capacity. This slight reduction in the COP of the system can be attributed to the fact that the overall heat transfer conductance decreases for different components at lower flow rates. At the operating conditions investigated here, the percentage decrease in the evaporator performance is greater than the decrease in the desorber and leads to the observed trend in the system COP. Similarly, at 50% capacity, the COP decreased to 0.56. Similar trends are observed during the phases when the coolant supply temperature is restored to the design condition via step changes in the setpoint.

Figure 6.27 shows the response of the actuators as the capacity demanded from the system is varied. The pump speeds for the concentrated solution and desorber coupling fluid are shown on the left vertical axis, and the desorber coupling fluid inlet temperature is shown on the right vertical axis. As discussed in the previous section, the solution pump and the desorber coupling fluid pumps respond faster to capacity control as compared to the desorber coupling fluid inlet temperature. At 75% capacity, the solution pump speed

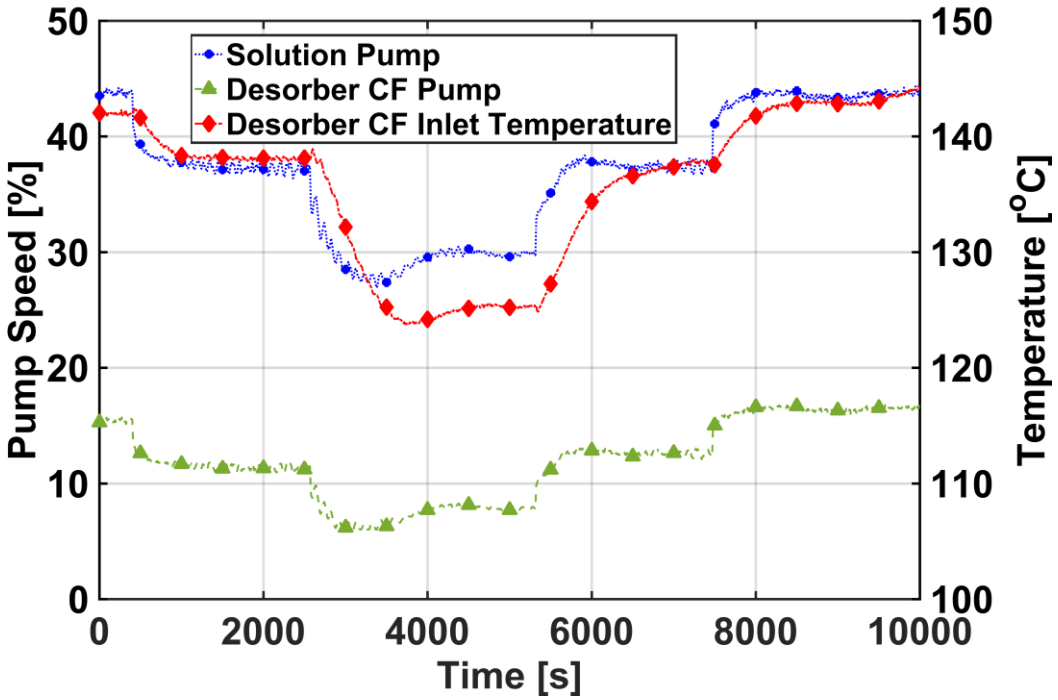

Figure 6.27: Capacity control loop actuators at part-load operation demanded by the user

decreased from 43.75% at design performance to 37.25% in ~ 600 s, while the desorber coupling fluid pump speed decreased from 15.5% to 11.25% in approximately the same duration. Meanwhile, the desorber coupling fluid inlet temperature decreased from ~142°C to ~138°C in ~800 s. At 50% capacity, the solution pump speed further decreased to 30% in ~1500 s, while the desorber coupling fluid pump speed decreased to ~8% in approximately the same duration. Meanwhile, the desorber coupling fluid inlet temperature decreased to ~125°C in approximately the same duration. Slight undershoot was observed at 50% capacity indicating possibilities of fine-tuning the controller.

Figure 6.28 (a) and (b) show the variation of evaporator temperature glide and the SHX approach temperature, and the valve positions, respectively. As the capacity is reduced, the glide temperature decreased due to the reduced heat transfer rate in the evaporator. The refrigerant valve then closed to reduce the refrigerant mass flow rate and

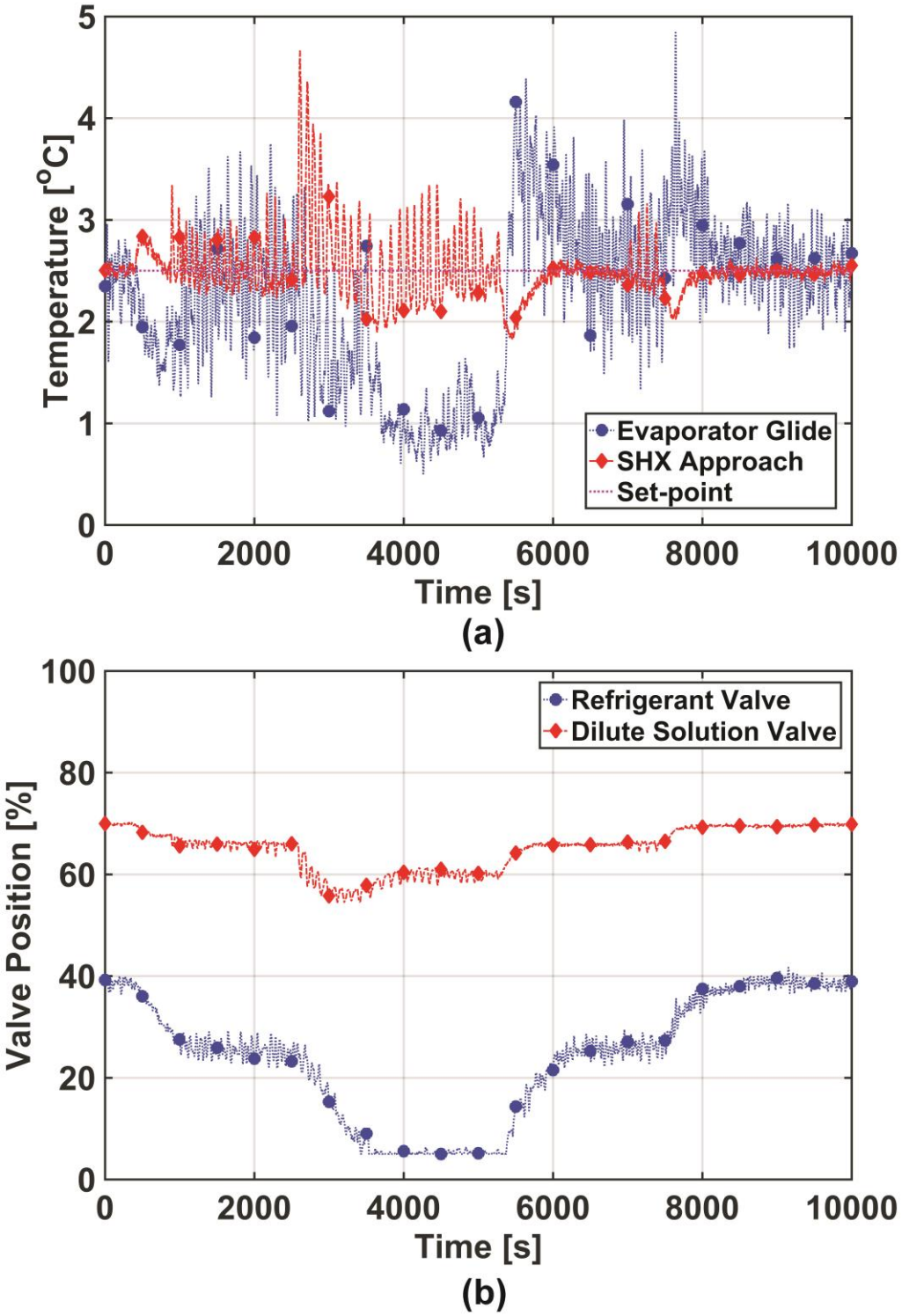

Figure 6.28: Evaporator glide and SHX approach temperatures (a) and valve positions (b) at part-load operation demanded by the user

restore the glide temperature at its set-point of 2.5°C. At 50% system capacity, the refrigerant valve cannot close enough to achieve the setpoint of temperature glide. This is observed in Figure 6.28 (b) as the valve remained at its lowest allowable setting of 5% opening. This is attributed to the valve being oversized for a 1.3 kW cooling capacity system. The manufacturer rating for the refrigerant expansion valve is for 1.75 – 3.5 kW cooling capacity systems. The desorber phase control loop responded well to the transience in system capacity as shown in Figure 6.28 (a). In response to a step decrease in the system capacity, the concentrated solution flow rate decreases and therefore, in the initial phase the dilute solution temperature leaving the desorber increases and the approach temperature in the SHX increases. In response, the dilute solution valve opening decreased (Figure 6.28 (b)) and the approach temperature achieved the setpoint value of 2.5°C. Overall, the response of the valves is stable and does not demonstrate hysteresis and hunting.

6.5.2.2 Reduced Cooling Load

The second case study on part-load operation involved a reduction in the cooling capacity implemented by reducing the cooling load and is manifested by a change in the temperature of the coolant return to the evaporator. This case study would be representative of a scenario such as the conditioned space cooling load changes due to reduced occupancy. The objective of the control algorithm is to maintain the temperature of the supplied coolant to the conditioned space at 9°C. The temperature of the return stream of the coolant to the evaporator was manipulated using the auxiliary heating loop on the evaporator. The inlet temperature of the cooling water to the absorber and the condenser remained constant at 37°C (representative of outdoor air temperature of 34°C) for this case as well. The resulting temperature profiles of the coolant temperatures, and heat transfer rates and COP are shown

in Figure 6.29 (a) and (b), respectively. As shown in Figure 6.29 (a), a change from 13°C to 12°C occurred in ~60 s (starting at t = 475 s). Due to this change in the coolant temperature entering the evaporator, the supply temperature dropped initially to ~8°C in the same duration and triggered the control action. With the control actions leading to a reduced cooling capacity, the supplied coolant temperature is restored to 9°C in ~250 s. This change amounts to a 25% decrease in the system capacity. The return temperature is further decreased by 1°C to 11°C in ~ 60 s (starting at t = 2750 s). As observed previously, the effect of this disturbance caused the temperature of the supplied coolant to decrease initially to ~8°C. The capacity control algorithm restored the supplied coolant temperature to its setpoint of 9°C in ~450 s. The system capacity decreased to 50% of its design capacity. The longer response time can be attributed to the increasing effects of the thermal capacitance of the system at decreasing heat transfer rates, similar to the previous case study. Similar trends were observed in coolant temperatures as the coolant return temperature was restored to its design value of 13°C in two instances of temperature variations at t = 5920 s to 12°C, and at t = 7780 s to 13°C. The temperature responses are fast and stable. Similar to the previous case, the system response was recorded for 10000 s with each new steady-state recorded for over 2000 s.

Figure 6.29 (b), shows the variation in the heat transfer rates in the desorber and the evaporator. As the coolant return temperature decreases, the heat transfer rate in the evaporator needs to be reduced to maintain the coolant supply temperature at its design condition. During the first variation of 25%, the desorber heat transfer rate changed from 4.40 kW to 3.40 kW, and the evaporator heat transfer rate changed from 2.70 kW to 2.0

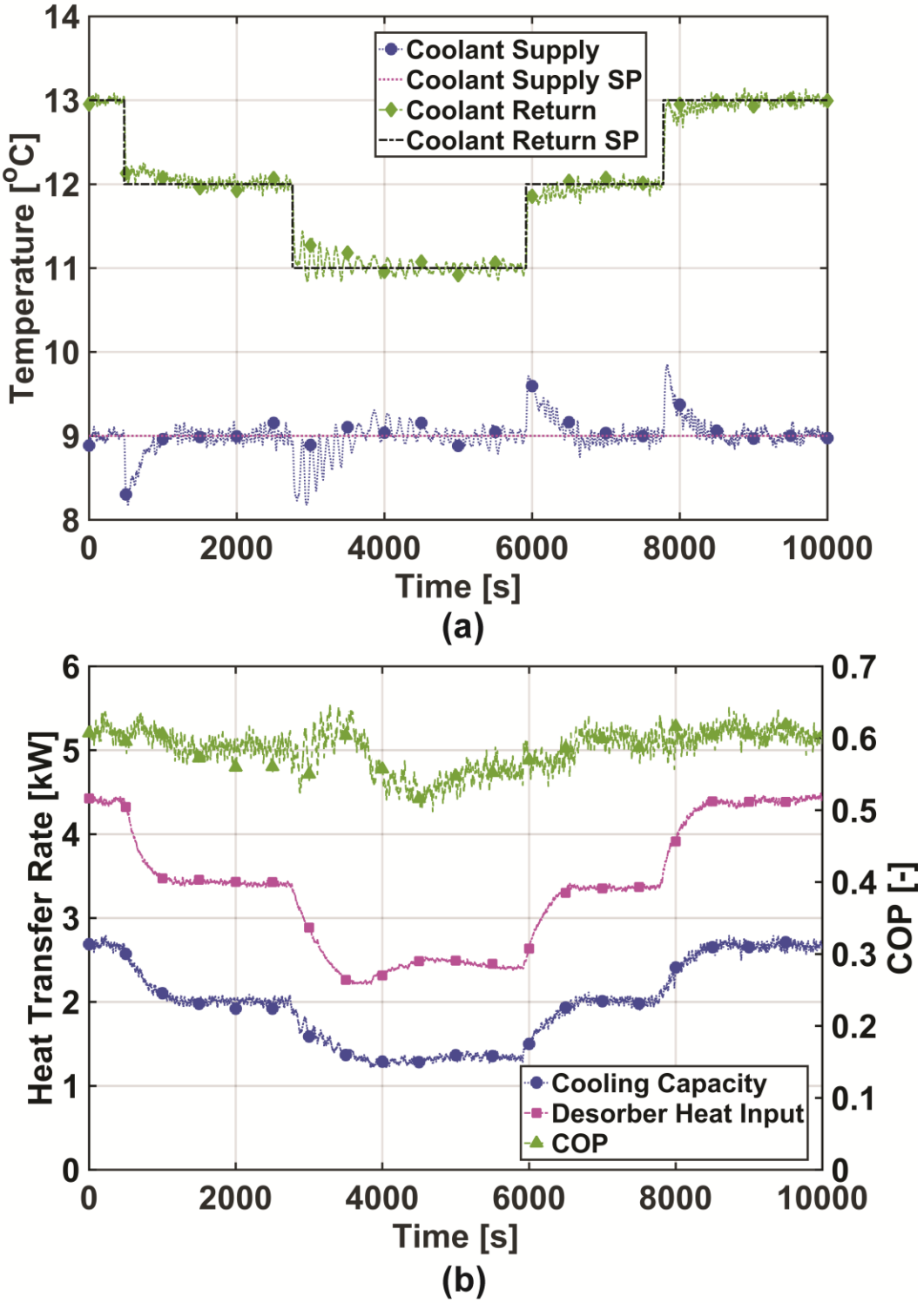

Figure 6.29: Coolant temperatures (a) and system performance (b) at part-load operation due to reduced cooling load

kW. During the next variation of another 25%, the desorber heat input decreased to 2.40 kW, while the evaporator heat transfer decreased to 1.35 kW.

The variation in the COP of the system is also shown in Figure 6.29 (b). The design COP is ~0.6. Similar to the previous test case, the COP increased to ~0.63 during the transient period, but finally achieved a slightly lower value of ~0.58 at the new steady state of 75% system capacity. At 50% capacity, the COP decreased to ~0.56. Similar trends are observed during the phases when the coolant supply temperature is restored to the design condition via step changes in the setpoint.

Figure 6.30 shows the response of the actuators as the cooling load is varied. The pump speeds for the concentrated solution and desorber coupling fluid are shown on the left vertical axis, and the desorber coupling fluid inlet temperature is shown on the right

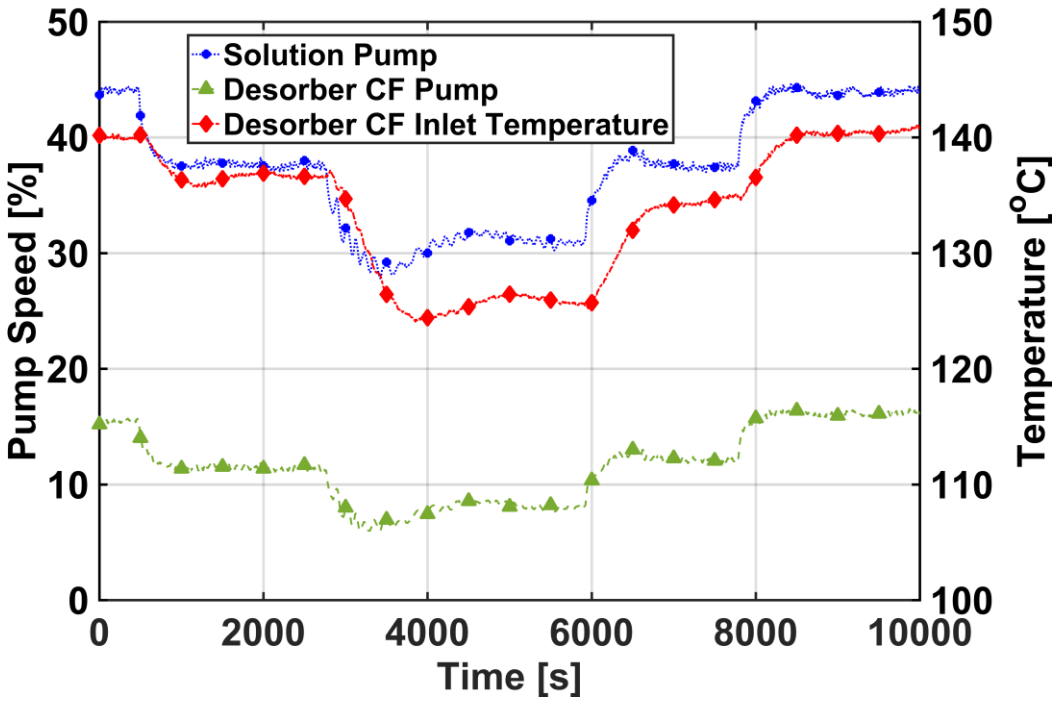

Figure 6.30: Capacity control loop actuators at part-load operation due to reduced cooling load

vertical axis. At 75% capacity, the solution pump speed decreased from 44% at design performance to 37.5% in ~ 600 s, while the desorber coupling fluid pump speed decreased from 15.5% to 11.5% in approximately the same duration. Meanwhile, the desorber coupling fluid inlet temperature decreased from 140°C to ~136.5°C in ~800 s. At 50% capacity, the solution pump speed further decreased to ~31% in ~1500 s, while the desorber coupling fluid pump speed decreased to ~8% in approximately the same duration. Meanwhile, the desorber coupling fluid inlet temperature decreased to ~125.5°C in the same duration. As the control parameters remained unaltered, a small degree of undershoot was observed at 50% capacity, indicating possibilities for further fine-tuning the controller.

Figure 6.31 (a) and (b) show the variation of evaporator temperature glide and the SHX approach temperature, and the valve positions, respectively. The results are very similar to those discussed in the previous section. As the capacity is reduced, the glide temperature decreased due to the reduced heat transfer rate in the evaporator. The refrigerant valve then closed to reduce the refrigerant mass flow rate and restore the glide temperature at its set-point of 2.5°C. Again, at 50% system capacity, the refrigerant valve cannot close enough to achieve the setpoint of temperature glide. This is observed in Figure 6.31 (b) as the valve remained at its lowest allowable setting of 5% opening. The desorber phase control loop responded well to the transience in system capacity as shown in Figure 6.31 (a). The dilute solution valve opening reduced in response to the increasing approach temperature (Figure 6.31 (b)) and the approach temperature achieved the setpoint value of 2.5°C.

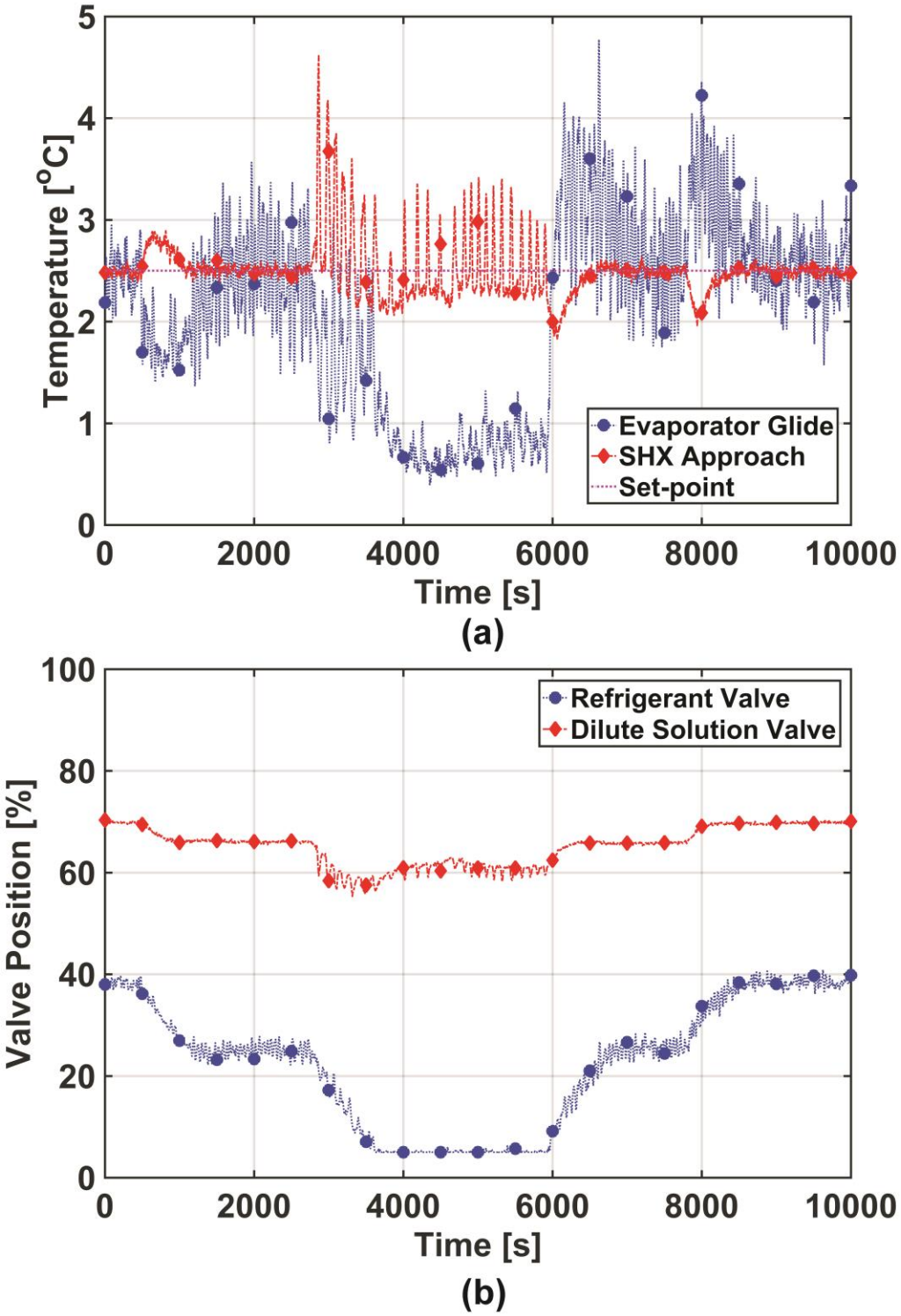

Figure 6.31: Evaporator glide and SHX approach temperatures (a) and valve positions (b) at part-load operation due to reduced cooling load

6.5.3 Variation in Ambient Conditions

In this final case study, the controller performance is evaluated in response to changes in the ambient conditions. Variation in ambient conditions is implemented on the breadboard system by changing the inlet temperature of the cooling water (heat sink) into the condenser and the absorber. The effects of variations in the cooling water temperature on overall system performance were discussed in the previous section on perturbation studies. A decrease in the heat sink temperature for the condenser and the absorber leads to higher system capacity and COP and vice versa. The controller performance is evaluated in terms of maintaining the supplied coolant temperature as the ambient temperature decreases below the design value. As the system and its components are designed for a specific heat sink temperature, the controller performance is measured in response to operating conditions below the design heat sink temperature.

Figure 6.32 shows the variation of the cooling water temperature as a function of time. At t = 400 s, the cooling water temperature started to decrease from its design condition of 37°C (representative of ambient air temperature of 34°C) and achieved a new steady state at 34°C (representative of ambient air temperature of 31°C) at t = 800 s. Similarly, at t = 2900 s, the cooling water temperature started to decrease from 34°C (representing ambient air temperature of 31°C) and achieved a new steady state of 31°C (representing ambient air temperature of 28°C) at t = 3300 s. In similar steps, the ambient temperature is restored to its design value.

Figure 6.33 (a) and (b) show the variation of coolant temperatures, and heat transfer rates and COP, respectively. Figure 6.33 (a) shows that the capacity control algorithm

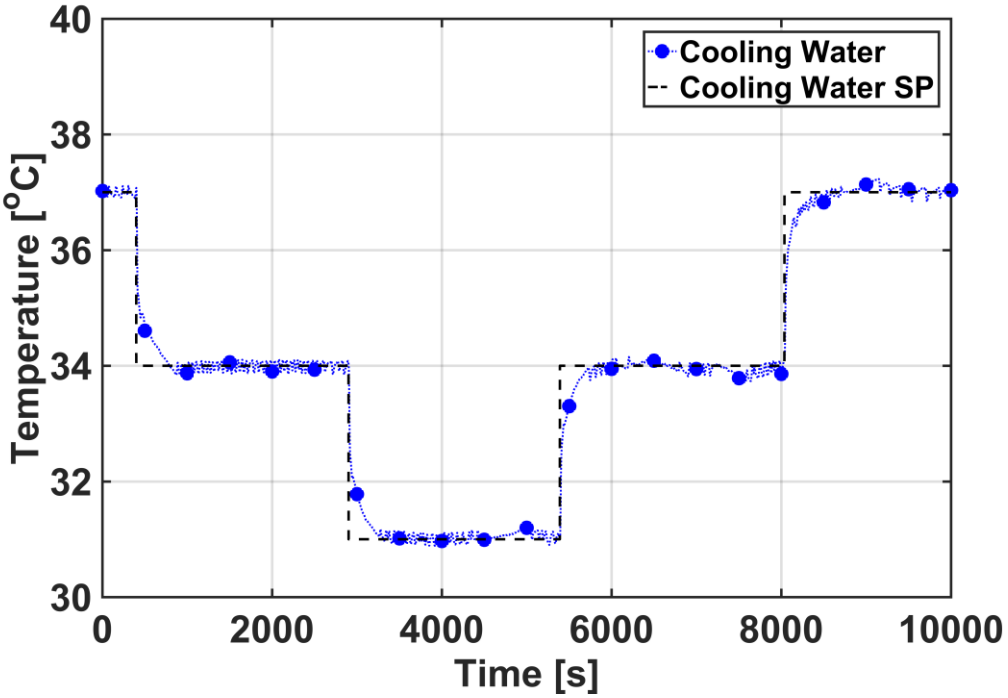

Figure 6.32: Variation of cooling water temperature entering the condenser and the absorber

maintained the system capacity at design conditions leading to consistent coolant supply temperature of 9°C throughout this case study. Maximum deviations of ±0.4°C were observed during the transience of cooling water temperature.

Figure 6.33 (b) shows the variation of heat transfer rates in the evaporator and the desorber and the COP of the system. As the temperatures of the supplied and return coolant streams in the evaporator remained at their design values, the cooling capacity of the system remained constant at ~2.70 kW. The desorber heat transfer rate decreased from 4.40 kW at 37°C cooling water temperature to 4.30 kW at 34°C. When the cooling water temperature decreased to 31°C, the desorber heat input rate did not decrease further and remained constant at ~4.30 kW. This can be attributed to larger temperature difference between the solution and the coupling fluid that compensates for effects of lower desorber coupling fluid inlet temperature.

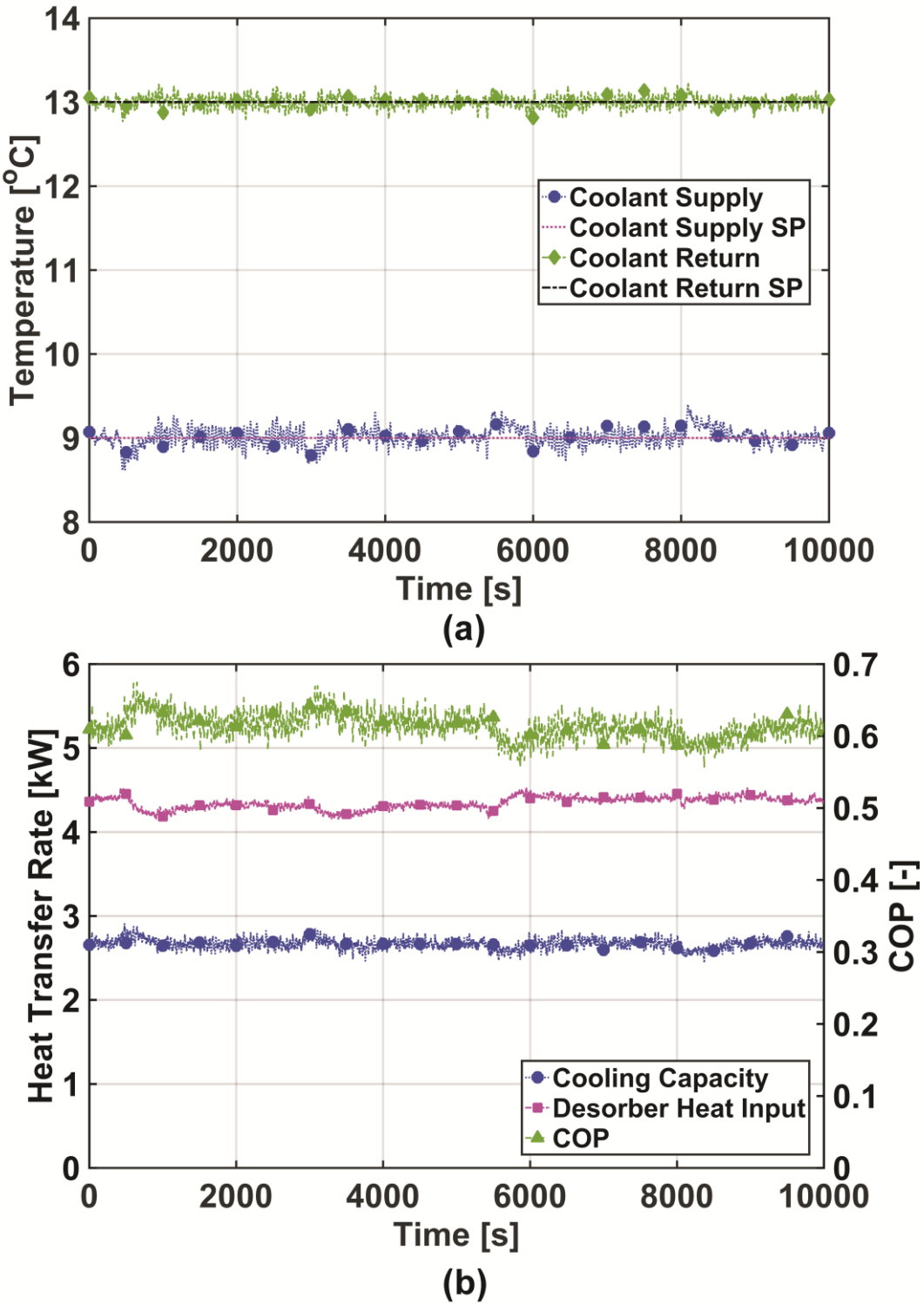

Figure 6.33: Coolant temperatures (a) and system performance (b) at varying ambient temperature

The variation of system COP is also shown in Figure 6.33 (b). The COP of the system increased from ~0.61 at 37°C cooling water temperature to ~0.63 at 34°C cooling water temperature. The increase in COP is due to the reduced heat transfer rate in the desorber. At a lower cooling water temperature of 31°C, the COP remained constant at 0.63 due to approximately constant heat transfer rates in the desorber and the evaporator. Additionally, the decrease in the solution temperature at the outlet of the absorber, due to a decrease in the cooling water temperature, led to increased condensation in the rectifier even though the solution flow rate in the rectifier was set at its minimum value. Increased rate of condensation of the generated ammonia vapor led to sustained level of heat transfer rate in the desorber and the condenser, and the evaporator portion of the system did not receive the additional refrigerant flow. Therefore, the system performance could not increase beyond a certain point. It is predicted that if the rectifier coolant flow can be controlled and reduced further, additional enhancement in the performance of the system will be achieved. The COP increased during the transient to ~0.65 – 0.66 due to slight undershoot in the heat input rate response of the desorber. The trends observed when the ambient temperature is restored back to its design value are explained in a similar manner.

Figure 6.34 shows the response of the actuators and process variables utilized in the capacity control algorithm. At lower cooling water temperatures, the solution pump speed decreased from 44.50% to 43.75%. The desorber coupling fluid heat transfer rate varied between 15.50 – 17.50%. The largest change was observed in the desorber coupling fluid inlet temperature and it changed from ~137°C at 37°C cooling water temperature to ~133°C at 34°C cooling water temperature, and finally to ~128°C at 31°C cooling water temperature. This indicated that the system can operate at much lower heat source

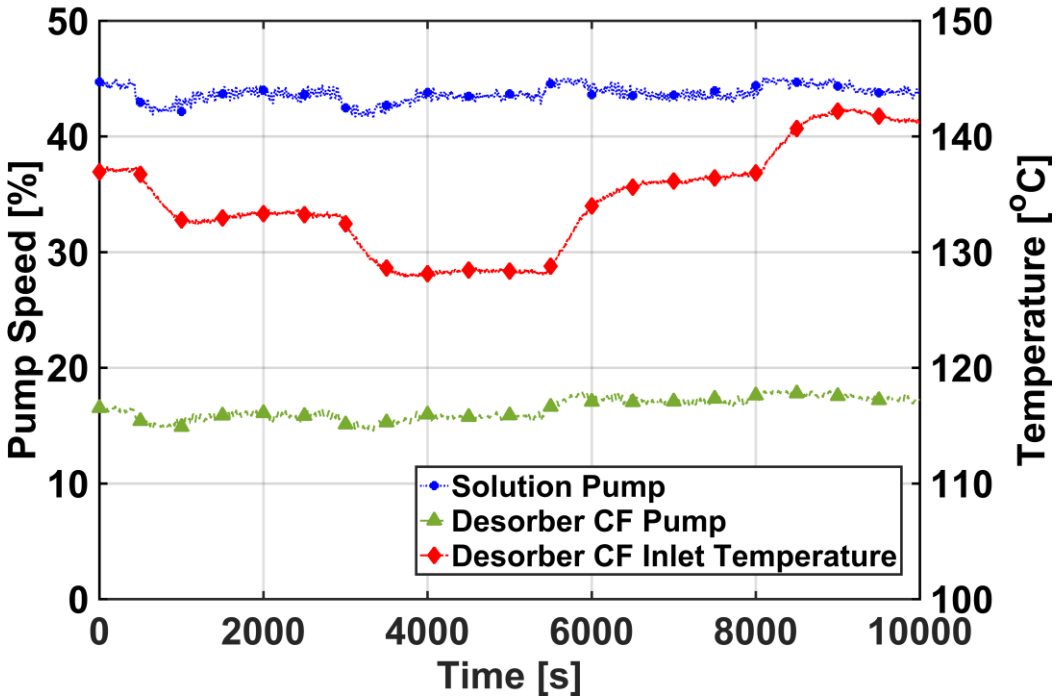

Figure 6.34: Capacity control loop actuators at reduced cooling water temperatures

temperatures at below design ambient temperatures. During the phase when the cooling water temperature was restored to the design value, the desorber coupling fluid temperature settled at a value of ~141°C, approximately 4°C higher than the initial starting point. This difference showed some potential for fine tuning the controller gains.

Finally, Figure 6.35 (a) and (b) show the variations in the evaporator glide and solution heat exchanger approach temperatures, and the positions of the refrigerant and dilute solution valves, respectively. Figure 6.35 (a) shows that the performance control loops maintained the glide and solution heat exchanger approach temperatures at the setpoint of 2.5°C. The valve positions varied to maintain the glide and the approach temperature as shown in Figure 6.35 (b). As the cooling water temperature decreased, the high-side pressure decreased leading to further opening of the valves. The dilute solution valve opened from 70.4% at 37°C cooling water temperature to 72.6% at 34°C cooling

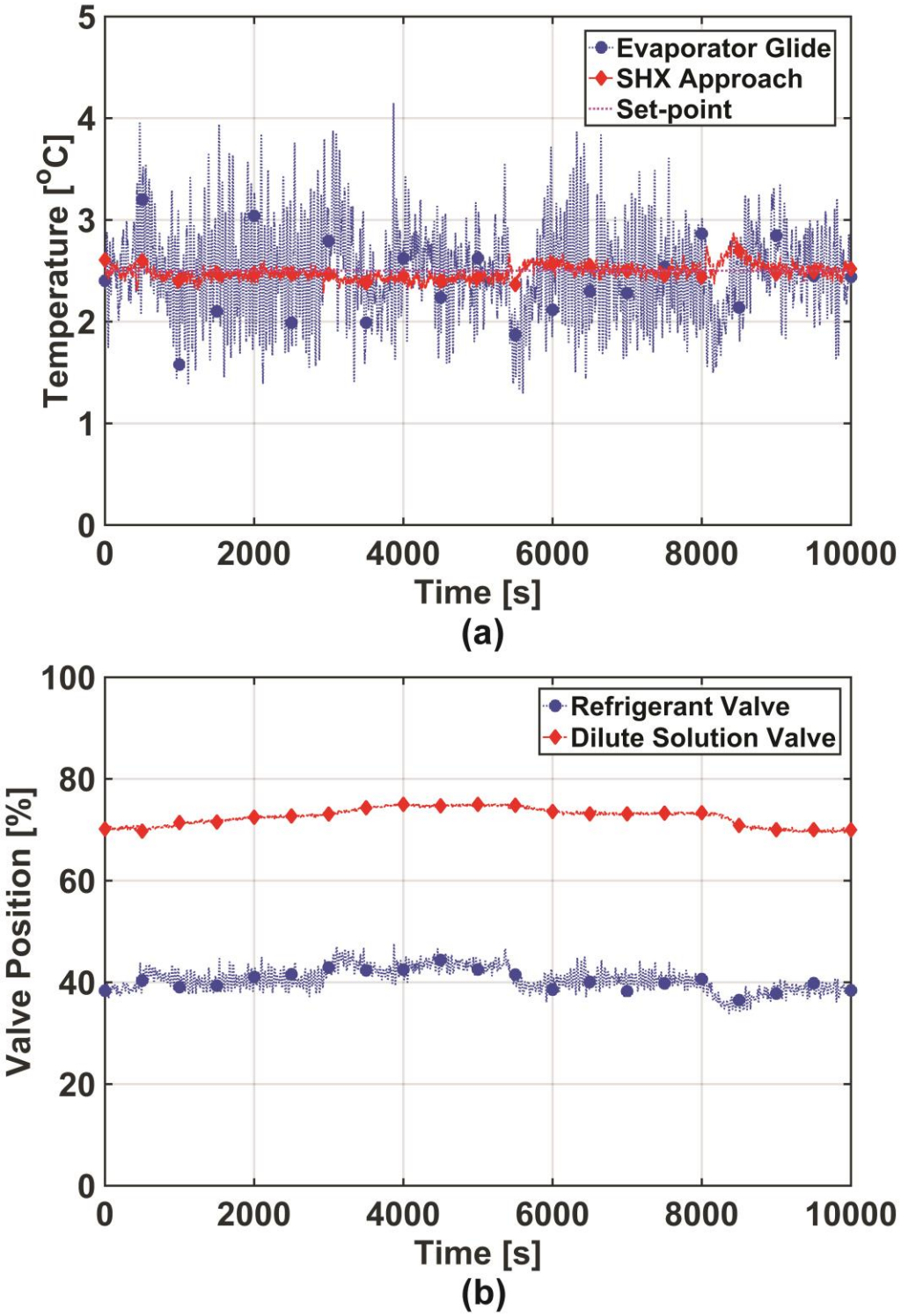

Figure 6.35: Evaporator glide and SHX approach temperatures (a) and valve positions (b) at varying ambient temperature

water temperature, and finally to 74.8% at 31°C cooling water temperature. Similarly, the refrigerant valve opened from 38.4% at 37°C cooling water temperature to 40.6% at 34°C cooling water temperature, and finally to 43.4% at 31°C cooling water temperature. The valves were able to retrace their positions as the cooling water temperature was restored to its design value.

6.6 Summary and Conclusions of Controls Experiments

In this study, advanced feedback control algorithms were developed that utilized all the available degrees of freedom in the system. This first ever multivariable feedback control approach is shown to perform well in many scenarios of system operation. Notably, the control algorithms can smoothly reduce the system performance to 50% of the design capacity while maintaining high COP. Figure 6.36 shows a qualitative assessment of the control system. Various control degrees of freedom are utilized in this study according to their impact on the system performance. The dynamic effects of various interactions in the system are accounted for in different time-scales of control algorithms in the design process, enabling stable and repeatable performance of the controller. The system is also able to regulate the system performance at off-design ambient conditions. The experiments also showed that the controller performance was as intended even for disturbances and capacity variation rates much steeper than are normally encountered in any application. This shows that for realistic operating situations the control algorithms should be able to address the variations in the operating conditions. Additional fine tuning of controller parameters can reduce the over/undershoot observed in some test cases.

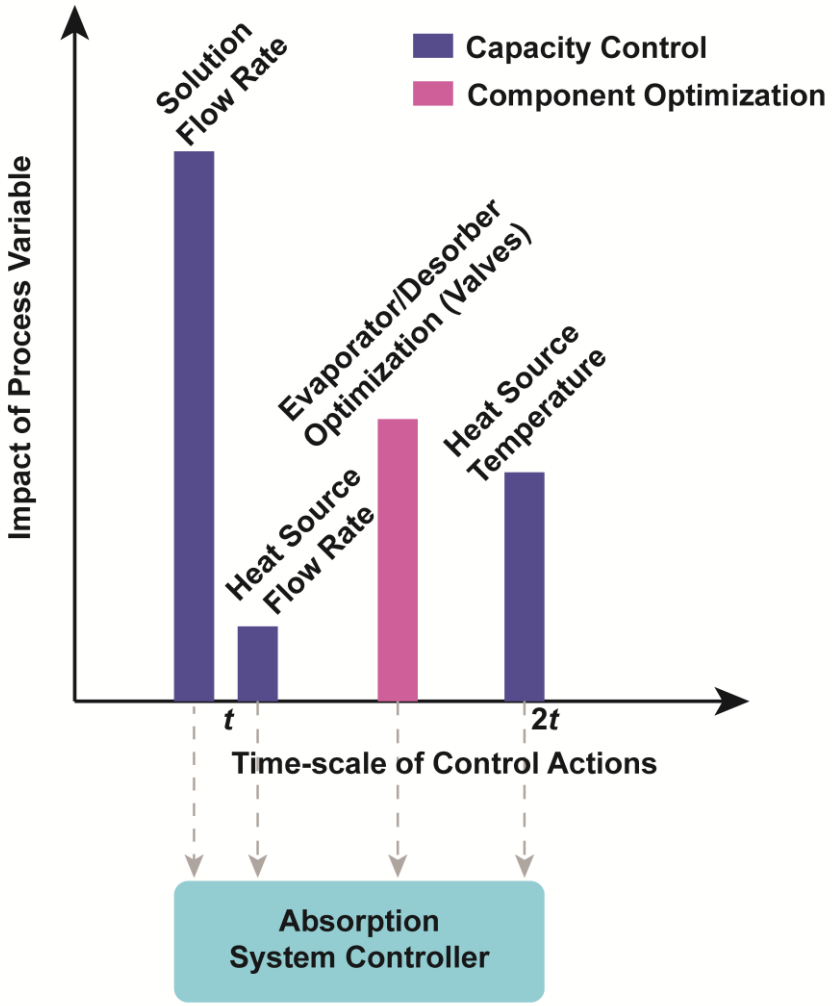

Figure 6.36: Summary of control system design

Some parts of experimental research are discussed at the end of this document in appendices. Appendix-III discusses the results on the performance of the system at severe ambient conditions of 50°C cooling water temperature at the inlet of the absorber and the condenser. Appendix-IV presents details of system fabrication, troubleshooting and operation of ammonia-water absorption systems for residential and mobile applications. Finally, details of a start-up and shutdown heuristic are explained in Appendix-V. The implementation of such a control algorithm is useful for a prototype system.

CHAPTER 7. TRANSIENT MODEL: SIMPLIFICATION AND VALIDATION

7.1 Introduction

The transient models for different components presented in Chapter 4 are useful in analyzing detailed property variations as a function of time. Especially, the discretized models can provide high spatial and temporal resolution. These models can be computationally expensive to solve a system of DAEs with over 100 equations. On the other hand, the MB method significantly reduces the computational expense associated with these simulations. However, the resulting models accounting for variable outlet phase can be complicated and require precise initial conditions. This chapter presents the analysis of methods to reduce the complexity of the discretized models and identify the tradeoff between the gains in computational speed and loss of accuracy. Additionally, the discussion highlights the applicability of the models for real-time controllers by validating their performance with experimental data.

7.2 Model Simplification

One of the key features of the model equations presented in Chapter 4 was that the final form of assembled equations represented a system of differential-algebraic equations (DAE). DAEs require specialized solvers and with large number of nodes in each component, they can significantly increase the computational overhead. The algebraic equation results from the mass conservation equation to calculate the interfacial mass flow rate. However, when microchannel geometries are considered for most components of the

absorption system, the fluid volume in the channels becomes negligibly small. The small fluid volume makes the dynamics of mass storage very fast and therefore can be assumed quasi-steady. This leads to only a system of ordinary differential equations for energy conservation. This can be solved with standard solvers and should provide savings in computational time when using advanced implicit solvers. The following sections present the formulation of the model using this approach, and compare the performance of the startup phase of a condenser under identical operating conditions of time varying boundary conditions using the simplified model and the detailed discretized model described in Chapter 4.

7.2.1 Model Equations

Neglecting refrigerant mass and species storage in the microchannel flow passages, Eq. 4.12 – 4.14 are reduced to:

$$\frac{\partial A_{cs}[\rho_f h_f - P_f]}{\partial t} + \frac{\partial \dot{m}_f h_f}{\partial z} + U_f Per_f (T_f - T_{hx}) = 0 \tag{7.1}$$

The energy conservation equations for the wall and coupling fluid element are:

$$\rho_{hx} Cp_{hx} A_{cs,hx} \frac{\partial T_{hx}}{\partial t} - U_f Per_f (T_f - T_{hx}) + U_{cf} Per_{cf} (T_{hx} - T_{cf}) = 0 \tag{7.2}$$

$$\rho_{cf} Cp_{cf} A_{cs,cf} \frac{\partial T_{cf}}{\partial t} + \frac{\partial (\dot{m}_{cf} Cp_{cf} T_{cf})}{\partial z} - U_{cf} Per_{cf} (T_{hx} - T_{cf}) = 0 \tag{7.3}$$

Eq. 7.1 – 7.3 are a set of unsteady partial differential equations for a condenser or an absorber. The computed variables are the refrigerant outlet enthalpy, wall temperature, and coupling fluid outlet temperature. The time varying boundary conditions for the system are

refrigerant inlet mass flow rate, concentration, temperature, pressure, and coupling fluid inlet mass flow rate and temperature. These are provided from other components of the absorption system. The geometric parameters and physical component dimensions are fixed constants for the component under consideration. Figure 7.1 shows a discretized representation of a counter-flow heat exchanger with refrigerant and coupling fluid exchanging heat through a wall element. Following the procedure outlines in Chapter 4, Eq. 7.1 – 7.3 are integrated over the control volume and discretized using an upwinding differencing scheme (UDS) (Patankar, 1980). The discretized energy conservation equations for refrigerant, wall and coupling fluid are:

$$V_{f,seg}\rho_{f,i}\frac{dh_{f,i}}{dt} = \dot{m}_{f,j-1}(h_{f,j-1} - h_{f,j}) - (UA)_f(T_{f,i} - T_{hx,i}) + V_{f,seg}\frac{dP_f}{dt} \tag{7.4}$$

$$(m_{hx}Cp_{hx})_i\frac{dT_{hx,i}}{dt} = (UA)_f\left(T_{f,i} - T_{hx,i}\right) - (UA)_{cf}\left(T_{hx,i} - T_{cf,i}\right) \tag{7.5}$$

$$(m_{cf}Cp_{cf})_i\frac{dT_{cf,i}}{dt} = \dot{m}_{cf}Cp_{cf}\left(T_{cf,j} - T_{cf,j-1}\right) + (UA)_{cf}\left(T_{hx,i} - T_{cf,i}\right) \tag{7.6}$$

$$h_{f,j} = h_{f,i} \tag{7.7}$$

$$T_{cf,j} = T_{cf,i+1} \tag{7.8}$$

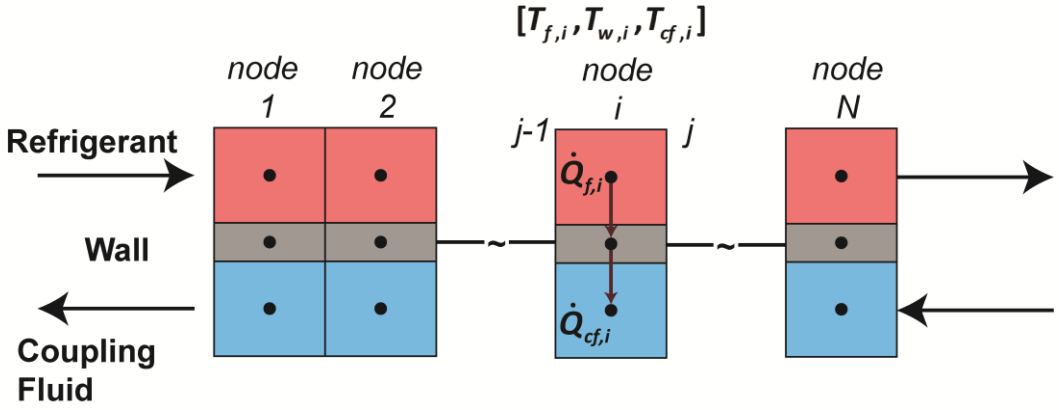

Figure 7.1: Schematic of finite volume discretization of heat exchanger

Eq. 7.4 – 7.6 along with Eq. 7.7 – 7.8 (UDS) are compiled for each node resulting in a system of 3*N* equations with identical number of unknowns. These are solved simultaneously using the implicit solver, *ode15s*, in MATLAB®. The profiles for time-dependent boundary conditions of inlet mass flow rates, inlet temperatures of both fluids, and refrigerant pressure are provided to the model. The physical parameters and heat transfer coefficients of the heat exchanger are summarized in Table 7.1.

A 20-node discretized model was simulated from startup at room temperature conditions to achieve steady-state performance. Time-dependent boundary conditions of refrigerant inlet mass flow rate, temperature and pressure were provided to the model as smooth cubic spines over the defined time duration and initial and final parameter values. Table 7.2 specifies the boundary conditions and their rates of variation. These values are similar to the system startup response observed during experiments.

Figure 7.2 shows the response of the condenser during startup using the boundary conditions and parameters of the condenser described above. Both the models, the first (full model) accounting for the compressibility effects of the refrigerant fluid, and the second

Table 7.1: Physical and heat transfer parameters of the condenser

Parameter	Refrigerant	Coupling Fluid	Wall
Heat transfer area per sheet (m^2)	0.01153875	0.0100665	
Mass of sheet pair (kg)			0.204
Number of channels per shim	75	75	
Number of sheets	25		
Channel hydraulic diameter (m)	453×10^{-06}		
Fluid volume per sheet (m^3)	2.272×10^{-06}	1.982×10^{-06}	
Heat transfer coefficient (W m^{-2} K^{-1})	3125	5578	
Total inlet mass flow rate (kg s^{-1})	0.00309	0.112	
Specific heat capacity (J kg^{-1} K^{-1})		4182	500
Density (kg m^{-3})		990.6	8000

Table 7.2: Boundary conditions for the condenser model

Parameter	Initial Value	Final Value	Initial Time (s)	Time span (s)
Condenser Pressure (kPa)	300	1878	1	1050
Refrigerant Inlet Temperature (°C)	25	60	1	900
Refrigerant inlet mass flow rate (kg s^{-1})	1×10^{-05}	0.0031	1	720
Air mass flow rate (kg s^{-1})	0	0.35	630	5
Refrigerant inlet mass quality (kg kg^{-1})	1	1	-	-

(reduced-order) model assuming the refrigerant to be incompressible are compared. Figure 7.2 (a) shows the variation of the heat transfer rate as computed on the refrigerant side. Both models predict identical heat transfer rates during the transient variation and at steady-state. The steady-state heat transfer rate is 3.21 kW. As shown in Figure 7.2 (b), the outlet mass flow rate predicted by both models is also identical, validating the assumption of incompressible flow of the refrigerant. Figure 7.2 (c) and (d) show the variation of the outlet temperatures of the refrigerant and the coupling fluid, respectively. Again, both models predict identical values of outlet temperatures (refrigerant = 46.95°C and coupling fluid = 44.35°C) at steady-state operation. The results indicate that the simplification in the model does not alter the accuracy. The time duration of these simulations was also recorded to compare the computational expense of these simulations. The "full model" took 64.8 s to complete the startup simulation while the "reduced-order" model took 49.6 s. Therefore, the simplification in the governing equations provided ~23% savings in the computational cost without compromising on the accuracy of the results.

The performance of the models was also evaluated for perturbations from steady-state. Figure 7.3 shows the results from simulations involving a 25% decrease in the inlet mass flow rate of the refrigerant over a duration of 30 s and restored to design condition in

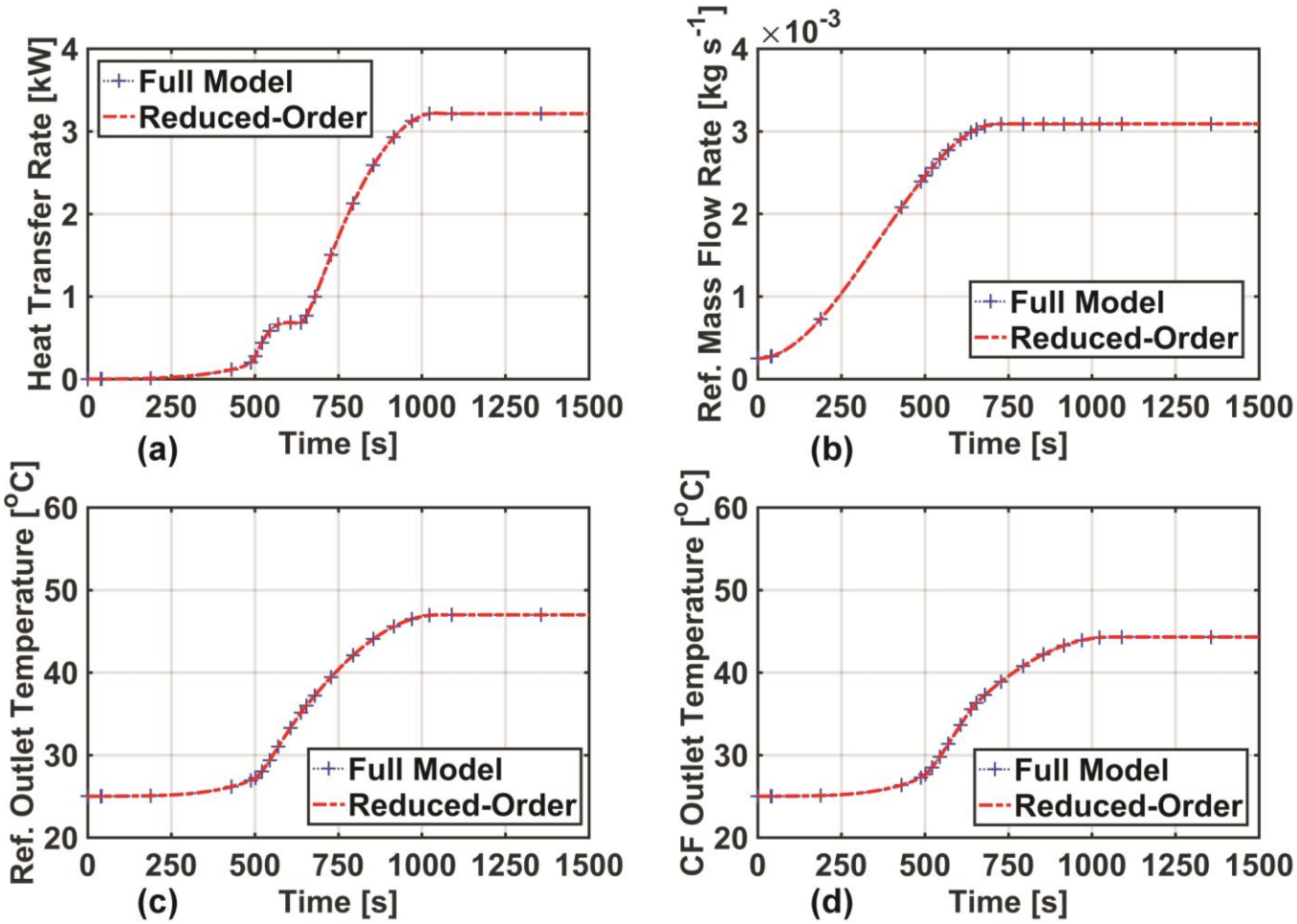

Figure 7.2: Comparison of modeling methods during startup

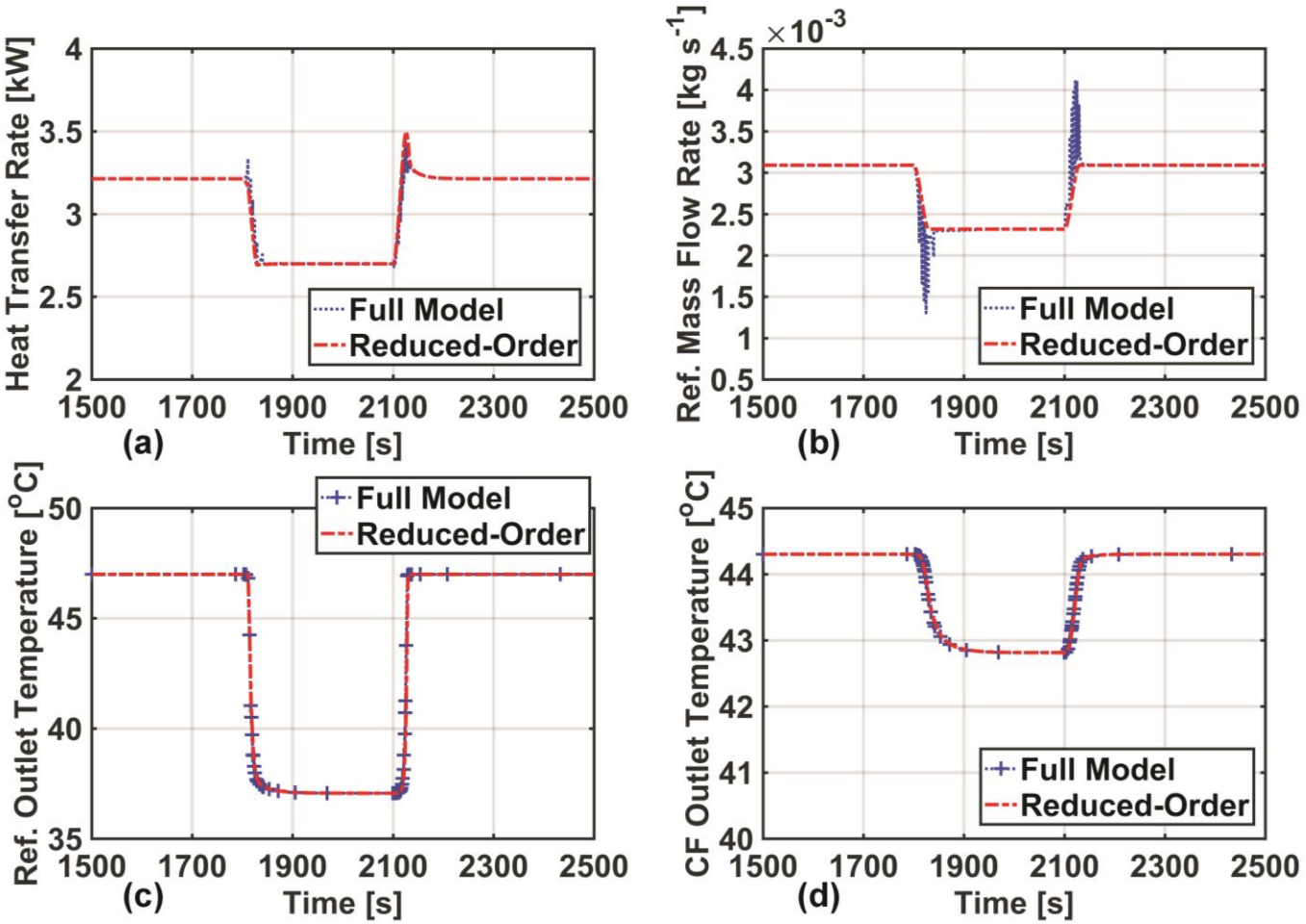

Figure 7.3: Comparison of modeling methods during mass flow transience

same duration after the new steady-state was achieved. As observed in Chapter 4, a mass flow transience demonstrates the ability of the model to capture effects of mass storage and thermal capacitance. Figure 7.3 (a) shows the effect on heat transfer rate. As the mass flow rate is reduced, the heat transfer rate decreases due to lower mass of refrigerant being condensed per unit time. Due to a decrease in the mass flow rate, the heat transfer rate decreases to 2.69 kW. Both models predict similar transient trends and final steady-state values. When the mass flow rate is restored to its design value, the heat transfer rate also returns to its baseline value of 3.21 kW with a slight overshoot of 0.27 kW. Some of the transient variations in the response of the heat transfer rate can be explained using the response of the refrigerant outlet mass flow rate, shown in Figure 7.3 (b). As the mass flow rate is reduced and the heat transfer coefficient remains unchanged, the extent of subcooling in the condenser increases, leading to additional stored liquid mass inside the heat exchanger. This is reflected in the slightly reduced value of the outlet mass flow rate during the transient duration in comparison to the inlet flow rate. Conversely, as the inlet flow rate is restored to its design value, the stored liquid is pushed out and the outlet flow rate is greater than the inlet flow rate during the transient period. Some numerical oscillations are observed due to the stiff nature of the system of equations. The reduced-order model does not capture these transient effects in the mass flow rate. However, as shown in the plots of fluid outlet temperatures and heat transfer rate, both the models predict identical values during the transient and at steady-state. The outlet temperature of the refrigerant (Figure 7.3 (c)) decreased to 37.05°C and the coupling fluid outlet (Figure 7.3 (d)) decreased to 42.85°C consistent with the predictions of both the models.

These studies indicate that the reduced-order model is applicable in simulating the transient response of microchannel heat exchangers used in the absorption systems discussed in this work. The important consideration is the fluid volume inside the heat exchangers, and if it is very small, these mass storage effects can be neglected without any loss in the accuracy of model predictions.

7.3 Performance of ANN Property Routines

7.3.1 Thermodynamic Consistency

The developed property routines were evaluated for thermodynamic consistency. Property derivatives were computed using the routines developed in this work and data available from EES. Table 7.3 summarizes the comparison of partial derivatives of properties computed numerically at various operating points in the absorption system investigated in this work. As shown, except for some deviations in the values of $\partial h / \partial P$, other property derivatives are in close agreement with EES data. This ensures that the property derivatives computed at each time during transient simulations remain physically consistent.

To further ensure the consistency of property predictions, mass and energy residuals were computed using Eqs. 4.53 – 4.57 presented earlier in Chapter 4. For transient simulation of the condenser using the *full model* presented in Section 7.2, mass and energy residuals were computed during the startup period. Throughout the simulation, the mass flow rate residual was computed be within $\pm 7 \times 10^{-20}$ kg s^{-1}, and the heat transfer rate residual was within ±1 W. This observation established the conservative property of the

Table 7.3: Property derivatives for evaluating thermodynamic consistency of ANN-based property routines

Property Derivative	EES	ANN
Desorber: P = 1870 kPa, T = 135°C, x = 0.27 kg kg^{-1}		
$\partial h / \partial T$ (kJ kg^{-1} K^{-1})	4.71	4.67
$\partial h / \partial x$ (kJ kg^{-1})	-362.1	-366.7
$\partial T / \partial x$ (K)	74.06	72.32
$\partial h / \partial P$ (kJ kg^{-1} kPa^{-1})	0.00035	0.00063
Condenser: P = 1870 kPa, T = 60°C, x = 0.997 kg kg^{-1}		
$\partial h / \partial T$ (kJ kg^{-1} K^{-1})	4.56	4.50
$\partial h / \partial x$ (kJ kg^{-1})	4669	5023
$\partial T / \partial x$ (K)	-1024	-1027
$\partial h / \partial P$ (kJ kg^{-1} kPa^{-1})	-0.082	-0.081
Absorber: P = 520 kPa, T = 37°C, x = 0.42 kg kg^{-1}		
$\partial h / \partial T$ (kJ kg^{-1} K^{-1})	4.42	4.41
$\partial h / \partial x$ (kJ kg^{-1})	-176.6	-180.7
$\partial T / \partial x$ (K)	40.01	38.20
$\partial h / \partial P$ (kJ kg^{-1} kPa^{-1})	0.0008	0.003
Evaporator: P = 520 kPa, T = 4.5°C, x = 0.42 kg kg^{-1}		
$\partial h / \partial T$ (kJ kg^{-1} K^{-1})	4.63	4.61
$\partial h / \partial x$ (kJ kg^{-1})	720.6	721.6
$\partial T / \partial x$ (K)	-155.8	-156.1
$\partial h / \partial P$ (kJ kg^{-1} kPa^{-1})	0.0005	0.0015

method and provided another method to evaluate the thermodynamic consistency of ANN-based property routines.

7.3.2 Computational Performance

The computational advantage offered by the property routines presented in Chapter 3 is presented in this section. The condenser model described in the previous section was simulated from startup at room temperature conditions to achieve steady-state performance. Both property routines, the EoS-based approach by Rattner and Garimella (2016) and ANN-based routines developed in this work were used to simulate the transient response of the condenser. The simulation results, during transience and at steady-state, agreed well between the two cases. Computed variables such as the heat transfer rate, outlet

subcooling and outlet quality, and nodal temperatures were predicted accurately by the ANN-based property routines. The computational time of condenser simulation from startup to steady state (500 s of simulation time) was recorded to compare the efficiency of the proposed method with the existing property libraries. **The simulation using the proposed methodology of ANN based thermodynamic routines took 26.6 s to complete, while the simulation using EoS based routines took 124.5 s. Therefore, the methodology proposed in this work enhances the computational efficiency of such transient simulation by approximately a factor of 5.**

7.4 Model Validation

This section presents results from validation studies performed using the component models developed in Chapter 4 and the previous section. The perturbation studies on the breadboard system enabled analysis of component and system performance. The major portion of the discussion in the previous chapter focused on the performance of the system. However, the measurements and calculations for various components also allow for deeper insights into the physics of the underlying heat transfer phenomena as the operating conditions vary. One of the key outcomes of the experiments was that the heat transfer coefficient for various components can significantly vary as the flow rates of the working fluids change. The assumption of a constant heat transfer coefficient in transient models would lead to underprediction of performance at above-design flow rates and overprediction at above-design flow rates. The overall average heat transfer conductance value for a component (on a very approximate basis, for such components with varying thermal capacity rates and phase change) can be computed using Eq. 7.9:

$$\dot{Q} = (UA)_{overall}(\Delta T_{LM}) \tag{7.9}$$

where $\dot{Q}$ is the component heat transfer rate, UA_{overall} is the overall average heat transfer conductance value, and ΔT_{LM} is the logarithmic temperature difference. Neglecting the heat transfer resistance of the heat exchanger wall, the total heat transfer resistance can we expressed as shown in Eq. 7.10.

$$\frac{1}{(UA)_{overall}} = \frac{1}{(UA)_f} + \frac{1}{(UA)_{cf}} \tag{7.10}$$

As the flow rate of the coupling fluid streams from heat sources and sinks typically remains constant, the heat transfer conductance of the coupling fluid slide can be assumed to be invariant. Accurate single-phase heat transfer correlations are utilized to estimate the coupling fluid side heat transfer coefficient (U_{cf}). Therefore, the experimentally computed value of the overall heat transfer conductance can provide an estimate of the working fluid side heat transfer conductance and its variation as the flow rate of the working fluid varies. This is shown in Eq. 7.11.

$$\frac{1}{(UA)_f} = \frac{1}{(UA)_{overall}} - \frac{1}{(UA)_{cf}} \tag{7.11}$$

The Kakac *et al.* (1987) correlation for single-phase heat transfer coefficients in microchannel geometries was used for the coupling fluid.

7.4.1 Evaporator Performance

Chapters 5 and 6 identified the importance of predicting and controlling the performance of the evaporator. This section discusses the modified evaporator model with

the heat transfer coefficient on the refrigerant-side varying as a function of the mass flow rate. Experimental data are utilized to define a simple mathematical function correlating the heat transfer coefficient with the mass flow rate.

First, the heat transfer coefficient on the coupling fluid side is calculated. For the defined geometry, fluid properties at the average temperature and fluid flow rate, the heat transfer coefficient on the coupling fluid side is computed to be 5237 W m^{-2} K^{-1}. The overall heat transfer conductance is 0.98 kW K^{-1} A detailed sample calculation is shown in Appendix-I.

Experimental data from all the perturbations studies are collected to analyze the distribution of refrigerant heat transfer coefficient as a function of its mass flow rate. Figure 7.4 shows the variation of the heat transfer conductance on the refrigerant side with the

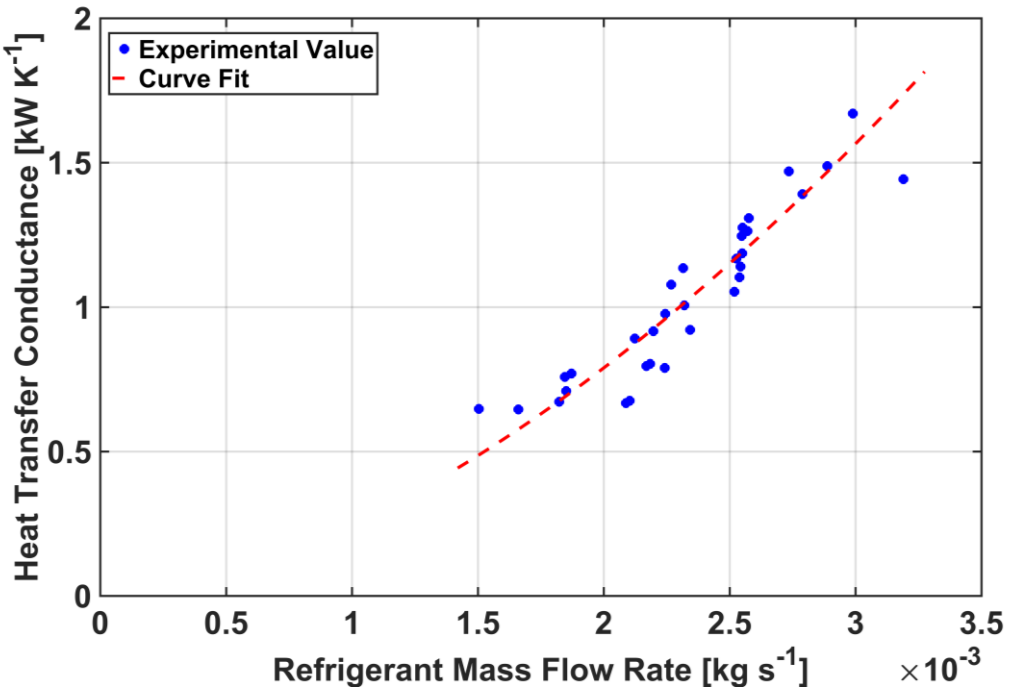

Figure 7.4: Variation in refrigerant side heat transfer conductance with refrigerant mass flow rate in the evaporator

mass flow rate of the refrigerant. A simple power-law fit is used to develop a correlation as shown in Eq. 7.12:

$$UA_{f,fit} = 2.851 \times 10^4 \dot{m}_f^{1.69} \tag{7.12}$$

Typically, the two-phase heat transfer coefficient is a complicated function of other parameters such as vapor mass quality, mass fraction of ammonia, Prandtl number, relative densities of the two-phases, etc. That level of detail is important for segmented steady-state models; however, for a component level dynamic model, the most dominant factor of fluid flow rate is captured in this representation. The average uncertainty in the experimentally calculated value of the overall heat transfer conductance is ~±23%. For the 32 experimental data points, the R^2 value for this power-law fit is 0.85.

The dynamic model of the evaporator is modified to account for this varying heat transfer coefficient. The response of the evaporator to a step change in temperature glide is evaluated. Time-dependent boundary conditions of refrigerant pressure, concentration, mass flow rate and inlet temperature are provided from the experimental study conducted on the step-response of the evaporator in Chapter 6. The simulated response of the heat exchanger with the variation of the glide temperature and the heat transfer rate are compared with the experimental values in Figure 7.5. The results indicate the ability of the modified model to correctly predict the trends in the variation of the temperature glide and the heat transfer rate. The temperature glide prediction is within ±0.25°C of the experimental value which is within the uncertainty of measurements. The trends in time constants are similar as well. The model predicts an approximate time constant of 250 s to achieve the new steady-state value of the temperature glide at ~1.2°C and the same value

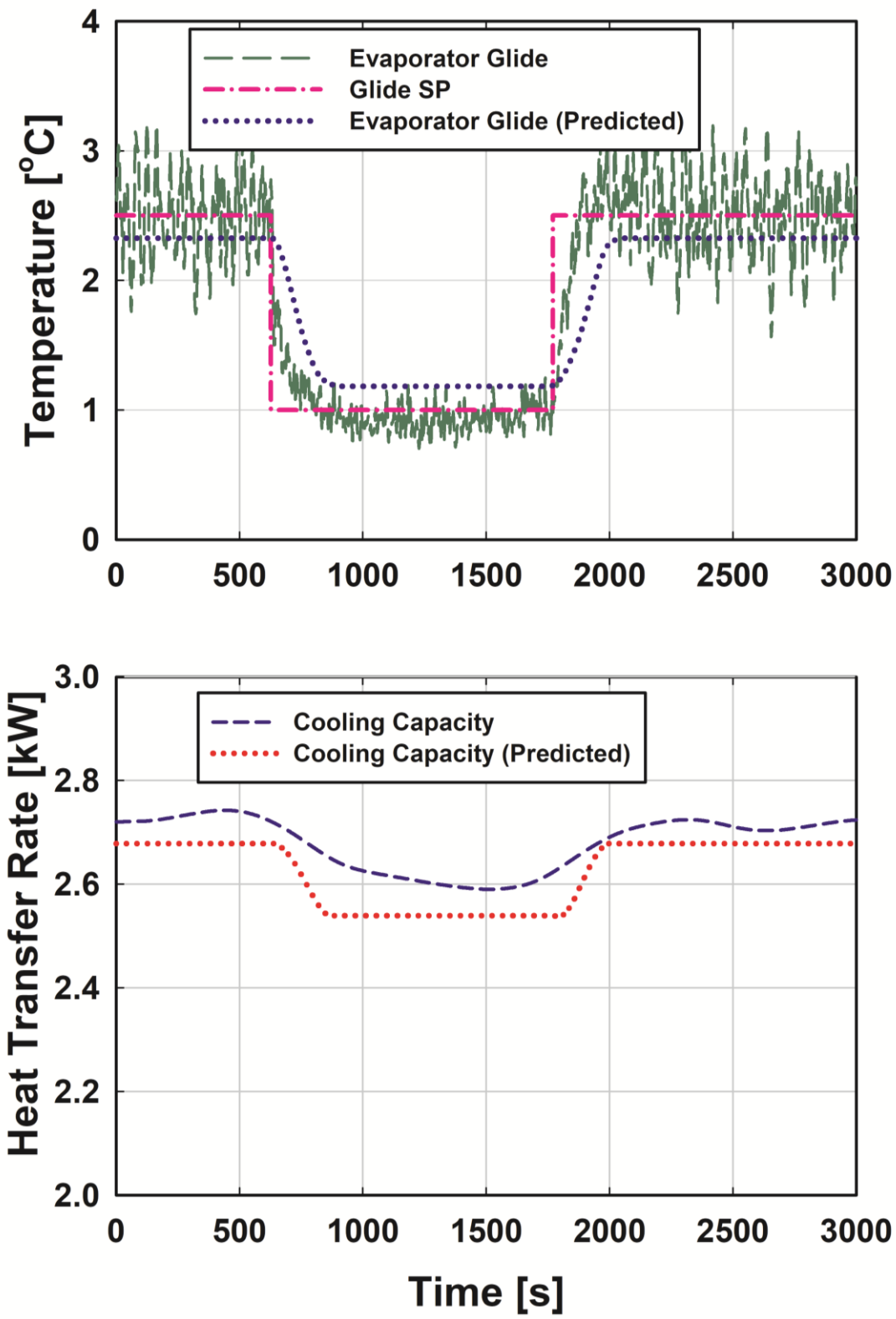

Figure 7.5: Comparison of evaporator temperature glide (top) and heat transfer rate (bottom) between simulation and experiments

of time constant when it is restored to its original value. The heat transfer response shows a minor discrepancy (~1.5%) between the model prediction and the experimental value. This may be due to the following: the uncertainty in the computation of heat transfer coefficient in the evaporator explained above, and the slight overshoot in the mass flow rate during the transient that is not captured in the boundary conditions being input to the model. This causes the prediction of the time constant for the heat transfer rate to differ somewhat from the experimental value. However, a complete system model that can capture the effects of pressure transience and the resulting mass flow rate variations, should be able to represent these phenomena.

Experimental data were used to develop similar expressions for other components of the system. The details of the curve-fit expressions are provided in Table 7.4. The analysis shows that the variation in the phase-change heat transfer conductance values can be correlated well using a power-law fit with the mass flow rate of the fluid undergoing phase-change. Correlations for the condenser and the refrigerant precooler are developed using the refrigerant mass flow rate. The desorber heat transfer conductance values on the concentrated solution side are correlated with the concentrated solution flow rate. Finally, the rectifier correlation is developed using the vapor mass flow rate entering the component. As the solution heat exchanger operated with single-phase liquid on both sides,

Table 7.4: Heat transfer conductance expressions obtained from experimental data

Component	Parameter	*UA* Expression	R^2
Condenser	Refrigerant mass flow rate	$UA_{vap,\,fit} = 6.805\times10^{05}\,\dot{m}_{vap}^{2.063}$	0.93
RPC	Refrigerant mass flow rate	$UA_{vap,\,fit} = 6.09\times10^{04}\,\dot{m}_{vap}^{2.22}$	0.83
Rectifier	Vapor mass flow rate	$UA_{vap,\,fit} = 1.788\dot{m}_{vap}^{0.67}$	0.88
Desorber	Solution flow rate	$UA_{fit} = 4.58\times10^{08}\,\dot{m}_{cs}^{4.21}$	0.88

an experimentally developed correlation is not necessary. The absorber, utilized in this experimental study is a proprietary shell-and-tube design with unknown heat transfer area on both sides of the component. This restricts development of such a correlation.

It should be noted that these correlations are specific to the system described and utilized in this work and are not generalizable. However, these expressions provide insight into variation of component characteristics as the inlet mass flow rate changes and provide guidance for the development of models for similar systems.

7.5 Accumulator Model

Accumulators are used in heat pump systems to maintain appropriate fluid phase inventory and serve as buffer during large transients. Absorption systems typically utilize three accumulators: one each on the refrigerant, dilute solution and concentrated solution stream. For simulation of system dynamics, these accumulators can also be utilized to set the value of the operating pressures in the system as a function of time. They can be modeled using the unsteady forms of mass, species and energy conservation equations, and utilizing the total fluid volume of the accumulator, and inlet and outlet fluid conditions. The accumulator formulation presented here separately models the vapor and liquid contents inside the total volume of the vessel. This simplifies the formulation of the accumulator and elucidates its true functionality in separating a two-phase mixture of liquid and vapor entering the vessel and setting the operating pressure. Figure 7.6 shows a schematic of the accumulator. It contains one inlet and outlet port. The analysis presented here is for a refrigerant accumulator located downstream of the condenser. The key assumptions involved in this model are:

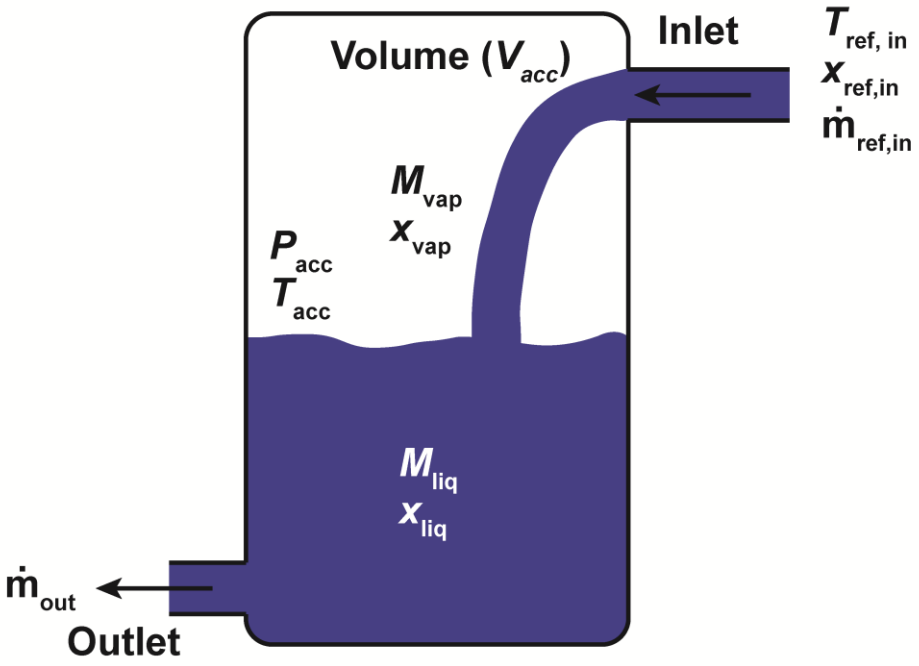

Figure 7.6: Schematic of refrigerant accumulator

- Inlet fluid phase is dependent on the accumulator pressure and condenser outlet conditions
- Outlet phase is always liquid
- Heat transfer from surrounding media is neglected
- Vapor and liquid phases are in thermal equilibrium at all time instants
- Chemical potential equilibrium exists at the liquid-vapor interface leading to absence of mass transfer between the phases
- Liquid and vapor phases can be characterized as separate single-phase entities with their average specific heats known as a function of temperatures and concentrations
- The pressure in the system is set by the vapor phase ammonia mass fraction and temperature ($Txq \rightarrow P_{acc}$)

Using the assumptions mentioned above, the equations representing the transient behavior of a refrigerant accumulator are shown below.

Vapor Phase Mass and Species Balance

$$\frac{dM_{vap}}{dt} = \dot{m}_{vap,in} \tag{7.13}$$

$$M_{vap}\frac{dx_{vap}}{dt} = \dot{m}_{vap,in}(x_{vap,in} - x_{vap}) \tag{7.14}$$

Liquid Phase Mass and Species Balance

$$\frac{dM_{liq}}{dt} = \dot{m}_{liq,in} - \dot{m}_{liq,out} \tag{7.15}$$

$$M_{liq}\frac{dx_{liq}}{dt} = \dot{m}_{liq,in}(x_{liq,in} - x_{liq}) \tag{7.16}$$

Combined Energy Balance

$$\frac{d}{dt}\{(M_{vap}Cp_{vap} + M_{liq}Cp_{liq})T_{acc}\} = (\dot{m}_{vap,in}Cp_{vap,in} + \dot{m}_{liq,in}Cp_{liq,in})T_{ref,in} - \dot{m}_{liq,out}Cp_{liq}T_{acc} \tag{7.17}$$

$$\begin{aligned} Cp_{liq,in} &\approx Cp_{liq} = Cp_{liq,avg} \\ Cp_{vap,in} &\approx Cp_{vap} = Cp_{vap,avg} \end{aligned} \tag{7.18}$$

$$(M_{vap}Cp_{vap,avg} + M_{liq}Cp_{liq,avg})\frac{dT_{acc}}{dt} = (\dot{m}_{vap,in}Cp_{vap,avg} + \dot{m}_{liq,in}Cp_{liq,avg})(T_{ref,in} - T_{acc}) \tag{7.19}$$

Phase Relations

$$
\begin{aligned}
q_{f,in} &= F(T_{f,in}, P_{acc}, x_{f,in}) \\
\dot{m}_{vap,in} &= \dot{m}_{f,in} q_{f,in} \\
\dot{m}_{liq,in} &= \dot{m}_{f,in}(1 - q_{f,in}) \\
x_{liq,in} &= F(T_{f,in}, P_{acc}, q = 0) \\
x_{vap,in} &= F(T_{f,in}, P_{acc}, q = 1) \\
q_{acc} &= \frac{M_{vap}}{M_{vap} + M_{liq}}
\end{aligned}
\tag{7.20}
$$

Operating pressure can be calculated as a dependent variable from the set of modeling equations.

$$P_{acc} = F(T_{vap}, x_{vap}, q = 1) \tag{7.21}$$

Eqs. 7.13-17.16 and 7.19-7.21 are used to simulate the transient response of the accumulator. A volume-based quality, q_{vol}, is defined to estimate the ratio of vapor volume relative to the total accumulator volume.

$$q_{vol} = \frac{1}{\left[1 + \frac{\rho_{vap}}{\rho_{liq}}\left(\frac{1}{q_{acc}} - 1\right)\right]} \tag{7.22}$$

Table 7.5 summarizes the physical parameters and operating conditions of the accumulator. The specified boundary conditions are: inlet and outlet mass flow rate, inlet refrigerant temeprature, and inlet mixture ammonia mass fraction.

Figure 7.7 shows the variation of accumulator temperature and pressure as a function of time. The prescribed boundary condition of inlet temperature achieves its steady-state value after 450 s of simulation time. The bulk temperature of the accumulator trails the

Table 7.5: Accumulator parameters

Parameter	Value
Accumulator volume (m^3)	0.0005
Initial temperature (°C)	25
Initial vapor mass quality – accumulator (kg kg^{-1})	0.9
Initial vapor phase ammonia mass fraction (kg kg^{-1})	0.997
Initial pressure (kPa)	294.9
Average specific heat capacity – vapor (kJ kg^{-1} K^{-1})	2.375
Average specific heat capacity – liquid (kJ kg^{-1} K^{-1})	4.75
Final inlet temperature (°C)	48
Inlet ammonia mass fraction (kg kg^{-1})	0.9975
Initial inlet mass flow rate (kg s^{-1})	0.0005
Initial outlet mass flow rate (kg s^{-1})	0
Final inlet mass flow rate (kg s^{-1})	0.003
Final outlet mass flow rate (kg s^{-1})	0.003

inlet temperature due to energy storage effects of the fluid inside the component volume and achieves a steady-state value of 48°C (identical to inlet temperature) after ~510 s of simulation time. As mentioned above, the pressure in the accumulator is dynamically set by the vapor phase temperature and concentration. Starting from the initial pressure of

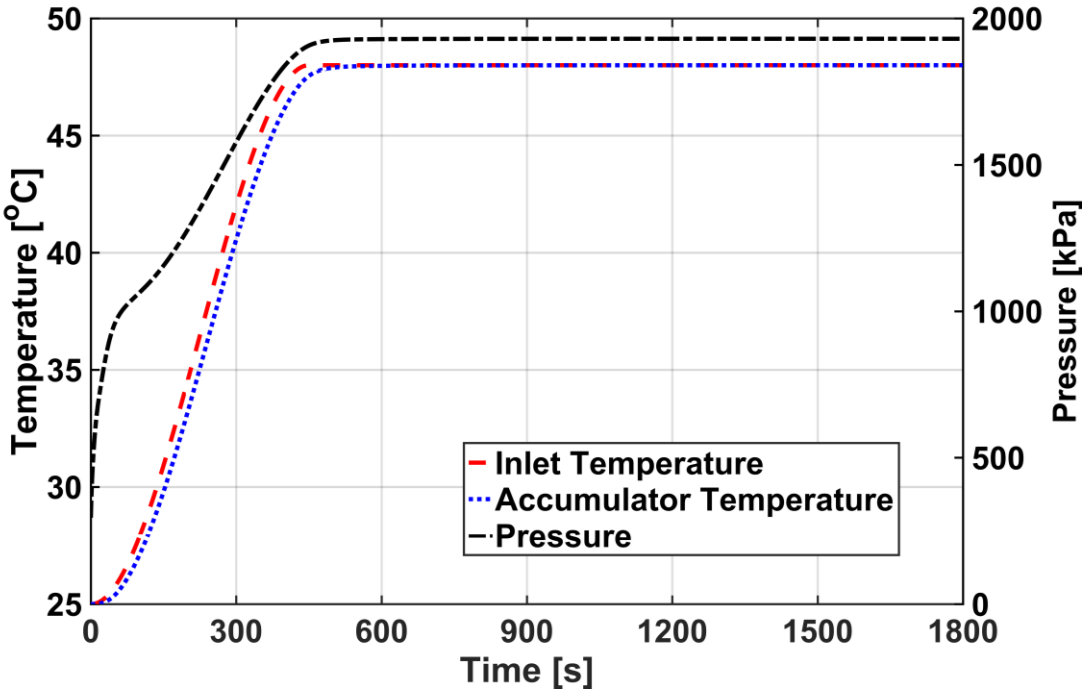

Figure 7.7: Temperature and pressure response of the accumulator

~295 kPa, a final steady-state value of 1930 kPa is achieved after ~640 s of simulation time. The pressure varies smoothly and increases at a higher rate in the beginning as compared to the later stage of transience. This is attributed to higher sensitivity of pressure towards vapor phase ammonia mass fraction which increases rapidly in the initial phase of transience due to higher vapor phase flow rate along with an increase in the temperature. After that point, the pressure becomes a function of temperature alone and increases at a slower rate to achieve its final steady-state value.

Figure 7.8 shows the variation of mass flow rates and the stored mass in the liquid and vapor phases, while Figure 7.9 shows the variation of qualities. The inlet and outlet mass flow rates are specified boundary conditions for the model and achieve their steady states after 420 s and 1200 s of simulation time, respectively. This simulation shows the behavior of the system during start-up. As the condenser outlet remains in vapor phase in the initial stages, the mass flow rate of the vapor phase remains approximately the same as the total inlet flow rate. Due to the increase in the system pressure, the inlet vapor mass quality starts to decrease (shown in Figure 7.9) after startup and continues to decrease until the inlet stream becomes subcooled. This causes the vapor phase mass flow rate to decrease and achieve a final value of zero at ~515 s. The stored mass of vapor also achieves a steady state (0.01 kg) simultaneously. Finally, as the outlet mass flow rate from the accumulator achieves steady state, the stored liquid mass also reaches its final value (0.85 kg). The final vapor mass quality in the accumulator is 0.012 with a corresponding volume-based quality of 0.31. This shows that after the system achieves steady state, the vapor phase accounts for 31% of the total accumulator volume.

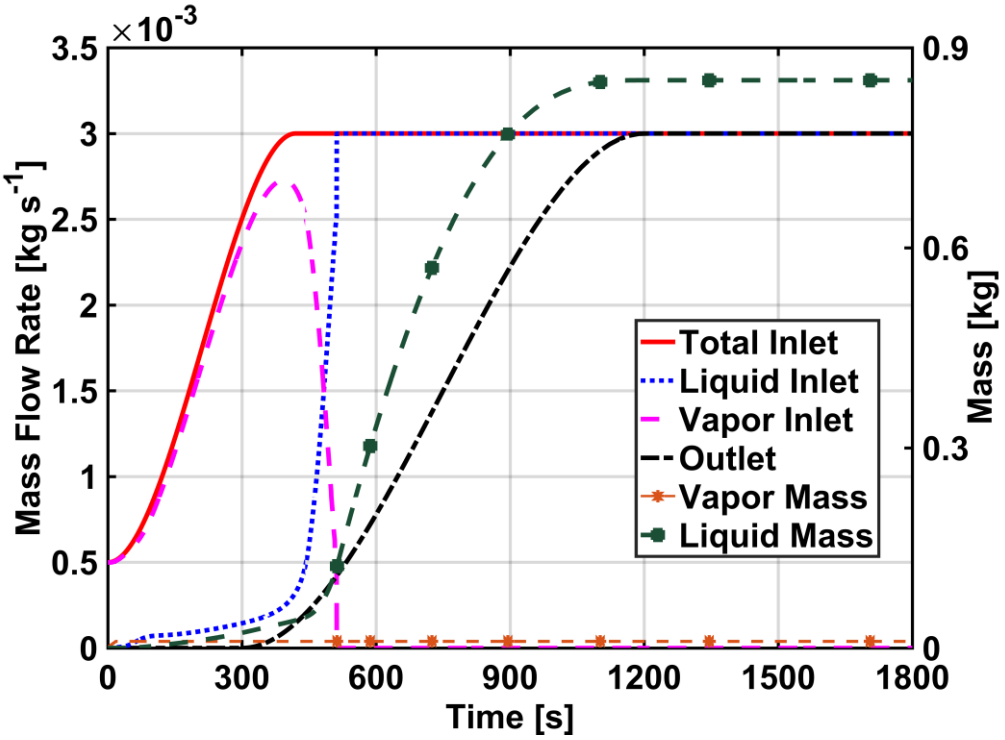

Figure 7.8: Mass flow rates and mass storage for the accumulator

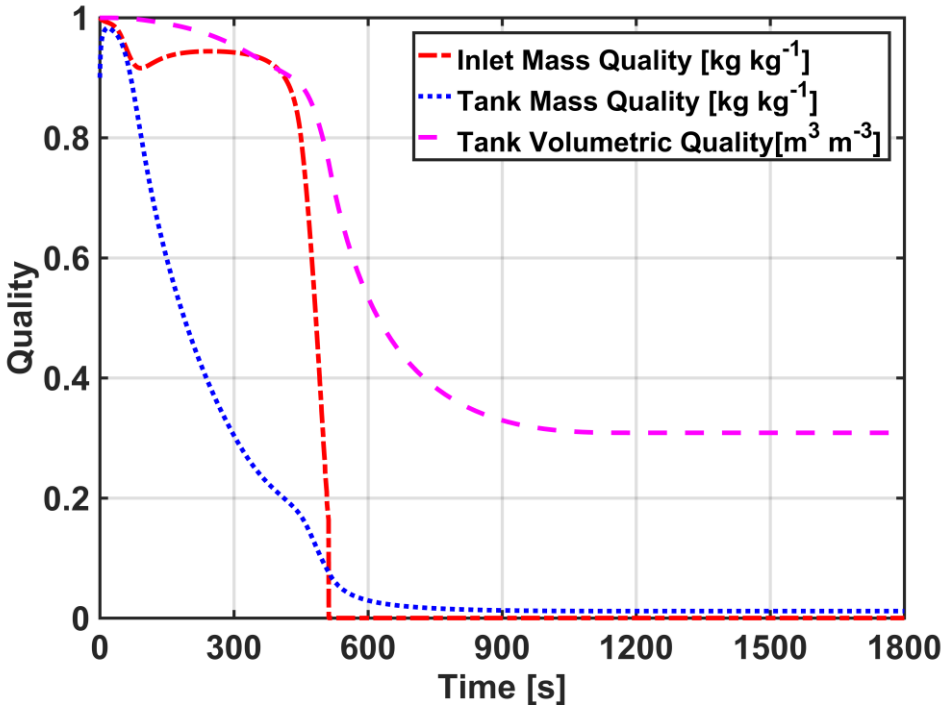

Figure 7.9: Quality variation for the accumulator

Finally, Figure 7.10 shows the variation of liquid phase ammonia mass fraction. The liquid phase ammonia mass fraction increases from its initial value of ~0.5 kg kg^{-1} to a final value of 0.9975 kg kg^{-1}. The various inflection points in the trend indicate the effects of changes in outlet mass flow rate which is a specified boundary condition.

7.6 Conclusion

Various aspects of dynamic models were addressed in this section. First, model reduction by neglecting mass storage inside microchannel passages helped reduce the complexity of heat exchanger models. The results from this model compared well with the original model accounting for the effects of compressibility of the phase-change fluid. The computational advantage from such a reduced-order model led to ~23% savings in the computational time.

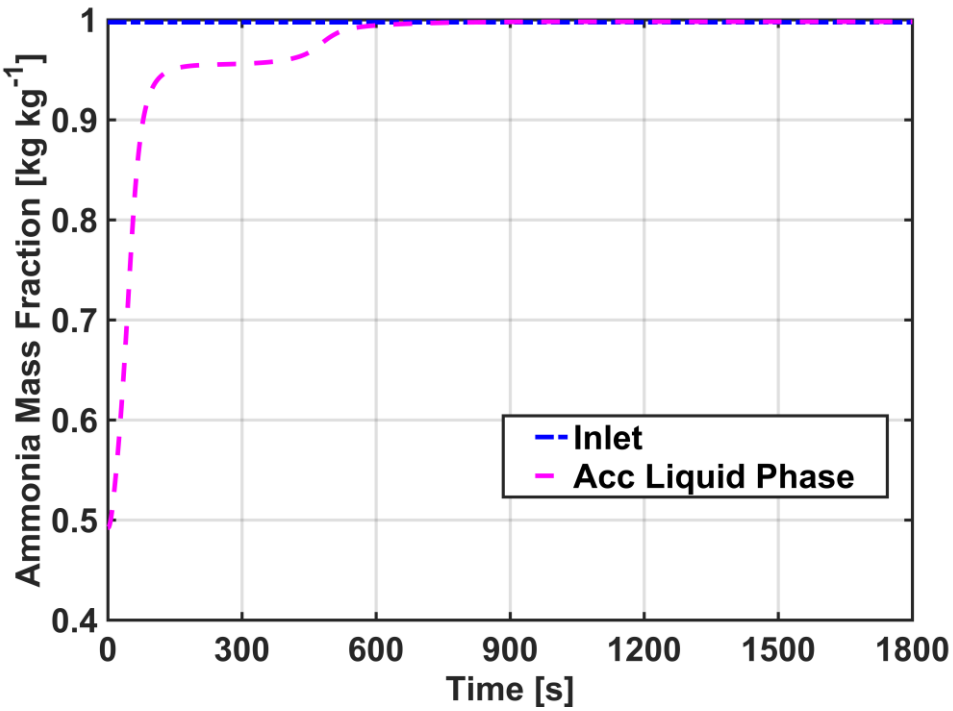

Figure 7.10: Concentration variation for the accumulator

Second, the computational speedup associated with ANN-based thermodynamic property routines was discussed using a case of transient simulation of the condenser. The property routines developed in this work led to ~80% decrease in the computational time as compared to existing EoS-based property libraries.

Thirdly, the experimental data were utilized to develop correlations for heat transfer conductance associated with different components of the absorption chiller. These correlations are formulated as a power-law function of the mass flow rate of the phase-change fluid. A sample study using experimental data on the transient response of the evaporator was utilized to validate the transient models. The model, with time-varying heat transfer conductance values, could predict the experimental response with high accuracy, both in terms of the magnitude and transient trends.

Finally, a formulation of the dynamic model of a refrigerant accumulator is presented. This formulation, based on conservation of mass and energy for liquid and vapor phases separately, predicts the performance of the accumulator and sets the high-pressure in the system. A similar model can be developed for the solution accumulator located downstream of the absorber and can be used to predict the evolution of the low-side pressure.

CHAPTER 8. CONCLUSIONS AND RECOMMENDATIONS

8.1 Conclusions

A comprehensive review of dynamic modeling methods and control methods for heat pumps is presented. The review identifies key methodologies available in the literature for developing dynamic models of varying complexity and computational expense. The transient models are crucial for understanding the dynamics of heat pumps in response to varying inputs and disturbances and developing control algorithms. Details of physics-based modeling methods are outlined, and the discretized finite volume and the moving-boundary methods are identified as potential techniques for transient simulations. Both the approaches have been used extensively in modeling the dynamics of vapor compression heat pumps. These methods are adapted in this study to simulate the transient response of ammonia-water absorption heat pumps. Review of control methodologies indicated that the research on the control of VAS is limited and seemingly unorganized in the literature. Numerous methods ranging from simple feedback control to advanced, non-linear. and model predictive control techniques have been developed for vapor compression systems. Analysis of degrees of freedom indicated that the controlled variables are identical for these systems and HVAC&R applications; therefore, the control algorithms can be suitably adapted for vapor absorption systems. The review identified directions for the development of advanced control algorithms for absorption systems.

Transient simulations utilizing discretized component models can require millions of thermodynamic property computations. These were identified to be a significant bottleneck in the computational efficiency of such simulations. In this work, ANN based property

routines for computing the thermodynamic properties of ammonia-water mixtures are developed. ANN based property calculations offer significantly enhanced computational speeds that can be a major advantage for large cycle simulations. Cascaded neural networks with multiple hidden layers are used to develop explicit property routines, which can utilize many combinations of property triplets as inputs and provide the desired thermodynamic states as outputs. The performance of these neural networks is assessed by comparing the predictions with established EoS property calculations. The error in the predictions is observed to be less than 0.5%. The computational efficiency of these routines is compared with two EoS implementations in EES® and MATLAB®, respectively. It is observed that ANN based property routines offer ~60% speedup in computing thermodynamic properties of ammonia-water mixtures.

Following the development of thermodynamic property routines, a detailed formulation for simulating the transient response of heat exchangers utilized in an ammonia-water absorption system is discussed. For single-inlet single-outlet components such as the condenser, evaporator and the absorber, emphasis is placed on the non-linear, DAE solver implementation, and comparison of FV and MB methods for solving the unsteady conservation equations is presented. The representative results are for a condenser; however, the formulation remains identical for simulating an evaporator or an absorber. The only modification is in the initial conditions and the formulation of heat transfer terms. The analysis of modeling and solution methods highlights the advantages of both FV and MB methods. While the FV method is simpler to formulate and the equation structure is fixed, the computational expense is very high for accurate simulations involving large number of nodes. The MB method provides significant computational

savings (more than 50 times reduction in computational time) and comparable accuracy. These features are presented through simulation test cases involving changes in refrigerant inlet mass flow rate and ambient temperature. Therefore, it is a recommended modeling paradigm for applications involving multiple evaluations of transient models and control design.

A detailed, physics-based dynamic model is developed to study the transient behavior of a small-scale ammonia-water desorber. A finite volume method is used to model the branched-tray desorber, with CVs placed around each desorber tray. The results of the steady-state models validated the modeling assumptions and demonstrated good agreement with the literature for the steady-state temperature profiles and heat transfer rate. Finally, simulations of perturbations in operating conditions were performed in which the desorber experienced a change from its design operating conditions by either increasing or decreasing the solution inlet mass flow rate, coupling fluid inlet temperature, or ambient temperature. The results of these simulations show the flexibility, accuracy, and efficiency of the detailed dynamic desorber model developed in this study. This model can be incorporated into a larger system model and assist in the evaluation of detailed and accurate system dynamics, as well as the development of robust control algorithms to improve the performance of small-scale ammonia-water absorption systems.

A previously developed dynamic model of an ammonia-water absorption system was utilized in a computational study to develop and evaluate novel control strategies for a small-scale (3.5 kW) ammonia-water absorption chiller. It was found that chiller performance can be controlled to yield an optimal evaporator temperature glide and modulate the evaporator cooling rate so that the delivered coolant temperature remains at

a set-point. Two separate feedback loops with proportional control were evaluated for controlling evaporator temperature glide and delivered coolant temperature. For a step change of 1.5°C in the evaporator temperature glide set-point, the controller requires ~250 s to bring the system to the new steady state condition. Also, combined control action using both loops was shown to satisfactorily track changes in load demand and ambient temperature, and leads to ~8% increase in COP as compared to a system operating without active control mechanisms. This model-based analysis of control schemes helped down select the control algorithms finally utilized in the experiments.

A small-capacity breadboard absorption chiller was fabricated to evaluate the transient performance of the system and evaluate the performance of the control algorithms developed in this study. The system capabilities involved simulation of part-load operation and variations in the ambient temperature, and included tunable inputs in the form of continuously variable actuators such as pumps, valves and heat source temperatures. The first part of the experimental studies involved perturbation in various inputs to the system. These studies indicated the relative impact of different inputs to the absorption system. It was observed that the system capacity was most significantly affected by changing the concentrated solution flow rate, followed by the change in desorber heat source conditions. The studies also highlighted the fact that a low-grade heat source could be utilized effectively by adjusting the concentrated solution flow rate. This can potentially enable the operation of ammonia-water absorption systems using a wider range of heat sources. A combination of the concentrated solution flow rate and heat source conditions could significantly change the system performance over wide range of cooling capacities.

The perturbation studies also indicated that the dilute solution valve position could be used to effectively control the outlet phase from the desorber. The refrigerant valve provided excellent control over the temperature glide in the evaporator. Therefore, the two valves could be used to optimize the performance of the desorber and the evaporator. The transient response of the system to these perturbations indicated that the effects of temperature changes required significantly longer time to propagate through the system in comparison to the changes in the solution mass flow rate. This information is used in the design of control algorithms and tuning of controller parameters.

In the second part of the experimental studies, advanced feedback control algorithms were developed that utilized all the available degrees of freedom in the system. This first ever multivariable feedback control approach is shown to perform well in many scenarios of system operation. Notably, the control algorithms can smoothly reduce the system performance to 50% of the design capacity while maintaining high COP. The dynamic effects of various interactions in the system are accounted for in the design of the control algorithms enabling stable and repeatable performance. The system is also able to regulate the system performance at off-design ambient conditions. The experiments also showed that the controller performance was as intended even for disturbances and capacity variation rates much steeper than are normally encountered in any application. This shows that for realistic operating situations, the control algorithms should be able to address the variations in the operating conditions.

The information from detailed experiments on the breadboard system and the computational limitations identified in previous studies on full-system simulations were utilized in the last part of this study to simplify the heat exchanger models. The complexity

involved in the solution of the system of DAE was reduced by neglecting the effects of fluid mass storage inside microscale geometries. These simplified models yielded significant computational savings without loss in accuracy. The experimental data were also utilized in validating the performance of the transient models. Modifications were made to relax assumptions made earlier about the time-invariant and uniform heat transfer coefficient in various components. The modified models showed good agreement with the experimental data and can be used in development of advanced model-based control algorithms.

8.2 Recommendations for Future Work

Various aspects of system dynamics and control for absorption heat pumps are addressed in this work, as outlined in the previous section. The computational framework for studying the transient response of the system and experimental demonstration of a multivariable feedback control methodology can be used for further research and development as discussed below.

- Optimized and experimentally validated computational models should be integrated to develop a complete system transient model that accurately predicts the performance of the system. As discussed in Chapter 7, some generalized correlations for heat transfer coefficients can be developed to predict the realistic variation of component performance as observed in experiments.
- A complete system model incorporating moving-boundary formulation for majority of the system components and reduced-order desorber-rectifier models

should be investigated. Such models can be used for system identification and analysis of advanced control algorithms.

- Experimentally validated models can be utilized in a model predictive control algorithm as shown in Figure 8.1. Pure feedback controllers provide only corrective action in the system once the effects of disturbances propagate to the controlled variables. In thermo-fluid systems with large time delays, such disturbances cannot be adequately rejected by a pure feedback controller and the system response can be sluggish. Predictive controllers are a better option in such cases as they can use a system model to predict the effect of the disturbances and provide necessary knowledge to the feedback controller to act faster and reject those disturbances. The system model will define a feedforward (FF) control law to predict the system response as disturbances in ambient

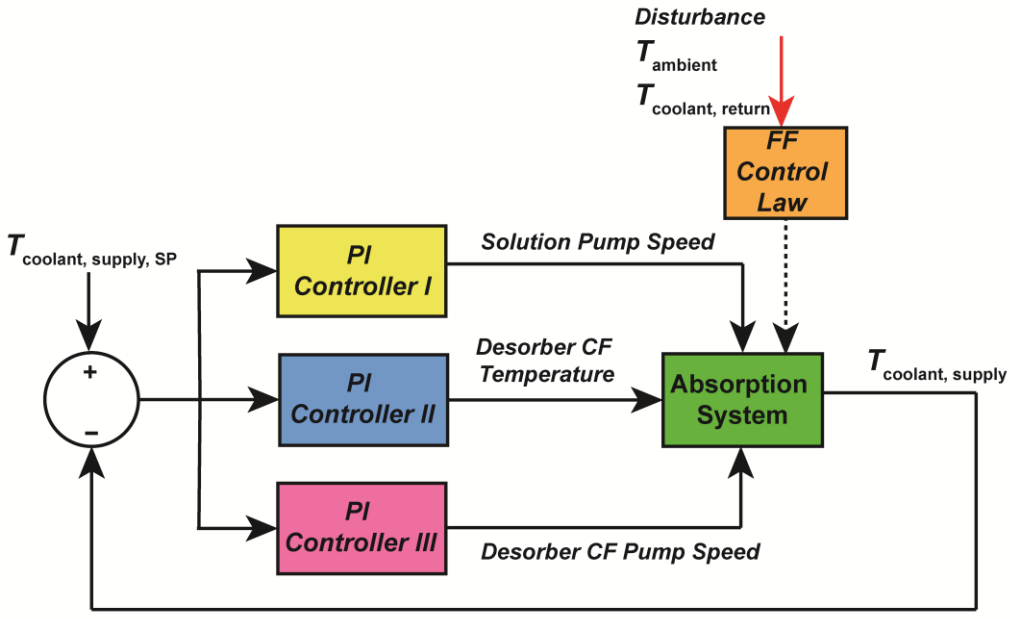

Figure 8.1: Advanced model-based control strategy

temperature and cooling load are detected. The feedback control law will then adjust the different manipulated variables to maintain system performance and the controlled variables at their desired values.

- Fine-tuning of the feedback control law proposed in this work can mitigate the slight over/undershoot observed in some test cases.
- Transient models also highlighted the non-linear nature of absorption systems. The information and model-based control can be employed in a non-linear control strategy to optimize the system performance while accounting for the complex relationships of different input-output variables. The system model can also be used to devise an optimal controller that can utilize a cost function based on either system efficiency or the cost of operation to optimize the system performance.
- Experimental evaluation of the control algorithms showed promising potential of the performance of the controller implemented on the breadboard system. The next step to further the technology will be to develop compact and inexpensive controllers that can be integrated with a prototype system. These can be in the form of miniaturized printed-circuit board (PCB) controllers that can significantly reduce the wiring and switches. A logic-based inexpensive controller hardware, such as programmable logic controller (PLC) that has been widely used in many process control applications and industries, can be a viable candidate for economic and large-scale development of these control systems.

- Finally, field testing of a small-capacity absorption system prototype with the controller mentioned above will provide deeper insights into the performance of the system in field conditions.

APPENDIX I: HEAT EXCHANGER PARAMETERS

This section presents the geometric parameters of different heat exchangers used in the ammonia-water absorption chiller presented in this work. The geometry is utilized in determining the heat transfer coefficients at the baseline operating condition. The heat transfer coefficient and the consequent heat transfer conductance values obtained here are representative of spatially averaged values. Typically, for a known flow rate at the incompressible/coupling fluid side of the component, a standard heat transfer correlation is utilized for the specified geometry. The calculated value of the heat transfer coefficient, known values of the heat transfer areas from the geometry of the heat exchangers, and the mean temperatures, flow rates, and the total heat transfer rate at baseline conditions are utilized to obtain an average heat transfer coefficient for the phase-change side. For more complicated geometries and flow configurations, such as the desorber and the rectifier, the heat transfer coefficients are obtained from the specific experimental results available in the literature. The parameters shown in bold represent the final values utilized in the dynamic model of each component. Other parameters are shown for calculation purposes. Figure A1.1 shows a schematic of the assembly of a microchannel heat exchanger with repeating units of refrigerant and CF sheets. The desorber and rectifier geometries were presented in Chapter 4 (Figure 4.9).

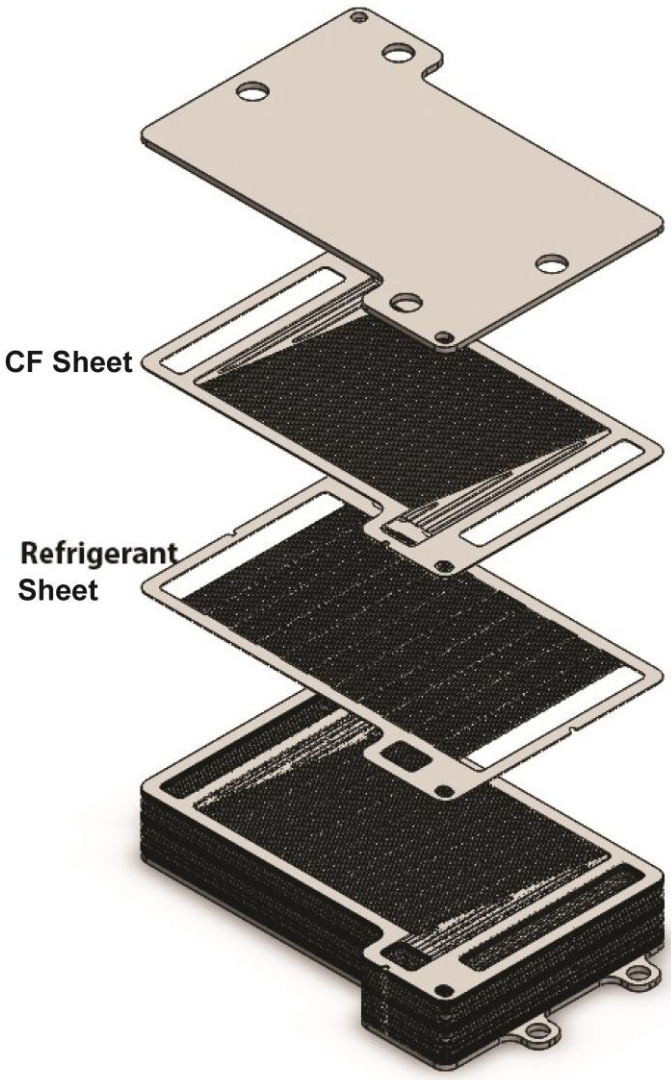

Figure A1.1: General schematic of a microchannel heat exchanger assembly (Absorber, Condenser, Evaporator, RPC, SHX)

Absorber

N_{sh} = 25 sheets
N_{ch} = 88 channels per sheet
D_h = 453 × 10^{-6} m
A_{cf} = 0.020803 m^2 per sheet
V_{cf} = 4.096 × 10^{-6} m^3 per sheet
$\dot{m}_{cf}$ = 0.112 kg s^{-1} (total)
$\dot{m}_f$ = 0.01175 kg s^{-1} (total)
$\frac{U_{cf} D_h}{k} = 2.0705(1 + 2.2916\phi - 2.5682\phi^2 + 1.4815\phi^3 - 0.0385\phi^4)$
$T_{cf,avg}$ = 43.1°C
$Cp_{cf,avg}$ = 4.182 kJ kg^{-1} K^{-1}
$\rho_{cf,avg}$ = 990.6 kg m^{-3}
Re_{cf} = 170
k = 0.6324 W m^{-1} K^{-1}
$2\varphi = \pi$
U_{cf} = 5702 W m^{-2} K^{-1}
UA_{cf} = 0.118 kW K^{-1} per sheet
$\dot{Q}_{cf}$ = 5.71 kW (total baseline)
$T_{f,avg}$ = 57.2°C
A_f = 0.02267 m^2 per sheet
V_f = 4.465 × 10^{-6} m^3 per sheet
U_f = 828.1 W m^{-2} K^{-1}
UA_f = 0.0187 kW K^{-1} per sheet
M_{hx} = 0.370 kg per sheet pair
Cp_{hx} = 0.50 kJ kg^{-1} K^{-1}
ρ_{hx} = 8000 kg m^{-3}

Condenser

N_{sh} = 25 sheets
N_{ch} = 75 channels per sheet
D_h = 453 × 10^{-6} m
A_{cf} = 0.01007 m^2 per sheet
V_{cf} = 1.982 × 10^{-6} m^3 per sheet
$\dot{m}_{cf}$ = 0.112 kg s^{-1} (total)
$\dot{m}_f$ = 0.0031 kg s^{-1} (total)

$$\frac{U_{cf} D_h}{k} = 2.0705(1 + 2.2916\phi - 2.5682\phi^2 + 1.4815\phi^3 - 0.0385\phi^4)$$

$T_{cf,avg}$ = 43.1°C
$Cp_{cf,avg}$ = 4.182 kJ kg^{-1} K^{-1}
$\rho_{cf,avg}$ = 990.6 kg m^{-3}
Re_{cf} = 191
k = 0.6294 W m^{-1} K^{-1}
$2\varphi = \pi$
U_{cf} = 5675 kW m^{-2} K^{-1}
UA_{cf} = 0.057 W K^{-1} per sheet
$\dot{Q}_{cf}$ = 3.473 kW (total baseline)
$T_{f,avg}$ = 47.04°C
A_f = 0.01154 m^2 per sheet
V_f = 2.272 × 10^{-6} m^3 per sheet
U_f = 3088 W m^{-2} K^{-1}
UA_f = 0.0356 kW K^{-1} per sheet
M_{hx} = 0.204 kg per sheet pair
Cp_{hx} = 0.50 kJ kg^{-1} K^{-1}
ρ_{hx} = 8000 kg m^{-3}

Evaporator

N_{sh} = 17 sheets (assembly of two CF sheets and one working fluid sheet)
N_{ch} = 62 channels per sheet
$D_h = 453 \times 10^{-6}$ m
A_{cf} = 0.01101 m^2 per sheet assembly
V_{cf} = 2.168 × 10^{-6} m^3 per sheet assembly
$\dot{m}_{cf}$ = 0.16 kg s^{-1} (total)
$\dot{m}_f$ = 0.0031 kg s^{-1} (total)

$$\frac{U_{cf} D_h}{k} = 2.0705(1 + 2.2916\phi - 2.5682\phi^2 + 1.4815\phi^3 - 0.0385\phi^4)$$

$T_{cf,avg}$ = 10.25°C
$Cp_{cf,avg}$ = 4.195 kJ kg^{-1} K^{-1}
$\rho_{cf,avg}$ = 999.7 kg m^{-3}
Re_{cf} = 120.5
k = 0.5793 W m^{-1} K^{-1}
$2\varphi = \pi$
U_{cf} = 5223 W m^{-2} K^{-1}
UA_{cf} = 0.057 kW K^{-1} per sheet assembly
$\dot{Q}_{cf}$ = 3.54 kW (total baseline)
$T_{f,avg}$ = 4.24°C
A_f = 0.00729 m^2 per sheet
V_f = 2.087 × 10^{-6} m^3 per sheet
U_f = 12062 W m^{-2} K^{-1}
UA_f = 0.0878 kW K^{-1} per sheet
M_{hx} = 0.295 kg per sheet pair
Cp_{hx} = 0.50 kJ kg^{-1} K^{-1}
ρ_{hx} = 8000 kg m^{-3}

Refrigerant Precooler

N_{sh} = 25 sheets
N_{ch} = 42 channels per sheet
$D_h = 453 \times 10^{-6}$ m
A_{cf} = 0.00748 m^2 per sheet assembly
V_{cf} = 1.473 × 10^{-6} m^3 per sheet assembly
$\dot{m}_{cf}$ = 0.0031 kg s^{-1} (total)
$\dot{m}_f$ = 0.0031 kg s^{-1} (total)
$\frac{U_{cf} D_h}{k} = 2.0705(1 + 2.2916\phi - 2.5682\phi^2 + 1.4815\phi^3 - 0.0385\phi^4)$
$T_{cf,avg}$ = 34.09°C
$Cp_{cf,avg}$ = 4.923 kJ kg^{-1} K^{-1}
$\rho_{cf,avg}$ = 569.5 kg m^{-3}
Re_{cf} = 40.1
k = 0.4562 W m^{-1} K^{-1}
$2\varphi = \pi$
U_{cf} = 4113 W m^{-2} K^{-1}
UA_{cf} = 0.0308 kW K^{-1} per sheet assembly
$\dot{Q}_{cf}$ = 0.330 kW (total baseline)
$T_{f,avg}$ = 25.10°C
A_f = 0.00835 m^2 per sheet
V_f = 1.644 × 10^{-6} m^3 per sheet
U_f = 265.1 W m^{-2} K^{-1}
UA_f = 0.0022 kW K^{-1} per sheet
M_{hx} = 0.188 kg per sheet pair
Cp_{hx} = 0.50 kJ kg^{-1} K^{-1}
ρ_{hx} = 8000 kg m^{-3}

Solution Heat Exchanger

N_{sh} = 25 sheets
N_{ch} = 42 channels per sheet
$D_h = 453 \times 10^{-6}$ m
A_{cf} = 0.00835 m^2 per sheet assembly
V_{cf} = 1.644 × 10^{-6} m^3 per sheet assembly
$\dot{m}_{cf}$ = 0.0084 kg s^{-1} (total)
$\dot{m}_f$ = 0.0118 kg s^{-1} (total)

$$\frac{U_{cf} D_h}{k} = 2.0705(1 + 2.2916\phi - 2.5682\phi^2 + 1.4815\phi^3 - 0.0385\phi^4)$$

$T_{cf,avg}$ = 100.6°C
$Cp_{cf,avg}$ = 4.404 kJ kg^{-1} K^{-1}
$\rho_{cf,avg}$ = 807.75 kg m^{-3}
Re_{cf} = 58.04
k = 0.5925 W m^{-1} K^{-1}
$2\varphi = \pi$
U_{cf} = 5342 W m^{-2} K^{-1}
UA_{cf} = 0.0446 kW K^{-1} per sheet assembly
$\dot{Q}_{cf}$ = 2.65 kW (total baseline)
$T_{f,avg}$ = 81.7°C
A_f = 0.00748 m^2 per sheet
V_f = 1.473 × 10^{-6} m^3 per sheet
U_f = 855 W m^{-2} K^{-1}
UA_f = 0.0064 kW K^{-1} per sheet
M_{hx} = 0.188 kg per sheet pair
Cp_{hx} = 0.50 kJ kg^{-1} K^{-1}
ρ_{hx} = 8000 kg m^{-3}

Rectifier (Staedter, 2018)

N_{sh} = 8 sheets
N_{ch} = 51 channels per sheet on coupling fluid side
D_h = 477 × 10^{-6} m
A_{cf} = 0.00553 m^2 per sheet assembly
V_{cf} = 1.347 × 10^{-6} m^3 per sheet assembly
$\dot{m}_{cf}$ = 0.00048 kg s^{-1} (total)
$\dot{m}_f$ = 0.00334 kg s^{-1} (total)
$\frac{U_{cf} D_h}{k} = 2.0705(1 + 2.2916\phi - 2.5682\phi^2 + 1.4815\phi^3 - 0.0385\phi^4)$
$T_{cf,avg}$ = 61.65°C
$Cp_{cf,avg}$ = 4.535 kJ kg^{-1} K^{-1}
$\rho_{cf,avg}$ = 825 kg m^{-3}
Re_{cf} = 55
k = 0.5332 W m^{-1} K^{-1}
$2\varphi = \pi$
U_{cf} = 4566 W m^{-2} K^{-1}
UA_{cf} = 0.0253 kW K^{-1} per sheet assembly
$\dot{Q}_{cf}$ = 0.867 kW (total baseline)
$T_{f,avg}$ = 82.5°C
UA_f = 0.0065 kW K^{-1} per sheet
M_{hx} = 0.388 kg per sheet pair
Cp_{hx} = 0.50 kJ kg^{-1} K^{-1}
ρ_{hx} = 8000 kg m^{-3}

Desorber (Staedter, 2018)

N_{sh} = 8 sheets (assembly of two CF sheets and one working fluid sheet)
N_{ch} = 85 channels per sheet on coupling fluid side
D_h = 477 × 10^{-6} m
A_{cf} = 0.03147 m^2 per sheet assembly
V_{cf} = 7.665 × 10^{-6} m^3 per sheet assembly
$\dot{m}_{cf}$ = 0.1075 kg s^{-1} (total)
$\dot{m}_f$ = 0.01175 kg s^{-1} (total)
$T_{cf,avg}$ = 136°C
$Cp_{cf,avg}$ = 2.431 kJ kg^{-1} K^{-1}
$\rho_{cf,avg}$ = 825 kg m^{-3}
U_{cf} = 1500 W m^{-2} K^{-1} (Staedter, 2018)
UA_{cf} = 0.0472 kW K^{-1} per sheet assembly
$\dot{Q}_{cf}$ = 4.64 kW (total baseline)
ε_{tray} = [0.7,0.7,0.75,0.75,0.85,0.85,1] (top to bottom)
A_f = 0.02003 m^2 per sheet
V_f = 42.15× 10^{-6} m^3 per sheet
U_f = 5000 W m^{-2} K^{-1} (Staedter, 2018)
UA_f = 0.1001 kW K^{-1} per sheet
M_{hx} = 1.163 kg per sheet pair
Cp_{hx} = 0.50 kJ kg^{-1} K^{-1}
ρ_{hx} = 8000 kg m^{-3}

APPENDIX II: SAMPLE CALCULATION: BASELINE EXPERIMENTAL DATA REDUCTION

Inputs/Measurements	Equation	Result
RPC $T_{liq,in}$ = 41.45 ± 0.5°C $T_{liq,out}$ = 9.95 ± 0.5°C $T_{vap,in}$ = 7.27 ± 0.5°C $T_{vap,out}$ = 36.6 ± 0.5°C P_{cond} = 1728 ± 1.034 kPa P_{evap} = 519.9 ± 0.3103 kPa $\dot{m}_{ref}$ = 0.00255 ± 0.00000255 kg s^{-1}	$\dot{Q}_{liq,RPC} = \dot{m}_{ref}(h_{liq,in} - h_{liq,out})$ $\dot{Q}_{vap,RPC} = \dot{m}_{ref}(h_{vap,out} - h_{vap,in})$ $h_{liq,in} = G(T_{liq,in}, P_{cond}, x_{ref})$ $h_{liq,out} = G(T_{liq,out}, P_{cond}, x_{ref})$ $h_{vap,in} = G(T_{vap,in}, P_{evap}, x_{ref})$ $h_{vap,out} = G(T_{vap,out}, P_{evap}, x_{ref})$ $\dot{Q}_{vap,RPC} = \dot{Q}_{liq,RPC}$	x_{ref} = 0.9951 ± 0.00154 kg kg^{-1} $\dot{Q}_{RPC}$ = 0.386 ± 0.009 kW ε_{RPC} = 0.9241 ± 0.01933
Evaporator $T_{ref,in}$ = 4.75 ± 0.5°C $T_{ref,out}$ = 7.33 ± 0.5°C $T_{cf,in}$ = 13 ± 0.5°C $T_{cf,out}$ = 9.04 ± 0.5°C P_{evap} = 519.9 ± 0.3103 kPa $\dot{m}_{ref}$ = 0.00255 ± 0.00000255 kg s^{-1} $\dot{m}_{cf}$ = 0.1595 ± 0.0001595 kg s^{-1}	$\dot{Q}_{cf,evap} = \dot{m}_{cf} Cp_{cf}(T_{cf,in} - T_{cf,out})$ $Cp_{cf} = G(T_{cf,avg}, P_{cf} = P_{amb})$	Cp_{cf} = 4.194 ± 0.000523 kJ kg^{-1} K^{-1} $\dot{Q}_{evap}$ = 2.65 ± 0.473 kW

Sample Calculation: Baseline Experimental Data Reduction (continued)

Condenser		
$T_{ref,in}$ = 59.07 ± 0.5°C $T_{ref,out}$ = 43.28 ± 0.5°C $T_{cf,in}$ = 36.98 ± 0.5°C $T_{cf,out}$ = 44.68 ± 0.5°C P_{cond} = 1728 ± 1.034 kPa $\dot{m}_{ref}$ = 0.00255 ± 0.00000255 kg s^{-1} $\dot{m}_{cf}$ = 0.0918 ± 0.000918 kg s^{-1}	$\dot{Q}_{ref,cond} = \dot{m}_{ref}(h_{ref,in} - h_{ref,out})$ $\dot{Q}_{cf,cond} = \dot{m}_{cf} Cp_{cf}(T_{cf,out} - T_{cf,in})$ $Cp_{cf} = G(T_{cf,avg}, P_{cf} = P_{amb})$ $h_{ref,in} = G(T_{ref,in}, P_{cond}, x_{ref})$ $h_{ref,out} = G(T_{ref,out}, P_{cond}, x_{ref})$	Cp_{cf} = 4.179 ± 0.000039 kJ kg^{-1} K^{-1} $\dot{Q}_{cond} = \dot{Q}_{cond,ref}$ = 2.88 ± 0.017 kW
Rectifier		
$T_{vap,in}$ = 106.7 ± 0.5°C $T_{ref,out}$ = 59.4 ± 0.5°C $T_{refl,out}$ = 72.34 ± 0.5°C $T_{cf,in}$ = 36.89 ± 0.5°C $T_{cf,out}$ = 70.46 ± 0.5°C P_{rec} = 1720 ± 1.034 kPa $\dot{m}_{ref,out}$ = 0.00255 ± 0.00000255 kg s^{-1} x_{ref} = 0.9951 ± 0.00154 kg kg^{-1} $x_{vap,in}$ = 0.952 ± 0.001121 kg kg^{-1}	$\dot{Q}_{cf,rec} = \dot{m}_{cf}(h_{cf,out} - h_{cf,in})$ $\dot{Q}_{f,rec} = \dot{m}_{vap,in} h_{vap,in} - \dot{m}_{ref,out} h_{ref,out} - \dot{m}_{refl,out} h_{refl,out}$ $\dot{Q}_{cf,rec} = \dot{Q}_{f,rec}$ $h_{vap,in} = G(T_{vap,in}, P_{rec}, x_{vap,in})$ $h_{ref,out} = G(T_{ref,out}, P_{rec}, x_{ref})$ $h_{refl,out} = G(T_{refl,out}, P_{rec}, x_{refl})$ $h_{cf,out} = G(T_{cf,out}, P_{rec}, x_{cs})$ $h_{cf,in} = G(T_{cf,in}, P_{rec}, x_{cs})$ $\dot{m}_{ref,out} = \dot{m}_{vap,in} - \dot{m}_{refl,out}$ $\dot{m}_{vap,in} x_{vap,in} = \dot{m}_{ref,out} x_{ref} + \dot{m}_{refl,out} x_{refl,out}$	$\dot{Q}_{rec}$ = 0.838 ± 0.038 kW $\dot{m}_{vap,in}$ = 0.002799 ± 0.0000321 kg s^{-1} $\dot{m}_{refl,out}$ = 0.0002494± 0.00003202 kg s^{-1} x_{refl} = 0.5115 ± 0.05227 kg kg^{-1} $\dot{m}_{cf}$ = 0.005607 ± 0.0002213 kg s^{-1}

Sample Calculation: Baseline Experimental Data Reduction (continued)

Desorber		
$T_{cs,in}$ = 105.5 ± 0.5°C $T_{ds,out}$ = 135 ± 0.5°C $T_{vap,out}$ = 107.8 ± 0.5°C $T_{cf,in}$ = 145 ± 0.5°C $T_{refl,in}$ = 72.34 ± 0.5°C $T_{cf,out}$ = 126.3 ± 0.5°C P_{des} = 1720 ± 1.034 kPa $\dot{m}_{cs,in}$ = 0.01212 ± 0.000009904 kg s^{-1} $\dot{m}_{ds,out}$ = 0.00957 ± 0.00000957 kg s^{-1} $\dot{m}_{cf}$ = 0.09833 ± 0.0006413 kg s^{-1} $\dot{m}_{refl,in}$ = 0.0002494± 0.00003202 kg s^{-1} $\dot{m}_{vap,out}$ = 0.002799 ± 0.0000321 kg s^{-1} x_{refl} = 0.5115 ± 0.05227 kg kg^{-1}	$\dot{Q}_{cf,des} = \dot{m}_{cf} Cp_{cf} (T_{cf,in} - T_{cf,out})$ $Cp_{cf} = G(T_{cf,avg}, P_{cf} = P_{amb})$ $\dot{Q}_{f,des} = \dot{m}_{vap,out} h_{vap,out} + \dot{m}_{ds,out} h_{ds,out} - \dot{m}_{cs,in} h_{cs,in} - \dot{m}_{refl,in} h_{refl,in}$ $x_{ds} = G(T_{ds,out}, P_{des}, q = 0)$ $x_{vap,out} = G(T_{vap,out}, P_{des}, q = 1)$ $h_{cs,in} = G(T_{cs,in}, P_{des}, x_{cs})$ $h_{vap,out} = G(T_{vap,out}, P_{des}, x_{vap,out})$ $h_{ds,out} = G(T_{ds,out}, P_{des}, x_{ds})$ $h_{refl,in} = G(T_{refl,in}, P_{des}, x_{refl})$	$\dot{Q}_{des}$ = 4.482 ± 0.172 kW x_{ds} = 0.2723 ± 0.002025 kg kg^{-1} $x_{vap,out}$ = 0.952 ± 0.001121 kg kg^{-1}
Absorber		
$T_{cs,in}$ = 71.54 ± 0.5°C $T_{cs,out}$ = 37.18 ± 0.5°C $T_{cf,in}$ = 37.17 ± 0.5°C $T_{cf,out}$ = 39.97 ± 0.5°C P_{abs} = 505.9 ± 0.3103 kPa $\dot{m}_{cf}$ = 0.3089 ± 0.00309 kg s^{-1} $\dot{m}_{ds,in}$ = 0.00957 ± 0.00000957 kg s^{-1} $\dot{m}_{ref,in}$ = 0.00255 ± 0.00000255 kg s^{-1}	$\dot{Q}_{cs,abs} = \dot{m}_{cs} (h_{cs,in} - h_{cs,out})$ $\dot{Q}_{cf,abs} = \dot{m}_{cf} Cp_{cf} (T_{cf,out} - T_{cf,in})$ $Cp_{cf} = G(T_{cf,avg}, P_{cf} = P_{amb})$ $h_{cs,in} = G(T_{cs,in}, P_{abs}, x_{cs})$ $h_{cs,out} = G(T_{cs,out}, P_{abs}, x_{cs})$ $\dot{Q}_{abs} = \dot{Q}_{des} + \dot{Q}_{evap} - \dot{Q}_{cond}$ $\dot{m}_{cs} = \dot{m}_{ds,in} + \dot{m}_{ref,in}$ $\dot{m}_{cs} x_{cs} = \dot{m}_{ds,in} x_{ds} + \dot{m}_{ref,in} x_{ref}$	$\dot{Q}_{abs}$ = 4.256 ± 0.5036 kW x_{cs} = 0.4244 ± 0.00164 kg kg^{-1} $\dot{m}_{cs}$ = 0.01212 ± 0.000009904 kg s^{-1}

Sample Calculation: Baseline Experimental Data Reduction (continued)

SHX	$\dot{Q}_{cs,SHX} = \dot{m}_{cs}(h_{cs,out} - h_{cs,in})$ $\dot{Q}_{ds,SHX} = \dot{m}_{ds}(h_{ds,in} - h_{ds,out})$ $h_{cs,in} = G(T_{cs,in}, P_{SHX}, x_{cs})$ $h_{cs,out} = G(T_{cs,out}, P_{SHX}, x_{cs})$ $h_{ds,in} = G(T_{ds,in}, P_{SHX}, x_{ds})$ $h_{ds,out} = G(T_{ds,out}, P_{SHX}, x_{ds})$	$\dot{Q}_{SHX}$ = 3.323 ± 0.03071 kW ε_{SHX} = 0.9703 ± 0.008347
$T_{cs,in}$ = 71.54 ± 0.5°C $T_{cs,out}$ = 37.18 ± 0.5°C $T_{ds,in}$ = 37.17 ± 0.5°C $T_{ds,out}$ = 39.97 ± 0.5°C P_{SHX} = 1720 ± 1.034 kPa $\dot{m}_{cs}$ = 0.01212 ± 0.000009904 kg s^{-1} $\dot{m}_{ds}$ = 0.3089 ± 0.00309 kg s^{-1}		
Overall System	$COP = \frac{\dot{Q}_{evap}}{\dot{Q}_{des}}$	COP = 0.5916 ± 0.1079
System Performance		

APPENDIX III: SEVERE AMBIENT OPERATION OF ABSORPTION SYSTEMS

This section presents results from testing of the breadboard system at severe ambient conditions of 50°C cooling water temperature at the inlet of the absorber and the condenser. Vapor compression systems using synthetic refrigerants and blends such as R22, R410a etc. demonstrate a steep decrease in the system COP as the ambient temperature increases. Motta and Domanski (2000) compared the performance of several commonly used refrigerants in vapor compression systems at elevated ambient temperatures. All refrigerants demonstrated a steep and sharp decrease in the system COP relative to the design value at 35°C ambient. Most systems demonstrated a reduction in system performance by > 20% even at temperatures approaching 45°C. Therefore, the aim of this study was to quantify the performance of the absorption system and characterize its resilience at elevated ambient temperatures.

This experiment was conducted at 50°C cooling water temperature corresponding to 46-47°C outdoor air temperature. Table A3.1 shows the heat transfer performance of the component in comparison to the baseline operating conditions at a 37°C cooling water temperature (representative of a 34-35°C ambient temperature). As the cooling water

Table A3.1: Steady-state system operation at severe ambient conditions

Component	Baseline Heat Transfer Rate (kW)	Heat Transfer Rate (kW)
Absorber	4.25	3.60
Condenser	2.88	1.94
Desorber	4.48	3.62
Evaporator	2.65	1.92
Rectifier	0.84	0.91
RPC	0.39	0.31
SHX	3.32	3.44

temperature increased, both the pressure levels in the system increased. The condenser pressure increased to 2283 kPa, while the absorber pressure is controlled such that the refrigerant temperature in the evaporator does not exceed values beyond which the capacity of the system would decrease to a very low value. To maintain the low-side pressure near design, the refrigerant flow rate was reduced by closing the refrigerant valve leading to a reduced ammonia mass fraction inside the absorber. The refrigerant flow rate at steady-state conditions was 0.0019 kg s^{-1}, leading to a concentration in the absorber of 0.392 kg kg^{-1} and an absorber pressure of 513.6 kPa. At high ambient temperatures and a desorber heat source temperature hotter than design (~155°C), the refrigerant vapor generated in the desorber contains a higher fraction of water as well. This led to an increase in the rectifier duty and the coolant flow rate in the rectifier was maximized. The system could still maintain high refrigerant purity with an ammonia-mass fraction of 0.995 kg kg^{-1}.

A COP of the system of 0.53 was achieved, which is ~88.3% of the system COP at 34-35°C ambient conditions. This shows that the COP of the absorption system did not decrease at sharply at severe ambient conditions. The major reason here is the flexibility of the system to operate at these operating conditions with tunable valve positions that maintain the desired pressure in the evaporator and the absorber, and the capability to adjust the performance of the desorber through changes in the solution flow rate and heat source conditions.

This was a proof-of-concept study and can potentially achieve improved performance using solution pump speed variations and appropriately sized valves. Specifically, the refrigerant valve became oversized at these operating conditions and was very marginally open to allow the flow of the refrigerant. It is believed that the capacity

can be increased such that the effects on the system COP are minimal (<10%) at severe ambient conditions. This effect was also observed in the parametric studies presented in Chapter 6. Figure A3.1 shows the variation in system capacity and COP as a function of the cooling water temperature. The relatively gentle slope in system COP with variation in the temperature of the cooling water demonstrates relatively small effect of increasing ambient temperature on system COP compared to the much larger deterioration of the COP with ambient temperature increases in vapor compression systems.

Several hydrodynamic considerations should also be accounted for when operating these systems at high-ambient temperatures. As the high-side pressure increases, the vapor generation in the desorber decreases, especially when the concentrated solution has a lower ammonia-mass fraction as compared to the design values. At this stage, a rapid increase in the solution flow rate can lead to potential flooding of the desorber and liquid solution flowing into the rectifier. This is typically harmful for the operation of ammonia-water heat

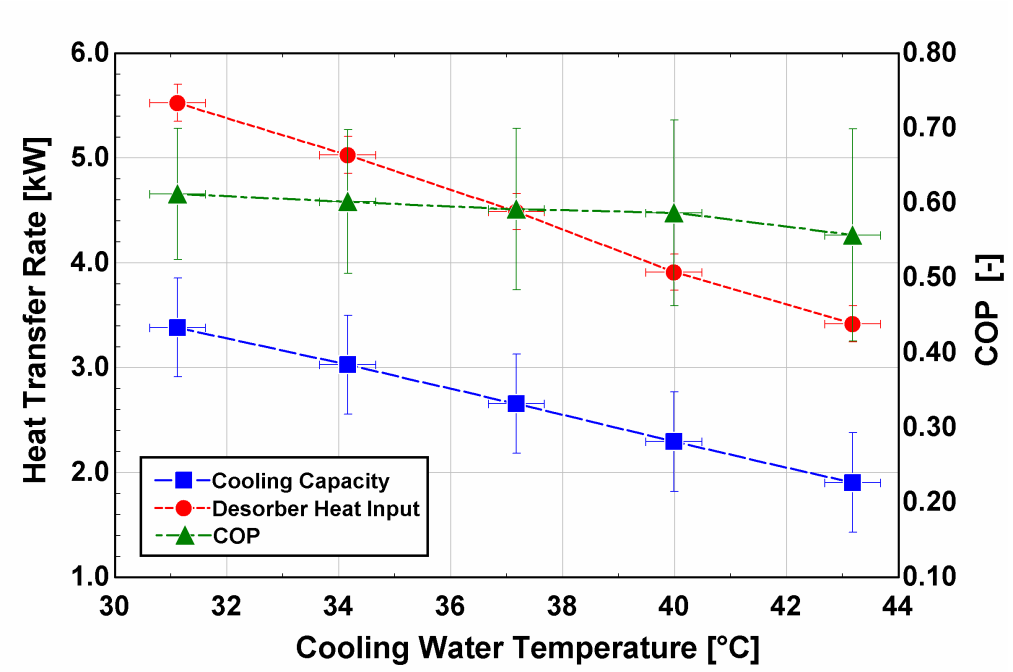

Figure A3.1: Effect of cooling water temperature: heat transfer rates and COP

pumps as the refrigerant mass fraction of ammonia decreases sharply and takes a long time to be restored back to its original value. On the other hand, if the heat source conditions interacting with the desorber are changed rapidly, it can also lead to very hot vapor at the outlet of the desorber and potential liquid entrainment. Therefore, mechanisms for capacity control should be applied more carefully for operating conditions beyond 45°C ambient temperature.

APPENDIX IV: ABSORPTION SYSTEM OPERATION

This section will discuss basics of absorption system fabrication, operation, troubleshooting steps to achieve design performance after initial testing, and guidelines for safe and repeatable system operation.

- **System Fabrication**

The fabrication of an absorption system involves important considerations for hydrodynamic and heat transfer effects. The fluid lines between different components should minimize pressure drops. Relative placement of components and flow configuration is also important. Some considerations are:

1. The condenser orientation should allow downward flow of the condensing fluid to minimize the two-phase pressure drop.
2. Similarly, the evaporating flow in the evaporator and refrigerant precooler should be in the upward direction.
3. If a vapor-liquid co-flow absorber is being utilized, the mixing of the two streams should occur upstream of the inlet to the absorber unless the absorber includes a design and mechanism for the mixing of liquid and vapor flows. The mixing section upstream of the absorber can be a tube-in-tube type of design or a vapor injection system inside the liquid stream. The final selection depends on which design would allow better mixing under the constraint of minimizing the pressure drop.

4. Excessive pressure drop on the low-side of the system can significantly affect the performance by increasing the temperature of the refrigerant at the inlet of the evaporator and decreasing the cooling capacity. To lower the temperature of the refrigerant, the refrigerant mass flow is typically reduced, which in turn causes a reduction in the cooling capacity too. Therefore, careful design and analysis should be performed to minimize the pressure drop in the system.
5. Fluid accumulators are crucial for providing the buffer fluid mass during transience and enable safe and steady operation of components such as the solution pump and the desorber. Liquid outlet must be ensured out of the accumulators. The solution pump should always receive liquid phase at the inlet from the solution accumulator to prevent instabilities in the flow and to prevent any damage to the pump. The refrigerant accumulator provides liquid refrigerant to the refrigerant precooler ensuring that the high-pressure side of the precooler is always single-phase liquid. Discharge ports should be provided at the top and bottom of each accumulator to release non-condensable gases.
6. The dilute solution accumulator serves the purpose of providing liquid phase dilute solution at the inlet of the solution heat exchanger. It also serves to maintain liquid level at the bottom of the desorber and prevents the refrigerant vapor generated in the bottom sections of the desorber to exit via the dilute solution stream. Therefore, the inlet port of the dilute solution accumulator is typically located approximately an inch above the bottom port of the desorber such that it maintains that height of liquid column. A vapor trap (u-shaped piece of tubing) is

added to feed into the dilute solution accumulator to further prevent the flow of the vapor through the dilute solution stream.

7. The reflux stream exiting the rectifier is mixed with the concentrated solution entering the desorber. A port is provided in the desorber to allow mixing of these two streams.
8. Coriolis mass flow sensors must be installed on single-phase fluid streams to ensure accurate measurements. Also, the concentrated solution flow rate should be measured downstream of the rectifier to allow for pulsations from the pump to subside and reduce the noise in the measurements. Figure 6.1 shows the location of measurement probes as installed on the system.
9. Further considerations involve installing the pressure transducers in a configuration such that the probe is pointing downward or sideways so that the tip of the probe does not collect any debris. The thermocouples should be installed such that the tip is placed in the bulk of the flow and not too close to the tube or header wall.
10. In-line sight glasses and level indicators should be installed to inspect the phase of the flow leaving the rectifier and the dilute solution, and fluid levels in different accumulators, respectively.
11. Isolation valves should be installed at the inlet and outlet of the pump to allow for easy replacement in the event of a malfunction. Isolation valves should also be installed between he high- and low-side components to allow for pressure testing at operating pressure levels.

12. Finally, particulate filters should be installed upstream of all pumps to prevent damage to pumps and clogging of microchannel flow passages.

- **Evacuation and Charging with Ammonia-Water**

1. After the assembly of the system, it should be pressure tested at the levels of actual system operation. Prior to charging with ammonia-water mixture, the system should be sealed at high-pressure, typically up to ~2500 – 3000 kPa. Most of the time, the leaks are detected by spraying soap solution along the fittings. For very small leaks, a refrigerant leak detector can be used by charging the system with a synthetic refrigerant such as R134a and boosting the pressure to the desired level using nitrogen.
2. After the system is pressure tested, it should be evacuated. Vacuum levels below 5 kPa are generally acceptable to minimize the amount of non-condensable gases present in the system.
3. An approximate amount of total required charge can be estimated from the steady-state models of different components. Average void fraction and ammonia mass fraction inside each component and accumulators can be calculated and used to estimate the amount of ammonia and water to be initially used for charging the system.
4. After evacuating the system, first liquid water is charged from the inlet manifold at the outlet of the absorber. Following that, liquid, high-pressure ammonia is allowed to enter through the same manifold. Due to sudden expansion from high pressure to almost vacuum, ammonia enthalpy and temperature will drop, causing condensation and freezing of ambient moisture on the outside surfaces of the inlet

manifold and the absorber. Initially, the ammonia charging process is slow to allow for mixing of ammonia in water. Rapid charging can cause very low temperatures and can lead to freezing of water in the coupling fluid channels of the absorber. As the system pressure increases, ammonia can be allowed to flow rapidly, and the charging process be completed. The system presented in this study was initially charged with 1.25 kg each of ammonia and water.

- **Shakedown Testing and Troubleshooting**

1. After charging a new system for the first time, it is beneficial to operate the system in manual mode. This would bypass automated control actions and prevent the system from entering unfavorable operating modes.
2. As the initial charge estimates can be inaccurate, the initial phase of experiments involves adjusting the charge and removal of trace amounts of non-condensable gases.
3. Non-condensable gases can be removed from the discharge ports located on the top of each accumulator during quasi-steady operation of the system. The valves should be opened slowly with a hose connection terminating in a bucket filled with water. The gases should be released until no more bubbles rise to the surface indicating that the vapor being released is then ammonia vapor which readily dissolves in water.
4. Shakedown operation of the system should focus on achieving the design heat source temperature and flow rate and the flow rate of the concentrated solution based on the cycle model. This sets the hydrodynamic and heat transfer performance in the desorber. The refrigerant valve should be closed ~80-85%

during startup to allow for buildup of pressure differential in the system. Initially, the dilute solution valve should be wide open to allow for fluid to circulate in the system and heat up. As the absorber solution outlet heats up, the circulation of cooling water/air through the absorber and the condenser should be started. As the heat source temperature and solution flow rate are increased gradually to their design conditions, the refrigerant vapor temperature entering the rectifier and the condenser will increase. When the vapor temperature starts to increase, the dilute solution valve should be gradually closed to allow the generated refrigerant to move into the refrigerant accumulator downstream of the condenser. As the refrigerant is generated and accumulated, pressure differential begins to develop in the system and the refrigerant valve can be gradually opened to allow cooling in the evaporator.

5. Charge adjustment should be carefully performed along with real-time analysis of system performance. Typical indicators of excess charge in the system are desorber fluctuations and pressure swings in the system. First the desorber fluctuations are discussed.
6. Excess charge in the system is typically stored in the accumulators and the desorber. If the system has excess water, the desorber performance will most likely be unsteady as heat input in the system will cause liquid to spill-over from the top of the desorber. This is indicated by rapid increase in the temperature of the fluid exiting the desorber and the rectifier. This phenomenon increases the water content in the condenser-evaporator side of the system. Once the liquid has spilled over, the system pressures decrease because of more homogeneous mass

fractions existing in different parts of the system. The system stabilizes at this operating point and the cycle repeats itself unless some correction in the amount of charge is performed. Typical approaches for mitigating this situation include gradually releasing the concentrated solution and dilute solution from the system.

7. Another feature of the situation with excess total charge in the system is indicated by the presence of very large amounts of liquids in the accumulators. Especially if the solution accumulator at the outlet of the absorber is almost full, it is indicated by pressure oscillations on the analog pressure gauge installed on the low side. The oscillations occur due to the pump operation and a lack of vapor volume in the accumulator to serve as a damping agent.
8. On the other hand, there can be a situation with excess ammonia present in the system. This is typically indicated by rapid rise in system pressures upon application of heat and above design values of the low-side pressure. Often this can be adjusted by adding more water in the system and then removing some concentrated solution from the system to adjust the total charge quantity. Another indication of excess ammonia in the system can be too much refrigerant storage in the refrigerant accumulator. This is observed through the glass-sight on the accumulator. In this case, some liquid refrigerant is released from the accumulator until steady level is obtained.
9. After initial charge adjustments, performance of individual components should be evaluated. The objective is to achieve, as closely as possible, the state-points determined in the cycle model. The ammonia-water side, heat source and heat sink temperatures should be maintained near design values. The flow rates of

coupling fluids and solution flow rate in the system can be adjusted to achieve the desired performance.

10. Typically, the condenser, RPC, rectifier and SHX perform near design. The major bottlenecks are encountered in the absorber, desorber and the evaporator. The performance of the evaporator can be evaluated by the cooling capacity as measured on the coupling fluid stream and by observing the temperature glide. Once the refrigerant concentration is determined from the rectifier and the desired flow rate and low-side pressure are established, the evaporator should have the heat transfer area required to achieve the cooling capacity and the temperature glide. If the temperature glide is smaller than the designed value, the evaporator is undersized, and vice-versa.
11. The performance of the absorber and the desorber can be coupled. The desorber generates the refrigerant vapor and establishes the concentration of the dilute solution stream. The absorber recombines the dilute solution and the refrigerant stream to generate the concentrated solution with its concentration determined by the mass flow rate and concentration of these two streams. If the absorber is limited by heat and mass transfer area, the desired concertation in the concentrated solution will be achieved at an absorber pressure higher than design conditions. This would adversely affect the cooling capacity. The solution is to either increase the absorber performance through additional heat and mass transfer area or reduce the refrigerant flow rate to reduce the absorber pressure. However, as the concentration of the concentrated solution decreases, the desorber performance also deteriorates. Therefore, a careful compromise is

established between the two components to achieve the design performance as closely as possible.

12. Finally, the solution flow rate is a good parameter to tune system capacity. It should be traversed until the limit of flooding is achieved in the desorber. The solution flow rate should be maintained below that limit at all operating conditions, but if the system is operating well below the flooding limit, the system capacity can be increased by increasing the solution flow rate. It also helps lower the absorber pressure, and therefore assists in lowering the refrigerant temperature in the evaporator.

Figure A4.1 shows the variation in the system capacity during shakedown testing. It shows the effects of many of the pointers discussed above. The major performance improvement occurs because of the charge adjustments to achieve the desired concentrations in different components of the system and the total amount of charge. The other important factor is the solution flow rate and as shown earlier in Chapter 6, it has a significant impact on the overall system capacity.

Finally, Table A4.1 summarizes the controller parameters for the coolant loop connected to the evaporator and the chiller valve coupling the lab chiller to the cooling water loop connected to the absorber and the condenser. Similar to the system controls, these loops also utilize a PI feedback loop to track the set-point temperature values.

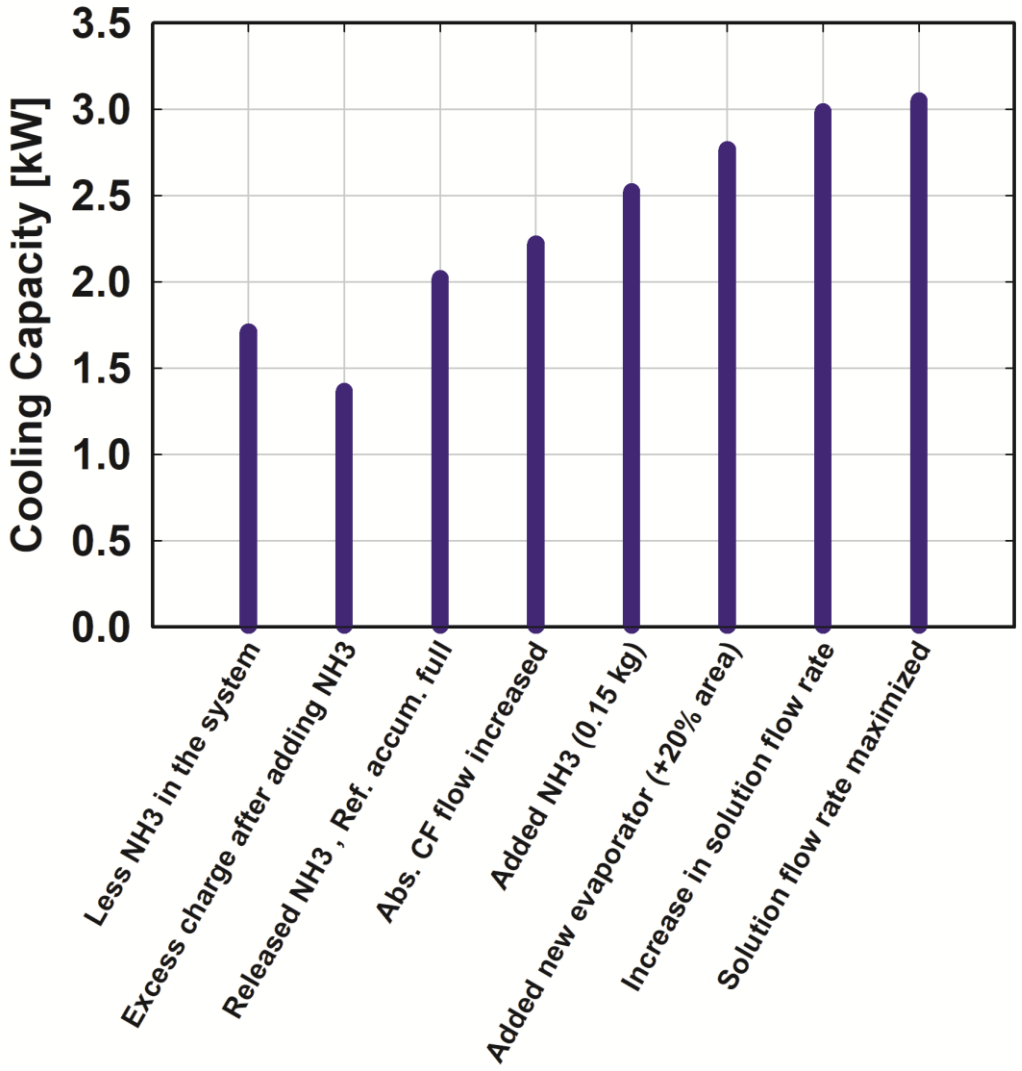

Figure A4.1: System performance variation during shakedown testing

Table A4.1: Parameters of heat source and sink control loops

Control Loop	Proportional gain (K_p)	Integral gain (K_i)	Sample Time (s)	Actuator Limits
Evaporator Coolant Heater	10	0.2 s	6	0 – 90%
Chiller Valve Control	2	0.01 s	6	25 – 100%

APPENDIX V: AUTOMATION OF ABSORPTION SYSTEMS

This section presents the details of automation as implemented on a packaged prototype absorption chiller driven using waste-heat from a diesel engine exhaust stream and directly coupled to ambient air for heat rejection. The packaged system controls include algorithms for automated operation from start-up, maintaining steady-state, and shutdown. The control sequence is shown in Figure A5.1.

After receiving the command for start-up, the desorber heat input is activated. Key temperatures and pressures are monitored to initiate several steps in the start-up sequence. When the desorber exhaust inlet temperature, which is simulated by an air-heater assembly, increases above 90°C, the solution pump is switched on. During the start-up phase, as the system pressures start to increase with heat input rate, the expansion valves are actuated as a linear or quadratic function of pressure difference in the system and closed very gradually from wide open positions. This allows for a smoother operation of the valve based on flow characteristics instead of controlling other variables such as evaporator temperature glide or dilute solution outlet temperature from the desorber. As the working fluid is circulated in the system, the fans are switched on when the concentrated solution exiting the absorber reaches a temperature of 30°C. The evaporator chilled water pump is switched on when the refrigerant temperature entering the evaporator goes below 2°C. The refrigerant temperature at the inlet of the condenser is used to switch to steady-state operation. When the temperature of the refrigerant increases over 45°C, the program switches to steady-state operation.

During steady-state, the expansion valves are regulated using a PI feedback loop. The refrigerant expansion valve can control the evaporator temperature glide to optimize the evaporator performance or to the evaporator inlet temperature for a set temperature. The dilute solution valve can either control the dilute solution temperature exiting the desorber or the flow rate based on flow characteristics of the valve.

The shutdown sequence is commenced if the operator initiates the shutdown sequence manually, or if there is a high-pressure signal or indication of any equipment failure as indicated by current switches. During shutdown, the heat input in the system is turned off, valves are allowed to open based on the pressure difference in the system, and the concentration solution is allowed to circulate until the pressure and temperature reach safe values. At that point, the fans and pumps are turned off.

During all the stages of the program, pressure switch and equipment failure conditions supersede the automated logic and in the event of any of those situations, the program goes into the shutdown mode to prevent any damage to the heat exchangers or equipment. This control logic is programmed in National Instruments® LabVIEW™ software and is implemented as a standalone code that does not require manual monitoring. The local controller unit on the unit performs the tasks of monitoring and control. The algorithm was tested extensively on the packaged unit and several operation scenarios were simulated to verify the correct sequence of operation.

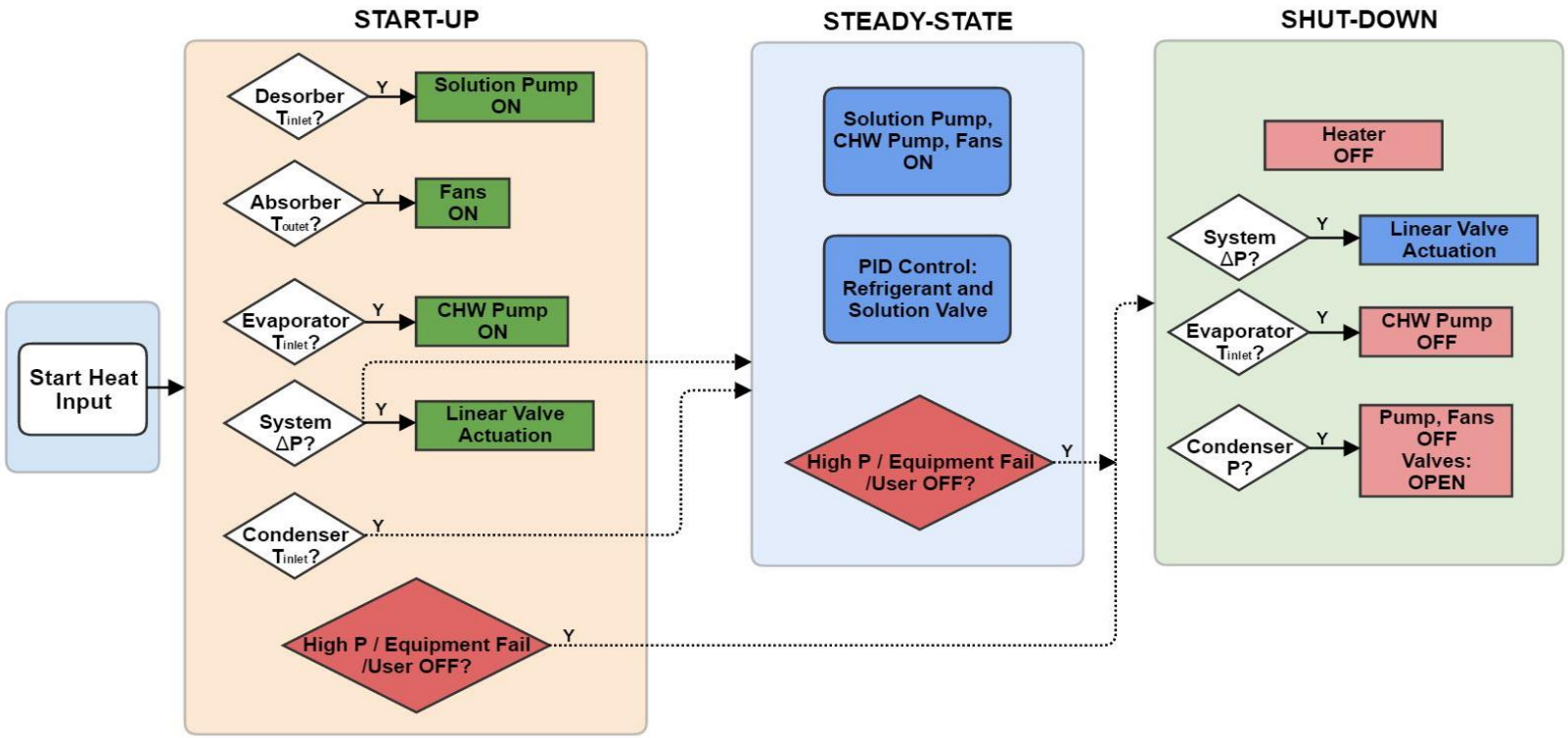

Figure A5.1: Packaged unit control algorithm flowchart

REFERENCES

Afram, A. and F. Janabi-Sharifi (2014a), "Review of Modeling Methods for HVAC Systems," *Applied Thermal Engineering* Vol. 67(1–2) pp. 507-519 DOI: http://dx.doi.org/10.1016/j.applthermaleng.2014.03.055.

Afram, A. and F. Janabi-Sharifi (2014b), "Theory and Applications of HVAC Control Systems – a Review of Model Predictive Control (MPC)," *Building and Environment* Vol. 72 pp. 343-355 DOI: http://dx.doi.org/10.1016/j.buildenv.2013.11.016.

Alvares, S. and C. Trepp (1987), "Simulation of a Solar Driven Aqua-Ammonia Absorption Refrigeration System Part 1: Mathematical Description and System Optimization," *International Journal of Refrigeration* Vol. 10(1) pp. 40-48 DOI: https://doi.org/10.1016/0140-7007(87)90095-8.

Anand, D. K., R. W. Allen and B. Kumar (1982), "Transient Simulation of Absorption Machines," *Journal of Solar Energy Engineering* Vol. 104(3) pp. 197-203 DOI: 10.1115/1.3266302.

Anderson, B. D. O. (1993), "Controller Design: Moving from Theory to Practice," *IEEE Control Systems* Vol. 13(4) pp. 16-25 DOI: 10.1109/37.229554.

Aprea, C., R. Mastrullo and C. Renno (2004), "Fuzzy Control of the Compressor Speed in a Refrigeration Plant," *International Journal of Refrigeration* Vol. 27(6) pp. 639-648 DOI: https://doi.org/10.1016/j.ijrefrig.2004.02.004.

ARI (1993). *Innovative Air Conditioning and Refrigeration Research: Meeting Global Opportunities*. Arlington, Virginia, Air-Conditioning and Refrigeration Institute.

Beghi, A. and L. Cecchinato (2009), "A Simulation Environment for Dry-Expansion Evaporators with Application to the Design of Autotuning Control Algorithms for Electronic Expansion Valves," *International Journal of Refrigeration* Vol. 32(7) pp. 1765-1775 DOI: http://dx.doi.org/10.1016/j.ijrefrig.2009.06.004.

Bendapudi, S. and J. E. Braun (2002). *A Review of Literature on Dynamic Models of Vapor Compression Equipment*. Atlanta, GA, ASHRAE Report #4036-5.

Bendapudi, S., J. E. Braun and E. A. Groll (2005), "Dynamic Model of a Centrifugal Chiller System-Model Development, Numerical Study, and Validation," *ASHRAE Transactions* Vol. 111(1) pp. 132-148.

Bendapudi, S., J. E. Braun and E. A. Groll (2008), "A Comparison of Moving-Boundary and Finite-Volume Formulations for Transients in Centrifugal Chillers," *International Journal of Refrigeration* Vol. 31(8) pp. 1437-1452 DOI: http://dx.doi.org/10.1016/j.ijrefrig.2008.03.006.

Bequette, B. W. (1998). *Process Dynamics : Modeling, Analysis, and Simulation*. Upper Saddle River, NJ, Prentice Hall PTR.

Bian, J., R. Radermacher and D. Moran (2005), "Transient Simulation of an Absorption Chiller in a Chp System," *Proceedings of Int. Sorption Heat Pump Conference*, Denver, USA.

Bong, T., K. Ng and A. Tay (1987), "Performance Study of a Solar-Powered Air-Conditioning System," *Solar Energy* Vol. 39(3) pp. 173-182 DOI: https://doi.org/10.1016/S0038-092X(87)80025-7.

Bonilla, J., S. Dormido and F. E. Cellier (2015), "Switching Moving Boundary Models for Two-Phase Flow Evaporators and Condensers," *Communications in Nonlinear Science and Numerical Simulation* Vol. 20(3) pp. 743-768 DOI: http://dx.doi.org/10.1016/j.cnsns.2014.06.035.

Borg, S. P. and N. J. Kelly (2012), "The Development and Calibration of a Generic Dynamic Absorption Chiller Model," *Energy and Buildings* Vol. 55 pp. 533-544 DOI: http://dx.doi.org/10.1016/j.enbuild.2012.08.046.

Brenan, K. E., S. L. Campbell and L. R. Petzold (1995). *Numerical Solution of Initial-Value Problems in Differential-Algebraic Equations*, SIAM.

Broersen, P. M. T. and M. F. G. van der Jagt (1980), "Hunting of Evaporators Controlled by a Thermostatic Expansion Valve," *Journal of Dynamic Systems, Measurement, and Control* Vol. 102(2) pp. 130-135 DOI: 10.1115/1.3149591.

Buehler, L. (1968), "Capacity Control," *ASHRAE Journal* Vol. 10(11) pp. 39-44.

Butz, D. and K. Stephan (1989), "Dynamic Behavior of an Absorption Heat Pump," *International Journal of Refrigeration* Vol. 12(4) pp. 204-212 DOI: http://dx.doi.org/10.1016/0140-7007(89)90045-5.

Cai, W., M. Sen and S. Paolucci (2012), "Dynamic Simulation of an Ammonia–Water Absorption Refrigeration System," *Industrial & Engineering Chemistry Research* Vol. 51(4) pp. 2070-2076 DOI: 10.1021/ie200673f.

Cecchinato, L. and F. Mancini (2012), "An Intrinsically Mass Conservative Switched Evaporator Model Adopting the Moving-Boundary Method," *International Journal of Refrigeration* Vol. 35(2) pp. 349-364 DOI: http://dx.doi.org/10.1016/j.ijrefrig.2011.10.007.

Chen, X., M. Anjanappa, C. B. Panchal, M. Mattingly, G. Anand and D. Erickson (2002), "PC-Based Control for Prototype Absorption Heat Pump," *International Sorption Heat Pump Conference*, Shanghai, China, pp. 124-129.

Chi, J. and D. Didion (1982), "A Simulation Model of the Transient Performance of a Heat Pump," *International Journal of Refrigeration* Vol. 5(3) pp. 176-184 DOI: http://dx.doi.org/10.1016/0140-7007(82)90099-8.

Chow, T., G. Zhang, Z. Lin and C. Song (2002), "Global Optimization of Absorption Chiller System by Genetic Algorithm and Neural Network," *Energy and Buildings* Vol. 34(1) pp. 103-109 DOI: https://doi.org/10.1016/S0378-7788(01)00085-8.

Courant, R., K. Friedrichs and H. Lewy (1928), "Über Die Partiellen Differenzengleichungen Der Mathematischen Physik," *Mathematische annalen* Vol. 100(1) pp. 32-74

Delahanty, J. C. (2015). *Desorption of Ammonia-Water Mixtures in Microscale Geometries for Miniaturized Absorption Systems*, Georgia Institute of Technology.

Delahanty, J. C., S. Garimella and M. A. Garrabrant (2015), "Design of Compact Microscale Geometries for Ammonia–Water Desorption," *Science and Technology for the Built Environment* Vol. 21(3) pp. 365-374 DOI: 10.1080/23744731.2015.1015906.

Den Braven, K., K. Herold, V. Mei, D. O Neal and S. Penoncello (1993), "Improving Heat Pumps and Air Conditioning," *Mechanical Engineering* Vol. 115(9) p. 98.

Determan, M. D. and S. Garimella (2011), "Ammonia–Water Desorption Heat and Mass Transfer in Microchannel Devices," *International Journal of Refrigeration* Vol. 34(5) pp. 1197-1208 DOI: http://dx.doi.org/10.1016/j.ijrefrig.2011.02.004.

Determan, M. D. and S. Garimella (2012), "Design, Fabrication, and Experimental Demonstration of a Microscale Monolithic Modular Absorption Heat Pump," *Applied Thermal Engineering* Vol. 47 pp. 119-125 DOI: http://dx.doi.org/10.1016/j.applthermaleng.2011.10.043.

Dhar, M. and W. Soedel (1979), "Transient Analysis of a Vapor Compression Refrigeration System," *Proceedings of the 15th International Congress of Refrigeration*, Venice, Italy, pp. 23-29.

Didion, D. and R. Radermacher (1984), "Part-Load Performance Characteristics of Residential Absorption Chillers and Heat Pump," *International Journal of Refrigeration* Vol. 7(6) pp. 393-398 DOI: http://dx.doi.org/10.1016/0140-7007(84)90011-2.

EIA (2014). *United States Energy Information Administration: Annual Energy Outlook.*

EIA (2016). *United States Energy Information Administration: Monthly Energy Review*.

Ekren, O., S. Sahin and Y. Isler (2010), "Comparison of Different Controllers for Variable Speed Compressor and Electronic Expansion Valve," *International Journal of*

Refrigeration Vol. 33(6) pp. 1161-1168 DOI: https://doi.org/10.1016/j.ijrefrig.2010.05.005.

Eldredge, B. D., B. P. Rasmussen and A. G. Alleyne (2008), "Moving-Boundary Heat Exchanger Models with Variable Outlet Phase," *Journal of Dynamic Systems, Measurement, and Control* Vol. 130(6) pp. 061003-061003-061012 DOI: 10.1115/1.2977466.

Elliott, M. S. and B. P. Rasmussen (2010), "On Reducing Evaporator Superheat Nonlinearity with Control Architecture," *International Journal of Refrigeration* Vol. 33(3) pp. 607-614 DOI: http://dx.doi.org/10.1016/j.ijrefrig.2009.12.013.

Elmqvist, H., D. Brück and M. Otter (1996), "Dymola-User's Manual," *Dynasim AB, Research Park Ideon, Lund, Sweden.*

Evola, G., N. Le Pierrès, F. Boudehenn and P. Papillon (2013), "Proposal and Validation of a Model for the Dynamic Simulation of a Solar-Assisted Single-Stage LiBr/Water Absorption Chiller," *International Journal of Refrigeration* Vol. 36(3) pp. 1015-1028 DOI: http://dx.doi.org/10.1016/j.ijrefrig.2012.10.013.

Fernández-Seara, J., A. Vales and M. Vázquez (1998), "Heat Recovery System to Power an Onboard NH3-H2O Absorption Refrigeration Plant in Trawler Chiller Fishing Vessels," *Applied Thermal Engineering* Vol. 18(12) pp. 1189-1205 DOI: http://dx.doi.org/10.1016/S1359-4311(98)00001-5.

Fernández-Seara, J. and M. Vázquez (2001), "Study and Control of the Optimal Generation Temperature in NH3–H2O Absorption Refrigeration Systems," *Applied Thermal Engineering* Vol. 21(3) pp. 343-357 DOI: http://dx.doi.org/10.1016/S1359-4311(00)00047-8.

Finn, D. P. and C. J. Doyle (2000), "Control and Optimization Issues Associated with Algorithm-Controlled Refrigerant Throttling Devices," *ASHRAE Transactions* Vol. 106 p. 524.

Fu, D. G., G. Poncia and Z. Lu (2006), "Implementation of an Object-Oriented Dynamic Modeling Library for Absorption Refrigeration Systems," *Applied Thermal Engineering* Vol. 26(2–3) pp. 217-225 DOI: http://dx.doi.org/10.1016/j.applthermaleng.2005.05.008.

Gani, R., C. A. Ruiz and I. T. Cameron (1986), "A Generalized Model for Distillation Columns—I," *Computers & Chemical Engineering* Vol. 10(3) pp. 181-198 DOI: http://dx.doi.org/10.1016/0098-1354(86)85001-3.

Garcıa-Valladares, O., C. Pérez-Segarra and J. Rigola (2004), "Numerical Simulation of Double-Pipe Condensers and Evaporators," *International Journal of Refrigeration* Vol. 27(6) pp. 656-670 DOI: https://doi.org/10.1016/j.ijrefrig.2004.01.006.

Garcia, C. E., D. M. Prett and M. Morari (1989), "Model Predictive Control: Theory and Practice—a Survey," *Automatica* Vol. 25(3) pp. 335-348 DOI: https://doi.org/10.1016/0005-1098(89)90002-2.

Garimella, S., C. M. Keinath, J. C. Delahanty, D. C. Hoysall, M. A. Staedter, A. Goyal and M. A. Garrabrant (2016), "Development and Demonstration of a Compact Ammonia–Water Absorption Heat Pump Prototype with Microscale Features for Space-Conditioning Applications," *Applied Thermal Engineering* Vol. 102 pp. 557-564 DOI: http://dx.doi.org/10.1016/j.applthermaleng.2016.03.169.

Goyal, A., A. S. Rattner and S. Garimella (2015), "Model-Based Feedback Control of an Ammonia-Water Absorption Chiller," *Science and Technology for the Built Environment* Vol. 21(3) pp. 357-364 DOI: https://doi.org/10.1080/10789669.2014.982412.

Grald, E. W. and J. W. MacArthur (1992), "A Moving-Boundary Formulation for Modeling Time-Dependent Two-Phase Flows," *International Journal of Heat and Fluid Flow* Vol. 13(3) pp. 266-272 DOI: https://doi.org/10.1016/0142-727X(92)90040-G.

Gruhle, W. D. and R. Isermann (1985), "Modeling and Control of a Refrigerant Evaporator," *Journal of Dynamic Systems, Measurement, and Control* Vol. 107(4) pp. 235-240 DOI: 10.1115/1.3140728.

He, X.-D., S. Liu and H. H. Asada (1997), "Modeling of Vapor Compression Cycles for Multivariable Feedback Control of HVAC Systems," *Journal of Dynamic Systems, Measurement, and Control* Vol. 119(2) pp. 183-191 DOI: 10.1115/1.2801231.

He, X.-D., S. Liu, H. H. Asada and H. Itoh (1998), "Multivariable Control of Vapor Compression Systems," *HVAC&R Research* Vol. 4(3) pp. 205-230 DOI: 10.1080/10789669.1998.10391401.

Hermes, C. J. and C. Melo (2008), "A First-Principles Simulation Model for the Start-up and Cycling Transients of Household Refrigerators," *International Journal of Refrigeration* Vol. 31(8) pp. 1341-1357 DOI: https://doi.org/10.1016/j.ijrefrig.2008.04.003.

Herold, K. E., R. Radermacher and S. A. Klein (2016). *Absorption Chillers and Heat Pumps*, CRC Press.

IEA (2018). *The Future of Cooling: Opportunities for Energy-Efficient Air Conditioning*, International Energy Agency.

Incropera, F. P., A. S. Lavine, T. L. Bergman and D. P. DeWitt (2007). *Fundamentals of Heat and Mass Transfer*, Wiley.

Iranmanesh, A. and M. A. Mehrabian (2013), "Dynamic Simulation of a Single-Effect LiBr–H2O Absorption Refrigeration Cycle Considering the Effects of Thermal

Masses," *Energy and Buildings* Vol. 60 pp. 47-59 DOI: http://dx.doi.org/10.1016/j.enbuild.2012.12.015.

Jain, N. and A. Alleyne (2015), "Exergy-Based Optimal Control of a Vapor Compression System," *Energy Conversion and Management* Vol. 92 pp. 353-365 DOI: http://dx.doi.org/10.1016/j.enconman.2014.12.014.

Jain, N. and A. G. Alleyne (2011), "Thermodynamics-Based Optimization and Control of Vapor-Compression Cycle Operation: Optimization Criteria," *American Control Conference (ACC), 2011*, IEEE, pp. 1352-1357.

Jensen, J. B. and S. Skogestad (2007), "Optimal Operation of Simple Refrigeration Cycles: Part I: Degrees of Freedom and Optimality of Sub-Cooling," *Computers & Chemical Engineering* Vol. 31(5-6) pp. 712-721 DOI: https://doi.org/10.1016/j.compchemeng.2006.12.003.

Jeong, S. (1999), "A Numerical Study on Dynamic Behavior of a Solar Absorption Cooling System," *International Sorption Heat Pump Conference*, Munich, Germany, pp. 173-180.

Jeong, S., B. H. Kang and S. W. Karng (1998), "Dynamic Simulation of an Absorption Heat Pump for Recovering Low Grade Waste Heat," *Applied Thermal Engineering* Vol. 18(1–2) pp. 1-12 DOI: http://dx.doi.org/10.1016/S1359-4311(97)00040-9.

Jia, X., C. P. Tso, P. K. Chia and P. Jolly (1995), "A Distributed Model for Prediction of the Transient Response of an Evaporator," *International Journal of Refrigeration* Vol. 18(5) pp. 336-342 DOI: http://dx.doi.org/10.1016/0140-7007(95)00015-4.

Kakac, S., R. K. Shah and W. Aung (1987). *Handbook of Single-Phase Convective Heat Transfer*, John Wiley and Sons Inc.,New York, NY.

Karimi, H. and F. Yousefi (2007), "Correlation of Vapour Liquid Equilibria of Binary Mixtures Using Artificial Neural Networks," *Chinese Journal of Chemical Engineering* Vol. 15(5) pp. 765-771 DOI: http://dx.doi.org/10.1016/S1004-9541(07)60160-8.

Kaushik, S., N. Sheridan, K. Lam and S. Kaul (1985), "Dynamic Simulation of an Ammonia-Water Absorption Cycle Solar Heat Pump with Integral Refrigerant Storage," *Journal of Heat Recovery Systems* Vol. 5(2) pp. 101-116 DOI: https://doi.org/10.1016/0198-7593(85)90042-6.

Keinath, C. M. (2015). *Direct-Fired Heat Pump for Multi-Pass Water Heating Using Microchannel Heat and Mass Exchangers*. Georgia Insitute of Technology.

Keinath, C. M., D. Hoysall, J. C. Delahanty, M. D. Determan and S. Garimella (2015), "Experimental Assessment of a Compact Branched Tray Generator for Ammonia–Water Desorption," *Science and Technology for the Built Environment* Vol. 21(3) pp. 348-356 DOI: 10.1080/23744731.2014.1000797.

Kim, B. and J. Park (2007), "Dynamic Simulation of a Single-Effect Ammonia–Water Absorption Chiller," *International Journal of Refrigeration* Vol. 30(3) pp. 535-545 DOI: https://doi.org/10.1016/j.ijrefrig.2006.07.004.

Kim, M., M. S. Kim and J. D. Chung (2004), "Transient Thermal Behavior of a Water Heater System Driven by a Heat Pump," *International Journal of Refrigeration* Vol. 27(4) pp. 415-421 DOI: https://doi.org/10.1016/j.ijrefrig.2003.11.009.

Kirkman, C. G. (1968), "Automatic Hot-Gas by-Pass,," *Air Conditioning, Heating and Ventilation* Vol. 65(1) pp. 64-68.

Klein, S. (2016). *Engineering Equation Solver (EES), Academic Commercial, F-Chart Software*.

Klein, S., W. Beckman, J. Mitchell, J. Duffie, N. Duffie, T. Freeman, J. Mitchell, J. Braun, B. Evans and J. Kummer (2017). *TRNSYS 18 – a Transient System Simulation Program*. Solar Energy Laboratory. University of Wisconsin-Madison.

Koeppel, E. A., S. A. Klein, J. W. Mitchell and B. A. Flake (1995), "Optimal Supervisory Control of an Absorption Chiller System," *HVAC&R Research* Vol. 1(4) pp. 325-340 DOI: 10.1080/10789669.1995.10391328.

Kohlenbach, P. (2006). *Solar Cooling with Absorption Chillers: Control Strategies and Transient Chiller Performance*, TU Berlin.

Kohlenbach, P. and F. Ziegler (2008a), "A Dynamic Simulation Model for Transient Absorption Chiller Performance. Part I: The Model," *International Journal of Refrigeration* Vol. 31(2) pp. 217-225 DOI: http://dx.doi.org/10.1016/j.ijrefrig.2007.06.009.

Kohlenbach, P. and F. Ziegler (2008b), "A Dynamic Simulation Model for Transient Absorption Chiller Performance. Part II: Numerical Results and Experimental Verification," *International Journal of Refrigeration* Vol. 31(2) pp. 226-233 DOI: http://dx.doi.org/10.1016/j.ijrefrig.2007.06.010.

Koury, R., L. Machado and K. Ismail (2001), "Numerical Simulation of a Variable Speed Refrigeration System," *International Journal of Refrigeration* Vol. 24(2) pp. 192-200 DOI: https://doi.org/10.1016/S0140-7007(00)00014-1.

Kühn, A., J. Corrales Ciganda and F. Ziegler (2008), "Comparison of Control Strategies of Solar Absorption Chillers," *Proceedings of the 1st International Conference on Solar Heating, Cooling and Buildings (Eurosun)*, pp. 7-10.

Larsen, L. F. S. (2006). *Model Based Control of Refrigeration Systems*. Department of Control Engineering. Denmark, Aalborg University.

Leducq, D., J. Guilpart and G. Trystram (2003), "Low Order Dynamic Model of a Vapor Compression Cycle for Process Control Design," *Journal of Food Process Engineering* Vol. 26(1) pp. 67-91 DOI: 10.1111/j.1745-4530.2003.tb00590.x.

Leducq, D., J. Guilpart and G. Trystram (2006), "Non-Linear Predictive Control of a Vapour Compression Cycle," *International Journal of Refrigeration* Vol. 29(5) pp. 761-772 DOI: http://dx.doi.org/10.1016/j.ijrefrig.2005.12.005.

Lee, S., L. K. Bohra, S. Garimella and A. K. Nagavarapu (2012), "Measurement of Absorption Rates in Horizontal-Tube Falling-Film Ammonia-Water Absorbers," *International Journal of Refrigeration* Vol. 35(3) pp. 613-632 DOI: http://dx.doi.org/10.1016/j.ijrefrig.2011.08.011.

Lei, Z. and M. Zaheeruddin (2005), "Dynamic Simulation and Analysis of a Water Chiller Refrigeration System," *Applied Thermal Engineering* Vol. 25(14) pp. 2258-2271 DOI: https://doi.org/10.1016/j.applthermaleng.2005.01.002.

Lemmon, E., M. Huber and M. McLinden (2013), "NIST Reference Database 23: Reference Fluid Thermodynamic and Transport Properties-REFPROP, Version 9.1," *Standard Reference Data Program.*

Li, B. and A. G. Alleyne (2010), "A Dynamic Model of a Vapor Compression Cycle with Shut-Down and Start-up Operations," *International Journal of Refrigeration* Vol. 33(3) pp. 538-552 DOI: http://dx.doi.org/10.1016/j.ijrefrig.2009.09.011.

Li, X., J. Chen, Z. Chen, W. Liu, W. Hu and X. Liu (2004), "A New Method for Controlling Refrigerant Flow in Automobile Air Conditioning," *Applied Thermal Engineering* Vol. 24(7) pp. 1073-1085 DOI: https://doi.org/10.1016/j.applthermaleng.2003.11.005.

Li, Z. F. and K. Sumathy (2001), "Simulation of a Solar Absorption Air Conditioning System," *Energy Conversion and Management* Vol. 42(3) pp. 313-327 DOI: http://dx.doi.org/10.1016/S0196-8904(00)00057-1.

Liao, X. and R. Radermacher (2007), "Absorption Chiller Crystallization Control Strategies for Integrated Cooling Heating and Power Systems," *International journal of Refrigeration* Vol. 30(5) pp. 904-911 DOI: https://doi.org/10.1016/j.ijrefrig.2006.10.009.

Lippmann, R. (1987), "An Introduction to Computing with Neural Nets," *IEEE ASSP Magazine* Vol. 4(2) pp. 4-22.

Llopis, R., R. Cabello and E. Torrella (2008), "A Dynamic Model of a Shell-and-Tube Condenser Operating in a Vapour Compression Refrigeration Plant," *International Journal of Thermal Sciences* Vol. 47(7) pp. 926-934 DOI: http://dx.doi.org/10.1016/j.ijthermalsci.2007.06.021.

Luyben, W. L. (1989). *Process Modeling, Simulation and Control for Chemical Engineers*, McGraw-Hill Higher Education.

Luyben, W. L. (1996), "Design and Control Degrees of Freedom," *Industrial & Engineering Chemistry Research* Vol. 35(7) pp. 2204-2214 DOI: http://10.1021/ie960038d.

Ma, Z. and S. Wang (2011), "Supervisory and Optimal Control of Central Chiller Plants Using Simplified Adaptive Models and Genetic Algorithm," *Applied Energy* Vol. 88(1) pp. 198-211 DOI: http://dx.doi.org/10.1016/j.apenergy.2010.07.036.

MacArthur, J. W. and E. W. Grald (1989), "Unsteady Compressible Two-Phase Flow Model for Predicting Cyclic Heat Pump Performance and a Comparison with Experimental Data," *International Journal of refrigeration* Vol. 12(1) pp. 29-41

Maplesoft (1998). *Maple* Waterloo, Ontario.

Marc, O., F. Sinama, J.-P. Praene, F. Lucas and J. Castaing-Lasvignottes (2015), "Dynamic Modeling and Experimental Validation Elements of a 30 kw LiBr/H2O Single Effect Absorption Chiller for Solar Application," *Applied Thermal Engineering* Vol. 90 pp. 980-993 DOI: http://dx.doi.org/10.1016/j.applthermaleng.2015.07.067.

Marcinichen, J. B., T. N. d. Holanda and C. Melo (2008), "A Dual SISO Controller for a Vapor Compression Refrigeration System," *International Refrigeration and Air-conditioning Conference*, West Lafayette, IN.

MathWorks (2016). *MATLAB and Neural Network Toolbox R2016b*. Natick, MA, United States.

Matsushima, H., T. Fujii, T. Komatsu and A. Nishiguchi (2010), "Dynamic Simulation Program with Object-Oriented Formulation for Absorption Chillers (Modelling, Verification, and Application to Triple-Effect Absorption Chiller)," *International Journal of Refrigeration* Vol. 33(2) pp. 259-268 DOI: http://dx.doi.org/10.1016/j.ijrefrig.2009.07.003.

McKinley, T. L. and A. G. Alleyne (2008), "An Advanced Nonlinear Switched Heat Exchanger Model for Vapor Compression Cycles Using the Moving-Boundary Method," *International Journal of Refrigeration* Vol. 31(7) pp. 1253-1264 DOI: http://dx.doi.org/10.1016/j.ijrefrig.2008.01.012.

Mithraratne, P., N. E. Wijeysundera and T. Y. Bong (2000), "Dynamic Simulation of a Thermostatically Controlled Counter-Flow Evaporator," *International Journal of Refrigeration* Vol. 23(3) pp. 174-189 DOI: https://doi.org/10.1016/S0140-7007(99)00048-1.

Modelica Association (2010). *Modelica Standard Library*.

Mohanraj, M., S. Jayaraj and C. Muraleedharan (2012), "Applications of Artificial Neural Networks for Refrigeration, Air-Conditioning and Heat Pump Systems—a Review," *Renewable and Sustainable Energy Reviews* Vol. 16(2) pp. 1340-1358 DOI: http://dx.doi.org/10.1016/j.rser.2011.10.015.

Monné, C., S. Alonso, F. Palacín and L. Serra (2011), "Monitoring and Simulation of an Existing Solar Powered Absorption Cooling System in Zaragoza (Spain)," *Applied Thermal Engineering* Vol. 31(1) pp. 28-35 DOI: https://doi.org/10.1016/j.applthermaleng.2010.08.002.

Motta, S. F. Y. and P. A. Domanski (2000), "Performance of R-22 and Its Alternatives Working at High Outdoor Temperatures," *8th International Refrigeration Conference*, Purdue University, USA, pp. 47-54.

Munch Jensen, J. and H. Tummescheit (2002), "Moving Boundary Models for Dynamic Simulations of Two-Phase Flows," *Modelica'2002 Proceedings* pp. 235-244.

N'Tsoukpoe, K. E., N. Le Pierrès and L. Luo (2012), "Numerical Dynamic Simulation and Analysis of a Lithium Bromide/Water Long-Term Solar Heat Storage System," *Energy* Vol. 37(1) pp. 346-358 DOI: http://dx.doi.org/10.1016/j.energy.2011.11.020.

Naidu, D. S. and C. G. Rieger (2011a), "Advanced Control Strategies for Heating, Ventilation, Air-Conditioning, and Refrigeration Systems—an Overview: Part I: Hard Control," *HVAC&R Research* Vol. 17(1) pp. 2-21 DOI: 10.1080/10789669.2011.540942.

Naidu, D. S. and C. G. Rieger (2011b), "Advanced Control Strategies for HVAC&R Systems—an Overview: Part II: Soft and Fusion Control," *HVAC&R Research* Vol. 17(2) pp. 144-158 DOI: 10.1080/10789669.2011.555650.

Nanayakkara, V. K., Y. Ikegami and H. Uehara (2002), "Evolutionary Design of Dynamic Neural Networks for Evaporator Control," *International Journal of Refrigeration* Vol. 25(6) pp. 813-826 DOI: https://doi.org/10.1016/S0140-7007(01)00090-1.

Nguyen, V. D., R. R. Tan, Y. Brondial and T. Fuchino (2007), "Prediction of Vapor–Liquid Equilibrium Data for Ternary Systems Using Artificial Neural Networks," *Fluid Phase Equilibria* Vol. 254(1–2) pp. 188-197 DOI: http://dx.doi.org/10.1016/j.fluid.2007.03.014.

Nyers, J. and G. Stoyan (1994), "A Dynamical Model Adequate for Controlling the Evaporator of a Heat Pump," *International Journal of Refrigeration* Vol. 17(2) pp. 101-108 DOI: https://doi.org/10.1016/0140-7007(94)90050-7.

Ochoa, A. A. V., J. C. C. Dutra, J. R. G. Henríquez and C. A. C. dos Santos (2016), "Dynamic Study of a Single Effect Absorption Chiller Using the Pair LiBr/H2O," *Energy Conversion and Management* Vol. 108 pp. 30-42 DOI: http://dx.doi.org/10.1016/j.enconman.2015.11.009.

Outtagarts, A., P. Haberschill and M. Lallemand (1997), "The Transient Response of an Evaporator Fed through an Electronic Expansion Valve," *International Journal of Energy Research* Vol. 21(9) pp. 793-807 DOI: https://doi.org/10.1002/(SICI)1099-114X(199707)21:9<793::AID-ER297>3.0.CO;2-P.

Palau, A., E. Velo and L. Puigjaner (1999), "Use of Neural Networks and Expert Systems to Control a Gas/Solid Sorption Chilling Machine: Utilisation Des Réseaux Neuronaux Et Des Systèmes Experts Pour Réguler Une Machine Frigorifique À Sorption Gaz/Solide," *International Journal of Refrigeration* Vol. 22(1) pp. 59-66 DOI: http://dx.doi.org/10.1016/S0140-7007(97)00046-7.

Patankar, S. (1980). *Numerical Heat Transfer and Fluid Flow*, CRC Press.

Pátek, J. and J. Klomfar (1995), "Simple Functions for Fast Calculations of Selected Thermodynamic Properties of the Ammonia-Water System," *International Journal of Refrigeration* Vol. 18(4) pp. 228-234 DOI: https://doi.org/10.1016/0140-7007(95)00006-W.

Petersen, R., A. Fredenslund and P. Rasmussen (1994), "Artificial Neural Networks as a Predictive Tool for Vapor-Liquid Equilibrium," *Computers & Chemical Engineering* Vol. 18 pp. S63-S67 DOI: http://dx.doi.org/10.1016/0098-1354(94)80011-1.

Pettit, N. B. O. L., M. Willatzen and L. Ploug-Sørensen (1998), "A General Dynamic Simulation Model for Evaporators and Condensers in Refrigeration. Part II: Simulation and Control of an Evaporator," *International Journal of Refrigeration* Vol. 21(5) pp. 404-414 DOI: http://dx.doi.org/10.1016/S0140-7007(97)00092-3.

Ponton, J. W. (1994), "Degrees of Freedom Analysis in Process Control," *Chemical Engineering Science* Vol. 49(13) pp. 2089-2095 DOI: https://doi.org/10.1016/0009-2509(94)E0033-M.

Qiao, H., V. Aute and R. Radermacher (2014). *An Improved Moving Boundary Heat Exchanger Model with Pressure Drop*. International Refrigeration and Air Conditioning Conference. West Lafayette, IN Vol. Paper 1414.

Qureshi, T. Q. and S. A. Tassou (1996), "Variable-Speed Capacity Control in Refrigeration Systems," *Applied Thermal Engineering* Vol. 16(2) pp. 103-113 DOI: http://dx.doi.org/10.1016/1359-4311(95)00051-E.

Rasmussen, B. P. (2012), "Dynamic Modeling for Vapor Compression Systems—Part I: Literature Review," *HVAC&R Research* Vol. 18(5) pp. 934-955 DOI: 10.1080/10789669.2011.582916.

Rasmussen, B. P. and A. G. Alleyne (2004), "Control-Oriented Modeling of Transcritical Vapor Compression Systems," *Journal of Dynamic Systems, Measurement, and Control* Vol. 126(1) pp. 54-64 DOI: 10.1115/1.1648312.

Rasmussen, B. P. and A. G. Alleyne (2006). *Dynamic Modeling and Advanced Control of Air Conditioning and Refrigeration Systems*, Air Conditioning and Refrigeration Center. College of Engineering. University of Illinois at Urbana-Champaign.

Rattner, A. S. and S. Garimella (2016), "Fast, Stable Computation of Thermodynamic Properties of Ammonia-Water Mixtures," *International Journal of Refrigeration* Vol. 62 pp. 39-59 DOI: http://doi.org/10.1016/j.ijrefrig.2015.09.009.

Rêgo, A. T., S. M. Hanriot, A. F. Oliveira, P. Brito and T. F. U. Rêgo (2014), "Automotive Exhaust Gas Flow Control for an Ammonia–Water Absorption Refrigeration System," *Applied Thermal Engineering* Vol. 64(1–2) pp. 101-107 DOI: http://dx.doi.org/10.1016/j.applthermaleng.2013.12.018.

Rodriguez, E. and B. Rasmussen (2017), "A Comparison of Modeling Paradigms for Dynamic Evaporator Simulations with Variable Fluid Phases," *Applied Thermal Engineering* Vol. 112 pp. 1326-1342 DOI: https://doi.org/10.1016/j.applthermaleng.2016.10.131.

Rodriguez, E. and B. P. Rasmussen (2016), "A Nonlinear Reduced-Order Modeling Method for Dynamic Two-Phase Flow Heat Exchanger Simulations," *Science and Technology for the Built Environment* Vol. 22(2) pp. 164-177 DOI: 10.1080/23744731.2015.1085280.

Ryu, C. J. (2011). *Modeling and Control of a Novel Semi-Closed Gas Turbine-Absorption Combined Cycle*, University of Florida.

Sami, S. and M. Comeau (1992), "Development of a Simulation Model for Predicting Dynamic Behaviour of Heat Pump with Nonazeotropic Refrigerant Mixtures," *International Journal of Energy Research* Vol. 16(5) pp. 431-444 DOI: https://doi.org/10.1002/er.4440160509.

Sami, S. M., T. N. Duong, Y. Mercadier and N. Galanis (1987), "Prediction of the Transient Response of Heat Pumps," *ASHRAE Transactions* Vol. 93 pp. 471-490.

Schurt, L. C., C. J. L. Hermes and A. T. Neto (2009), "A Model-Driven Multivariable Controller for Vapor Compression Refrigeration Systems," *International Journal of Refrigeration* Vol. 32(7) pp. 1672-1682 DOI: http://dx.doi.org/10.1016/j.ijrefrig.2009.04.004.

Seborg, D. E., D. A. Mellichamp, T. F. Edgar and F. J. Doyle III (2010). *Process Dynamics and Control*, John Wiley & Sons.

Seem, J. E. (1998), "A New Pattern Recognition Adaptive Controller with Application to HVAC Systems," *Automatica* Vol. 34(8) pp. 969-982 DOI: http://dx.doi.org/10.1016/S0005-1098(98)00033-8.

Şencan, A. (2007), "Modeling of Thermodynamic Properties of Refrigerant/Absorbent Couples Using Data Mining Process," *Energy Conversion and Management* Vol. 48(2) pp. 470-480 DOI: http://dx.doi.org/10.1016/j.enconman.2006.06.018.

Şencan, A. and S. A. Kalogirou (2005), "A New Approach Using Artificial Neural Networks for Determination of the Thermodynamic Properties of Fluid Couples," *Energy Conversion and Management* Vol. 46(15–16) pp. 2405-2418 DOI: http://dx.doi.org/10.1016/j.enconman.2004.11.007.

Şencan, A., İ. İ. Köse and R. Selbaş (2011), "Prediction of Thermophysical Properties of Mixed Refrigerants Using Artificial Neural Network," *Energy Conversion and Management* Vol. 52(2) pp. 958-974 DOI: http://dx.doi.org/10.1016/j.enconman.2010.08.024.

Seo, J. A., Y. Shin and J. D. Chung (2012), "Dynamics and Control of Solution Levels in a High Temperature Generator for an Absorption Chiller," *International Journal of Refrigeration* Vol. 35(4) pp. 1123-1129 DOI: http://dx.doi.org/10.1016/j.ijrefrig.2012.01.020.

Shah, R., B. P. Rasmussen and A. G. Alleyne (2004), "Application of a Multivariable Adaptive Control Strategy to Automotive Air Conditioning Systems," *International Journal of Adaptive Control and Signal Processing* Vol. 18(2) pp. 199-221 DOI: 10.1002/acs.787.

Shampine, L. F. and M. W. Reichelt (1997), "The MATLAB ODE Suite," *SIAM Journal on Scientific Computing* Vol. 18(1) pp. 1-22 DOI: 10.1137/s1064827594276424.

Sharma, R., D. Singhal, R. Ghosh and A. Dwivedi (1999), "Potential Applications of Artificial Neural Networks to Thermodynamics: Vapor–Liquid Equilibrium Predictions," *Computers & Chemical Engineering* Vol. 23(3) pp. 385-390 DOI: http://dx.doi.org/10.1016/S0098-1354(98)00281-6.

Shin, Y., J. A. Seo, H. W. Cho, S. C. Nam and J. H. Jeong (2009), "Simulation of Dynamics and Control of a Double-Effect LiBr–H2O Absorption Chiller," *Applied Thermal Engineering* Vol. 29(13) pp. 2718-2725 DOI: http://dx.doi.org/10.1016/j.applthermaleng.2009.01.006.

Sibik, L. L. (1999), "An Advanced Microprocessor-Based Multi-Variable/Multi-Objective Control Design for LiBr Absorption Water Chillers," *International Sorption Heat Pump Conference*, Munich, Germany, pp. 157-167.

Singh, J., N. Singh and J. Sharma (2006), "Fuzzy Modeling and Control of HVAC Systems-a Review," *Journal of Scientific and Industrial Research* Vol. 65(6) pp. 470-477.

Skogestad, S. (1997), "Dynamics and Control of Distillation Columns: A Tutroial Introduction," *Chemical Engineering Research and Design* Vol. 75(6) pp. 539-562 DOI: http://dx.doi.org/10.1205/026387697524092.

Slotine, J.-J. E. and W. Li (1991). *Applied Nonlinear Control*, Prentice-Hall Englewood Cliffs, NJ.

Soave, G. (1972), "Equilibrium Constants from a Modified Redlich-Kwong Equation of State," *Chemical Engineering Science* Vol. 27(6) pp. 1197-1203 DOI: https://doi.org/10.1016/0009-2509(72)80096-4.

Sözen, A., E. Arcakliogˇlu and M. Özalp (2005), "Formulation Based on Artificial Neural Network of Thermodynamic Properties of Ozone Friendly Refrigerant/Absorbent Couples," *Applied Thermal Engineering* Vol. 25(11–12) pp. 1808-1820 DOI: http://dx.doi.org/10.1016/j.applthermaleng.2004.11.003.

Sözen, A., M. Özalp and E. Arcaklioğlu (2004), "Investigation of Thermodynamic Properties of Refrigerant/Absorbent Couples Using Artificial Neural Networks," *Chemical Engineering and Processing: Process Intensification* Vol. 43(10) pp. 1253-1264 DOI: http://dx.doi.org/10.1016/j.cep.2003.12.008.

Srikhirin, P., S. Aphornratana and S. Chungpaibulpatana (2001), "A Review of Absorption Refrigeration Technologies," *Renewable and Sustainable Energy Reviews* Vol. 5(4) pp. 343-372 DOI: http://dx.doi.org/10.1016/S1364-0321(01)00003-X.

Staedter, M. A. (2018). *Optimal Thermal Compressors for Miniaturized Ammonia-Water Absorption Systems*. Georgia Insitute of Technology.

Sun, D.-W. (1997), "Thermodynamic Design Data and Optimum Design Maps for Absorption Refrigeration Systems," *Applied Thermal Engineering* Vol. 17(3) pp. 211-221 DOI: http://dx.doi.org/10.1016/S1359-4311(96)00041-5.

The Mathworks Inc. (2016). *MATLAB and Simulink*. Natick, MA.

Tian, J., Q. Feng and R. Zhu (2008), "Analysis and Experimental Study of MIMO Control in Refrigeration System," *Energy Conversion and Management* Vol. 49(5) pp. 933-939 DOI: http://dx.doi.org/10.1016/j.enconman.2007.10.027.

Tillner-Roth, R. and D. G. Friend (1998), "Survey and Assessment of Available Measurements on Thermodynamic Properties of the Mixture {Water+ Ammonia}," *Journal of Physical and Chemical Reference Data* Vol. 27(1) pp. 45-61 DOI: https://doi.org/10.1063/1.556014.

Urata, S., A. Takada, J. Murata, T. Hiaki and A. Sekiya (2002), "Prediction of Vapor–Liquid Equilibrium for Binary Systems Containing Hfes by Using Artificial Neural Network," *Fluid Phase Equilibria* Vol. 199(1) pp. 63-78 DOI: https://doi.org/10.1016/S0378-3812(01)00814-7.

Vargas, J. V. C., I. Horuz, T. M. S. Callander, J. S. Fleming and J. A. R. Parise (1998), "Simulation of the Transient Response of Heat Driven Refrigerators with Continuous Temperature Control," *International Journal of Refrigeration* Vol. 21(8) pp. 648-660 DOI: http://dx.doi.org/10.1016/S0140-7007(98)00009-7.

Vargas, J. V. C. and J. A. R. Parise (1995), "Simulation in Transient Regime of a Heat Pump with Closed-Loop and on-Off Control," *International Journal of Refrigeration* Vol. 18(4) pp. 235-243 DOI: http://dx.doi.org/10.1016/0140-7007(95)96862-Z.

Vinther, K., R. J. Nielsen, K. M. Nielsen, P. Andersen, T. S. Pedersen and J. D. Bendtsen (2015a), "Absorption Cycle Heat Pump Model for Control Design," *2015 European Control Conference (ECC)* pp. 2228-2234.

Vinther, K., R. J. Nielsen, K. M. Nielsen, P. Andersen, T. S. Pedersen and J. D. Bendtsen (2015b), "Analysis of Decentralized Control for Absorption Cycle Heat Pumps," *Control Conference (ECC), 2015 European*, pp. 2235-2241.

Viswanathan, V. K., A. S. Rattner, M. D. Determan and S. Garimella (2013), "Dynamic Model for a Small-Capacity Ammonia–Water Absorption Chiller," *HVAC&R Research* Vol. 19(7) pp. 865-881 DOI: 10.1080/10789669.2013.833974.

Wang, H. and S. Touber (1991), "Distributed and Non-Steady-State Modelling of an Air Cooler," *International Journal of Refrigeration* Vol. 14(2) pp. 98-111 DOI: https://doi.org/10.1016/0140-7007(91)90082-R.

Wang, K., O. Abdelaziz, P. Kisari and E. A. Vineyard (2011), "State-of-the-Art Review on Crystallization Control Technologies for Water/LiBr Absorption Heat Pumps," *International Journal of Refrigeration* Vol. 34(6) pp. 1325-1337 DOI: http://dx.doi.org/10.1016/j.ijrefrig.2011.04.006.

Wedekind, G. L., B. L. Bhatt and B. T. Beck (1978), "A System Mean Void Fraction Model for Predicting Various Transient Phenomena Associated with Two-Phase Evaporating and Condensing Flows," *International Journal of Multiphase Flow* Vol. 4(1) pp. 97-114 DOI: http://dx.doi.org/10.1016/0301-9322(78)90029-0.

Wei, D., X. Lu, Z. Lu and J. Gu (2008), "Dynamic Modeling and Simulation of an Organic Rankine Cycle (Orc) System for Waste Heat Recovery," *Applied Thermal Engineering* Vol. 28(10) pp. 1216-1224 DOI: http://dx.doi.org/10.1016/j.applthermaleng.2007.07.019.

Willatzen, M., N. B. O. L. Pettit and L. Ploug-Sørensen (1998), "A General Dynamic Simulation Model for Evaporators and Condensers in Refrigeration. Part I: Moving-Boundary Formulation of Two-Phase Flows with Heat Exchange," *International Journal of Refrigeration* Vol. 21(5) pp. 398-403 DOI: http://dx.doi.org/10.1016/S0140-7007(97)00091-1.

Wu, C., Z. Xingxi and D. Shiming (2005), "Development of Control Method and Dynamic Model for Multi-Evaporator Air Conditioners (MEAC)," *Energy Conversion and Management* Vol. 46(3) pp. 451-465 DOI: https://doi.org/10.1016/j.enconman.2004.03.004.

Xu, Y.-j., S.-j. Zhang and Y.-h. Xiao (2016), "Modeling the Dynamic Simulation and Control of a Single Effect LiBr–H2O Absorption Chiller," *Applied Thermal Engineering* Vol. 107 pp. 1183-1191 DOI: http://dx.doi.org/10.1016/j.applthermaleng.2016.06.043.

Yao, Y., M. Huang and J. Chen (2013), "State-Space Model for Dynamic Behavior of Vapor Compression Liquid Chiller," *International Journal of Refrigeration* Vol. 36(8) pp. 2128-2147 DOI: http://dx.doi.org/10.1016/j.ijrefrig.2013.05.006.

Yao, Y., W. Wang and M. Huang (2015), "A State-Space Dynamic Model for Vapor Compression Refrigeration System Based on Moving-Boundary Formulation," *International Journal of Refrigeration* Vol. 60 pp. 174-189 DOI: https://doi.org/10.1016/j.ijrefrig.2015.07.027.

Yaqub, M. and S. M. Zubair (2001), "Capacity Control for Refrigeration and Air-Conditioning Systems: A Comparative Study," *Journal of Energy Resources Technology* Vol. 123(1) pp. 92-99.

Yebra, L. J., M. Berenguel and S. Dormido (2005), "Extended Moving Boundary Model for Two-Phase Flows," *IFAC Proceedings Volumes* Vol. 38(1) pp. 368-373 DOI: http://dx.doi.org/10.3182/20050703-6-CZ-1902.00062.

Zhang, W.-J. and C.-L. Zhang (2006), "A Generalized Moving-Boundary Model for Transient Simulation of Dry-Expansion Evaporators under Larger Disturbances," *International Journal of Refrigeration* Vol. 29(7) pp. 1119-1127 DOI: http://dx.doi.org/10.1016/j.ijrefrig.2006.03.002.

Ziegler, B. and C. Trepp (1984), "Equation of State for Ammonia-Water Mixtures," *International Journal of Refrigeration* Vol. 7(2) pp. 101-106 DOI: http://dx.doi.org/10.1016/0140-7007(84)90022-7.

Zinet, M., R. Rulliere and P. Haberschill (2012), "A Numerical Model for the Dynamic Simulation of a Recirculation Single-Effect Absorption Chiller," *Energy Conversion and Management* Vol. 62 pp. 51-63 DOI: http://dx.doi.org/10.1016/j.enconman.2012.04.007.

Zivi, S. (1964), "Estimation of Steady-State Steam Void-Fraction by Means of the Principle of Minimum Entropy Production," *Journal of Heat Transfer* Vol. 86(2) pp. 247-251 DOI: http://10.1115/1.3687113.

Zubair, S. and V. Babel (1989), "Compressor Capacity Modulation Scheme," *Heating, Piping, Air Conditioning* Vol. 61(1) pp. 135-143.